# JOURNAL OF APPLIED PHYSICS

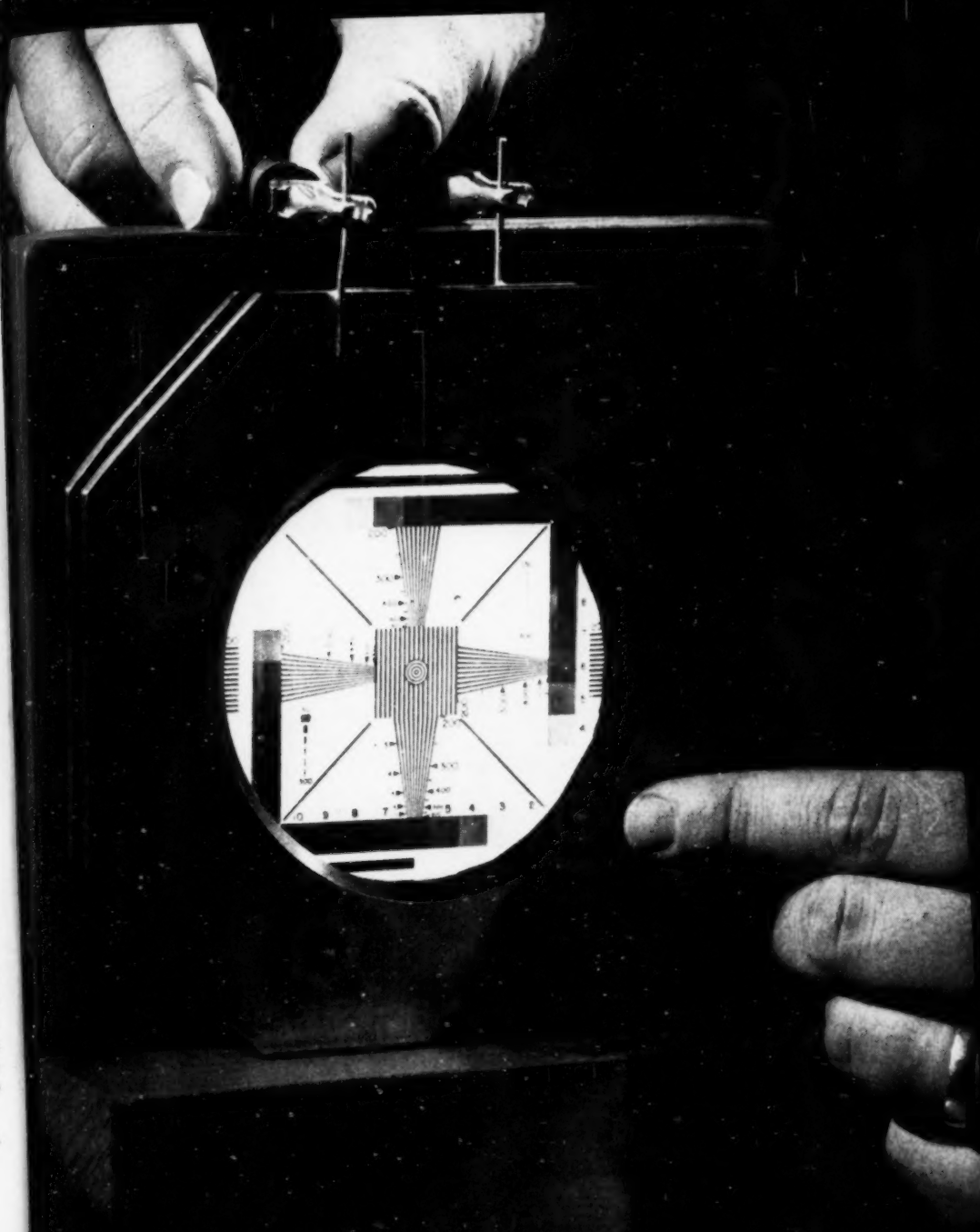

# Norelco Announces Availability...

either

## PROPORTIONAL OR SCINTILLATION DETECTORS

***...with counting rates in excess of 100,000 cps, designed to extend range of existing equipment***

The Norelco Proportional Detector is designed with a side window to provide a homegeneous field for obtaining true distribution of pulse energies while maintaining the same efficiency as the Geiger Counter at all wavelengths. *It is the only high speed detector suitable for soft x-radiation to wavelengths below 3 A°.* It will maintain a very high counting rate with linear response—in excess of 100,000 counts per second.

The Scintillation Detector possesses *a relatively uniform response at all wavelengths shorter than 3 A°.* Carefully selected scintillation crystals transform X-ray quanta to light which strikes a photomultiplier tube. Overall efficiency is high; the thin crystal absorbs almost 100% over the entire X-ray spectrum up to 100 KV.

Illustrating maximum utility, either of these detectors may be easily interchanged with Geiger tubes. Norelco electronics are available to amplify voltage level of pulses. The speed of these detectors provide high accuracies and short reading times. Because of the *linearity* of the amplifier used, the addition of a pulse height analyzer permits the detectors to be used as a secondary monochromator to increase signal-to-noise ratio, thus, discriminating against radiations other than the wavelength selected by the crystal or specimen.

Norelco PRODUCT NORTH AMERICAN

*Serving Science and Industry*

PHILIPS COMPANY, INC.

750 South Fulton Avenue, Mount Vernon, N. Y.

In Canada: Rogers Majestic Electronics Ltd., 11-19 Brentcliffe Road, Leaside, Toronto 17, Ontario

# JOURNAL OF APPLIED PHYSICS

Vol. 26, No. 3 MARCH, 1955


## *In This Issue*


Page

**Review of Measurements of the Resonance Absorption of Neutrons by Uranium in Bulk** . . . . . E. Creutz, H. Jupnik, T. Snyder, and E. P. Wigner 257

**Resonance Absorption of Neutrons by Spheres** . . . E. P. Wigner, E. Creutz, H. Jupnik, and T. Snyder 260

**Effect of Geometry on Resonance Absorption of Neutrons by Uranium** . . . . . E. Creutz, H. Jupnik, T. Snyder, and E. P. Wigner 271

**Effect of Temperature on Total Resonance Absorption of Neutrons by Spheres of Uranium Oxide** . . . . . E. Creutz, H. Jupnik, and E. P. Wigner 276

**Temperature Dependent Creep in Zinc Crystals** . . . . . Donald O. Thompson 280

**Creep of Zinc Crystals** . . . . . E. P. T. Tyndall, R. A. Artman, C. A. Wert, and Robert Eisner 286

**Analysis of Scintillation Spectrometer Observations of the Penetration of $Cs^{137}$ Gamma Radiation through Water** . . . . . R. B. Theus, L. A. Beach, and W. R. Faust 294

**Bistatic Radar Cross Section of Surfaces of Revolution** . . . . . K. M. Siegel, H. A. Alperin, R. R. Bonkowski, J. W. Crispin, A. L. Maffett, C. E. Schensted, and I. V. Schensted 297

**Electromagnetic and Acoustic Scattering by a Semi-Infinite Body of Revolution** . . . Craige E. Schensted 306

**Electromagnetic and Acoustical Scattering from a Semi-Infinite Cone** . . . . . K. M. Siegel, J. W. Crispin, and C. E. Schensted 309

**Techniques for Nuclear Magnetic Resonance Measurements on Granular Hygroscopic Materials** . . . . . T. M. Shaw and R. H. Elsken 313

**Gap Problem in Antenna Theory** . . . . . Ronold King 317

**Acceleration of Slender Bodies of Revolution through Sonic Velocity** . . . . . J. D. Cole 322

**Use of Space Charge in Electron Optics** . . . . . E. A. Ash 327

**Radiation Characteristics of a Conical Helix of Low Pitch Angle** . . . . . J. S. Chatterjee 331

**Studies of the Diffraction of Electromagnetic Waves by Circular Apertures and Complementary Obstacles: The Near-Zone Field** . . . . . Morris J. Ehrlich, Samuel Silver, and Gedeliahu Held 336

**Replica Studies of Bulk Clays** . . . . . J. J. Comer and J. W. Turley 346

**Letters to the Editor:**

**Velocity Spectrography of Electron Dynamics in a Traveling Field** . . . . . O. T. Purl and H. M. VonFoerster 351

**Novel Microwave Attenuator Using Germanium** . . . . . J. B. Gunn and C. A. Hogarth 353

**Circularly Polarized Cavities for Measurement of Tensor Permeabilities** . . . . . E. G. Spencer, R. C. LeCraw, and F. Reggia 354

**Sparked Hydrogen Treatment of Germanium Surfaces** . . . . . Nick Holonyak, Jr., and Harry Letaw, Jr. 355

**Barkhausen Noise from a Cylindrical Core** . . . . . D. Haneman 355

**Books Reviewed** . . . . . 357

**Errata** . . . . . 358

**Books Received** . . . . . 358

**Announcement** . . . . . 358

**Cover Photograph** . . . . . 358

**Index to Advertisers** . . . . . xlii

# JOURNAL OF APPLIED PHYSICS

*A journal of applications of physics to other sciences and to industry*


**Published by the**

**American Institute of Physics**



**OFFICERS**

FREDERICK SEITZ
*Chairman*

GEORGE B. PEGRAM
*Treasurer*

**GOVERNING BOARD**

ROBERT F. BACHER
J. W. BUCHTA
KARL K. DARROW
S. A. GOUDSMIT
DEANE B. JUDD
HUGH S. KNOWLES
C. C. LAURITSEN
W. H. MARKWOOD, JR.
WILLIAM F. MEGGERS
PHILIP M. MORSE
BRIAN O'BRIEN
HARRY F. OLSON
GEORGE B. PEGRAM
ERIC RODGERS
RALPH A. SAWYER
FREDERICK SEITZ
WILLIAM SHOCKLEY
RICHARD M. SUTTON
J. H. VAN VLECK
MARK W. ZEMANSKY

**Consultant on Printing**

MELVIN LOOS

**ADMINISTRATIVE STAFF**

HENRY A. BARTON
*Director*

WALLACE WATERFALL
*Executive Secretary*

THEODORE VORBURGER
*Advertising Manager*

RUTH F. BRYANS
*Publication Manager*

EDITH I. NEFTEL
*Circulation Manager*

KATHRYN SETZE
*Assistant Treasurer*

*Editor*
Robert L. Sproull

*Editorial Board*

Maurice A. Biot
Walker Bleakney
Wallace J. Eckert
Elmer Hutchisson
D. O. North
Louis A. Pipes
W. R. Smythe
Arthur V. Tobolsky
A. M. Weinberg


THE JOURNAL OF APPLIED PHYSICS is devoted to the application of physics to other sciences, to engineering, and to industry. Previous to 1937, this journal was called PHYSICS.

The JOURNAL OF APPLIED PHYSICS welcomes articles of two distinct kinds: (1) Descriptions of new results in experimental or theoretical physics which are of general interest to applied physicists. The author should explain his contribution in such a way that a physicist or engineer in another field of specialization can appreciate its objectives and essential features. (2) Critical reviews of particular areas of applied physics. Authors contemplating writing such reviews should correspond with the Editor before they begin writing.

The JOURNAL OF APPLIED PHYSICS welcomes letters to the editor which describe in a few words the content of laboratory reports and theses and which tell readers how they may obtain copies of such reports.

**Manuscripts** should be submitted to the Editor, Rockefeller Hall, Cornell University, Ithaca, New York. Authors should read the "Information for Contributors," facing page 1 of the January issue, before writing articles or letters. The *Style Manual* of the American Institute of Physics is also helpful to writers preparing manuscripts for journals published by the American Institute of Physics. It can be obtained for $1.00 from the American Institute of Physics, 57 East 55th Street, New York 22, New York.

**Corrected proofs** and all correspondence concerning papers in the process of publication should be addressed to the Publication Manager, American Institute of Physics, 57 East 55 Street, New York 22, New York.

**Subscriptions, renewals, and orders for back numbers** should be addressed to the American Institute of Physics, 57 East 55 Street, New York 22, New York.

| **Subscription Price** | U.S. / Can. |
|---|---|
| To members of the American Institute of Physics and Affiliated Societies | $10. |
| To all others | 12. |

**Back Number Prices**

Yearly back number rate when complete year is available: $15.00.
Single copies: $1.50 each.

**Changes of address** should be sent to the American Institute of Physics.

**Advertising rates** supplied on request. Orders, advertising copy, and cuts should be sent to the American Institute of Physics.


Entered as second class matter January 22, 1937, at the Post Office at Lancaster, Pennsylvania, under the Act of March 3, 1879. Accepted for mailing at the special rate of postage provided for in paragraph (d-2), section 34.40, P. L. & R. of 1948, authorized May 2, 1932.

Journal
of
Applied Physics

Volume 26, Number 3 March, 1955

## Nuclear Reactor Issue

The first four articles in this issue describe some of the early experimental investigations leading to the nuclear reactor. Although these papers have just recently been declassified, they have already become "classics" in the science of reactor technology. The editors are indebted to Professors Wigner and Creutz for their cooperation in presenting these papers and for the review of other work which is provided by the first paper.

---

# Review of the Measurements of the Resonance Absorption of Neutrons by Uranium in Bulk

E. Creutz,* H. Jupnik,† T. Snyder,‡ and E. P. Wigner
*Princeton University, Princeton, New Jersey*
(Received December 11, 1954)

THE work reported in the following three articles dates back to the end of 1941, or the early part of 1942. The editors of this Journal suggested that we preface our reports by a short description not only of the work which preceded ours in the field of our investigation but also by a brief review of the work done subsequently. This task proved more difficult than we anticipated because little of the work on resonance absorption of material in bulk was published in regular scientific journals and because the references even to the published literature were difficult to collect. It is quite likely, therefore, that we missed some important papers and we wish to offer our apologies to those concerned. We hope that our omissions will be brought to our attention.

At the time our work was undertaken, the opinions of our colleagues were quite divided concerning the possibility of establishing a self-sustaining fission chain reaction with natural uranium. Most of our responsible physicists were inclined to question this possibility. However, Fermi and Szilard had made their historic decision to explore first the possibility of using thermal neutrons as chain carriers. This decision implied that the fission neutrons would have to be slowed down somehow to thermal energy; in the course of this "moderating process" they would have to pass through the energy region in which $U^{238}$ was known to have strong absorption lines. That the neutron absorption at these resonance lines would not result in fission and fission neutrons and that it would therefore interrupt the chain, was surmised already by Meitner, Hahn, and Strassmann,[1] and it followed from N. Bohr's theory[2] that only $U^{235}$ can undergo fission when absorbing low-energy neutrons. Bohr also noted that even if the chain reaction could be established while the uranium in the system was cold, the fission heat would increase the temperature of the uranium and thereby increase its resonance absorption. He suspected that this might bring the chain reaction to an early standstill. The point that not only one but several lines participate in the resonance absorption was particularly emphasized by G. Placzek. On the other hand, both Fermi and Szilard recognized that the resonance absorption could be diminished, to a certain degree, by "lumping" the uranium, i.e., concentrating it into finite chunks, rather

* Now at Carnegie Institute of Technology, Pittsburgh, Pennsylvania.
† Now at American Optical Company Research Laboratory, Southbridge, Massachusetts.
‡ Now at Knolls Atomic Power Laboratory, Schenectady, New York.

[1] Meitner, Hahn and Strassmann, Z. Physik, **106**, 249 (1937) and **109**, 538 (1938). The processes called 1 and 2 in this article were later shown by these workers to be the fission process. See also Halban, Kowarski, and Savitch, Compt. rend. **208**, 1396 (1939), also Haxley, Shoupp, Stephens, and Wells, Phys. Rev. **57**, 1088A (1940), **58**, 199A (1940).
[2] See N. Bohr, Phys. Rev. **55**, 548L (1939).

than distributing it uniformly over the reactor. They also recognized that the resonance absorption can be decreased, to any desired degree, by increasing the amount of the moderator, so that the neutrons would pass through the resonance region very fast. The amount of moderator is limited, however, because it itself acts as chain interrupter by absorbing the neutrons after it has slowed them down to thermal energy, thus decreasing the number of neutrons which may cause thermal fission in uranium.

Therefore, the problems which faced the would-be designers of chain reactors early in 1941 were (1) the choice of the proper moderator to uranium ratio, and (2) the size and shape of the uranium lumps which would most likely lead to a self-sustaining chain reaction, i.e., give the highest "multiplication factor." In order to solve these problems, one had to understand the behavior of the fast, of the resonance, and of the thermal neutrons. We were concerned with the second problem which itself consisted of two parts. The first was the measurement of the characteristics of the resonance lines of isolated uranium atoms, the second, the composite effect of this absorption on the neutron spectrum and total resulting absorption. One can liken the first task to the measurement of atomic constants, such as molecular diameter, the second one, to the task of kinetic gas theory which obtains the viscosity and other properties of the gas from the properties of the molecules. The first task was largely accomplished by Anderson[3] and was fully available to us when we did our work. Anderson's and Fermi's work on the absorption of uranium, and on neutron absorption in general, also acquainted us with a number of technics which will be mentioned in the third and fourth of the reports of this series. Finally, Fermi, Anderson, and Zinn carried out, in collaboration with us in Princeton,[3a] one measurement of the resonance absorption. This will be discussed in the third article of this series.

The foregoing facts fairly summarize the information which was available to us when we undertook the investigations to be reported below. Earlier or simultaneous work on resonance absorption includes, first of all, Bethe's calculation[4] of the absorption of uniformly distributed material in a hydrogeneous moderator. Bethe's results were adapted to the particular case of resonance absorption by uniformly distributed (i.e., not lumped) uranium and generalized to other moderators in a classified report by J. A. Wheeler (A-88). We did not learn about this report until some time in 1943. In addition, both J. Fisk and W. Shockley, and also Eckart, treated the resonance absorption of uranium lumps embedded in a moderator. We still know very little about Fisk's and Shockley's work. Eckart's work became available later in 1942. It was only part of a much larger undertaking and attributed all the resonance absorption to the surface of the lump and endeavored to express it in terms of an energy interval in which the surface is black. The absorption outside this interval was considered negligible.

None of the foreign work on uranium fission was available to us and much of it is unavailable now. At present, we know the German work best.[5] The lumping of the uranium was suggested in Germany by Harteck in 1939, carbon as moderator by Heisenberg in the same year. This was practically simultaneous with the American work. The resonance absorption of uniformly distributed uranium was treated theoretically by Flügge and by Flügge and Sauerwein, as early as 1939. The absorption by $U^{238}$, both in the thermal and in the resonance region, was studied experimentally by Volz, Haxel, and Sauerwein toward the turn of the year 1942—just about one year after our studies. The importance of the higher absorption lines was recognized and experimentally demonstrated but the magnitude of the resonance absorption, as of all absorption by $U^{238}$, grossly underestimated (by a factor of about 10). We are unable to account for this error unless it was caused by some error in calibration.[6] It re-emphasizes the value of the careful measurements of Fermi and his collaborators. The effect of temperature on resonance absorption was anticipated and experimentally demonstrated. (The results are, in this case, considerably in excess of ours.) An improved theory of the resonance absorption was given later by V. Weizsacker. His work remains unreported but we surmise that it must have applied to lumped uranium.

The early French and British work closely paralleled the United States and German work.[7] The heterogeneous arrangement, as well as the use of moderators other than ordinary hydrogen, was proposed as early as 1939 by Halban, Kowarski, and Joliot.[8] It may be of interest to note that the arrangement for a chain reaction with hydrogeneous material and $U_3O_8$ proposed by these authors is not far from the arrangement which comes closest to being chain-reacting. Measurements were carried out to obtain the resonance escape probability of uniformly distributed uranium in hydrogeneous moderators and again, the values obtained are close to those now considered correct.[9] The effect

[3] H. L. Anderson, Phys. Rev. **80**, 499 (1950). See also reference 1.

[3a] Smyth, Fermi, and Anderson, Report A-12, June, 1941.

[4] H. A. Bethe, Revs. Modern Phys. **9**, 69 (1937). See also W. H. Furry, Phys. Rev. **51**, 592 (1937); O. Haxel and H. Volz, Z. Physik **120**, 493 (1942).

[5] See W. Heisenberg, Nature **160**, 211 (1947), also *Nuclear Physics* (Methuen and Company, Ltd., London, 1953), and the so-called Fiat report *Kernphysik und Kosmische Strahlung* (Dieterich'sche Verlagsbuchhandlung, Wiesbaden, 1948). Part 1, Articles by Hahn, Seelmann-Eggebert, Gotte, Flammersfeld, Droste, Flügge, Sauerwein, and Jentschke, pp. 171–224.

[6] Dr. W. K. Jentschke kindly informs us that the error was indeed one of calibration. However, Sauerwein's estimate [Z. Naturforsch. **2a**, 73 (1947)] of the resonance integral of the higher absorption lines of $U^{238}$ is entirely reasonable.

[7] Cf. L. Kowarski, J. phys. radium **7**, 253 (1946).

[8] Cf. Halban, Kowarski, and Joliot, Compt. rend. **229**, 909 (1949).

[9] Halban, Joliot, Kowarski, and Perrin, J. phys. radium **10**, 428 (1939); Halban, Kowarski, and Savitch, Compt. rend. **208**, 1396 (1939).

of self-reversal was noted.[10] However, as far as we could ascertain, no calculations or measurements on the resonance absorption of lumped uranium were carried out at this early date.

When writing the present article we were informed of measurements of the resonance absorption in heterogeneous media. The reports on these measurements by Broda, Fennig, Graham, Guéron, Halban, Kowarski, and Seligman are still classified. Their dates extend from 1942 to 1944. Several of the French-British references were received through the courtesy of Dr. Cockcroft, Dr. Halban, Dr. Kowarski, and Dr. H. D. Young and we wish to express our appreciation for their help.

The Russian work is, since the war, much more closely guarded than the American. We found the article of Zeldovic and Chariton[11] very interesting and informative both from the technical point of view and also in its indication of the state of progress in Russia around 1940.

Our own results are described in the articles which follow. The experimental work was since repeated and extended by A. C. G. Mitchell and his collaborators. C. O. Muelhouse and S. Untermyer obtained values for the resonance absorption by a method fundamentally different from ours in 1949, Arfken, Caldwell, Cuykendall, Risser, and Stephenson by a more similar method in 1950.

[10] Halban, Joliot, and Kowarski, Nature **143**, 680 (1939) (last sentence of article).

[11] J. Zeldovic and J. Chariton, J. Exptl. Theoret. Phys. (U.S.S.R.) **10**, 29 (1940).

The measurements of Anderson[3] and Fermi on the resonance lines of $U^{238}$ were repeated also, in addition to Germany, by Hellstrand and Persson in Sweden, and by Levin and Hughes[12] at Brookhaven. Their results differ from those of reference 3 quite drastically. In particular, the lowest resonance line, the only one measured by Anderson, appears to be several times narrower than given in reference 3. On the other hand, the absorption at the center of the line is several times greater so that the total absorption of the line remains close to the figure which we used. It is not clear whether the cancellation of errors in Anderson's work is accidental. The measurements of reference 12 have not yet been reported in detail.

Among the theoretical work which is subsequent to ours, we wish to mention the calculations of S. M. Dancoff and M. Ginsburg, contained in report CP-1589. This report gives, on the basis of Anderson's measurements,[3] a quantitative explanation of the results of our third and fourth paper. Our second paper, written before the results of the third and fourth became available, gives only the functional dependence of the resonance absorption on size and shape of the uranium lumps and, as will be seen, only a crude numerical estimate of the absolute magnitude of the resonance absorption of lumps. No calculations have yet been carried out on the basis of the data of reference 12; they are planned, however, when the detailed results become available.

[12] Hellstrand and Persson, Arkiv. Fysik **6**, 57 (1953); J. S. Levin and D. J. Hughes, Phys. Rev. **95**, 645A (1954).

# Resonance Absorption of Neutrons by Spheres

E. P. WIGNER, E. CREUTZ,* H. JUPNIK,† AND T. SNYDER‡
*Princeton University, Princeton, New Jersey*
(Received September 15, 1954)

By concentrating uranium into lumps, one can decrease its resonance absorption as compared with the resonance absorption of the same amount of uranium spread out uniformly in a moderator. It is shown here that this decrease is caused principally, not by the diminished over-all density of the neutrons at the lump, but by their changed energy distribution. This shows deep minima at the resonance lines, i.e., where the uranium absorbs most strongly. The considerations here presented show that the decrease in absorption is largest for the low energy resonances of $U^{238}$ which are responsible for the bulk of the absorption in the case of uniform distribution. As a result, the resonance absorption of uranium lumps extends over a very large energy region—up to about 5000 ev. It can be decomposed, approximately, into two parts: the mass absorption, proportional to the number of $U^{238}$ atoms present; and a surface absorption, proportional to the surface of the lump. The total decrease of the resonance absorption produced by lumping (the "advantage factor" of lumping) can be estimated to reach, under favorable conditions, a value as high as 20.

## INTRODUCTION AND SUMMARY

THE work incorporated in the present article was done during the summer and fall of 1941. Its purpose was to provide a preliminary estimate of the magnitude of the resonance absorption of uranium lumps embedded in a moderating medium and, even more important, to enable us to carry out and interpret the experiments which are described in the following two articles. The most important result of the following considerations was that the resonance absorption of lumps embedded in a moderator can be divided into two parts: the mass absorption and the surface absorption. The former is proportional to the total number of $U^{238}$ atoms present in the lump, the proportionality constant depending principally on the total scattering cross section (not the slowing-down power) associated with a U atom. It is, therefore, larger for $U_3O_8$ than for U metal. This fact showed the importance of eliminating any container of extraneous material from the uranium sample, the absorption of which sample was to be considered representative of the absorption of the whole lump: The scattering by the container material invariably increased the absorption of the sample contained therein and often led to erratic results. The importance of the second part of the resonance absorption, that of the surface absorption, turned out to be much smaller than was estimated before and is not much more than a correction to the mass absorption as long as the diameter of the lumps is not less than a couple of centimeters. Our considerations implicitly assume that the lumps have at least this dimension. The surface absorption also depends on the total scattering cross section of the materials admixed to the uranium, but this dependence is weaker than that of the mass absorption and decreases with increasing scattering cross section of the admixtures.

The work is reported here with hardly any alterations from the original manuscript,[1] except for the omission of less significant material, adoption of a more customary notation, correction of some minor numerical errors, and the redrawing of the figures to save space. It should be noted that metallic uranium was not available at the time the present work and most of the experiments described in following articles were done. Hence, our attention and interest were focused principally on the properties of $U_3O_8$. This is mentioned explicitly because the present treatment of the absorption in the lowest resonance level of $U^{238}$ is very crude. The absorption of this level plays only a subordinate role in the oxide but is rather important in the metal. A more accurate consideration of the absorption of this level was given in CP-1589 by S. M. Dancoff and M. Ginsburg. This report also contains, implicitly, much of the work reported at the end of this article.

## GENERAL DESCRIPTION OF THE ABSORPTION LINES

The so-called resonance absorption differs from ordinary absorption mainly because, over the most important range of energy, the absorption coefficient is a rapidly fluctuating function of energy. It is caused by rather narrow absorption lines, with an average spacing of about 20 ev. The first of these lies at 5.8 ev, the second, probably, at 30 ev, but nothing is known about the location of the higher ones.[2] Anderson and Fermi[3] measured the relevant constants of the absorption. They concluded from their measurements that the most important line lies around 10 ev. The self-absorp-

* Now at Carnegie Institute of Technology, Pittsburgh, Pennsylvania.
† Now at Optical Company Research Laboratory, Southbridge, Massachusetts.
‡ Now at Knolls Atomic Power Laboratory, Schenectady, New York.

[1] The material originally appeared in Document C-4. It was declassified by authority of the U. S. Atomic Energy Commission on December 29, 1953.
[2] Baker, Bacher, and McWilliams, Report A-23. The experimental information now available can be found in Supplement 2 to the Neutron Cross Section Compilation (AECU-2040) issued by the U. S. Atomic Energy Commission on June 15, 1953. See also J. S. Levin and D. J. Hughes, Phys. Rev. **95**, 645A (1954).
[3] Report A-2. Also H. L. Anderson, Phys. Rev. **80**, 499 (1950).

tion of the resonance activity is $5000\times10^{-24}$ cm², and they find for the integral over the absorption cross section $\sigma_a(E)$

$$\int \frac{\sigma_a(E)}{E}dE=239\times10^{-24}\text{ cm}^2. \quad (1)$$

It will be attempted to show at least a rough picture of the absorption on the basis of the foregoing data.

It will be assumed that the absorption cross section can be represented in the neighborhood of a line at $E_i$ by the formula

$$\sigma_a(E)=\frac{0.65\times10^{-18}}{E^{\frac{1}{2}}}\frac{a\Gamma}{(E-E_i)^2+\frac{1}{4}(\Gamma+aE^{\frac{1}{2}})^2}\text{cm}^2. \quad (2)$$

*Although it is probably far from being true, we shall assume that the γ-ray width Γ and the constant a in the neutron width $aE^{\frac{1}{2}}$ are the same for all lines* and use the foregoing data of Fermi and Anderson to find their values.[4]

This will be done in two ways, to be distinguished as assumptions *a* and *b*. The first one assumes that the lines are at 5.8, 3×5.8, 5×5.8, etc. ev and that the above data give the sum of the effects of all lines. It follows that the integral (1) is a sum of the integrals due to the various lines

$$\int \frac{\sigma_a(E)}{E}dE=\sum_i \frac{2\times0.65\times10^{-18}\pi a\Gamma}{E_i^{\frac{1}{2}}(\Gamma+aE_i^{\frac{1}{2}})}. \quad (3)$$

When integrating (2), it was assumed that the line is sharp, i.e., $\Gamma+aE_i^{\frac{1}{2}}$ is much smaller than the distance of the lines—a condition which is satisfied for the relevant lines. Since, furthermore, only the low lines play an important role in (3) and since for these $aE_i^{\frac{1}{2}}\ll\Gamma$, we can write

$$1.3\times10^{-18}\pi a\left(\frac{1}{5.8^{\frac{1}{2}}}+\frac{1}{(3\times5.8)^{\frac{1}{2}}}+\frac{1}{(5\times5.8)^{\frac{1}{2}}}\cdots\right)=239\times10^{-24}$$

from which

$$a=4.8\times10^{-4}(\text{ev})^{\frac{1}{2}} \quad (3a)$$

follows (the number of all equations and figures based on assumptions *a* will be followed by an a). If we make the assumption that the energy spectrum of the neutrons used for the measurement of the self-absorption followed the $dE/E$ law, we can interpret this quantity in a similar way. We obtain

$$\Gamma=3.8\times10^{-2}\text{ ev} \quad (4a)$$

for the γ-ray width.

[4] The consequences of possible fluctuations of the quantities *a* and Γ have been explored by Dancoff and Ginsburg report CP-1589. In an earlier report (CP-1092) they have analyzed the data of reference 3 much more carefully than they are analyzed here. In the notation here adopted, they conclude that for the 5.8-ev line $a=9\times10^{-4}$ ev$^{\frac{1}{2}}$, $\Gamma=0.065$ ev.

Assumption *b* postulates that both the integral (1) and also the self-absorption are due to a single line at 5.8 ev. It gives, for the foregoing quantities,

$$a=8.2\times10^{-4}(\text{ev})^{\frac{1}{2}} \quad (3b)$$

$$\Gamma=9\times10^{-2}\text{ ev}. \quad (4b)$$

Furthermore, we shall assume unber *b* that the higher lines are located at 30, 50, 70, etc., ev and that their *a* and Γ are given by (3b) and (4b). It follows from this assumption that the integral of $\sigma_a(E)/E$ over the whole energy spectrum is larger than $239\times10^{-24}$ cm² since the first line already contributes this amount. The total integral is, under assumption *b*, $310\times10^{-24}$ cm².

The purpose of carrying out the following consideration with two sets of constants is to obtain some information concerning the sensitivity of the results with respect to variations of these constants. It may be argued that assumptions *a* are more reasonable[5] than assumptions *b*. It is sure, however, that neither set is correct. Both lead to values of *a* and Γ of the same order of magnitude as was found by Fermi and Anderson for other elements,[1] except I, *viz.*, $10^4a=1.80$, 8.5, 8.0, 20.5, and $10^2\Gamma=12.5$, 9.8, 9, 11 for Rh, Ag (22-sec activity) In, Au, respectively. For the ratio of the reduced neutron width $\gamma^2$ and the level spacing *D*, assumptions *a* and *b* both give $0.09\times10^{-13}$. Both are below the theoretical values but agree, as far as order of magnitude is concerned, with the values of $\gamma^2/D$ for other heavy elements.[6] The connection between γ and *a* is $a=4.4\times10^9\gamma^2$.

For the thermal absorption, assumptions *a* and *b* give $2.2\times10^{-24}$ cm² and $9\times10^{-24}$ cm², respectively, if one neglects the effect of all but the lowest line. The experimental value[2] is $3\times10^{-24}$ cm² indicating that the actual value of *a* may be between the values given by assumptions *a* and *b*.

One can obtain, by integrating (2), an expression for the average absorption coefficient. If we denote the average spacing of the lines by *D*, this becomes $D^{-1}$ times the integral of (2), i.e.,

$$\langle\sigma_a(E)\rangle_{\text{Av}}=\frac{1.3\times10^{-18}\pi a\Gamma}{E^{\frac{1}{2}}(\Gamma+aE^{\frac{1}{2}})D}. \quad (5)$$

With

$$D=11.6\text{ ev} \quad (6a)$$

$$D=20\text{ ev} \quad (6b)$$

this gives the two curves of Fig. 1. For $E=200$ kev, assumptions *a* and *b* give $0.57\times10^{-25}$ and $0.74\times10^{-25}$, respectively. Both values are considerably lower than the one given by J. Marshall and Szilard, *viz.*, $5\times10^{-25}$.

[5] The results of the measurements reported in the following two papers later led us to believe that assumptions *b* may be the ones closer to reality.

[6] See T. Teichmann and E. P. Wigner, Phys. Rev. **87**, 123 (1952).

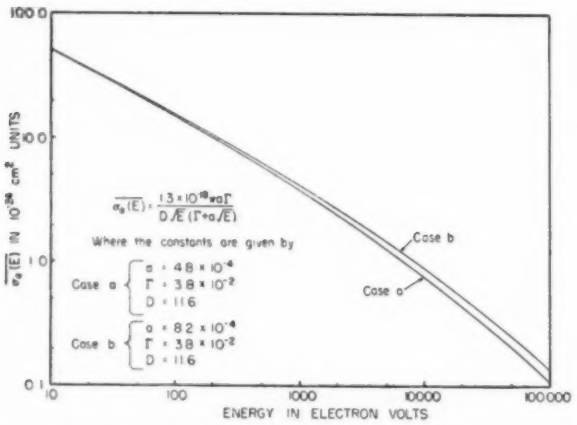


FIG. 1. The average absorption coefficient of uranium for neutrons as a function of energy under assumptions *a* and *b* described in the text.

However, this value for the absorption cross section may refer to a lower energy.[7]

We shall denote the ordinary scattering cross section of the material associated with one atom $U$, by $\sigma_{sn}$. Thus, for the metal

$$\sigma_{sn}=12\times10^{-24}\text{ cm}^2 \tag{7}$$

is the scattering cross section of the U nucleus.[8] For the oxide $U_3O_8$, this must be augmented by 8/3 times the scattering cross section of O, giving

$$\sigma_{sn}=22\times10^{-24}\text{ cm}^2. \tag{7a}$$

According to the usual theory of resonance processes, an anomalous scattering cross section is associated with the absorption. It is given, in the neighborhood of the line $E_i$, by

$$\sigma_{sa}(E)=\frac{0.65\times10^{-18}a^2}{(E-E_i)^2+\frac{1}{4}(\Gamma+aE^{\frac{1}{2}})^2}=\frac{aE^{\frac{1}{2}}}{\Gamma}\sigma_a(E). \tag{8}$$

The total scattering cross section is $\sigma_s=\sigma_{sn}+\sigma_{sa}$.

It is probably useful to remark that the total natural line width $\Gamma+aE^{\frac{1}{2}}$ is essentially $\gamma$-ray width below 6500 ev and that the neutron width, $aE^{\frac{1}{2}}$, can be neglected compared with $\Gamma$ if one is well below this energy. Above 6500 ev, $\Gamma$ becomes smaller than $aE^{\frac{1}{2}}$.

The magnitude of the anomalous scattering is smaller than the absorption below 6500 ev, larger above. Below this limit its value at the center of a line is about $4\times10^{-22}$ cm$^2$; i.e., very much larger than the ordinary scattering cross section. Above 6500 ev, its value at the center of the line decreases, it becomes equal to the ordinary scattering cross section of the metal at 150,000 ev.

## THE DOPPLER EFFECT

The foregoing considerations neglect the temperature motion of the U nuclei which causes a broadening of the lines the significance of which, in connection with our problem, was first pointed out by J. A. Wheeler.

Let us consider a neutron of energy $239/238E$, colliding with a U atom which has velocity components $v_{\parallel}$ and $v_{\perp}$ parallel and perpendicular to the velocity of the neutron. The relative energy $E'$ of neutron and U is then

$$E'=\frac{1}{2}\frac{238}{239}M\left\{\left[\left(\frac{2\times239E}{238M}\right)^{\frac{1}{2}}+v_{\parallel}\right]^2+v_{\perp}^2\right\}$$
$$\approx E+(2EM)^{\frac{1}{2}}v_{\parallel}, \tag{9}$$

where $M$ is the mass of the neutron, 238 $M$ that of the U nucleus. From (9), the probability that the relative energy be between $E'$ and $E'+dE'$ becomes

$$\frac{dE'}{(2EM)^{\frac{1}{2}}}\left(\frac{238M}{2\pi kT}\right)^{\frac{1}{2}}\exp\left[-\frac{238M}{2kT}\frac{(E'-E)^2}{2EM}\right]. \tag{10}$$

In order to obtain the cross section for neutrons of energy $239E/238$, (10) must be multiplied with the cross section for the relative energy $E'$ and integrated over $E'$. For the former, we use (2), assuming that $E$ and $E'$ are in the neighborhood of $E_i$

$$\sigma_a(E)=\frac{0.65\times10^{-18}a\Gamma}{E}\left(\frac{238}{4\pi kT}\right)^{\frac{1}{2}}$$
$$\times\int\exp\left[\frac{-238}{4kTE}(E'-E)^2\right]$$
$$\times\frac{dE'}{(E'-E_i)^2+\frac{1}{4}(\Gamma+aE_i^{\frac{1}{2}})}. \tag{11}$$

This integral has been tabulated recently.[9]

## THE PRACTICAL WIDTH

It is useful for the following to define a practical width of the absorption lines. This width, $2\Delta$, is the distance of the two points, at the wings of the line, for which the sum of absorption and anomalous scattering cross sections $\sigma_a+\sigma_{sa}$ becomes equal to the ordinary scattering cross section $\sigma_{sn}$. Of course, for very high levels, $\sigma_a+\sigma_{sa}$ does not become equal to the ordinary scattering cross section even in the middle of the line and we shall say, in this case, that the practical width is zero. In fact, one has no real line absorption at these levels.

The practical width was calculated on the basis of the approximate evaluation (12) of the integral (11) and is given in Figs. 2(a) and 2(b). The calculation will not be given in detail here; its approximate nature is evident from the kinks in the figures.

The origin of these kinks is as follows: The absorption due to the natural line width decreases, far from the

[7] This possibility was suggested by Marshall and Szilard. The discrepancy is not fully cleared up even now.

[8] The value now accepted is $9.5\times10^{-24}$ cm$^2$. See reference 2.

[9] Report BNL 257, issued by the U. S. Atomic Energy Commission.

center of the line, as $(E-E_i)^{-2}$; that due to the Doppler, broadening decreases exponentially. It is possible, therefore, to approximate the integral (11) by

$$\sigma_a(E)=\frac{0.65\times10^{-18}a\Gamma}{E_i}\left\{\frac{E_i^{\frac{1}{2}}}{(E-E_i)^2+\frac{1}{4}(\Gamma+aE_i^{\frac{1}{2}})^2}+\frac{(238\pi/kT)^{\frac{1}{2}}}{\Gamma+aE_i^{\frac{1}{2}}}\exp\frac{-238(E-E_i)^2}{4kTE_i}\right\}. \quad (12)$$

The first term predominates far from the line, where the absorption is already relatively low, the second one is larger close to $E_i$ where the absorption is still relatively high. If one equates $\sigma_a(E)$ to $\sigma_{sn}$, the first term of (12) will be important at the low $E_i$ where $\sigma_{sn}$ is relatively small. This is the region to the left of the kinks and will be called the natural width region. For the lines at high $E_i$, the normal scattering cross section $\sigma_{sn}$ is a relatively large cross section and the second term of (12) is the more important one in the region where $\sigma_a(E)$ is equal to $\sigma_{sn}$. The $E_i$ for which this condition prevails are said to lie in the Doppler region which is to the right of the kinks in the figures. Different approximations are useful in different parts of the energy spectrum and in the following the different regions will be treated separately.

The natural width region extends for the metal to 70 and 200 ev under assumptions *a* and *b*, respectively, at 300°K. At 900°K, the corresponding limits are 32 and 90 ev. For the oxide, the natural width region extends at 300°K to 50 and 140 ev, at 900°K to 25 and 55 ev for assumptions *a* and *b*, respectively.

One sees that the Doppler region is very important under assumption *a*, but becomes narrower if the constants *b* are adopted. The temperature dependence of the resonance absorption is due to the Doppler region. It will be seen from the experimental data to be presented later that the temperature coefficient of the resonance absorption is actually very small. This favors the constants *b*.

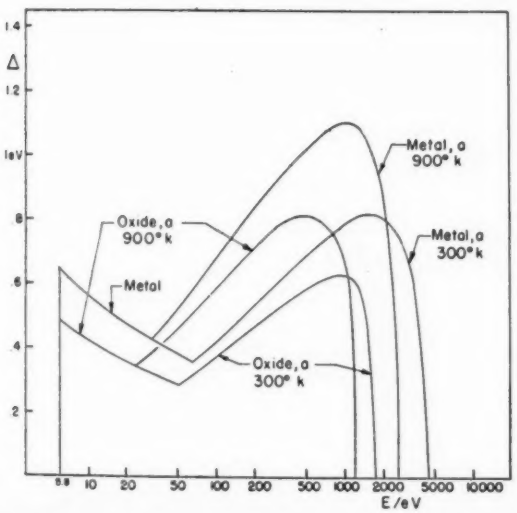


FIG. 2(a). One-half of the practical width of the uranium absorption lines plotted as a function of neutron energy for assumption *a* given in the text.

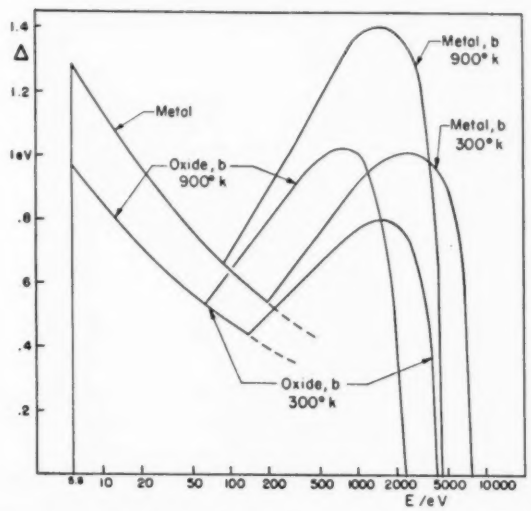


FIG. 2(b). One-half of the practical width of the uranium absorption lines plotted as a function of neutron energy for assumption *b* given in the text.

The energy range beyond the upper limit of the Doppler region will be called continuous region.

## GENERAL FEATURES OF LINE ABSORPTION

Over the most important part of the spectrum, the absorption is concentrated in lines. The absorption of a block is, in these regions, much smaller than that of the same amount of material spread out thinly over the slowing down material. It is also much smaller than it would be if the absorption were not concentrated in lines but spread out uniformly over the whole energy range. The reason for this is that the number of neutrons with energies within an absorption line is strongly decreased by the absorption and much fewer absorbable neutrons remain than would be present in a material with continuous absorption.

Let us denote the number of neutrons per cm³ and unit energy range by $Q/Ev$ where $v=(2E/M)^{\frac{1}{2}}$ is the velocity corresponding to energy $E$. The $Q$ is the number of collisions which some material with 1 cm² cross section would suffer per second from the neutrons of unit logarithmic energy range (one hundred times the number of collisions with neutrons with energies between $E$ and $1.01\,E$). Let us further denote the average of a quantity over an energy range containing several absorption lines by a bar.[10] The barred quantities, such as $\bar{Q}$, will vary only slowly with energy (and position). The consideration of such average quantities is particularly useful in the energy region in which the widths of the lines are small compared with the average energy loss of a neutron per collision. Even in the metal, this

[10] For typographical reasons, some of the bars had to be changed to $\langle\ \rangle_{Av}$. This symbol and the bar are equivalent.

region extends from about 120 ev to the upper limit of line absorption, i.e., the upper limit of the Doppler region. The considerations of the present section apply only to that part of the spectrum where the lines are narrow in the above sense.

The line absorption consists of two parts: the mass absorption and the surface absorption.

We first consider the *mass absorption*. If the U block had no absorption, the number of neutrons which are, within a cm³, thrown out of the energy range between $E$ and $E+dE$ by collisions would be $N\sigma_s Q dE/E$, where $N$ is the number of U atoms per cm³. Under the same conditions, this would be also the number of neutrons entering the same energy range from above—in fact $N\langle\sigma_s Q\rangle_{Av}dE/E$ is the correct expression for the number of neutrons entering this energy range in spite of the absorption because these neutrons originate over a considerable energy range which contains several lines. On the other hand, the number of neutrons leaving the same energy range is determined by the local density and cross sections so that we have

$$N\langle\sigma_s Q\rangle_{Av}dE/E=N(\sigma_a+\sigma_s)QdE/E. \tag{13}$$

This gives

$$Q=(\sigma_a+\sigma_s)^{-1}\langle\sigma_s Q\rangle_{Av} \tag{14}$$

showing that $Q$ has sharp minima where $\sigma_a+\sigma_s$ has maxima, i.e., in the absorption lines. If averaged over $E$, (14) gives $\bar{Q}=\langle(\sigma_a+\sigma_s)\rangle_{Av}^{-1}\langle\sigma_s Q\rangle_{Av}$. Since $\sigma_a+\sigma_{sa}$ is larger than $\sigma_{sn}$ only within the relatively small practical width, the average of the reciprocal value of $\sigma_a+\sigma_s=\sigma_a+\sigma_{sa}+\sigma_{sn}$ will be practically equal to the reciprocal of $\sigma_{sn}$. It will be smaller by an amount of the order $1-2\Delta/D$ where $2\Delta$ is the "practical width" and $D$ is the average spacing of the $\lambda$ lines, but the accuracy of the present calculations hardly justifies carrying on such factors. We shall write, therefore, $\sigma_{sn}^{-1}$ for $\langle(\sigma_a+\sigma_s)\rangle_{Av}^{-1}$ and we have $\sigma_{sn}\bar{Q}=\langle\sigma_s Q\rangle_{Av}$. The absorption in the energy range $dE$ becomes,

$$N\sigma_a QdE/E=\frac{N\sigma_a}{\sigma_a+\sigma_s}\sigma_{sn}\bar{Q}\frac{dE}{E}, \tag{15}$$

and the average mass absorption $\bar{A}_v$ per unit energy interval

$$\bar{A}_v=N\frac{\bar{Q}}{E}\left\langle\frac{\sigma_a\sigma_{sn}}{\sigma_a+\sigma_s}\right\rangle_{Av}. \tag{16}$$

The *surface absorption* is caused by the fact that the energy spectrum of the neutrons which strike the surface from the outside is uniform, $Q=\bar{Q}$. It does not show the deficiency of neutrons within the line which the $Q$ calculated from (14) manifests. The number of neutrons of unit energy interval which strike unit area of the surface from the outside is $\frac{1}{4}\bar{Q}/E$. It shows a surplus of

$$\frac{\bar{Q}}{4E}-\frac{\bar{Q}}{4E}\frac{\sigma_{sn}}{\sigma_a+\sigma_s}=\frac{\bar{Q}}{4E}\frac{\sigma_a+\sigma_{sa}}{\sigma_a+\sigma_s} \tag{17}$$

over the number of neutrons of the same velocity and direction in the inside. Of the neutrons (17), the fraction $\sigma_a/(\sigma_a+\sigma_s)$ will be absorbed, the rest suffers a scattering collision and is, from then on, one of the regular neutrons of the inside. Hence, the surface absorption per unit surface and unit energy range $\bar{A}_s$ is

$$\bar{A}_s=\frac{\bar{Q}}{4E}\left\langle\frac{(\sigma_a+\sigma_{sa})\sigma_a}{(\sigma_a+\sigma_s)^2}\right\rangle_{Av}. \tag{18}$$

Even from the comparison of (18) and (16) it is evident that, while the mass absorption is proportional for given volume to $N$, and therefore to the density of the block, the surface absorption is independent of this quantity. The absorption of an average U atom in a lump of volume $V$ and surface $S$ becomes per unit logarithmic energy range

$$\frac{E\bar{A}}{N}=\frac{E}{N}\left(\bar{A}_v+\frac{S}{V}\bar{A}_s\right)$$

$$=\bar{Q}\left\langle\frac{\sigma_a\sigma_{sn}}{\sigma_a+\sigma_s}\right\rangle_{Av}+\frac{S\bar{Q}}{NV}\left\langle\frac{(\sigma_a+\sigma_{sa})\sigma_a}{4(\sigma_a+\sigma_s)^2}\right\rangle_{Av}. \tag{19}$$

Naturally, this formula does not hold for the bottom part of the energy region where the number of resonance levels per unit logarithmic energy range is small. One may remember that $\bar{Q}$ is essentially inversely proportional to the slowing down power of the moderator.

The two averages in (19) have simple interpretations. If the nucleus with absorption cross section $\sigma_a$ were not shielded by the other nuclei, its absorption would be, per unit logarithmic energy range, $\bar{Q}\sigma_a$. Hence, if we replace $\sigma_a$ by

$$\sigma_{\text{eff}}=\left\langle\frac{\sigma_a\sigma_{sn}}{\sigma_a+\sigma_s}\right\rangle_{Av}, \tag{19a}$$

we can neglect the effect of the mutual shielding of the nuclei and obtain their mass absorption. Similarly, nuclei with total cross section $S$ would have an absorption $\bar{Q}S$ per unit logarithmic energy range. Hence, the surface absorption of the lump is equal to the absorption of unshielded atoms with the total surface of $Sf$ where

$$f=\left\langle\frac{(\sigma_a+\sigma_{sa})\sigma_a}{4(\sigma_a+\sigma_s)^2}\right\rangle_{Av}. \tag{19b}$$

The total absorption of the lumps can be described as the absorption of unshielded nuclei with a total surface of $(NV)\sigma_{eff}+Sf$ where $NV$ is the total number of nuclei and $S$ the surface of the lump

$$A\,(\text{lump})=\bar{Q}\int[(NV)\sigma_{eff}+Sf]dE/E. \tag{19c}$$

This formula neglects possible variations of $\bar{Q}$ over energy and position within the lump. If the lumps are of

considerable size these may have to be corrected. In such a case, $\bar{Q}$ has to be under the integral sign and $N\bar{Q}$ has to be replaced by integration of $N\bar{Q}$ over the volume of the lump. This was not necessary for the interpretation of the experiments to be described in the two articles which follow, but has been necessary for the calculation of the reproduction factor of some of the chain reacting units.[11]

We now go over to the detailed consideration of the absorption in the different energy regions.

## THE DOPPLER REGION

The preceding considerations can be applied directly in the Doppler region. For the calculation of the average in (16) we need the integral

$$\int \frac{\sigma_a}{\sigma_a+\sigma_s}dE=\int \frac{\sigma_a dE}{\sigma_a+\sigma_{sa}+\sigma_{sn}} \tag{20}$$

over a line. Evidently, the integrand is zero far away from the center of the line and nearly 1 near to the center. For $\sigma_{sa}\ll\sigma_a$ it is $\frac{1}{2}$ at the edge of the practical width. In order to calculate (20), we need an accurate value of $\sigma_a$ and $\sigma_a+\sigma_{sa}=\sigma_a(1+aE^{\frac{1}{2}}/\Gamma)$ only in the neighborhood of the practical width. Thus we can substitute for $\sigma_a$ the second term of (12) except, perhaps, at the lower end of the Doppler region (which will turn out to be a relatively unimportant region). Thus,

$$\int \frac{\sigma_a dE}{\sigma_a+\sigma_s}=\frac{\Gamma}{\Gamma+aE^{\frac{1}{2}}}\int \frac{dE}{1+\gamma\exp[238(E-E_i)^2/4kTE_i]}$$

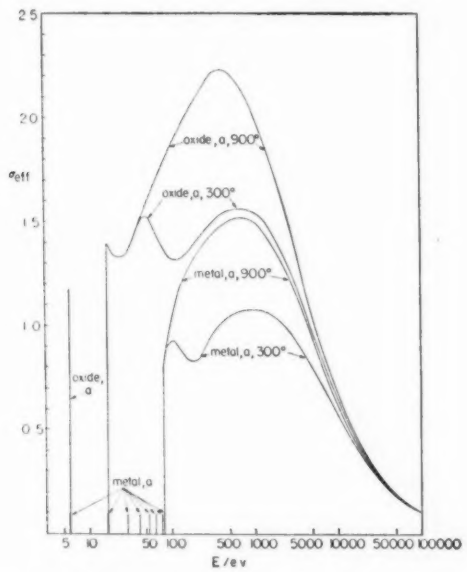


FIG. 3(a). The effective absorption cross section plotted as a function of neutron energy under assumption *a* given in the text.

[11] Cf. S. Glasstone and M. C. Edlund, *The Elements of Nuclear Reactor Theory* (D. Van Nostrand Company, Inc., New York, 1952), Secs. 9.36–9.41, pp. 261–263.

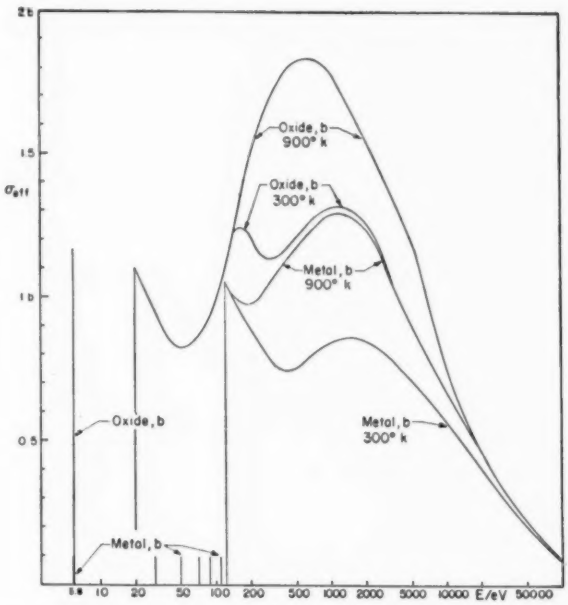


FIG. 3(b). The effective absorption cross section plotted as a function of neutron energy under assumption *b* given in the text.

where

$$\gamma=\frac{\sigma_{sn}E_i(kT)^{\frac{1}{2}}}{1.8\times10^{-17}a}. \tag{21}$$

It is not to be confused with the reduced width. Furthermore, this expression remains valid even in the continuous region where the practical width becomes meaningless. In this case, the 1 in the denominator can be neglected and one obtains the ratio of the integral of (2) to $\sigma_{sn}$. If one substitutes a new variable for the argument of the exponential, the integral in (21) assumes the form which occurs in the electron theory of metals and can be evaluated in the same way.

For practically all of the Doppler region, $\gamma\ll1$ which corresponds to strong degeneracy. In this case, the exponential in the denominator of (21) changes very rapidly in the neighborhood of the edge of the practical width. Hence, the integrand is practically 1 within the practical line, 0 outside, and the integral (20) becomes $2\Delta$. The mass absorption is, therefore,

$$\bar{A}_v=(N\bar{Q}/E)\sigma_{eff}=2N\bar{Q}\sigma_{sn}\Delta/[ED(1+aE^{\frac{1}{2}}/\Gamma)], \tag{22}$$

where $D$ is the spacing of the lines, $1/D$ the number of lines per unit energy interval. The $\sigma_{eff}$ is plotted in Figs. 3(a) and 3(b).

Near the upper end of the Doppler region $\sigma_a$ does not change rapidly at the distance $\Delta$ from the center of the line. In this case, one has to evaluate the integral (21) graphically or use the tabulated values therefor. For $\gamma=0.5$, 1, 1.33, and 2, the value of the integral in (21) is $(4kTE/238)^{\frac{1}{2}}(1.58, 1.07, 0.9, 0.67)$.

For the calculation of the surface absorption we need

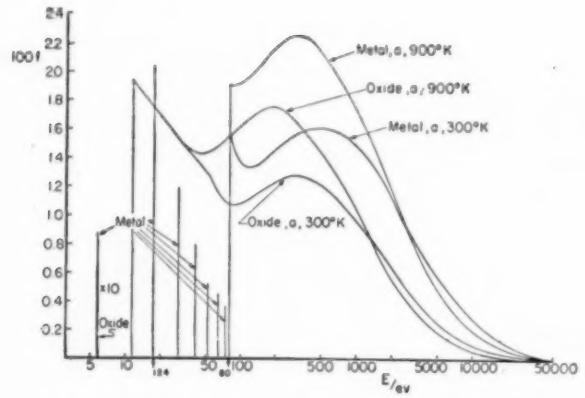


FIG. 4(a). 100×function $f$ plotted as a function of neutron energy under assumption $a$ given in the text.

the integral

$$\int \frac{\sigma_a^2(1+aE^{\frac{1}{2}}/\Gamma)dE}{\sigma_a(1+aE^{\frac{1}{2}}/\Gamma)+\sigma_{sn})^2}$$

$$=\frac{\Gamma}{\Gamma+aE^{\frac{1}{2}}}\int\frac{dE}{[1+\gamma\exp(238(E-E_i)^2/4kTE)]^2}. \quad (23)$$

Again, in the lower part of the Doppler region the exponential increases very rapidly at $|E-E_i|=\Delta$. The integrand is nearly 1 for $|E-E_i|<\Delta$, it is very small for $E-E_i>\Delta$. Hence, we have for the surface absorption

$$\bar{A}_s=(\bar{Q}/E)f=\bar{Q}\Delta/[2ED(1+aE^{\frac{1}{2}}/\Gamma)]; \quad (24)$$

$f$ is plotted in Figs. 4(a) and 4(b). The approximation (24) is much poorer than (22). Actually, the value of the integral is $(4kTE/238)^{\frac{1}{2}}(1.35, 0.80, 0.40, 0.16)$ for $\gamma=0.25, 0.50, 1$, and 2.

In the lower part of the Doppler region the absorptions per unit logarithmic energy interval, $E\bar{A}_v$ and $E\bar{A}_s$, actually increase with increasing energy because they are proportional to $\Delta$ which is roughly proportional to the square root of the energy. The mass absorption is, furthermore, proportional to $\sigma_{sn}$; it is for the metal 12/22 times smaller than for the oxide. In the upper part of the Doppler region the absorption becomes increasingly independent of the temperature and $\sigma_{eff}$ and becomes, in the continuous region, equal to the ordinary absorption.

The ratio of the second, or surface term of (19), to its first or mass term is

$$S\bar{A}_s/V\bar{A}_v=S/4NV\sigma_{sn}. \quad (25)$$

This is 8.3 $S/\rho V$ for the metal and 6.15 $S/\rho V$ for the oxide where $\rho$ is the density of the material in the block.

It may be mentioned here that the actual mass absorption is smaller than (22) because $\bar{Q}$ is smaller in the sphere than is its average value in the cell.[11] For a similar reason, the ratio of surface and volume absorptions is somewhat larger in the lower Doppler region than (25).

## NATURAL WIDTH REGION

If we continue to assume that the average energy loss is large compared with the line width, (16) and (18) will give the mass and surface absorptions. An easy integration over the natural line shape gives for these

$$\bar{A}_v=(N\bar{Q}/E)\sigma_{eff}=\pi N\bar{Q}\sigma_{sn}\Delta/ED(1+aE^{\frac{1}{2}}/\Gamma) \quad (26)$$

$$\bar{A}_s=(\bar{Q}/E)f=(\pi/8)\bar{Q}\Delta/DE(1+aE^{\frac{1}{2}}/\Gamma). \quad (27)$$

At the dividing point of the natural width and Doppler width region, (26) should become equal to (22). This is not the case, however, because the same width is attributed in (22) and (26) to different causes: the Doppler width in (22) and the natural width in (26). This causes a discrepancy by a factor $\pi/2$ at the point where the two terms of (12) are equal and where (12) is least accurate. The curves corresponding to (22) and (26) had to be joined as smoothly as possible in the neighborhood of this point and this could not be done without any arbitrariness. It causes the characteristic wiggles in the curves for $\sigma_{eff}$. It also resulted in a slightly higher $\sigma_{eff}$ than either (22) or (26) alone would have given. This is in the right direction to compensate the inaccuracy of (12). Also, the natural width region is slightly extended as far as mass absorption is concerned. Hence, the $\Delta$ for (26) and (27) was needed somewhat beyond the point where the values calculated from the first and second terms of (12) become equal. These are given by the broken lines in Figs. 2(a) and 2(b) and were used to calculate $\sigma_{eff}$ for (26) somewhat beyond the kinks in Figs. 2(a) and 2(b).

The ratio of surface and volume absorptions becomes, according to (26) and (27), half as great as in the Doppler region. The reason is again the difference in the shape of the lines of the two regions. The absorption as given by (26) and (27), is independent of the temperature and inversely proportional only to the square root of $\sigma_{sn}$. This gives to the metal a smaller advantage over the oxide than it has in the Doppler region.

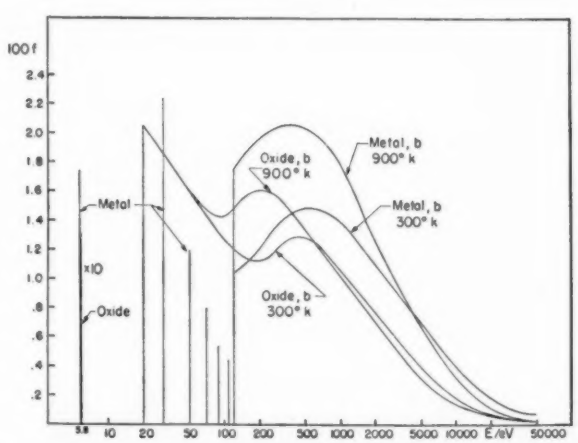


FIG. 4(b). 100×function $f$ plotted as a function of neutron energy under assumption $b$ given in the text.

According to (26), the absorption per unit logarithmic energy interval $E\bar{A}_v$ increases in the natural width region with decreasing energy. In spite of this, if one adopts the constants $a$, even the low energy portion of the natural width region fails to become as important as the upper part of the Doppler region is. On the other hand, if one adopts the constants $b$, the lowest energy region is about as important for the oxide as the top of the Doppler region. For the metal, the bottom of the Doppler region is always relatively unimportant which makes the inadequacy of our approximation at the dividing line between Doppler and natural width regions less objectionable.

As mentioned at the beginning of this section, (26) and (27) hold only if the average energy loss is large compared with the practical width of the line. This is true for scattering collisions on oxygen, down to the lowest level, but it is not true in the metal below 80 ev under assumptions $a$ and below 120 ev under assumptions $b$. This limits the region of validity of (26) and (27), particularly in the case of the metal, to a very narrow energy band. The reason is that, in the metal, the neutron cannot jump over the levels below 80 or 120 ev, respectively, and the absorption of these levels becomes equal to the number of neutrons which would be slowed down below this level if no absorption were present. This number is Fermi's "slowing down density" $\bar{Q}N\sigma_{sn}(2/239)$ so that the volume absorption of every level below 80 or 120 ev becomes

$$A_v=2\bar{Q}N\sigma_{sn}/239. \tag{28}$$

The average absorption as given by (28) is lower than (26) would indicate, the ratio being just the ratio of the average energy loss $2E/239$ to $\pi/2$ times the practical width $2\Delta$ of the level. The reason for this diminution of the absorption is that the neutrons cannot reach at all the lower part of the line since all have been caught in the upper part. Thus, the low energy side of the line has practically no absorption. It follows from (28), which is valid only for the metal, that the absorption per logarithmic energy interval becomes again smaller below 80 or 120 ev. One has the paradoxical situation that the volume absorption of a block is smallest where the absorption coefficient is largest.

The absorption of the lines below 120 ev in the metal is given in Figs. 3(a) and 3(b) and Figs. 4(a) and 4(b) directly, i.e., it is not distributed continuously over an energy range. This is reasonable because the number of levels per unit logarithmic energy range is not large enough for defining the average of the absorption per unit $d\ \ln E$. Hence, if one defines $\int\sigma_{eff}dE/E$ so that the total mass absorption becomes equal to $\bar{Q}N\int\sigma_{eff}dE/E$, the ordinates at the levels (which represent $2\sigma_{sn}/239$) must be added to the integral under the curves of Figs. 3(a) and 3(b),

For the oxide, (26) remains valid except that one has to use, below 80 and 120 ev, for $\sigma_{sn}$ only the cross section of the oxygen, i.e., $10\times10^{-24}$ cm$^2$. Only the lowest level is too broad to be jumped after a collision with an oxygen nucleus and its absorption is

$$A_v=\bar{Q}\times10\times10^{-24}N\times2/17. \tag{29}$$

This also is given as a separate ordinate in Figs. 3(a) and 3(b) and Figs. 4(a) and 4(b).

Although the mass absorption in the lowest energy region is smaller than (26) would indicate, the surface absorption is larger than (27) since (see (17)) of the $\frac{1}{4}\bar{Q}dE/E$ neutrons entering through unit surface, practically none would be present, were it not for the surface. Hence, particularly for the lowest levels, the surface absorption is

$$A_s=\frac{1}{4}\frac{\bar{Q}}{E}\int\frac{\sigma_a(E)}{\sigma_a(E)+\sigma_{sn}}dE=(\pi/4)\bar{Q}\Delta/E \tag{30}$$

or twice larger than (27). The absorption of the metal for the first few resonances is almost entirely a surface absorption, compared with which the volume absorption is negligible.

In the oxide (27) remains valid except for the lowest resonance. However, below 80 and 120 ev, when calculating $\Delta$, one has to use for $\sigma_{sn}$ only the cross section of oxygen, i.e., $10b$. For the lowest level, (30) was used.

The characteristics of the neutron absorption vary very strongly within the natural width region. At the lowest end, the mass absorption of the metal should be negligible as compared with that of the oxide (and even the oxide's absorption may be less than 1/30th of the absorption of uniformly distributed material). On the other hand, at the high energy end, the absorption of the oxide is greater than that of the metal only by a factor $\sqrt{22/12}$, while in the Doppler region this ratio becomes 22/12. Similarly, the ratio of surface absorption to mass absorption is extremely large at the low energy end for the metal and even for the oxide larger than it is in the Doppler region. At the high energy end of the natural width region, the ratio of surface and volume absorptions is only half as great as in the Doppler region. Finally, the whole importance of the natural width region depends strongly on the assumptions one makes for the constants; the whole region is of lesser significance if the constants $a$ are valid, it is an important region if the constants $b$ hold.

## THE CONTINUOUS REGION

We have already dealt with the absorption in the lower part of the continuous region, i.e., beyond the point where $\Delta$ drops to zero, in the section dealing with the Doppler region. The problem reduces, mathematically, to the evaluation of the integrals (21) and (23) for large $\gamma$. For this we found the approximate formulas

$$\int_{-\infty}^{\infty}\frac{dx}{1+\gamma\exp x^2}\approx\frac{\pi^{\frac{1}{2}}}{\gamma}\left(1-\frac{1}{8\frac{1}{2}\gamma}\right), \tag{31}$$

$$\int_{-\infty}^{\infty}\frac{dx}{(1+\gamma\exp x^2)^2}\approx\frac{\pi^{\frac{1}{2}}}{\gamma^2}\left(1-\frac{2}{3\gamma}\right), \tag{32}$$

quite useful and sufficiently accurate. Neither (31) nor (32) have any good mathematical foundation, except for $\gamma=\infty$, but they give roughly correct results for $\gamma>1$. In the very high energy region, the mass absorption is as large as that of uniformly spread out material and the advantage factor is 1. Neither the temperature, nor the substitution of metal for oxide influence the absorption beyond about 15 000 ev. Whether our equations describe the cross section up to the highest neutron energies of about 2 Mev is, of course, not known. It seems rather unlikely that no changes should occur in the density of levels or in the constants $a$ or $\Gamma$ at these high energies. All levels which play any role at low energies have angular momentum $\frac{1}{2}$, and levels with higher angular momenta may play a role at high energies. Szilard and Marshall's value[7] of $0.4\times10^{-24}$ cm$^2$ for the absorption cross section at 200 000 ev may be already an indication in this direction. However, the absorption is presumably quite small at high energies and the inaccuracy of our picture in the high-energy region surely causes less errors than its inaccuracy at low energies.

The surface absorption per unit logarithmic energy range $E\bar{A}_s$ is, for very high $E$, inversely proportional to $E^2$ while the mass absorption was inversely proportional to $E$. This is only another expression for the absence of surface absorption at very high energies. Furthermore, for the same energy, the surface absorption is lower for higher temperatures and also lower for the oxide than for the metal. The reason for the latter is that an incoming neutron in the oxide has a chance to hit an oxygen nucleus first, in which case it did not contribute to the surface absorption. The reason for the decrease of the surface absorption with increasing temperature is that at higher temperatures the lines are more completely washed out and the neutron density $Q$ is a more uniform function of the energy, i.e., is more nearly equal to $\bar{Q}$.

This completes the discussion of the mass and surface absorptions in the different energy regions for given $\bar{Q}$ The remaining section of the original report, dealing with the variation of $\bar{Q}$ within a cell, will be omitted. Instead, we insert a short comparison of the experimental data of the succeeding two papers with the preceding calculations. These data were, or course, not available when the present report was written and it would have been surprising to find a close agreement between the two. After all, the constants given in (3), (4), and (6) constituted only crude estimates.

## COMPARISON OF THE CALCULATIONS WITH THE EXPERIMENTAL RESULTS

Even a crude survey of the Figs. 3a and 3b and Figs. 4a and 4b leads one to the following qualitative conclusions:

1. That the total resonance absorption of a sphere can be represented in a good approximation by a mass absorption and a surface absorption. The former is, for a definite material, proportional to the total mass of the sphere, (hence, for a given radius, proportional to the density) the second is proportional to the surface. The ratio of the surface and mass absorptions depends mainly on the importance of the absorption in the continuous region (above 6000 ev) and is the smaller the greater this is. It should be of the order of $5S/M$.

2. The resonance absorption of the metal should be smaller than that of the oxide by a factor of about 1.4. The greater the continuous absorption is, the smaller is this ratio.

3. Increasing the temperature increases the absorption proportionally with about the cube root of the absolute temperature. The dependence on the temperature is weaker if the high energy absorption is larger.

TABLE I. Mass absorption.

| | Metal | | Oxide | |
|---|---|---|---|---|
| | 300°K | 900°K | 300°K | 900°K |
| Experimental | 7.3 barns | 8.4 barns | 10.9 *b* | 12.5 *b* |
| Constants *a* | 3.9 b | 5.1 *b* | 7.7 *b* | 9.1 *b* |
| Constants *b* | 4.85 b | 8.15 *b* | 8.7 *b* | 10.2 *b* |

The foregoing qualitative statements, taken from the original report, can now be supplemented by Table I, a more detailed comparison with the experimental results taken from the following two articles.

The measurement of the absorption, leading to the constants of Table I, will be discussed in the ensuing two articles. The calculated values are the areas under the curves of Figs. (3a) and (3b) augmented by the lengths of the lines representing the absorption of the low levels. The experimental results are usually expressed in the form

$$\int \sigma_a(\text{total})_{\text{eff}} dE/E = A(1+\mu S/M) \qquad (33)$$

and Table I gives the first part of it

$$\int \sigma_a(\text{mass})_{\text{eff}} dE/E = A. \qquad (33a)$$

The $A$, as determined experimentally, is given in the first row. (It should be remembered that Figs. 3(a) and 3(b) refer to the mass absorption only.)

The agreement between calculation and experiment is surely not good, but it could be hardly expected to be much better. Naturally, one could obtain higher values for the mass absorption, by either increasing both $a$ and $\Gamma$, or by decreasing $D$. It appears more likely, however, that the actual situation differs from that assumed in the body of the report in another way. It is possible that the absorption decreases less rapidly with increasing energy than previously assumed or that part of the absorption which we have attributed to surface absorption is measured as mass absorption. Discussion of the

TABLE II. Surface absorption.

| | Metal (%) | | Oxide (%) | |
|---|---|---|---|---|
| | 300°K | 900°K | 300°K | 900°K |
| Experimental | 5.8 | 5.5 | 4.6 | 4.2 |
| Constants *a* | 18.2 | 19.1 | 11.2 | 11.8 |
| Constants *a* 1st line | 8.8 | 8.8 | 6.5 | 6.5 |
| Constants *b* | 27.7 | 29.3 | 19.6 | 21.0 |
| Constants *b* 1st line | 17.5 | 17.5 | 13.1 | 13.1 |

second possibility will follow. The oft quoted measurements of Szilard and Marshall appear to support the first possibility. Increased absorption in the continuous region would add the same amount to all calculated numbers of Table I and thus decrease both the temperature coefficient of the absorption and the difference between oxide and metal.

While the preceding calculations give at least the right order of magnitude for the mass absorption, they are entirely incorrect as far as the surface absorption is concerned. Table II gives the integrals over $f$, i.e., $\int f dE/E$, augmented again by the absorption in the lines. In order to convert the experimental values for the same quantity, we note that the surface absorption of one uranium atom, in units of $10^{-24}$ cm$^2$, will be denoted by $A\mu S/M$ in the two articles which follow. For the whole lump, this is $(NV/M)\times A\mu S\times 10^{-24}$ cm$^2$ and $(NV/M)A\mu\times 10^{-24}=\int f dE/E$ per unit surface. Since $NV/M$ is the reciprocal of the mass associated with one uranium atom, we have, in the case of the metal

$$\int f dE/E = 2.5\times 10^{-3} A\mu, \tag{33b}$$

and for the oxide

$$\int f dE/E = 2.15\times 10^{-3} A\mu. \tag{33c}$$

In addition to the calculated total, Table II also gives the contribution of the 5.8 ev line alone, and one sees that the contribution of this line alone already exceeds the whole experimental value by a factor of the order 3.

When reviewing the calculation presented above, we have indeed found a point where the approximations are particularly poor. This is after (17) where it is implicitly assumed that all the neutrons entering the lump will suffer some kind of collision therein. This assumption may be permissible in very large lumps but is not permissible in lumps of the size used in our experiments or the usual chain-reacting units. It is not difficult, however, to correct for this circumstance, i.e., take into account the fact that some of the neutrons entering the lump will cross it without suffering a collision in the lump. We shall carry out the calculation for a spherical lump.

The argument leading to (17) shows that the excess number of neutrons, crossing unit area of the surface in unit time with a direction cosine between $\mu$ and $\mu+d\mu$ is

$$\frac{\bar{Q}}{2E}\frac{\sigma_a+\sigma_{sa}}{\sigma_a+\sigma_s}\mu d\mu. \tag{34}$$

The distance which a particle entering with the direction cosine $\mu$ travels inside the sphere is $2r\mu$. Hence, the probability that it suffers any collision in the sphere is $1-\exp[-2\mu r N(\sigma_a+\sigma_s)]$ and the probability that this collision leads to absorption is $\sigma_a/(\sigma_a+\sigma_s)$. This gives for the surface absorption, instead of (18)

$$A_s=\int dE\frac{\bar{Q}}{2E}\int_0^1 \mu d\mu[1-e^{-2\mu r N(\sigma_a+\sigma_s)}]\frac{\sigma_a(\sigma_a+\sigma_{sa})}{(\sigma_a+\sigma_s)^2}. \tag{35}$$

It differs from (18) by the square bracket.

The integration over $\mu$ can easily be carried out in (34) and yields ($\Sigma=(\sigma_a+\sigma_s)N$)

$$\tfrac{1}{2}+e^{-2\Sigma r}\left(\frac{1}{2\Sigma r}+\frac{1}{(2\Sigma r)^2}\right)-\frac{1}{(2\Sigma r)^2}\approx\frac{\Sigma r}{3+4\Sigma r}. \tag{35a}$$

The right side is an approximation to the correct value; it is introduced to enable one to carry out the integration over $E$. This gives, when extended over a single line in the natural width region and divided by $D$

$$\bar{A}_s=\frac{\bar{Q}}{E}f=\frac{\pi\bar{Q}\Delta}{DE}\left(1+\frac{aE^{\frac{1}{2}}}{\Gamma}\right)\frac{2}{1+(1+\frac{3}{4}\sigma_{sn}Nr)^{\frac{1}{2}}}. \tag{36}$$

The scattering cross section $\sigma_{sn}$ is neglected in (35) when compared with the absorption at the center of the line. This is justified except at the high energy end of the Doppler region where the surface absorption is very small anyway. Expression (36) differs from (27) in the last factor which results from the square bracket in (35). It not only decreases the surface absorption, it also renders (36) dependent on $Nr$ which will result in part of (36) appearing as mass absorption and only part of it as surface absorption.

Even though (36) was derived only for the natural width region, its correction factor can be used also in the Doppler region. We conclude that the area under the curve $f$ should be multiplied with the factor

$$c_2=\frac{2}{1+(1+\frac{3}{4}\sigma_{sn}Nr)^{\frac{1}{2}}}. \tag{36a}$$

The possibility of a collision-free traversal of the lump can be taken into account in the same fashion for the calculation of the surface line absorption (i.e., on the expression (30)). This must be replaced by

$$A_s=\int dE\frac{\bar{Q}}{2E}\int_0^1 \mu d\mu[1-e^{-2\mu r N(\sigma_a+\sigma_s)}]\frac{\sigma_a}{\sigma_a+\sigma_s}$$
$$\approx\int dE\frac{\bar{Q}}{2E}\frac{\sigma_a Nr}{3+4(\sigma_a+\sigma_s)Nr} \tag{37}$$

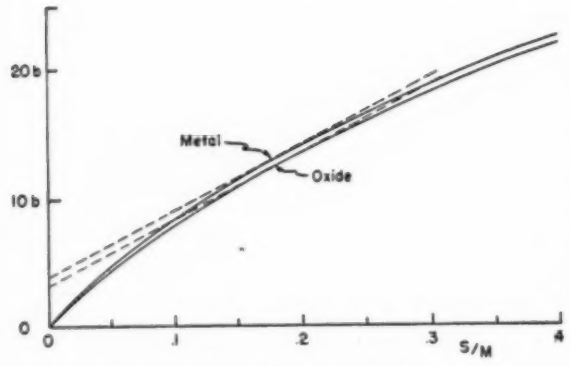


FIG. 5. The surface absorption of spheres plotted as a function of their surface to mass ratio.

where the approximate formula (35a) was used again for the integral of the square bracket. The integration can be carried out again, and neglecting $\sigma_{sn}$ against the cross section at the middle of the line, gives instead of (30)

$$A_s=\frac{\pi}{4}(\bar{Q}\Delta/E)(1+\tfrac{3}{4}\sigma_{sn}N\tau)^{-\frac{1}{2}}. \quad (38)$$

The correction of (30) is the last factor

$$c_1=(1+\tfrac{3}{4}\sigma_{sn}N\tau)^{\frac{1}{2}} \quad (38a)$$

with which the contributions of the lines of Figs. 4(a) and 4(b) must be multiplied.

As a result of the correction factors (36a) and (38a), the surface absorption is not strictly proportional to the surface. Instead, assumption *b* gives, in the case of the metal at 300°K,

$$\int fdE/E=2.5\times10^{-3}A\mu=17.5c_1+5.2c_1+5c_2. \quad (38b)$$

The first term on the right side is due to the lowest line, the second to all other resonance lines up to 120 ev, the last term to the integral of the curve of Fig. 4(b) above 120 ev. Similarly, in the case of the oxide one has

$$\int fdE/E=2.15\times10^{-3}A\mu=13.1c_1+6.5c_2. \quad (38b')$$

The surface absorption of spheres, obtained from (38b) and (38b'), is plotted in Fig. 5 against $S/M$. The ordinate on the left side is $A\mu$. One sees that the surface absorption is not proportional to $S/M$ but can be well approximated by a straight line for $S/M$ values around 0.2 where most measurements were carried out. The equation of the line for the metal is $4+50\ S/M$, that for the oxide $3+50\ S/M$. Adding to these expressions the mass absorption from Table I, one obtains the total absorptions given in Table III. The apparent mass absorptions now agree almost exactly which is, unquestionably, fortuitous in view of the arbitrariness in the choice of the constants. (One might remember also that the values of $\sigma_{sn}$ of (7) and (7a) are too high. Reducing them to the now accepted values would decrease the calculated values.) The calculated value of the apparent surface absorption, however, remains too high by a very considerable factor. This absorption is due, principally, to the lowest line (at 5.8 ev) and we come, reluctantly, to the conclusion that the constants

TABLE III.

| | Metal 300°K | Oxide 300°K |
|---|---|---|
| Experimental | $7.3+23.5\ S/M$ | $10.9+21\ S/M$ |
| Recalculated *b* | $8.85+50\ S/M$ | $11.7+50\ S/M$ |

given for this line are inaccurate, in particular that $\Gamma$ must be too high.[12] As was mentioned before, such a change is indicated also by the relatively low thermal absorption cross section of $U^{238}$.

A variety of assumptions could be made to explain the low temperature coefficient of the resonance absorption. The calculated temperature coefficient is due to the absorption in the Doppler region. The extent of the Doppler region could be decreased, most simply, by increasing the *a* and $\Gamma$ of the lines. If this interpretation is correct, it re-emphasizes the great variability in the constants of the various lines. In view of the experimental data which have been accumulated in the last few years[6] on the constants of resonance lines, such a variability should be even less surprising now than it was when our reports were written.

It seems to us that the preceding calculations show that the measurement of the resonance absorption of lumps may in many cases yield the average values of the constants of resonance levels more directly and, perhaps, even more easily than a detailed measurement of several levels.

[12] This conclusion is borne out, however, by the measurements of Levin and Hughes, reference 2.

# Effect of Geometry on Resonance Absorption of Neutrons by Uranium*

E. Creutz,† H. Jupnik,‡ T. Snyder,§ and E. P. Wigner
*Princeton University, Princeton, New Jersey*

(Received September 15, 1954)

The total resonance absorption of neutrons by spheres of uranium and uranium oxide imbedded in graphite and bombarded with essentially a $dE/E$ spectrum is found to be given by $1/\alpha = c[1+(\kappa/\rho R)]$ where $\alpha$ is the advantage factor, that is, the ratio of absorption of uranium when distributed uniformly throughout graphite to the absorption when it is lumped in a sphere. $R$ is the radius of the sphere and $\rho$ is its density. $c$ and $\rho$ were measured in various parts of a large graphite block exposed to cyclotron neutrons from the reaction Li $(p,n)$. Values of $c$ and $\rho$, respectively, are 0.051 and 5.1 g/cm² for $U_3O_8$. In a newer notation, $A=10.9$ barns and $\mu=1.95$ g/cm².

## INTRODUCTION

WHEN uranium with its natural mixture of isotopes is exposed to neutrons in a chain-reacting pile there is a competition by several processes for the absorption of the neutrons. One of the chief competitors to the absorption by $U^{235}$ to cause fission is the absorption by $U^{238}$ to produce the compound nucleus $U^{239}$. This system may re-emit the neutron or emit a gamma ray. In the second case, the remaining beta active nucleus $U^{239}$ decays with a 24-min half-life.[1]

The capture of neutrons above thermal energies is described rather well by the Breit-Wigner formulas,[2] and an analysis of the case, assuming that one resonance level predominates, is given by Anderson.[3] A more accurate analysis was given subsequently by S. Dancoff and M. Ginsburg.

Since the neutrons with energies above thermal are predominantly absorbed in narrow resonances, there should be a significant difference in the specific absorption of neutrons near the surface and in the volume of a chunk of uranium, so that the total loss of neutrons by this process might be reduced by choosing the proper size of chunk. Thus, the "self-reversal" effect of the strong resonance absorption would produce a spectrum of neutrons in the chunk which would be deficient in the energies of the resonances. This would suggest making the chunk, for example, a sphere, with a small surface-to-volume ratio. But clearly a limitation on the optimum size of a sphere would be reached because (1) in too large a sphere fission-producing neutrons would be depleted before the center portions were reached, and (2) the uranium of the sphere itself would produce some energy losses by scattering of the neutrons and thus destroy the self-reversed character of the neutron spectrum.

## EARLY WORK

In June, 1941, preliminary work on the absorption of resonance neutrons in spheres of uranium oxide was carried out by Fermi and Anderson together with R. R. Wilson and others of the Princeton group. This work verified the fact that the total absorption could be divided roughly into a surface effect and a volume effect with much higher specific absorption taking place at the surface.

The spheres for the first work described below were made of $U_3O_8$ powder tamped into thin Cu shells which in turn were covered with cadmium to remove thermal neutrons. They were imbedded in a large graphite block 81 by 81 by 107 cm³ which was bombarded with neutrons from the reaction $Li^7(p,n)Be^7$ produced by 8-Mev protons in the Princeton cyclotron. The resonance absorption was measured by sampling the material in the sphere, removing fission products and UX by the method described by Anderson,[3] and counting the induced 24-min beta activity. This method suffered from certain inaccuracies. A second improved method was therefore used later. Both methods and the results obtained with them are described below.

## FIRST METHOD

Spheres of diameter $2\frac{1}{4}$, 3, 4, 5, 6, 7, and 8 in., consisting of thin copper shells packed with $U_3O_8$, were prepared. Into a cylindrical cavity extending to the center of each shell, a cadmium cone could be placed. This cone, which was intended to sample the surface and the volume in the correct ratio, was filled with $U_3O_8$ to furnish the activity for measuring after bombardment. The bombarded material was thoroughly mixed and a sample of it was painted thinly on paper, using a small amount of dilute collodion as a binder, or else the powder was pressed onto Scotch tape. This latter method gave a very uniform and rather thin sample. If a still thinner sample was desired, a second piece of Scotch tape was stuck to the coated one and pulled away when a very thin layer of $U_3O_8$ particles would adhere to it. Each bombardment was monitored with a thin $U_3O_8$ sample in a standard place, so all runs could be compared to a standard irradiation. The

* This work was supported by the NDRC in 1941. It was declassified by authority of the U. S. Atomic Energy Commission on May 27, 1952.

† Now at Carnegie Institute of Technology, Pittsburgh, Pennsylvania.

‡ Now at American Optical Company Research Laboratory, Southbridge, Massachusetts.

§ Now at General Electric Company, Schenectady, New York.

[1] Meitner, Hahn, and Strassman, Z. Physik **106**, 249 (1937).

[2] G. Breit and E. Wigner, Phys. Rev. **49**, 519 (1936).

[3] Herbert L. Anderson, Phys. Rev. **80**, 499 (1950).

amount of resonance absorption in the sphere was thus measured by the 24.2-min $U^{239}$ activity counted with an argon-alcohol-filled thin glass-wall Geiger counter. To compare the absorption in different spheres, the relative weights of the samples prepared from them had to be determined. For comparing the effective weights of very thin samples it had been found satisfactory to bombard them all on a motor-driven rotating wheel in a cavity inside the graphite block, so that they would, on the average, all be in the same position and receive the same irradiation. Their weights were then assumed proportional to their induced activities. This effective weight method (in samples of various thicknesses) corrects for self-absorption of the beta rays, but also is affected by self-absorption of the neutrons in the sample. This is not what was wanted. Since, for samples prepared from the material in the spheres, it was necessary to know a quantity actually proportional to the activity per milligram, some method of calibrating them must be found which was independent of neutron self-absorption in the samples.

The method used was to irradiate them inside a vessel having thick walls of $U_3O_8$, so only those neutrons having the property of not being easily absorbed (hence, not suffering self-absorption) would induce the calibrating activity. The samples were thin enough so the beta absorption was negligible.

To compare the activity per milligram produced in the spheres with that which would have been induced had the $U_3O_8$ been uniformly distributed throughout the graphite, a very thin sample was prepared and bombarded. This sample was calibrated for thickness in the thick-walled vessel as were the sphere samples.

The ratio of the activity per milligram induced in a thin sample to the average that is induced in a given sphere gives a measure of the advantage of thus lumping the uranium, and hence may be called the advantage factor, $\alpha$, for the sphere. This factor will vary with the size of the sphere since the specific absorption of the surface layer is considerably greater than that of the volume. Measured $\alpha$'s are listed below. The advantage is seen to increase as larger spheres are used as expected since the surface becomes smaller relative to the volume. These data were taken with the spheres 20 cm from the front of the graphite block which was surrounded with borax and paraffin so that few neutrons could enter except from the front, which was shielded with $1\frac{1}{2}$ in. of $B_2O_3$ to pass only neutrons of energy $\lesssim 1000$ ev.

| Radius of sphere (cm) | Advantage |
|---|---|
| 2.86 | 8.92 |
| 5.35 | 10.7 |
| 7.55 | 12.7 |

## SECOND METHOD

Because of the difficulty of obtaining calibrations of the effective thickness of the samples made from the spheres by the first method, and also because of the small activity obtainable in the thin samples, a thick sample method was used. In this method the counter samples were all made infinitely thick for the beta rays, so no calibration was necessary. This was accomplished by making dishes by sealing 0.002-in. Al foil between two brass rings $2\frac{1}{2}$ in. in diameter and $\frac{1}{8}$ in. deep, which could be filled with the bombarded $U_3O_8$. This dish was supported in a Bakelite cradle which fitted tightly inside the lead counter shield so that the geometry could be accurately reproduced. That this was possible was proven by the fact that the slopes of the growth curves of UX activity taken with various $U_3O_8$ samples from which the UX had been previously removed chemically were the same to within about 1 percent. About 25 grams of $U_3O_8$ were required to fill the dish. The spherical shells used in this method were spun in two hemispheres from cadmium sheet. Each was filled with $U_3O_8$ and covered across the equatorial plane with a sheet of 0.002-in. Al, held in place by Scotch tape. The two halves thus covered were held together with more tape. After bombardment of such a sphere inside a graphite block one of the hemispheres was opened and its contents were sampled. This eliminated the difficulty with the earlier cadmium cone method, namely, the difficulty of insuring that the base of the cone was flush with the sphere surface. The cadmium cone also slowed neutrons into resonances inside the sphere to an uncertain extent. The sampling of the hemisphere was done by placing its contents in a large bottle, which was thoroughly shaken to mix. The mixing method had been previously tested with black and white powders, which gave a uniform gray after a few seconds. A portion of the $U_3O_8$ so shaken was then dissolved in $HNO_3$, and ether was added. The ether solution of $UO_2(NO_3)_2$ was made neutral with $Na_2CO_3$, dried with $CaCl_2$, and decanted into a separatory funnel after which about 1 cc of water to 100 cc of ether was added and the contents vigorously shaken. The separation was then made to remove fission products and UX which are selectively soluble in the water. The ether was then blown off, and the residue calcined, ground, and put in the Al foil-bottomed dish for counting. Up to ten times, the UX background was observed for the initial 24-min counting rate one hour after bombardment.

The magnitude of the 24-min activity relative to the various monitors was computed from the counter data by a least squares method. The decay period was assumed known as 24.2 min and the slope of the growth curve of UX was frequently measured and known to about 1 percent; thus, the net strength of the $U^{239}$ activity at a certain time could be calculated as the difference between the total observed activity at that time and the extrapolated UX activity.

## MONITORS

At first, the neutron beam was monitored with two thin $PbI_2$ samples placed on either side of the cyclotron in cadmium envelopes. It was supposed that if the

ratio of the activities in these two monitors remained the same from run-to-run, the neutron beam probably was reasonably consistent in its spectrum since it must have originated from the same part of the cyclotron. Since the frequency and other conditions of the cyclotron were not entirely constant, some variation in this ratio was found. Therefore, the later experiments were monitored inside the graphite block. A small correction to the relative irradiations had to be made in comparing the 25-min iodine activities with the 24.2-min uranium activities, but this amounts to only about 4 percent for a one-hour bombardment. A calculation showed that this correction did not change appreciably even if the beam was very unsteady.

In most of the experiments, a thin iodine monitor was taped to the outside of the sphere to measure the neutron density at that point. To obtain the specific volume activity, a surfaceless or "infinite" sphere was made by surrounding a small sphere of $U_3O_8$ by a larger one. The activity induced in the central sphere was only measured then. In most cases a $2\frac{1}{4}$ in. sphere imbedded in a 6 in. sphere was used for this purpose. A monitor was placed in the center of the sphere and also on the surface.

## "NO-SPHERE" EXPERIMENTS

To obtain the activity of a thin sample of uranium, a piece of filter paper was soaked in $UO_2(NO_3)_2$ solution. This was then dried, weighed, wrapped in Cd, and bombarded inside the graphite block. It was then possible to obtain the advantage factors for spheres by purifying and calcining the material from this thin sample, and measuring the activity in the same way as was done with the sphere samples with which it was compared. This type of experiment was called a "no-sphere" experiment. In order to obtain the absolute reciprocal advantage for a given configuration it was only necessary to divide the value of the absorption relative to one kind of monitor for that configuration, by the no-sphere absorption relative to its monitor of the same kind. Figures 1 and 2 are typical and show the

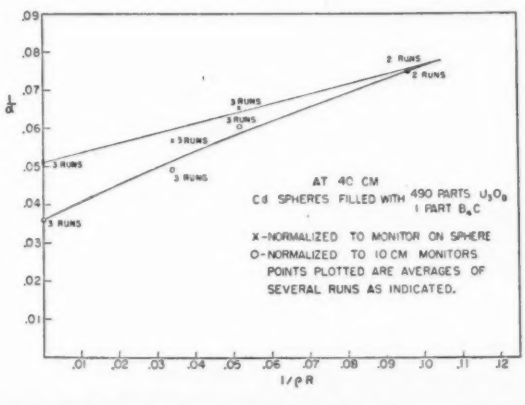


FIG. 1. Reciprocal advantage factor for spheres of $U_3O_8$ containing $B_4C$ plotted as function of reciprocal product of sphere radius and sphere density.

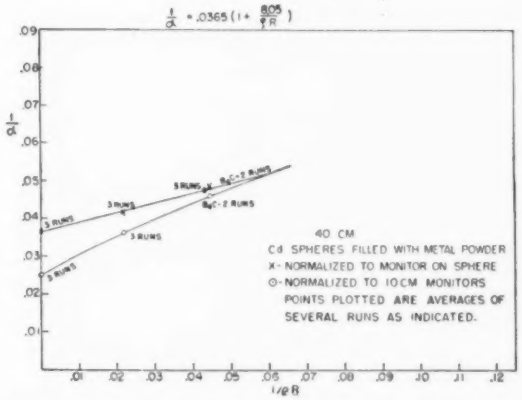


FIG. 2. Reciprocal advantage factor for spheres of metal powder plotted as function of reciprocal product of sphere radius and sphere density.

measured reciprocal-advantage factor is plotted as a function of $1/\rho R$ where $\rho$ is the density of the material in the sphere and $R$ is the radius of this sphere. In each figure two curves are shown, the upper one represents the data obtained by using as monitor the detector fastened to the surface of this sphere, the lower curve shows the data calculated by using as monitor a detector near the front of the graphite block (called 10-cm monitors). Because of depression of the true neutron density in the vicinity of the sphere, the more meaningful values are those obtained with the surface monitor, that is, those shown on the upper curve in each case. The theoretical form

$$\frac{1}{\alpha}=c\left(1+\frac{\kappa}{\rho R}\right)$$

was assumed and straight lines were drawn.

## METAL POWDER

Rough values for absorption by spheres of metal powder were obtained. Since U metal powder is highly pyroforic, these spheres were filled in a covered washtub containing a $CO_2$ atmosphere maintained by several large chunks of dry ice. After bombardment, the powder was dumped into a flask with small chunks of dry ice. The flask was kept in the washtub, with its neck protruding through a hole in a cover to the tub, and shaken to mix. No explosions were encountered. The metal powder was divided into ten portions, each of which was added slowly to a separate beaker of dilute $HNO_3$. Considerable $H_2$ and $N_2O_4$ were evolved. In one case when the powder was added too fast, it ignited. The fire was easily put out with a $CO_2$ extinguisher. In subsequent experiments the $H_2$ was blown off by a stream of air as it was evolved, and no more trouble was experienced.

## RESULTS

The total resonance absorption by a sphere of U or $U_3O_8$ has been found to consist of a term proportional

to the total mass and another term proportional to the surface of the sphere. Thus, the reciprocal of the advantage factor may be expressed as

$$1/\alpha \propto M + dS$$

where $d$ is a constant, $M$ the mass of the sphere, and $S$ is the surface. This may be written

$$1/\alpha = a + (b/R)$$

since to a good approximation the specific volume absorption is independent of the radius, $R$. The effective "thickness" of the surface is inversely proportional to the number of atoms of uranium per cm³, so finally:

$$\frac{1}{\alpha} = c\left(1+\frac{\kappa}{R\rho}\right)$$

where $\rho$ is the density of the sphere and constants $c$ and $\kappa$ are to be determined. Some qualitative knowledge of the variation of $c$ and $\kappa$ with the neutron spectrum was obtained by making measurements at 20, 30, 40, and 45 cm from the front of the block since the average neutron energy decreases with the increasing depth.

Since this work was carried out, it has become customary to express these and related results in terms of the resonance integral. Here,

$$\int \sigma_c(E)dE/E,$$

assumes a $dE/E$ neutron spectrum. For an extremely dilute mixture of uranium in a noncapturing, slowing-down medium this integral is accepted as having the value of 240 barns. For lumped arrangements of uranium and its oxide, these experiments show that this integral may be expressed as follows:[4]

$$\left(\int_{\text{lump}} \sigma_c(E)\frac{dE}{E}\right)_{\text{effective}} = A\left[1+\mu\frac{S}{M}\right],$$

where $S$ is the surface of the lump in square centimeters and $M$ is its mass in grams. $A$ and $\mu$ are then the experimentally determined quantities. Comparing this expression with ours for the reciprocal advantage factor,

$$\frac{1}{a} = c\left(1+\frac{\kappa}{R\rho}\right) = \left(\int_{\text{lump}} \sigma(E)\frac{dE}{E}\right)_{\text{effective}} \Big/ 240 \text{ barns},$$

it is seen that $\mu = \kappa/3$ and $A = 240c$ barns.

TABLE I. The constant $A$ measured for various materials.

| Material | Average $\sigma_s$ per U atom $=\bar{\sigma}_s$ | $(\bar{\sigma}_s)^{\frac{1}{2}}$ | $A$ (measured) |
|---|---|---|---|
| U | 9.5 | 3.08 | 7.4 |
| $U_3O_8$ | 20.7 | 4.55 | 12.2 |
| 5 $U_3O_8$+2C (By weight) | 66 | 8.10 | 22.6 |

[4] Phys. Today **5**, 32 (May, 1952).

To study the effect of slowing-down-material in the sphere, such as the oxygen of $U_3O_8$, spheres were filled with a mixture of $U_3O_8$ and graphite of such proportions that the total scattering of the graphite in the mixture was twice as much as that of the uranium and the oxygen, namely, 5 parts $U_3O_8$ to 2 parts of graphite by weight. As was expected, the activity per milligram of $U_3O_8$ was larger under these conditions. As an extreme dilution, an 8-in. cube was filled with a mixture of 10 parts of graphite to 1 part of $U_3O_8$. The $U_3O_8$ was removed after bombardment by panning, as in separating gold from sand. The advantage of this homogeneous mixture was only about 3 showing it to be much less effective for depressing the resonance absorption than are spheres of pure $U_3O_8$.

According to theory the volume absorption should vary as the square root of the average scattering cross section, per uranium atom, of the material in the sphere. Values of this cross section,[5] its square root, and measured values of $A$, are given in Table I. These values are plotted in Fig. 3 and are seen to fall near a straight line. In the same figure are plotted values of $\mu$ for various materials.

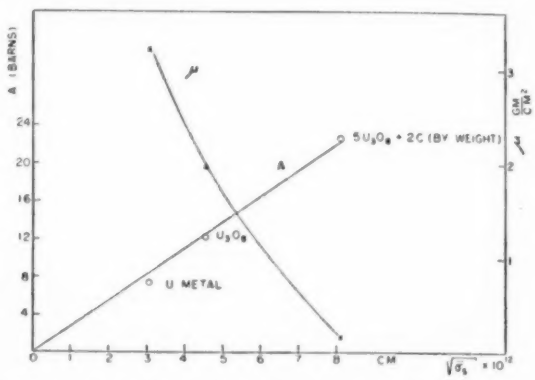


FIG. 3. Effective volume absorption $A$ (barns) and effective mass absorption coefficient, $\mu$, of spheres of uranium to which are mixed different amounts of scattering material, plotted as a function of the square root of the average scattering cross section, per uranium atom, of the material in the sphere.

A 2-in. cube was filled with $U_3O_8$ of different densities, including the standard one of 3.76, to determine the effect of density, as well as the relative advantages of a cube and a sphere. The cube of standard density showed 12 percent more resonance absorption than would a sphere of the same density and mass.

To estimate the effect of the $1/v$ neutrons, spheres filled with 1/491 parts by weight of $B_4C$ were used. This is enough to absorb about 80 percent of the $1/v$ neutrons. Its effect was to reduce the 24-min activity by less than 10 percent in general. However, the data are just good enough to justify applying a correction to the $A$ values obtained with spheres not containing

[5] At the time our measurements were undertaken, the accepted value for the scattering cross section of uranium was 12$b$.

boron. This correction, due to the $1/v$ tail above the cadmium cutoff, is given by

$$\int_{0.45}^{\infty} \sigma_{\text{thermal}} \left(\frac{E_{\text{thermal}}}{E}\right)^{\frac{1}{2}} \frac{dE}{E}$$

$$= 2.85(0.025)^{\frac{1}{2}}[-2/E^{\frac{1}{2}}]_{0.45}^{\infty} = 1.35 \text{ barns.}$$

Applying this correction to the constant $A$ improves the consistency of the data. This correction is applied only to the volume effect since the penetrating power of these neutrons is too great to cause surface absorption. The correction to $A$ changes $\mu$ slightly since $\mu$ is calculated in terms of $A$. The corrected $\mu$ is listed with $A$ and the uncorrected $\kappa$, $c$, and $\mu$ in Table II.

Because the $c$'s depend on the "no-sphere" experiments, their absolute values are less accurate than the ratios of those for various spheres at a given distance in the block.

TABLE II. Constants for $U_3O_8$ spheres.

| Material | $\kappa$ | $c$ | $\mu=\kappa/3$ | $A=[240c-1.35 \text{ barns}]$ | $\mu$ corrected g/cm³ |
|---|---|---|---|---|---|
| U[a] | 7.1 | 0.036 | 2.7 | 7.3 | 3.2 |
| $U_3O_8$ | 5.1 | 0.051 | 1.7 | 10.9 | 1.95 |
| 5 $U_3O_8$+2C (By weight) | 0.43 | 0.078 | 0.14 | 17.4 | 0.155 |

[a] Values for U metal less accurate than for $U_3O_8$ due to greater experimental difficulties.


## ACKNOWLEDGMENT

Much credit for finishing these experiments is due Mrs. E. Creutz for her work in compiling and computing data, to T. Lanahan for his consistent efforts to keep the cyclotron in operation and help in numerous other ways, and to E. Frank, who constructed and maintained the Geiger counters. Similar experiments were carried out later by A. C. G. Mitchell and his collaborators at the University of Indiana. The accuracy of their experiments was greater than that of ours, but the general results were similar.

# Effect of Temperature on Total Resonance Absorption of Neutrons by Spheres of Uranium Oxide*

E. Creutz,† H. Jupnik,‡ and E. P. Wigner
*Princeton University, Princeton, New Jersey*
(Received September 15, 1954)

In the expression $1/\alpha=\epsilon[1+(\kappa/\rho R)]$ for the advantage ($\alpha$) of decreased resonance absorption of uranium in a $dE/E$ neutron spectrum brought about by lumping $UO_2$ into spheres, the temperature dependence of $\epsilon$ is measured and $\kappa$ is measured also. $\rho$ is the density of $UO_2$ in g/cm³; $R$ the radius of the sphere in cm. In the range 20° to 1000°C, $\Delta\epsilon/\Delta T$ averages $1.8\times10^{-6}$ per degree centigrade and is positive as expected. This temperature dependence decreases by about a factor of three from the lowest to the highest measured temperatures. $\kappa$ is 5.06 g/cm³ leading to a value of $\mu$ in the expression [Phys. Today **5**, 32 (May, 1952)]

$$\left(\int\sigma(E)\frac{dE}{E}\right)_{eff}=A\left[1+\mu\frac{S}{M}\right]$$

of 1.69 g/cm².

$\frac{\Delta A}{\Delta T}$ is $4\times10^{-4}\ \frac{\text{barns}}{°\text{C}}$.

## INTRODUCTION

THE reaction rate of a moderated uranium pile depends on temperature. For example, in a reactor in which the neutron spectrum is approximately Maxwellian, the average velocity will increase with temperature, thus decreasing the absorption cross sections for the low-energy neutrons which vary as $1/v$. Resonance levels will be broadened by the Doppler effect, and if lumping of the uranium has been made use of to decrease the total resonance absorption as proposed by Szilard,[1] and later found experimentally to be effective,[2] increased temperature will decrease the advantage thus gained.

In order to design a method for controlling the reaction rate of the nuclear chain reaction a knowledge of the variation with temperature of the number of neutrons absorbed at the resonances by uranium is, therefore, important.

## METHOD

For studying this effect a furnace was constructed, eliminating as much as possible elements whose neutron absorptions are large or unknown. This furnace was immersed in a graphite block 100 cm square by 125 cm long, and bombarded with neutrons from the reaction $Li^7(p,n)Be^7$ using 8-Mev protons from the Princeton cyclotron. Various arrangements of uranium oxide were surrounded by material containing B or Cd to absorb thermal neutrons, and the 24-min activity induced by resonance neutrons was measured.

The furnace itself consisted of a block of graphite 16 in. square by 12 in. long surrounded on all sides by a 4 in. layer of lampblack. Twelve standard type Globar (silicon carbide) heating elements were arranged symmetrically in a circle of radius 18 cm about a central block 4×4×10 in. which could be removed and loaded with the uranium sample. A sketch of the furnace is shown in Fig. 1. As may be seen, the center of the sphere was separated from the front face (towards cyclotron) of the graphite block by 35 cm of graphite and 10 cm of lampblack (density ~0.1). The graphite outside of the lampblack layer stayed below about 30°C during all experiments. The temperature of the furnace was measured by two thermocouples, one placed $2\frac{1}{2}$ in. from the center of the sphere, and one placed about 1 in. from one of the Globars. The furnace was heated by passing current through the Globars until the thermocouple near one of them registered a temperature about 50°C above the desired temperature, at which time the temperature near the sphere was about 50°C less than that desired. The power was then turned off for about 15 min while the two temperatures equalized, after which bombardment was started. After an hour, the sphere was usually a few degrees hotter than the Globars. During the actual bombardment all the furnace graphite and the sphere were at the same temperature within about 25°C.

After bombardment, the hot central-sphere block was removed and the uranium oxide from one hemisphere was taken out and broken up in a mortar, dissolved in $HNO_3$, and the ether purification made, as described by Anderson,[3] after which a thick-dish sample was prepared for counting, as in previous work.[2] The cyclotron beam was monitored from run-to-run with (a), two $PbI_2$ samples placed at 10 cm in the block (at room temperature), (b), with a $PbI_2$ sample placed on the cyclotron outside the block, and (c), with a thin

* This material originally appeared in Document C-110 in 1942 reporting research supported by the NDRC. It was declassified by authority of the U. S. Atomic Energy Commission on May 27, 1952.

† Now at Carnegie Institute of Technology, Pittsburgh, Pennsylvania.

‡ Now at American Optical Company Research Laboratory, Southbridge, Massachusetts.

[1] Private communication.

[2] Creutz, Jupnik, Snyder, and Wigner, J. Appl. Phys. (to be published).

[3] Herbert L. Anderson, Phys. Rev. **80**, 499 (1950).

layer of KI melted onto a steel or platinum dish behind and at 10 centimeters from the center of the sphere and at the temperature of the sphere. The KI layer contained less than 7 mg/cm² of iodine in each case and was prepared in the same way each time, by evaporating 1.5 cm³ of an alcohol solution, so the correction for self-absorption should be negligible and not vary appreciably from run-to-run. After bombardment, the KI was converted to $PbI_2$ which was washed and pressed onto Scotch tape for counting.

All monitors were surrounded by cadmium or $CdSO_4$. When half a dozen or so of these monitor samples had accumulated they were placed in a tilting rotating peanut-roaster type cylindrical mixer and bombarded with neutrons including thermals, inside the large graphite block, after which their relative activities were assumed to give their relative weights. Since they were only about 2 to 3 mg/cm² thick, this method should quite accurately give the relative numbers of atoms present.

Since KI melts at 723°C and has an appreciable vapor pressure below that temperature, a substance was sought for use as a monitor which was physically and chemically stable at higher temperatures and became radioactive after resonance-neutron capture with a period not far different from 24.2 min. The material chosen was $Ga_2O_3$, since it is stable and not appreciably volatile at 1200°C, and $Ga(n,\gamma)$ gives a period of 21 min. There is also a period of 14 hours, which introduces a correction, small for short bombardments.

In an attempt to determine how the actual number of resonance neutrons inside the furnace relative to those outside varied with temperature, caused by the different temperature-dependence of absorption by the carbon and other materials, two types of check experiments were made. At each temperature several bombardments were made of the cyclotron monitor, the 10-cm monitor, and the hot-dish monitor, but with no uranium present, leaving a hole in the graphite where its uranium oxide sphere was otherwise placed. These experiments were not very accurate, but they show that for a given bombardment of the furnace the number of neutrons absorbed by a hot iodine or Ga sample inside the hot furnace is the same within 8 percent as when the furnace is cold.

The interpretation is complicated by the fact that the iodine levels may change their effectiveness by Doppler broadening as the temperature is raised. Therefore, a second type of check was made in which the dish monitor inside the hot furnace was separately water-cooled. In this case, the sensitivity of the monitor could not depend on the temperature of the graphite. Although there appears to be a slight increase in the resonance-neutron density within the graphite at higher temperatures, these experiments indicate no effect on the cold iodine in the hot furnace greater than 6 percent, which is within their accuracy. Part of this effect was probably caused by the leakage of thermal

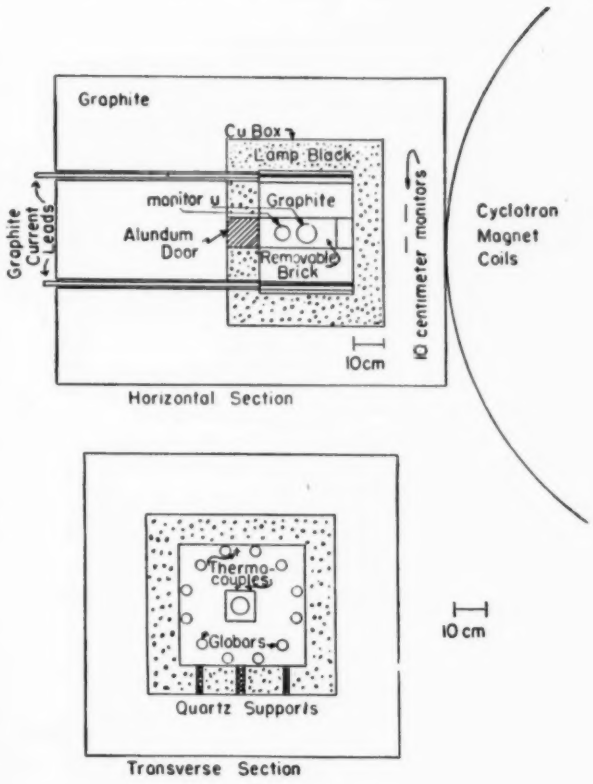


FIG. 1. Furnace.

neutrons through the cadmium shield of the monitor as discussed later. Because of the uncertainties, the values of the absorption relative to the 10-cm monitors are believed to be more reliable than those relative to the hot monitors.

The uranium oxide was held in most cases in steel shells 6.8 by $10^{-2}$ cm thick, surrounded by shields to absorb thermal neutrons. No difference was found if copper shells were used in place of the steel. The thermal neutron shields were of two types: one a mixture of $CdSO_4$ and $Al_2O_3$ such that there was 0.49 g/cm² of Cd around the sphere, and the other $B_4C$ and $Al_2O_3$, sufficient to place 0.13 g/cm² of B around the sphere. Above 700°C, in the CO atmosphere generated by diffusion of air into the furnace, the $CdSO_4$ decomposed, and CdS and Cd boiled off. Therefore, a chemical analysis of the shell was made after use, showing that some of the experiments were done with less Cd around the uranium than were others. To partially remedy this trouble, $CdSiO_3$ shells were prepared, but they also partly decomposed to Cd which evaporated.

Three types of spheres were used: an approximately 2 in. sphere of uranium oxide of density 4.12, a $3\frac{1}{4}$ in. sphere of the same density; and an "infinite" sphere, i.e., a 1 in. sphere imbedded in a $3\frac{1}{4}$ in. sphere, from which only the activity of the material in the 1 in. sphere was measured, giving a sphere with little or no surface effect for absorption.

TABLE I. Heat experiments—typical data.

| Material | Outer shell | Sphere, cm | $1/\rho R$ | Temp., °C | No. sphere/adv. |
|---|---|---|---|---|---|
| 2 in. spheres, 10-cm monitors. Density of all materials in spheres was 4.12 g/cc | | | | | |
| $UO_2$ | $CdSO_4$ | Fe; $R=2.45$ | 0.0990 | room temp. | weighted av: 0.03065±0.0003 |
| $UO_2$ | $CdSO_4$ | Fe; $R=2.45$ | 0.0990 | 300 | weighted av: 0.0302±0.0003 |
| $UO_2$ | $CdSO_4$ | Fe; $R=2.45$ | 0.0990 | 700 | weighted av: 0.0350±0.0003 |
| $UO_2$ | $CdSO_4$ (0.344 g/cm²) of Cd | Fe; $R=2.45$ | 0.0990 | 1000 | 0.0358±0.0006 |
| $UO_2$ | $B_4C$ | Fe; $R=2.55$ | 0.0953 | room temp. | weighted av: 0.0197±0.0003 |
| $UO_2$ | $B_4C$ | Fe; $R=2.55$ | 0.0953 | 300 | 0.0212±0.0002 |
| $UO_2$ | $B_4C$ | Fe; $R=2.55$ | 0.0953 | 700 | weighted av: 0.0227±0.0002 |
| $UO_2$ | $B_4C$ | Fe; $R=2.55$ | 0.0953 | 1000 | 0.0260±0.0007 |
| $3\frac{1}{4}$ in. spheres, 10-cm monitors. All spheres were filled with $UO_2$; density=4.12 g/cc | | | | | |
| $UO_2$ | $CdSO_4$ | Fe; $R=4.11$ | 0.0591 | room temp. | weighted av: 0.0252 |
| $UO_2$ | $CdSO_4$ | Fe; $R=4.11$ | 0.0591 | 300 | weighted av: 0.0269±0.0003 |
| $UO_2$ | $CdSO_4$ | Fe; $R=4.11$ | 0.0591 | 700 | weighted av: 0.0276±0.0002 |
| $UO_2$ | $B_4C$ | Fe; $R=4.11$ | 0.0591 | room temp. | weighted av: 0.0164±0.0001 |
| $UO_2$ | $B_4C$ | Fe; $R=4.11$ | 0.0591 | 300 | 0.01731±0.0003 |
| $UO_2$ | $B_4C$ | Fe; $R=4.11$ | 0.0591 | 700 | weighted av: 0.0191±0.0006 |
| ∞ spheres, 10-cm monitors. All spheres were filled with $UO_2$; density=4.12 g/cc | | | | | |
| $UO_2$ | $CdSO_4$ | Fe; $R=1.27$ inside $R=4.11$ | 0 | room temp. | weighted av: 0.0190±0.0001 |
| $UO_2$ | $CdSO_4$ | Fe; $R=1.27$ inside $R=4.11$ | 0 | 300 | weighted av: 0.0203±0.0007 |
| $UO_2$ | $CdSO_4$ | Fe; $R=1.27$ inside $R=4.11$ | 0 | 700 | weighted av: 0.0211±0.0006 |
| $UO_2$ | $CdSO_4$ (0.108 g/cm²) of Cd | Fe; $R=1.27$ inside | 0 | 1000 | 0.0224±0.0003 |
| $UO_2$ | $B_4C$ | Fe; $R=1.27$ inside $R=4.11$ | 0 | room temp. | weighted av: 0.0142±0.0001 |
| $UO_2$ | $B_4C$ | Fe; $R=1.27$ inside $R=4.11$ | 0 | 300 | 0.0145±0.0002 |
| $UO_2$ | $B_4C$ | Fe; $R=1.27$ inside $R=4.11$ | 0 | 700 | weighted av: 0.0147±0.0003 |
| $UO_2$ | $B_4C$ | Fe; $R=1.27$ inside $R=4.11$ | 0 | 1000 | 0.0148±0.0004 |
| $U_3O_8$ | None | none (thin sample) | ∞ | 20 | weighted av: 0.333 |

Besides using these concentrated arrangements of uranium, measurements were made to obtain the activity that would be induced in uranium oxide if it were thinly dispersed throughout the graphite. These were made by painting a thin layer of $UO_2$ and rubber cement on the inside of a steel shell, which was then filled with a graphite sphere. Such an experiment was called a "no-sphere" experiment. The self-absorption of the layer was rather small, and could be corrected since its thickness was only about 5 mg/cm² of uranium. The shells were always held together by Scotch tape which gave enough support even at 700°C, due to the formation of a rather rigid ash.

## RESULTS

The sphere experiments are listed in Table I with activity given relative to the 10-cm monitors. To obtain the reciprocal advantage factor for a given configuration and temperature, the quantity "no-sphere"/advantage is to be divided by the "no-sphere" (thin sample) value of 0.333 given at the end of Table I.

At room temperature both $UO_2$ and $U_3O_8$ spheres were used. The resonance absorption in the spheres of the higher oxide was greater, as expected, due to the increased scattering of the neutrons by the extra oxygen, thus dropping more neutrons into uranium resonance levels inside the sphere. At the higher temperatures it

was known that $U_3O_8$ would have been reduced to $UO_2$ to some uncertain extent, so only $UO_2$ was used. On opening the red-hot sphere in air after bombardment, the $UO_2$ was partly oxidized to $U_3O_8$. A chemical analysis of some of these used under various conditions shows how far this proceeded. These analyses indicate that the original "$UO_2$" was partly $U_3O_8$. Analysis before heating gave 71.5 percent $UO_2$, 28.5 percent $U_3O_8$. (After heating to 700°C and opening in air, 40 percent $UO_2$, 60 percent $U_3O_8$.)

To reduce errors because of changes in the composition of the shields or the furnace during the experiments, data were taken first at room temperature (20°C), then at 700°C, 300°C, room temperature again, 700°C again, and 1000°C. The return to room temperature and 700°C gave checks on the first results. New $CdSO_4$ shells prepared gave a check on the values obtained with those that had been used several times and had lost some Cd.

A 2-in. copper shell filled with $UO_2$, not surrounded with Cd, showed about 15 percent less absorption at 700°C than at 20°C. This is due to the smaller effectiveness of the "thermal" neutrons at the higher temperature since the cross section decreases as $1/v$.

From Table I we obtain the average values given under $[\int\sigma(dE/E)]_{eff}$ uncorrected of Table II. The corrected values were obtained by subtracting the epicadmium absorption of 1.35$b$.[2]

Table III gives the calculation of $\mu$. One sees that the values of $\mu$ obtained at the two values of $1/\rho R$ differ somewhat, but hardly in excess of the accuracy of the measurements. They give for $\mu$ the value 2.27 at 20°C

TABLE II.

| $[\int(dE/E)\sigma]_{eff}$ uncorrected | | | | | $[\int(dE/E)\sigma]_{eff}$ corrected | | | | |
|---|---|---|---|---|---|---|---|---|---|
| $1/\rho R$ | 20 | 300 | 700 | 1000°C | $1/\rho R$ | 20 | 300 | 700 | 1000°C |
| 0 | 13.5 | 14.6 | 15.2 | 16.1 | 0 | 12.15 | 13.25 | 13.85 | 14.75 |
| 0.059 | 18.1 | 19.4 | 19.9 | ... | 0.059 | 16.75 | 18.04 | 18.65 | ... |
| 0.099 | 21.8 | 21.9 | 25.2 | 27.3 | 0.099 | 20.55 | 20.65 | 23.85 | 25.95 |

TABLE III.

| | Total absorption / Mass absorption | | | | $\mu$ | | | |
|---|---|---|---|---|---|---|---|---|
| $1/\rho R$ | 20 | 300 | 700 | 1000°C | 20 | 300 | 700 | 1000°C |
| 0.059 | 1.38 | 1.36 | 1.35 | | 2.27 | 2.17 | 2.04 | |
| 0.099 | 1.69 | 1.56 | 1.72 | 1.76 | 2.27 | 1.85 | 2.43 | 2.54 |
| Av | | | | | 2.27 | 2.01 | 2.23 | 2.54 |

TABLE IV.

| $[\int\sigma(dE/E)]_{eff}$ Cd shields | $[\int\sigma(dE/E)]_{eff}$ $B_4C$ shields |
|---|---|
| $=10 + 23\ S/M$ at 20°C | $=10.3+18.7\ S/M$ at 300°C |
| $=11.5+21.5\ S/M$ at 700°C | $=10.4+19.8\ S/M$ at 700°C |
| $=11.3+21.7\ S/M$ at 600°C | $=10.5+19.8\ S/M$ at 1000°C |

TABLE V. Values of $[\int\sigma(dE/E)]_{eff}$.

| | 20°C | 700°C |
|---|---|---|
| U | $7.3+23.5\ S/M$ | $8.4+22\ S/M$ |
| $U_3O_8$ | $10.9+21\ S/M$ | $12.5+19.5\ S/M$ |

which is almost exactly equal to the average of the $\mu$ values[3] of 1.95 and 3.2, for $U_3O_8$ and U, taken with weights 3:1. While this is a satisfactory agreement with the data of the preceding article, the absolute value of the absorption, i.e., the mass absorption coefficient, is considerably in excess of the similar average of the mass absorption coefficients of $U_3O_8$ and U. We attribute this to difficulties in monitoring (i.e., the 0.33 "no-sphere" value) and write for $UO_2$ the results in Table IV. The figure at 600°C is simply interpolated. It is satisfactory that the surface absorption coefficient remains practically independent of temperature.

We have assumed in the first article here presented that the temperature dependence of the absorption of U and $U_3O_8$ is the same as that of $UO_2$. In view of the inaccuracy of the measurements it does not seem worthwhile to attempt a more refined interpretation. This then gives the figures of Table V.

## ACKNOWLEDGMENT

The authors wish to thank E. O. Wollan and R. J. Stephenson for constructing the furnace and for their many suggestions and aid in getting the experiment going. Also, thanks are due to Heyroth and Bovee of the Globar Division of the Carborundum Company for their advice on the design of the furnace, to E. Frank for help in taking the data, to T. Lanahan for his work on the cyclotron, and to Mrs. E. Creutz for a very great amount of data-compiling and computation. The experiments could not have been carried out in the relatively short time of three weeks without the excellent cooperation of all those named, as well as others called on from time to time.

# Temperature Dependent Creep in Zinc Crystals*

DONALD O. THOMPSON†
*State University of Iowa, Iowa City, Iowa*
(Received April 14, 1954)

Tensile creep measurements beginning in a tensile strain region of about $10^{-6}$ have been made upon a set of seven single crystals of zinc of 99.99+ percent purity. Measurements were made both by means of electrical resistance strain gauges and an optical lever system. Some of the measurements made in the latter apparatus lasted 100 hours or more, and in both systems, measurements were made at several temperatures.

The creep results obtained in this work can be best described by the single empirical relation

$$\eta = bt^m$$

in which $\eta$ is the shear strain, $t$ is the time after completion of the application of stress to the crystal, and $b$ and $m$ are constants for a given creep test under given experimental conditions. It is found that $b$ increases with the stress but does not vary greatly with temperature. The values of $m$ are practically independent of stress but vary with temperature, and appear to fit best the equation,

$$m = m_0 \exp(-To/T)$$

in the temperature interval investigated. For these crystals $To = 1580°K$, $m_0 = 120$, and the temperature at which $m = 1$ is 58°C. Values of $m > 1$ are interesting in dislocation theory.

## I. INTRODUCTION

CONSIDERABLE interest has been shown during the past several years in the creep of metals and metal single crystals, and several investigations have been carried out with zinc single crystals in particular. The interest shown in single crystals of zinc can be attributed to several factors. In general, the effects of grain boundaries are eliminated in single crystals. Moreover, zinc single crytsals have only one well-defined and operative glide system which includes one of three equivalent directions in the (0001) plane. Both of these properties contribute to the simplicity of any analysis. Experimentally, zinc crystals are quite easily prepared, and the stresses needed to obtain creep results are easily attainable.

A few years ago Tyndall[1,2] proposed for the creep of zinc crystals a modified Andrade[3] equation,

$$e = at^m, \tag{1}$$

in which $e$ is the tensile strain and $t$ is the time. Both $e$ and $t$ were set at zero at the instant of the completion of the loading process. Thus, the elastic strain and any permanent strain which occurred during the addition of the load (sometimes called "instantaneous strain") were not included in $e$. The exponent $m$ had values close to 0.5 at room temperature, and was quite independent of stress while the parameter $a$ was stress dependent. The relation may be expressed also as

$$\eta = bt^m, \tag{2}$$

in which $\eta$ is the shear strain, and $b$ is another stress-dependent parameter which is proportional to $a$ of Eq. (1) for a given crystal specimen. Weinberg[4] has also found this law valid for zinc crystals under direct shearing stresses.

The chief purposes of this work were to extend the creep observations to temperatures other than room temperature and to study the effect on room temperature measurements of previous anneals. The experimentation was so arranged that the anneals could be made without removing the specimen from the measuring apparatus, thus preventing possible accidental strains caused by handling. Two methods of measuring the creep were employed, one covering about the same low strain region of reference 1 and 2, and the other capable of testing the creep law at larger strains and over longer times.

## II. EXPERIMENTAL PROCEDURE

The single crystals of zinc were prepared from 99.99+ percent pure Bunker Hill zinc. This particular lot (part of an original 50-lb slab) is designated BH.[4] All the specimens were grown in a horizontal furnace from seed crystals. The finished specimens were 16.5 cm long, 0.5 $cm^2$ in cross-sectional area, and had the cross-sectional shape of an equilateral triangle. After growth the crystals were etched in about a 25 percent solution of HCl, and then the ends were affixed in brass cups in preparation for measurement. A length of 3 or 4 cm was always left between the position of the brass cups and the nearest strain gauge mounting so that effects of cutting and mounting should be minimized in the

* Taken in part from a thesis submitted in partial fulfillment of the requirements for the degree of Doctor of Philosophy in the Department of Physics in the Graduate College of the State University of Iowa.

† Present address: Oak Ridge National Laboratory, Solid State Division, Oak Ridge, Tennessee.

[1] E. P. T. Tyndall, J. Appl. Phys. **21**, 939 (1950).

[2] E. P. T. Tyndall, *Report of Carnegie Institute of Technology and O. N. R. Symposium on Plastic Deformation of Crystalline Solids* (Pittsburgh, Pennsylvania, May, 1950), p. 49.

[3] E. N. daC Andrade, Proc. Roy. Soc. (London) **A84**, (1910).

[4] E. H. Weinberg, J. Appl. Phys. **24** 734 (1953).

central portion of the crystal over which the measurements were to be made.

The mounting equipment consisted of a framework to which the crystal was attached through a universal joint, a load bucket which was fastened to the crystal through a second universal joint, and a furnace which could be placed around the specimen after all mounting and handling was completed. Since the furnace was not evacuated, some question can be raised as to whether or not effects caused by increased oxidation may be superposed on effects caused by the annealing and higher temperatures in the creep tests. This point will be discussed later in the paper.

The majority of strain measurements were made with electrical resistance strain gauges and the necessary detection equipment, but some long-time creep tests were made with optical levers. The latter system consisted of two optical levers attached to opposite sides of the crystal. Strains were determined as the average of these two measurements. An extension of $7\pm1\times10^{-4}$ cm was the "least count" of this arrangement. The electrical resistance gauges were individually made from one-mil resistance wire purchased from the C. O. Jelliff Company and commercially called "Alloy 45." In Fig. 1 is shown the arrangement of strain gauges on the crystal with the universal joints attached. For each measurement four active gauges were used. They were arranged symmetrically around the crystal, and electrically connected in series by connectors on the insulating rings alternately at the top and bottom. A second pair of dummy gauges was also rigged for each measurement as indicated in Fig. 1; to provide thermal compensation. This pair was also connected in series. The two sets of gauges, active and dummy, then formed two resistive arms of a bridge. Bridge balance was obtained through the use of additional resistance boxes in the dummy arm. The detection equipment consisted of a narrow band amplifier, centered at 42 cps, and a lock-in detector which drove an Esterline-Angus recording instrument. The maximum sensitivity of the electrical system was such that values of the change in resistance per unit of resistance of about $2\pm0.5\times10^{-7}$ were measurable using four strain gauges of about 12 cm each and a crystal length of about 9.5 cm. This corresponded to longitudinal crystal strains of $1.3\pm0.3\times10^{-7}$.

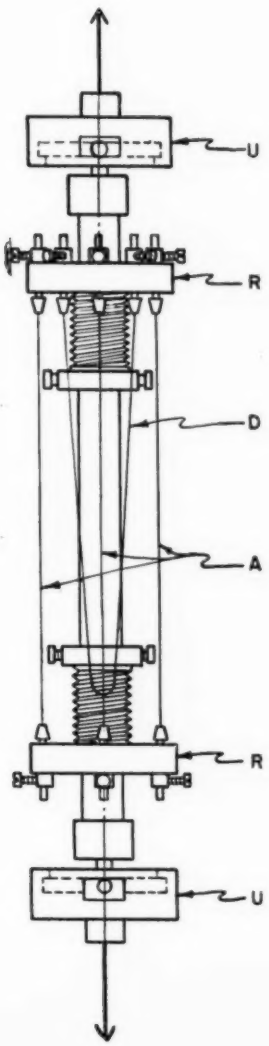


FIG. 1. Diagram of strain gauge mounting.

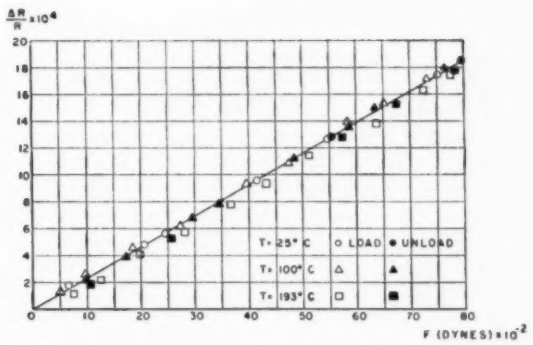


FIG. 2. $\Delta R/R$ *vs* applied tensile force for strain gauge wire at several temperatures.

Several calibrations and measurements were made upon the gauge wire itself. They were:

(1) A measurement of $\Delta R/R$, the change in resistance per unit of resistance, as a function of wire strain. This calibration was accomplished by mounting the strain-gauge wires upon a steel rod and measuring $\Delta R/R$ as a function of the stress applied to the steel rod. The wire strain was then computed using previously measured values for Young's modulus of steel.

(2) A direct measurement of Young's modulus of the wires.

(3) A $\Delta R/R$ *vs* stress curve for the wires (see Fig. 2). The first calibration yielded all the information that was necessary, namely, the value of the wire constant $G(\Delta R/R=GS$, in which $S$ is the wire strain). This value is 1.96. Measurements (2) and (3) were used to provide a check upon this value. From their combination a

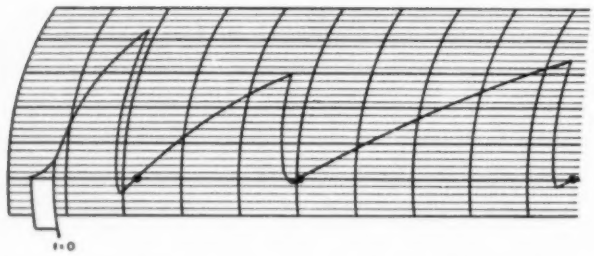


FIG. 3. Example of creep test record. In this figure, the heavy curved lines are 30 seconds apart, and the loading interval is blocked off with the $t=0$ marker shown. Bridge balance points are indicated with heavy black dots, (●).

value of 1.88 was obtained. This is a satisfactory agreement, when it is considered that the manufacturer's nominal wire size was used to compute the cross-sectional area of the wire. As a further check Young's modulus was also measured for several crystals using the factor $G$. Agreement with expected values was good.[5]

Although direct measurements were not made upon $G$ at elevated temperatures, enough calibration data were obtained to show that the numerical change in $G$ is not very great from room temperature to about 200°C. In Fig. 2 the change in resistance of the wire is seen to be directly proportional to the applied stress, with very nearly the same constant of proportionality at the three temperatures. From these curves and the expected change in Young's modulus with temperature, a variation of not more than −5 percent at 193°C compared with the room temperature value may be deduced.

The general techniques followed in making the creep tests are those given by Tyndall.[1,2] Briefly, a series of strain measurements was taken in succession, beginning with the stress at which creep was first observed and continuing from there by increments to larger stresses. Zero time was counted at the end of the loading interval. An example of this procedure is given in Fig. 3, which shows the early minutes of a creep test. The beginning and ending of the loading interval are marked, and the relative smallness of the creep occurring within this interval is plainly shown. No annealing was done within a series of successive tests. However, intervals of time varying from one to several days were allowed between the series of tests, and higher temperature anneals were made in these intervals also. Usually the specimen was not handled in these interim periods.

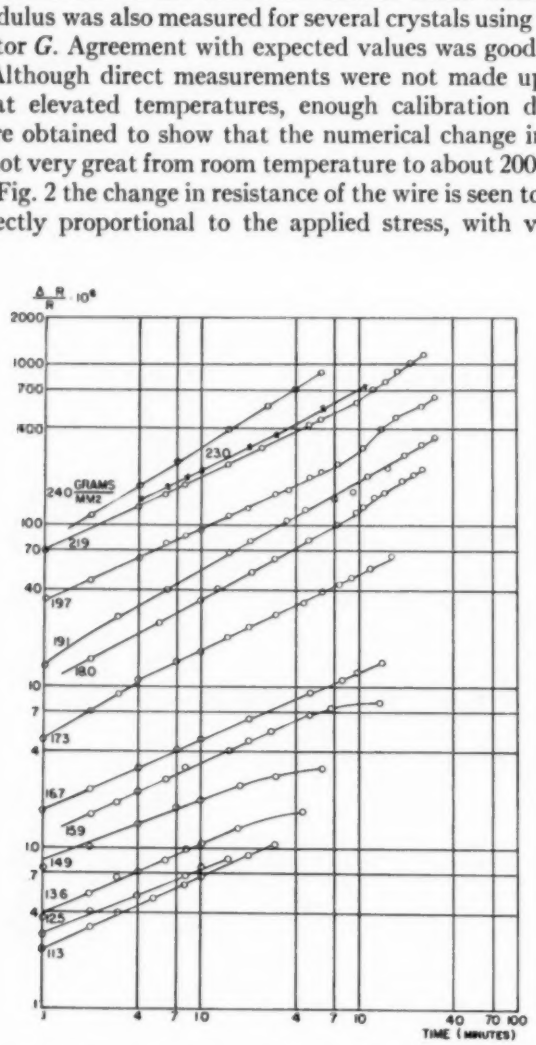


FIG. 4. Creep curves for crystal No. 4. The tensile creep strain is given by $e=0.64\ \Delta R/R$, and the shear creep strain by $\eta=2.56\ \Delta R/R$. The stresses which are listed beside the curves are r.s.s. values.

[5] C. A. Wert and E. P. T. Tyndall, J. Appl. Phys. **20**, 587 (1949).

## III. EXPERIMENTAL RESULTS

Seven crystals of suitable orientation were grown for investigation. These are described in Table I. The angle

TABLE I. Crystal data.

| Crystal No. | 2 | 3 | 4 | 5 | 6 | 9 | 10 |
|---|---|---|---|---|---|---|---|
| $\theta$ | 57° | 72° | 75° | 81° | 66° | 56° | 60° |
| $f$ | 0.46 | 0.29 | 0.25 | 0.16 | 0.36 | 0.46 | 0.43 |

$\theta$ is the primary orientation angle, and is defined as the angle between the length of the crystal and the normal to the basal or (0001) plane. A function of this angle is $f$, which will be defined shortly. The secondary orientation angle, defined as the smaller angle between one of the equivalent slip directions and the projection of the length of the crystal into the basal plane, is not given since in all cases this angle was small (2° or less).

Although the significant quantities in this experiment are the shear strain and resolved shear stress, some of the work is more conveniently presented in terms of the directly measured tensile strain and tensile stress. It will be evident from the text which of these quantities is meant. The relation between tensile and shear strain for crystals with secondary orientation near zero is

$$e=\tfrac{1}{2}\eta \sin 2\theta = f\eta, \qquad (3)$$

in which $e$ is the tensile strain and $\eta$ the shear strain. Equation (3) is valid for $\eta \ll 1$, and follows in this approximation from Schmid and Boas.[6] The geometrical factor $f$ is defined by this equation. In a similar manner, the tensile stress $L$ and the resolved shear stress $\sigma$ are

[6] E. Schmid and W. Boas, *Plasticity of Crystals* (F. A. Hughes and Company, Limited, London, 1950), p. 60, Eq. (26/5).

related[7] by

$$L=\frac{1}{f}\sigma. \tag{4}$$

A typical set of room temperature creep curves is shown in Fig. 4. This crystal No. 4, throughout several series of such curves, gave the most regular curves of any tested. It was also "softer" in the sense that the smallest stress at which a run could be taken was in general smaller than that for the other crystals. The lowest stress in Fig. 4, 11.3 g/mm², is, moreover, from 3 to 6 g/mm² lower than for the corresponding lowest curves on any of the preceding sets. Before taking the series of Fig. 4, the crystal had an anneal of 36 hours at 115°C. The six other crystals were taken through from one to four series at room temperature. The values of the parameter $m$ were about the same in all these runs. A principal difference in one crystal from another is in the stress required to initiate observable creep, which is closely connected with the stress dependence of the parameter $b$. Crystals also appear to differ in their reaction to anneals or rest periods between series of runs. Although one case of appreciable softening by an anneal is cited above, this did not occur with four other crystals which were variously annealed. Little or no effect was observed in this group except for one case which, contrary to the result for crystal No. 4, showed a distinct hardening. Also, perhaps related to this, a crystal which was run at room temperature following some high temperature runs was distinctly harder than it had ever been before.

Data were also obtained for the plastic strain which occurs in the loading process. These were taken in the loading interval from records like that of Fig. 3 and represent the difference between the total measured strain and elastic strain, computed as a function of the value of the incremental stress which is assumed to vary in direct proportion to time. Examples of these are given in Fig. 5 for crystal No. 4. These are the "instantaneous" parts which precede the curves of Fig. 4. The last point of each of these curves is plotted at the end of the loading interval, and the index to the curves is the stress value at which the succeeding creep test was made. The curves approximate straight lines except for some bending near the ends. No special significance can be attached to the bending of the curves near their ends, for it is very possible that the rate of loading is smaller here than earlier in the curves. This means that the stress values as plotted are larger than the actual values with the result that the curves bend.

In addition to the room temperature creep tests, experiments were performed on three crystals, Nos. 3, 5, and 10, at elevated temperatures in the strain gauge apparatus. Figure 6 shows four creep tests on crystal No. 3 obtained on different days and at different

[7] E. Schmid and W. Boas, *Plasticity of Crystals* (F. A. Hughes and Company, Limited, London, 1950), p. 105, Eq. (40/1).

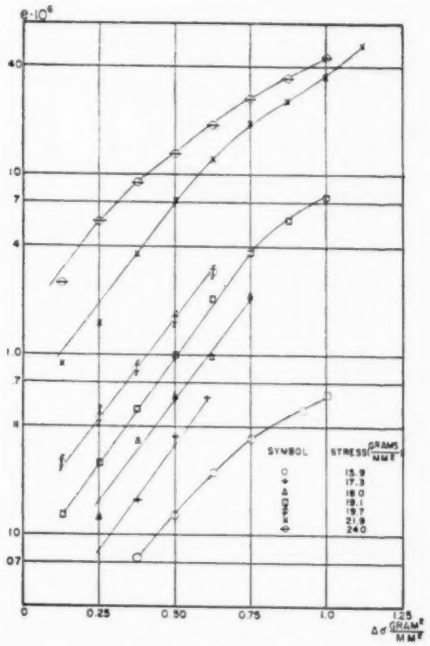


FIG. 5. Plastic tensile strain during loading for crystal No. 4. The stress indices indicate that that particular curve is the "instantaneous" strain which preceded the correspondingly labeled creep curve of Fig. 4. The indices are: (○), 15.9 g/mm²; (+), 17.3; (Δ), 18.0; (□), 19.1; (𝒻), 19.7; (×), 21.9; (⊖) 24.0. These values are r.s.s.

temperatures. They were chosen to be represented on a single plot from several sets of curves because they lasted the longest of any which had roughly the same

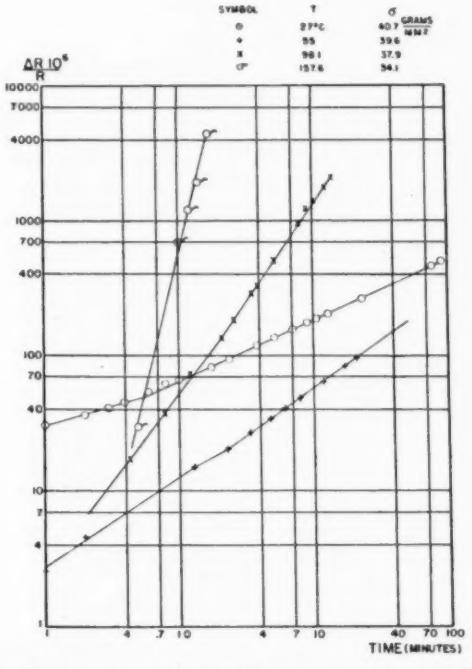


FIG. 6. Creep curves at several temperatures for crystal No. 3. The tensile and shear strains are, respectively, $e=0.57\ \Delta R/R$ and $\eta=1.97\ \Delta R/R$. (○), $T=27°C$, $\sigma=40.7$ g/mm²; (+), $T=55°C$, $\sigma=39.6$ g/mm²; (×), $T=98.1°C$, $\sigma=37.9$ g/mm²; (𝒻), $T=157.6°C$; $\sigma=34.1$ g/mm².

stress values. It should be pointed out that at higher temperatures, it was impossible, because of the accelerating creep, to extend the measurements as long in time as at lower temperatures. This was due to two conditions, the principal one of which was the desire to "conserve" the crystal so that more separate measurements could be made upon the particular specimen before it had acquired a large accumulative strain, and the second reason was the breaking of the strain gauges. Only one test at 158°C was possible before the gauges broke. In this test, approximately a quarter percent tensile strain was attained within 2 minutes after completion of the loading. As already implied, the particular feature to be noted in Fig. 6 is the increase in the slope of the curves with increasing temperature.

Several measurements of creep which lasted over periods of time far greater than any described so far were made using the optical lever system previously mentioned. In Fig. 7 are shown four curves obtained from crystal No. 4. Previous to these curves, the specimen had rested for 4 months at room temperature after acquiring a total tensile strain of about 1 percent in the electrical gauge equipment. The two room temperature curves shown in Fig. 7 were taken without unloading between them, just as the series of tests were performed in the electrical gauge equipment. It should be noted that the simple, single creep law is valid for these curves even though they extend for a considerable period of time and cover a different strain region from the one covered by the more sensitive apparatus. Subsequent to the 22.5 g/mm² test at room temperature, the crystal was unloaded and the furnace switched on. The 22.5 g/mm² test at 37°C then followed after an interim of about 12 hours with the temperature kept near or at 37°C. It will be noticed in Fig. 7 that this curve (Δ points) begins leveling off after 40 hours of creep at 0.8 percent strain. After this run, the crystal was unloaded and the temperature raised. On the succeeding day, another run was started at the same stress and a temperature of 76°C. Between these runs, the crystal remained in the apparatus and spent nearly a day at this temperature. The data obtained in this test ($Q$ points) show a leveling off which begins after 5 hours of creep and approximately the same strain as in the preceding test.

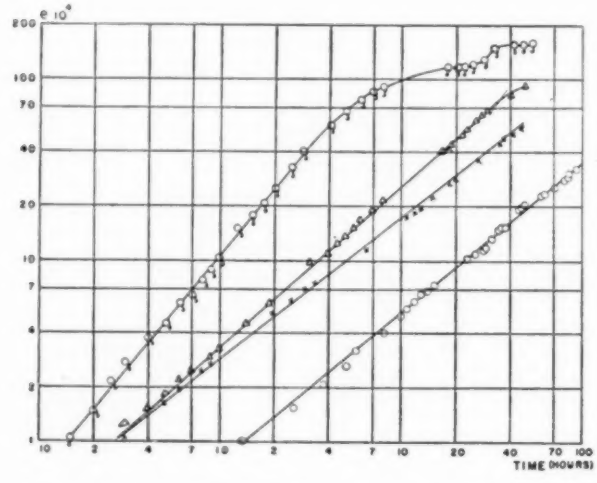


FIG. 7. Long-time creep for crystal No. 4. The shear strain is given by $\eta = 4.0\epsilon$, where $\epsilon$ is the tensile strain. (○), $T = 27°C$, $\sigma = 20$ g/mm² r.s.s.; (×), $T = 27°C$, $\sigma = 22.5$ g/mm² r.s.s.; (Δ), $T = 37°C$, $\sigma = 22.5$ g/mm² r.s.s.; ($Q$), $T = 76°C$, $\sigma = 22.5$ g/mm² r.s.s.

The data presented so far support the validity of the creep law $\eta = bt^m$, in which $b$ usually increases regularly with the stress in a set of successive runs, and $m$ appears to be temperature dependent, but largely independent of stress. The deviations from this simple situation are: (1) Creep runs may be irregular and not strictly represented by single straight lines as may be seen in Fig. 4. (2) Runs may be represented by more than one straight line as mentioned previously; these latter may be said to have an $m$ and a $b$ for each straight section. (3) The parameter $b$ does not always increase regularly with stress, as may be seen, for instance, by comparing the 23 g/mm² curve of Fig. 4 with the preceding run; this irregularity in $b$ grows greater if the incremental stress from curve to curve is taken too small.

## IV. DISCUSSION

In spite of the irregularities just mentioned, the results may well be discussed in terms of the parameters $m$ and $b$. The behavior of the latter's dependence upon stress has been experimentally observed and treated several times,[2,4,8–10] and therefore will not be discussed further here. It, however, may be noted that the data shown in Fig. 5 and other similar data for the plastic strain which occurs during loading show the same stress dependence as the $b$ coefficients in the following way. A set of values for the plastic shear strain is computed by subtracting the calculated elastic shear strains from the total measured shear strains at some particular stress increment, such as 0.75. If these values are called $b'$ and their logarithms are plotted against the total resolved shear stress (resolved shear stress of the preceding creep test plus 0.75, for example), the line so obtained is straight and has the same slope as the line obtained in a log$b$ *vs* $\sigma$ plot from the same set of data. This procedure has been carried out at several stress increments for two crystals. Slifkin and Kauzmann[8] have reported a direct proportionality between a "transient creep parameter" and the instantaneous tensile strain. Since their transient creep parameter is proportional to the product $bm$ in the present notation, the two results are in agreement, for $m$ does not vary much at any one temperature and the product $bm$ is consequently proportional to $b$.

In Fig. 8 is shown a logarithmic plot of $m$ *vs* $1000/T$,

[8] L. Slifkin and W. Kauzmann, J. Appl. Phys. **23**, 746 (1952).
[9] Peter Haasen and G. Liebfried, Z. Metallkunde **43**, 317 (1952).
[10] Tyndall, Artman, Wert and Eisner, J. Appl. Phys. **26**, 286 (1955).

where $T$ is the Kelvin temperature. The indicated spreads in the points are the values of the root-mean-square deviations. The point at $1000/T=2.32$ for crystal No. 3 corresponds to only one creep test, so that no spread is shown. Only one test was possible before the strain gauges broke at this temperature. The point at $1000/T=3.14$ for crystal No. 5 is given with no spread for the two tests at this temperature gave the same value of $m$. The points obtained in the optical apparatus are not shown with a spread either, for only one test was made at a given temperature.

Although attempts were made at fitting these data for $m$ to other temperature dependencies, they appear to fit best the relation,

$$m=m_0\exp(-To/T), \qquad (5)$$

as shown in Fig. 8. The line is drawn through the points by the least squares fitting, and from its slope, $To$, is deduced to be 1580°K. The line also indicates that $m=1$ at $T=58$°C, and $m_0=120$.

In addition to the data obtained for crystals given in Table I, creep tests were performed upon a spectrographically pure crystal (99.999+ percent pure) at elevated temperatures. Because it is thought that this crystal may have been bent in the mounting prodecure, the data are not included. However, there was indication that the $m$ values for this crystal did not get appreciably larger than 0.5, the values which it yielded at room temperature. These results, nevertheless, must be regarded as uncertain since only one S.P. crystal was used, and it may have been bent.

The observed results cannot be interpreted simply in terms of surface oxidation of the crystals. It might be expected that each high temperature run and anneal would increase the oxide layer on the crystal and thereby produce some regular variance of $b$ and $m$, since the crystals were never etched after they had once been mounted in the apparatus. However, no regular variation of these parameters was found which would indicate a simple dependence upon the amount of surface oxidation.

The Frank-Read mechanism seems to be the best one yet suggested for the interpretation of the experimental results although there is considerable difficulty in accounting for the time dependence[11,12] of the creep. The growth under stress of a small anchored segment of dislocation line into a loop, which in passing out of the crystal causes a slip of one lattice spacing and leaves behind a new segment to repeat the process, will explain continuing creep. This alone, however, is not sufficient. The rate at which the process goes on must be such as to satisfy the creep law, and thus one must look for mechanisms which at relatively low temperatures, where $m<1$, continually diminish the strain velocity but at relatively high temperatures increase it since $m>1$. Qualitatively, it might be expected that an interaction between expanding loops and inactive line segments could account for either accelerating or decelerating creep, depending upon the average number of active dislocations which appeared following the interaction. This average number could be either greater or less than unity and would probably depend upon the temperature. Similarly, jamming of active loops near the surface would contribute to a diminishing strain velocity. Instead of thinking, however, of one active loop starting another, it is possible to consider that a segment anchored in several points loses some of the anchor points and effectively becomes a larger segment capable of being moved by the stress which had previously been unable to move it at the start of the creep test. Since anchor points may be vacancies or impurity atoms, they may be expected to be more mobile the higher the temperature, and therefore, anchor the dislocation line less effectively the higher the temperature. Eventually, both of these behaviors should reach a limit since the number of available segments would be exhausted. This may account for the fact that the creep law, though holding for many hours, eventually fails, and fails, moreover, by showing a marked decrease in strain velocity.

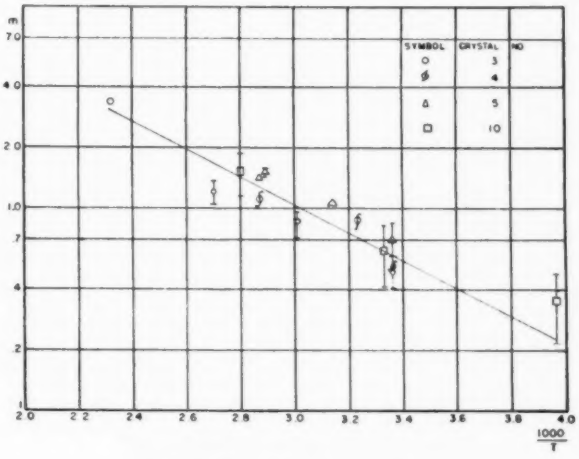


FIG. 8. Plot of log$m$ *vs* $1000/T$.

The author wishes to express his indebtedness to Professor E. P. T. Tyndall who directed this research and who provided valuable discussion, and to Dr. G. A. Alers for his assistance in obtaining the long-time creep data and his general interest.

[11] N. F. Mott, *Imperfections in Nearly Perfect Crystals*, edited by W. Shockley (John Wiley and Sons, Inc., New York, 1952), p. 173.

[12] N. F. Mott, Phil. Mag. 44, 742 (1953).

# Creep of Zinc Crystals

E. P. T. TYNDALL, R. A. ARTMAN,* C. A. WERT,† AND ROBERT EISNER‡
*Department of Physics, State University of Iowa, Iowa City, Iowa*
(Received April 14, 1954)

The plastic extension of zinc crystals in the region just beyond the elastic limit is found to obey the empirical law, $\eta = bt^m$ in which $\eta$ is the resolved shear strain, $t$ is the time, $m$ is a constant with a value close to 0.5 for initially unstrained crystals, and $b$ is dependent on the resolved shear stress. Application of a theory due to Koehler shows that $b$ should be related to stress ($\sigma$) in such a way that a plot of $\ln(mb\sigma^2/\Delta\sigma)$ against $1/\sigma$ should be a straight line of slope $-cG$. In this, $\Delta\sigma$ is the stress increment from one creep curve to the next, $G$ is the shear modulus, and $c$ is the concentration of anchor points which determines the lengths of segments of dislocation lines which generate according to the Frank-Read mechanism. The experiments are in fair agreement with this theory and values of $c$ obtained are roughly equal to the concentrations of metallic impurities. The small amount of dissolved gases appears to play no significant part in the creep process.

## INTRODUCTION

STUDIES of the plastic deformation of metal crystals in the region just beyond the elastic limit, or the end of the Hooke's law region, may be expected to give valuable information about the dislocations existing in the crystal directly after growth and of their first movement or modification by stress. Previously reported work[1] in this laboratory has shown that zinc crystals under constant shear stress obey a creep law of the form $\eta = bt^m$ in which $\eta$ is the shear strain and $b$ and $m$ are parameters. That creep may occur as a power of time appears now to be quite usual both for single and polycrystalline specimens.[2–4]

## EXPERIMENTAL PROCEDURE

Since the present work is a continuation of that reported in reference 1(b), the same general procedure was followed. The crystal specimen was mounted in the measuring apparatus, which is described below, and was first loaded and unloaded only in the elastic region, both to determine the Young's modulus and to make sure that no hysteresis[5] was present. After several days it was loaded by steps to beyond the elastic region, the end of which was made evident first by deformation increasing beyond the proportional size observed in the elastic region and then by noticeable creep occurring in a minute or two. Such time-dependent creep was followed until its rate became too small to follow further. The load was then increased by a small increment and the creep again followed with time. In all cases a small "instantaneous deformation" occurred during the adding of the load, but this was not included in the creep strain. Five or six such runs could be taken before the general creep rate became too rapid to follow. The crystal was then unloaded and usually left unloaded for various lengths of time before taking another set of runs. For each crystal several sets of such runs were taken lasting sometimes several months, since intervals were allowed between sets for annealing. The crystal remained mounted in the apparatus throughout the period of testing, except as otherwise noted.

Extensions were measured by an optical lever strain gauge. It is shown in Fig. 1. The two collars are attached to the crystal with three screws, two of which show in the drawing. The upper collar has two projecting arms with slotted hooks from which are suspended two "connectors."[6] The wire loop at the lower end of each connector engages a hook in the T-shaped lever to which mirror and counterpoise are attached. The levers are pulled down by small wire loops which engage hooks in the members attached to the lower collars. The reflecting surfaces of the mirrors face each other. A beam of parallel light passes close to the right-hand mirror, strikes the other mirror, is reflected to the right-hand one, and is by it reflected so as to pass by the left-hand one. The parallel beam of light comes from a 90-cm focal length lens which has a finally divided scale in its focal plane. After reflection from the mirrors the light is focused by a second lens to form an image which is viewed by a lower power microscope. This type of optical system is due to Roberts.[7] The magnification of the device is easily seen to be

$$\Delta s/\Delta l = 4F/c,$$

* Present address: Physics Department, Scientific Laboratory, Ford Motor Company, Dearborn, Michigan.
† Present address: University of Illinois, Urbana, Illinois.
‡ Present address: Research Laboratories, Westinghouse Electric Corporation, East Pittsburgh, Pennsylvania.
[1] (a) E. P. T. Tyndall, J. Appl. Phys. **21**, 939 (1950). (b) E. P. T. Tyndall, Rept. of Carnegie Inst. of Tech. and Office of Naval Research Symposium on Plastic Deformation, Pittsburgh, Pennsylvania, May, 1950, page 49. (c) E. H. Weinberg, J. Appl. Phys. **24**, 734 (1953).
[2] L. Slifkin and W. Kauzmann, J. Appl. Phys. **23**, 746 (1952).
[3] P. Haasen and G. Leibfried, Metallkunde **43**, 317 (1952).
[4] T. H. Hazlett and E. R. Parker, J. Metals **5**, 319 (1953).
[5] Since the crystals always showed hysteresis after a set of runs, the nonappearance of hysteresis directly after mounting was a fair assurance that the crystal had not been strained by handling during the mounting process. The hysteresis occurring after each set of runs was precisely like that previously described by Read and Tyndall [J. Appl. Phys. **17**, 713 (1946)]. It grew progressively less with rest and usually disappeared in a few days.
[6] The material of the connector is chosen to match the thermal expansion of the crystal.
[7] J. K. Roberts, *Heat and Thermodynamics* (Blackie and Son Limited, London, 1940).

in which $\Delta s$ is change in scale reading corresponding to change in length, $\Delta l$, in the specimen; $F$ is the focal length of the first lens; and $c$ is the distance, measured horizontally, from the upper hook on the T-shaped levers to the line through the two lower hooks. With $c$ about 0.4 cm and a gauge length of 10 cm, one division (0.1 mm) of the scale corresponds to a strain, $\Delta l/l$, of $1.1\times10^{-6}$. Since one may observe with certainty the movement of a fifth of a division past the microscope cross hair, the least surely perceptible strain is about $2\times10^{-7}$. The levers respond to changes in length of the specimen in an exceedingly smooth fashion, in spite of the simple scheme of supporting them with loops of wire in hooks instead of the more usual construction using knife edges. The apparatus has been extensively tested in the elastic region where smoothness of response has been shown to hold to about one-twentieth of the smallest strain mentioned above.[8]

The upper end of the crystal specimen was soldered into a cylindrical cup with Wood's metal. This cup has two projecting cylindrical arms, or rollers, which rest on two rails on a platform which itself has two more rollers, at right angles to the two on the cup, which rest on fixed rails. Thus the crystal is supported at the top by a "universal joint." A similar construction at the bottom end of the crystal supports the load, a container into which mercury may be admitted and siphoned out. The container hangs freely and the crystal is thus always pulled vertically between two points in its upper and lower ends. This gets away from bending which must occur near the "grips" in some types of tensile test machine whenever increase of length takes place by glide on a plane inclined to the axis of the specimen. It may also be mentioned that by adjusting the position of the rollers, each optical lever may be made to deflect equally.[9] This assures axiality of the stress one azimuth at least. No precise adjustment of axiality is available in the azimuth ninety degrees from the first, but care in mounting the crystal and adjusting the positions of the rollers symmetrically seems to assure it with reasonable certainty.

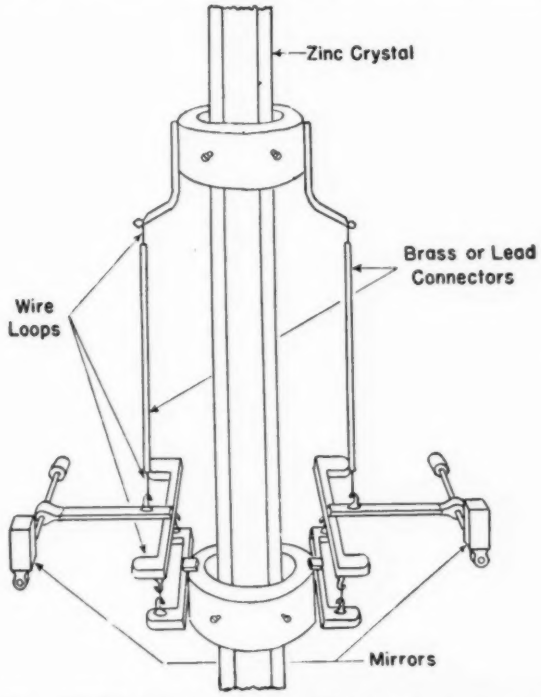


FIG. 1. Optical lever strain gauge. Material for "connectors" is chosen to give minimum temperature drift.

[8] I. H. Swift and E. P. T. Tyndall, Phys. Rev. **61**, 359 (1942).

TABLE I. Description of crystals.

| Crystal No. | Material | $\theta$(deg) | $\alpha$(deg) | $f$ | $(\eta/s)\times10^5$(mm$^{-1}$) |
|---|---|---|---|---|---|
| 1 | S.P. | 14.5 | 1 | 0.242 | 5.48 |
| 2 | *BH*4 | 78.0 | 2 | 0.203 | 5.25 (4.92)[c] |
| 3 | *BH*2 | 78.0 | 2 | 0.203 | 5.52 (5.30)[c] |
| 4 | *R*212 | 77.5 | 1.5 | 0.211 | 5.20 |
| 5 | *BH*4[a] | 77.5 | 2.2 | 0.211 | 6.8 |
| 6 | *BH*4[b] | 76.0 | 1.5 | 0.235 | 4.45 |
| 7 | *BH*4 | 77.0 | 23.5 | 0.192 | 4.89 |
| 8 | *BH*4 | 77.0 | 20.0 | 0.205 | 4.97 |

[a] Prior to making the casting the zinc was boiled in a vacuum.
[b] Same boiled zinc, but nitrogen gas was, in addition, bubbled through the molten zinc for a few minutes.
[c] Second run, after remounting.

The crystals were of trapezoidal cross section (0.50 cm$^2$) and 15 cm long. They were grown by the horizontal mold technique. Several lots of high purity zinc were used, as shown in Table I. The designation S.P. is used for the New Jersey Zinc Company's spectrographically pure zinc; *BH*2 and *BH*4 are two lots of Bunker Hill zinc, taken from different 50-lb slabs; *R*212 is a lot of zinc which was kindly donated by the New Jersey Zinc Company and stated to be nearly as pure[10] as the S.P. zinc. Qualitative spectrographic tests in this laboratory show that the two lots of *BH* zinc differ from the S.P. mainly in the appearance of a Ag ($\lambda=3383$ A) and a Cd ($\lambda=2288$ A) line and a few of the most sensitive Fe lines, certain in *BH2* and very faint in the *BH*4. The writers believe that the purity is certainly as high as 99.995 percent and the usual designation of 99.99+ percent is amply justified.

Beside the principal orientation angle,[11] $\theta$, another angle is needed to describe the orientation of the lattice with respect to the specimen. The angle so used, $\alpha$, is the smallest of the three angles between the three slip directions and the projection of the length of the specimen into the basal plane of the lattice. When this angle is appreciably different from zero, the factor, $f$, for converting longitudinal quantities into shear quantities is[12] $\cos\theta\sin\theta\cos\alpha$. This factor is given in Table I.

[9] Each lever may be supported in a slightly elevated position so that the connector no longer pulls on it. This detail has been omitted from Fig. 1.

[10] An analysis furnished by the New Jersey Zinc Company gives Pb, Cd, Fe, Cu, As, in a total amount of about 0.0013 percent.

[11] See, e.g., E. P. T. Tyndall, reference 1(b).

[12] Instead of $\theta$ and $\alpha$, angles $\chi$ and $\lambda$ are often used; $\chi$ is the complement of $\theta$ and $\lambda$ is the angle between length of specimen and slip direction. The complete factor $f$ is then given by $f=\sin\chi\cos\lambda=\sin\theta\cos\theta\cos\alpha$.

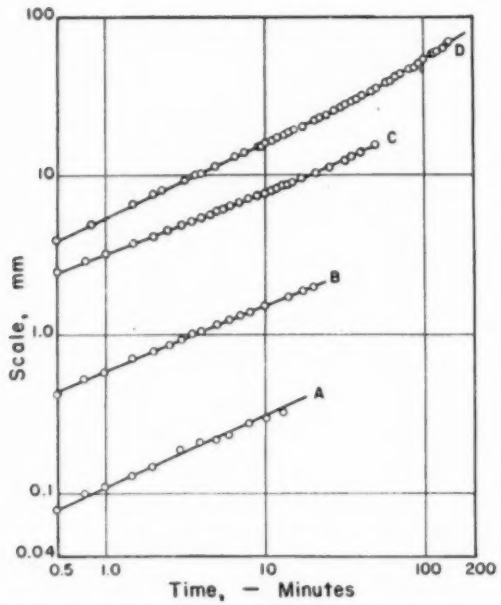


FIG. 2. Crystal No. 2. Resolved shear stress in g/mm²: A 11.2; B 12.4; C 13.5; D 14.2.

Also in the table will be found the factor to convert the scale reading, $s$(mm), to resolved shear strain, $\eta$. Besides $f$ and the optical lever magnification, this factor depends on the length of crystal measured.

While these experiments have all been done at constant load it must be pointed out that for each creep curve the situation is one of constant tensile and constant resolved shear stress, since the alteration of cross section and geometric change of orientation are absolutely negligible for strains of the size considered here.

## RESULTS

### A. Creep When $\alpha \simeq 0$

For six of these crystals the secondary orientation angle, $\alpha$, was nearly zero. They gave the most regular creep curves. A set of runs is shown in Fig. 2 for crystal No. 2. It is seen that the relation $s = at^m$ is very closely obeyed, that the curves are nearly parallel (thus they have nearly the same value of $m$) and are well separated. Two of them, $C$ and $D$, show a double slope characteristic (these were the only runs of this type in about 25 runs on this crystal). The set of runs shown in Fig. 2 was the last of a series of six sets taken in a period of about six weeks. Before this sixth set the crystal had rested for three weeks and had accumulated in the preceeding five sets shear strain of about $1.5 \times 10^{-3}$. How well this last set agreed with previous sets will be shown later.[13]

All the crystals with $\alpha \simeq 0$ gave sets of runs nearly as regular as that shown in Fig. 2. Those which deviated from this pattern showed differences of two types: (a) somewhat of a scatter in the values of $m$ and (b) more irregularity in the separation of the individual runs, even when the load increments were approximately the same. A set of runs illustrating these points is shown in Fig. 3, curves D, E, F, G, and H. The set of curves A, B, and C (the first set made on this crystal) illustrate still another phenomenon occasionally observed. After two normal creep curves, A and B, a run was made (curve C) in which a large jump was observed in the first minute of creep. This did not occur again for this crystal in 27 more runs; it was also observed once for three other crystals, Nos. 4, 5, and 8.

The general correctness of this "incremental-stress" method of studying creep is important in the discussion which will follow. To illustrate this correctness, in Fig. 4 are shown three sets of runs for crystal No. 4 (taken on successive days). Only the first set (curves A and B) may strictly be said to have started with an unstrained crystal. However, it is seen that the sets on the following two days are very similar to the first set, with, however, a softening of the crystal in the sense that the curves of a later date lie above those with the same stress of an earlier date. This is not true for all crystals. These sets of curves show that the incremental stress between curves is not of great importance. Curves A and B and G, H, and I are taken with increments of 1.2 g/mm², whereas curves C to F are for increments of 0.6 g/mm². Had intermediate stress curves been taken, say between G and H and I, there is then every reason to believe that such curves would have come about halfway between, and that H and I would still be about the same. This is a fortunate occurrence since otherwise the method of testing might be considered as exceedingly arbitrary.

It is, of course, well known that any testing in the plastic region is done with more or less arbitrarily imposed procedures, since the relation between stress

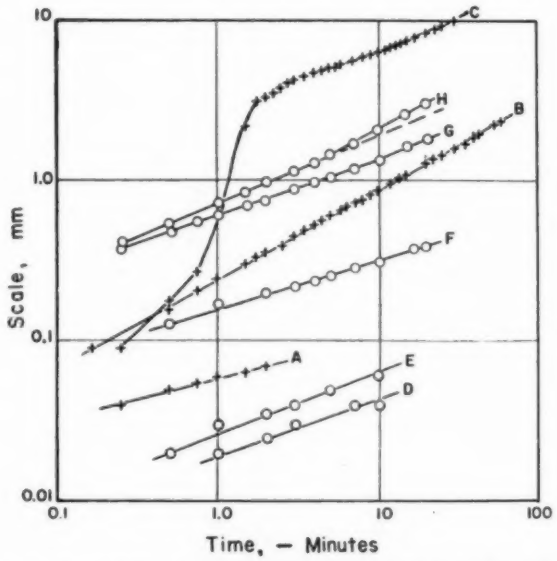


FIG. 3. Crystal No. 3. Resolved shear stress in g/mm²: A 17.4; B 18.5; C 19.2; D 15.3; E 16.4; F 17.5; G 18.6; H 19.1.

[13] In Figs. 3 and 4 of reference 1(b) are given two earlier sets of runs on this crystal. Note that in these figures the titles are unfortunately interchanged.

and strain is no longer the simple proportion that it is in the elastic region. The present procedure enables one at least to relate successive creep curves of any one set to the stress under which each is taken. Were the specimen unloaded and annealed between curves, no such relation would be possible, because annealing cannot be counted on to restore the crystal to the condition it was in before the first curve was taken. Another factor which favors this method of testing, provided the increment between loads is taken large enough to produce well-separated curves, is that the total creep in a given curve is exceeded by its successor at the next higher load in a short space of time. Thus what goes on at the higher load is practically independent of the relatively small deformations that have preceded it with all the lower loads.

### B. Creep When $\alpha \gg 0$

Crystals in which the angle $\alpha$ is appreciably different from zero behaved less regularly than, but still in a similar fashion to, crystals with small $\alpha$.[14] A set of runs for one of these crystals with $\alpha \simeq 25°$ is shown in Fig. 5. The difference between this and the curves of Figs. 2, 3, and 4 is apparent. Slopes are quite varied and the lines are often curved. The failure to follow the normal order in B and C and G and H may be due to the small incremental load; for curves E and F this does not seem likely.

It should not be presumed that crystals of this type always produced such irregular sets of data; indeed the data shown in Fig. 5 constitute actually one of the least regular sets. However, experiments with crystals of this type do not seem very profitable. The use of tensile testing to study what is essentially a "shear" phenomenon is not helped by making the relation between longitudinal and shear effects any more complicated than it needs to be.[15]

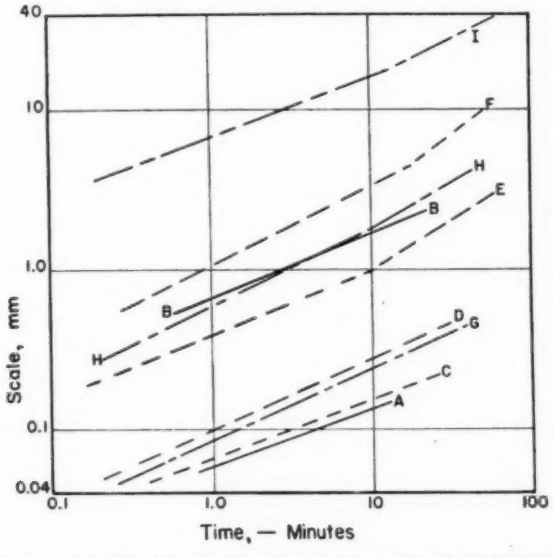


FIG. 4. Crystal No. 4. Resolved shear stress in g/mm²: (1) A 17.0; B 18.2; (2) C 15.9; D 16.5; E 17.0; F 17.6; (3) G 15.9; H 17.0; I 18.2.

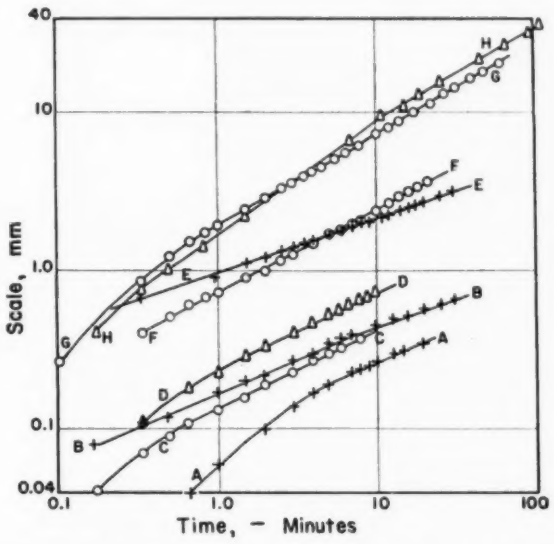


FIG. 5. Crystal No. 7. Resolved shear stress in g/mm²: A 15.9; B 16.5; C 17.0; D 17.6; E 18.5; F 19.3; G 20.2; H 20.6.

### C. Summary of Data

In Table II results obtained for the slope, $m$, are summarized by giving for each crystal the number, $N$, of creep curves, the mean value of $m$, and the rms deviation from the mean (the latter is to give some idea of the variation of $m$ for each crystal). Some abnormal runs on crystals 2, 3, and 6 are placed at the bottom of the table to separate them from the first normal runs.[16] The weighted mean value of $m$ for the first 6 crystals ($\alpha \simeq 0$) is 0.487. All of this is in good agreement with observations at room temperature by D. O. Thompson (to be published) and with similar values found by Weinberg.

There seems little doubt that, under the conditions of experimentation and in the strain region covered, time-dependent creep is describable by a single empirical formula and that division of it into two processes, "transient" and "steady-state" is unnecessary, at least for zinc. It is true that when plots are made of strain against time they appear to correspond to this artificial division, since the strain velocity is at first relatively

[14] In reference 1(b) the statement was made that such crystals (with $\alpha \gg 0$) behaved very differently from those with small $\alpha$. This conclusion was based on earlier work of R. E. Holland and was not substantiated by the two crystals of this type in this investigation. It is difficult at present to account for the failure of older work to agree with the present work.

[15] Crystals with $\alpha$ nearly 30° would be interesting. One such crystal has been run in this laboratory (reference 5). It is discussed somewhat in reference 1(b) but the conclusion reached there needs further checking.

[16] These abnormal runs gave exceptionally low values of $m$ and frequently showed curved creep curves on plots of log strain *vs* log time. They were made either (1) after deliberate attempts to strain these crystals or (2) after attempts (apparently unsuccessful) to anneal the crystals.

TABLE II. Slopes of creep curves.

| No. | N | Mean $m$ | rms Deviation |
|---|---|---|---|
| 1 | 27 | 0.460 | 0.128 |
| 2 | 23 | 0.458 | 0.068 |
| 3 | 30 | 0.495 | 0.111 |
| 4 | 19 | 0.455 | 0.104 |
| 5 | 20 | 0.500 | 0.106 |
| 6 | 17 | 0.578 | 0.046 |
| 7 | 19 | 0.589 | 0.124 |
| 8 | 12 | 0.412 | 0.070 |
| 2 | 6 | 0.335 | 0.081 |
| 3 | 25 | 0.312 | 0.143 |
| 6 | 21 | 0.307 | 0.049 |

large and thereafter decreases at a smaller and smaller rate so that after some time plots of strain against time appear straight and of constant slope. However, it is evident that the strain velocity does not become and remain constant.[17] A straight log$s$ *vs* log$t$ plot (except for slope=1) always means a changing velocity.

The parameter, $b$, from any one set of creep curves increases with stress. To show this increase and to compare $b$'s from different sets, it is convenient to plot log$b$ *vs* $\sigma$ or $1/\sigma$. In either case a linear relation seems to be indicated [reference 1(b), (c)] with several sets for one crystal not identical but covering only a small region of stress. Crystals may, however, differ widely from each other in the stress region covered. Attempts to relate $b$ accurately to $\sigma$ on the basis of the foregoing and similar experiments have had poor success, both because of the irregularity of the results and because the rapid change of $b$ with stress makes only a small stress region accessible. Thus $1/\sigma$ and $\sigma$ plots appear

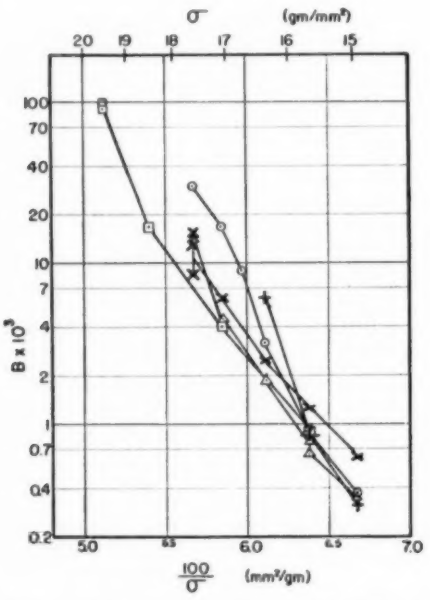


FIG. 6. Crystal No. 1, +, ○ (2), △ (1), × (4), □ (4).

[17] This point is discussed briefly in reference 1(b), and at much greater length in reference 4.

equally good and only extension over further stresses can decide between them.

## DISCUSSION

Although a unique interpretation of creep data in terms of elementary processes may not yet be possible, the authors have attempted to interpret the information obtained on these crystals by means of presently accepted views of dislocation behavior. The time-dependent deformation is presumed to take place by the Frank-Read mechanism of generation of dislocation loops. The creep which takes place at a given stress, $\sigma$, after an increment in stress, $\Delta\sigma$, is presumed to be caused by a new group of dislocation segments which are brought into play at the higher stress. Since the stress at which a segment of length $L$ will become operative is given by $\sigma=Ga/L$ (in which $G$ is the shear modulus and $a$ is the

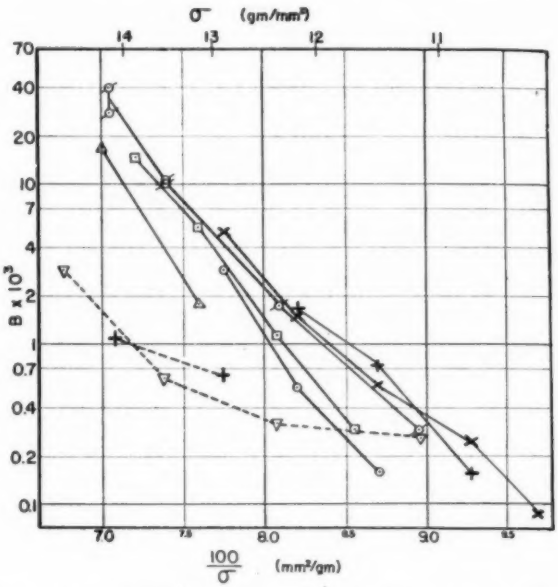


FIG. 7. Crystal No. 2. Solid line, +, ○ (7), △ (2), × (18), □ (1), ∅ (21). After remounting, dashed line, +, ▽ (6).

interatomic distance or Burger's vector), one needs then to find the distribution in length of dislocation segments. This distribution in length, $N(L)$, has been derived by Koehler.[18] His expression is

$$N(L)=c(1-c)^{L/a}\approx c\exp[-cL/a], \qquad (1)$$

in which $c$ is the concentration of anchor points along a dislocation line.

A very similar relation may be derived in a slightly different fashion analogous to the calculation of the distribution of mean free paths, as follows: To get the probability that an anchored segment of a dislocation line will have a length between $L$ and $L+dL$, one thinks of a large number of lines ($q_0$) spreading radially from one anchor point. This point is surrounded by a

[18] J. S. Koehler, Phys. Rev. **86**, 52 (1952).

spherical shell of radius, $L$, and thickness, $dL$. It contains, per unit volume, $n_1$ anchor points and $N_1$ atoms. Each anchor point has an effective cross section $A$. If $q$ lines reach the inside of this shell the fraction intercepted will be

$$-\frac{dq}{q}=\frac{n_1 A 4\pi L^2 dL}{4\pi L^2}, \tag{2}$$

which is the ratio of the cross-sectional area of anchor points to area of shell. Integration gives

$$q=q_0 \exp[-n_1 A L]. \tag{3}$$

If one now takes $A$ to be equal to $a^2$, $N_1$ to be $1/a^3$, and $c$ equal to $n_1/N_1$, one obtains the distribution in length

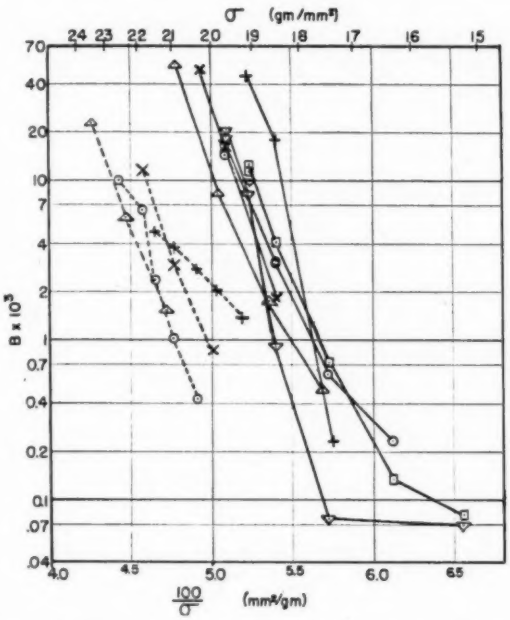


FIG. 8. Crystal No. 3 solid line, +, ○ (1), △ (17), × (36), □ (1), ▽ (0). After annealing and remounting, dashed line, +, ○ (11), △ (28), × (100).

of anchored segments:

$$-dq=N(L)dL=(cq_0/a)\exp(-cL/a)dL. \tag{4}$$

This is Koehler's distribution, except that $c$ is a volume concentration rather than the line concentration.

Application of this experssion to the present data is made in the following way. Differentiation of the creep equation $\eta=bt^m$ shows that the product $mb$ is the strain velocity at unit time (in this case, one minute). If $\dot{\eta}_1$ is the rate of shearing strain of each generating segment at one minute and $N$ is the number of segments operative, then $mb=N\dot{\eta}_1$. Hence,

$$mb=\dot{\eta}_1\int_{L+\Delta L}^{L} N(L)dL$$

$$=-\dot{\eta}_1(cq_0/a)\exp(-cL/a)dL, \tag{5}$$

$$=(\dot{\eta}_1 q_0 Gc\Delta\sigma/\sigma^2)\exp(-cG/\sigma). \tag{6}$$

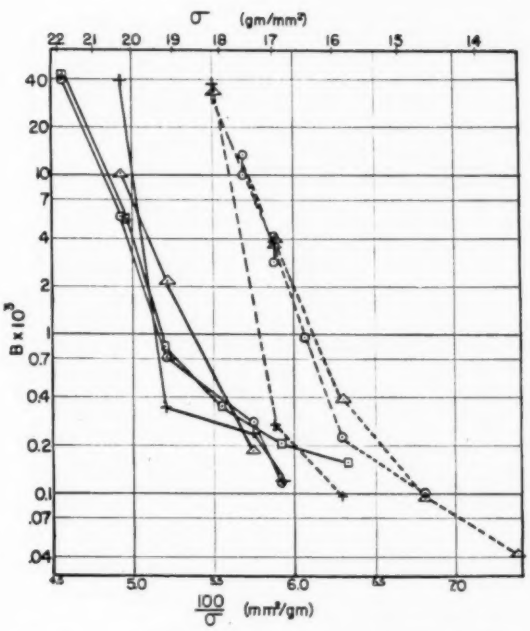


FIG. 9. Crystal No. 4, dashed line, +, ○ (1), △ (1). Crystal No. 5, solid line, +, ○ (10), △ (1), □ (15).

Then, If $\dot{\eta}_1$ is a constant,§

$$\ln(mb\sigma^2/\Delta\sigma)=-cG/\sigma+\text{constant}. \tag{7}$$

A plot of $\ln(mb\sigma^2/\Delta\sigma)$ against $1/\sigma$ should be a straight line of slope $-cG$.

The experimental data have been so tested as shown in Figs. 6 to 11. (In these figures $B$ is defined as $mb\sigma^2/\Delta\sigma$.) Each point represents a creep curve, and each set

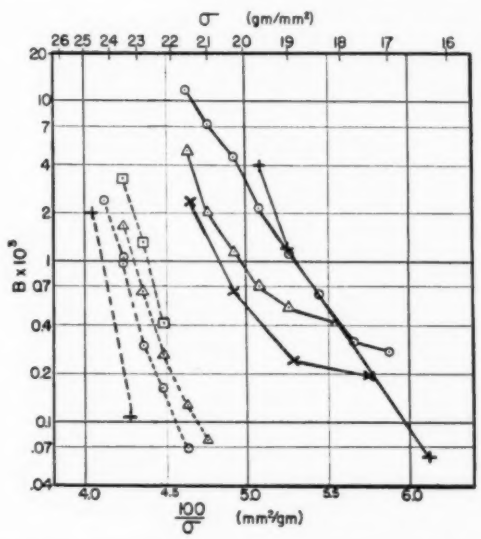


FIG. 10. Crystal No. 6, dashed line, +, ○ (14), △ (7), □ (50). Low slope runs, solid line, +, ○ (6), △ (2), × (8).

§ This is a major assumption for the application of this theory to our results. Its chief justification is in the consistency of the experimental results with the deductions of the theory as so intepreted. $\dot{\eta}_1$ is closely connected with the relation $\eta=bt^m$, as yet not satisfactorily theoretically explained.

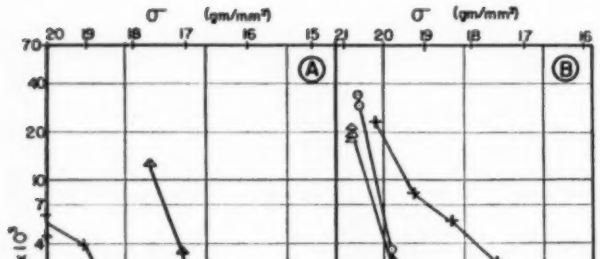


FIG. 11. A. Crystal No. 8, +, ○ (60), △ (45).
B. Crystal No. 7, +, ○ (8), △ (5).

of points with the same symbol and connected by straight line segments, a set of curves taken without intermediate unloading. Two or more points at one stress value indicate multiple slope curves on the log$s$ *vs* log$t$ plots. The history dependence of the data is indicated in the figure titles by keying the sets in chronological order and by giving in parentheses the number of days rest preceding the set. For the first set this is not indicated. Before this was taken it was usual to let the crystal rest several days. Study of these figures shows for each crystal a roughly reproducible dependence on stress, as the curves lie in a relatively narrow region of the diagram. No unique dependence on rest (annealing time) between runs is apparent, except perhaps in Fig. 7 (Crystal No. 2), in which the runs after longest rest (including the first) are at the right. In general, however runs taken after only a day's rest may be either in good agreement with the preceding set or differ appreciably. In one case, Fig. 8, Crystal No. 3, a second set was taken almost immediately following another. These two sets of runs are shown by the □ and ▽ points. The specimen was completely unloaded following the former and then the latter run was started at once. Except in the lower stress range the second curve (▽ points) agrees fairly well with its predecessor. Thus considerable creep at the higher stresses in the first curve has changed very little the ability of the crystal to creep again in practically the same way as the set of runs is repeated.

The great regularity found for crystals with $\alpha$ nearly equal to zero is not repeated for crystals with $\alpha$ about 20° (see Fig. 11). The data for the "abnormal" runs of Crystals 2, 3, and 6 also show, in these plots, some deivations from the "normal" sets of runs on these same crystals, though the slopes of the lines may not vary much from the "normal" runs, especially at the higher stresses.

In considering the data presented in these figures it will be seen that, within the uncertainty which depends on the small stress range, the results are at least roughly in accord with the theory. For each crystal one may with fair accuracy (except for Nos. 7 and 8) take a mean slope from the plot and thus arrive in obvious fashion at the value of $c$, since $G$ is known. In Table III, these $c$ values are given and, where it is known, the weight percentage of dissolved gases.[19] Included is an analysis of a small sample cut from the 50-lb block of *BH*4 zinc. Analyses given by Wain[20] for his zinc are included for comparison. The untreated material is "as received." The "treated" has been caused to absorb nitrogen gas. Returning to the $c$ values, the average is close to $10^{-4}$ Since the average by weight of metallic impurities in the several samples of zinc probably does not exceed about 0.005 percent, we may set the atomic concentration at about $5\times10^{-5}$ if we neglect the not very great correction for difference between atomic weight of zinc and the metallic impurities. It seems then that the number of metallic impurities, if they have all diffused to and settled on dislocation lines, is about right (slightly too small perhaps) to produce the required number of anchor points.

Anchor points may, however, consist of vacancies, or notably of gas atoms, probably in interstitial positions. Cottrell and his colleagues have supposed that $N_2$ plays a major role in this respect. The nitrogen content of the crystals which were analyzed, with the exception of No. 5, is still approximately the same as the *BH*4 stock material and is roughly only one-fourth as much as Wain's untreated material. Crystal No. 5, from which it was hoped to free[21] any possible dissolved $N_2$, has

TABLE III. Concentrations of anchor points and gas analyses.

| Crystal No. | $c\times10^4$ | Weight percent $\times10^3$ of: $H_2$ | $N_2$ | $CO_2$ | CO | $O_2$ | $CH_4$ |
|---|---|---|---|---|---|---|---|
| 1 | 1.0 | | | | | | |
| 2 | 0.66 | 0.04 | 0.07 | 0.2 | 0 | 0 | 0.04 |
| 2′[a] | 0.64 | | | | | | |
| 3 | 1.7 | | | | | | |
| 3′[a] | 1.5 | | | | | | |
| 4 | 1.5 | | | | | | |
| 5 | 1.4 | 0.05 | 0.2 | 0.2 | 0.09 | 0 | 0.07 |
| 6 | 1.9 | | | | | | |
| 6′[a] | 0.90 | | | | | | |
| 7 | 1.0 | 0.02 | 0.03 | 0.2 | 0 | 0 | 0.02 |
| 8 | 1.5 | | | | | | |
| *BH*4 stock | | 0.02 | 0.05 | 0.3 | 0.09 | 0 | 0 |
| Wain[b] | | 0.37 | 0.2 | | | 0 | |
| Wain[c] | | 0.48 | 2.2 | | | 0.1 | |

[a] 2′, 3′, 6′ are low slope ($m$ <0.4) runs for crystals 2, 3, and 6.
[b] Untreated or "as received" zinc.
[c] Treated, so as to absorb $N_2$.

[19] The gas contents were obtained by mass spectrographic analysis in the Ford Motor Company Scientific Laboratory. The writers are greatly indebted to Mr. James Neerman for making these analyses.

[20] H. L. Wain, Proc. Phys. Soc. (London) **B65**, 886 (1952).

[21] The zinc was not boiled in a really high vacuum but in one produced by a fore pump only. This was sufficient to keep its surface shiny and free from oxide. That $N_2$ should have been absorbed under these circumstances appears surprising, but this is the only difference in treatment of the material used for Crystal No. 5 and that used for the other *BH*4 crystals. Crystal No. 6

actually absorbed $N_2$ up to the amount of Wain's untreated material but is still far below Wain's treated zinc. It seems, therefore, that the occasional big jumps (Curve *C*, Fig. 3) can hardly be caused, as seemed likely at one time, by the same mechanism which caused the yield point observed by Wain, since much more $N_2$ is needed to produce the latter phenomenon. The atomic concentration of the $N_2$ for the *BH*4 sample is about $10^{-6}$ and thus far below the experimental values for $c$ in Table III. All the other gases contribute something like $10^{-5}$ and it does not seem very likely that gas atoms play any appreciable role. This leaves the metallic impurities as the anchor points and, as has been shown, the concentration of these seems to be of the right order of magnitude. It is, however, somewhat disappointing that the variation in the $c$'s is not more consistent with the known purity of the material. Thus one would expect Crystal No. 1 and perhaps No. 4 to have lower $c$'s than the others. One can only suppose, in the failure of this expectation, that in some cases, notably Crystal No. 2, the diffusion of impurities to dislocation lines is far from complete.

On the basis of the theory advanced and as shown by the slopes of the $\log B$ *vs* $1/\sigma$ curves one must assume that the distribution in length of anchored segments is very similar from crystal-to-crystal. Where, however, one crystal has at a given stress a far larger $B$ value (and therefore $mb$ value) than another it appears that there must be for the first many more of the segment lengths which correspond to this stress. If the $c$'s for the two crystals were the same, then the summation of the anchored lengths of dislocation line (per cm³) would be in the same ratio as the $mb$ values at a given stress. This is on the continued assumption that $\dot{\eta}_1$ of Eq. (5) is the same for all crystals. Since the $c$'s are not the same, one must make a somewhat more elaborate calculation to get relative lengths of dislocation lines. The total length of dislocation line is

$$\mathfrak{L}=\int_0^\infty LN(L)dL$$

$$=\int_0^\infty q_0(cL/a)\exp[-cL/a]dL=q_0a/c,$$

and one may replace $q_0$ in Eq. (6) by its value, $q_0=c\mathfrak{L}/a$ and solve for $\mathfrak{L}$ after introducing the value of $B$. Then one obtains

$$\mathfrak{L}=(aB/c^2G\dot{\eta}_1)\exp[cG/\sigma]. \quad (8)$$

Since $\dot{\eta}_1$ is unknown $\mathfrak{L}$ cannot be calculated, but any two $\mathfrak{L}$'s can be compared by making use of the $c$ values from Table II and choosing from each of Figs. 6 to 11 a mean $B$ for a chosen $1/\sigma$. The ratio of $\mathfrak{L}$ for each crystal to that of the first has been computed and is given as $\mathfrak{L}_j/\mathfrak{L}_1$ in Table IV. The variation of this ratio is extremely large; in fact, the ratio of longest to shortest $\mathfrak{L}$ is about $10^8$. To the writers this indicates that the extrapolation of the experimental results, which apply for each crystal to only a small range of dislocation length, over all possible lengths[22] is, to say the least, very uncertain. The experimental results are, nevertheless, not inconsistent with the idea that for a limited stress range, which differs from crystal-to-crystal, there exists a distribution in length similar to that given by the theory. As the stress range is increased it is quite possible that the distribution function levels off at higher stress (shorter length) or even decreases. If this occurs then the integration above for the total length of dislocation line is invalid, although an integration over the actual functions for each crystal (if known) might give much less variation in the ratio of the $\mathfrak{L}$'s. Estimates of total length of dislocation line seem at present quite uncertain. Thus Koehler[18] obtains from 0.2 to 4 cm per cm³ while he quotes a "usually accepted" value of $10^8$ cm per cm³.

TABLE IV. Ratios of total lengths of anchored segments.

| Crystal No. $j$ | $\mathfrak{L}_j/\mathfrak{L}_1$ |
|---|---|
| 1 | 1.0 |
| 2 | 0.11 |
| 2′[a] | $2.9\times10^{-3}$ |
| 3 | $8.1\times10^{-4}$ |
| 3′[a] | 19 |
| 4 | $6.3\times10^{4}$ |
| 5 | 37 |
| 6 | $2.1\times10^{2}$ |
| 6′[a] | $2.1\times10^{-3}$ |
| 7 | 0.31 |
| 8 | $3.2\times10^{4}$ |

[a] See footnote a, Table III.

If the general premise is accepted, that distribution in length of dislocation segments is the basis for creep, then it is certainly feasible to extend the experiments over a much larger stress region, which will not only test the present simple relation but also, in the event of its failure to hold, will lead to an empirical determination of the distribution. Also since it seems extremely likely that each crystal when grown has a certain pattern of dislocation lines and anchor points, experiments are in order to determine what conditions govern the establishment of such a pattern. One may look obviously to the seed from which the crystal is started since it might propagate a pattern; also small variations in growth conditions might have large effects. Some experimentation along this line has been started in this laboratory.

Besides the crystals for which data are given above,

since it was grown from this same boiled zinc and in addition had $N_2$ bubbled through it should have at least as much $N_2$ as No. 5, and perhaps more.

[22] The integration of Eq. (7) is from 0 to $\infty$. If the limits are taken as $a$ and something like the diameter of the crystals, the result for $\mathfrak{L}$ is not changed appreciably.

two crystals were grown which, from the first run on, showed only discontinuous creep or creep in regular steps. This phenomenon has been observed by many previous workers and is still largely unexplained. The explanation given in reference 1(b), that such behavior is caused by a secondary orientation, $\alpha$, of from 5° to 10°, appears to be incorrect, as these two crystals had $\alpha=3°$ and $\alpha=19°$, respectively.

The writers are indebted to Mr. J. G. Sentinella for his careful construction of the strain gauge and to Dr. F. T. Cole for many helpful discussions during the writing of the paper.

---

JOURNAL OF APPLIED PHYSICS VOLUME 26, NUMBER 3 MARCH, 1955

# Analysis of Scintillation Spectrometer Observations of the Penetration of $Cs^{137}$ Gamma Radiation through Water

R. B. Theus, L. A. Beach, and W. R. Faust
*Naval Research Laboratory, Washington, D. C.*
(Received April 7, 1954)

Spectral modifications of $Cs^{137}$ gamma radiations produced by penetration and diffusion through water have been observed. A single crystal of NaI(Tl) was used to observe the pulse-height distributions produced by radiation from both plane parallel and point isotropic sources. Inversion of the pulse-height distribution was carried out by use of an analog computer to obtain the spectral distribution of radiation.

## INTRODUCTION

PENETRATION and diffusion of gamma radiation through a material medium modifies the spectral distribution of intensity by multiple Compton scattering and direct absorption. Attenuation of $Co^{60}$ gamma rays in an infinite water medium and variations in spectral shape as a function of distance were calculated by Spencer and Fano.[1] The attenuation calculations were verified experimentally by White[2] using integrated dose measuring devices and Geiger counters. Evans Hayward[3] found good agreement between the electron spectra above 0.1 Mev predicted by Spencer and Fano and those observed with an anthracene detector. Weiss and Bernstein[4] studied in detail by use of NaI(Tl) spectrometers the shape and attenuation of the lower-energy portion of the spectrum diffusing through a water medium from a $Co^{60}$ source and found good agreement with theoretical predictions of Spencer and Fano.

We have observed spectral modifications produced by penetration of the 0.66-Mev gamma rays of $Cs^{137}$ in water by use of a scintillation spectrometer. Both point isotropic and plane parallel source geometries were used in order to observe differences in the corresponding build-up factors. Spectral distributions of radiation were deduced from spectrometer pulse-height distributions by numerical inversion of the integral equation connecting the pulse-height and spectral distribution. This spectral distribution was utilized to calculate an expected counting rate of a Geiger counter at various penetration distances to be compared with experimental measurements.

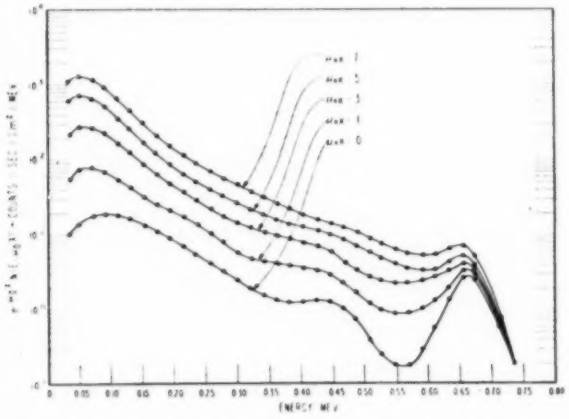

FIG. 1. Pulse-height distribution for a plane-parallel source.

## EXPERIMENTAL METHOD

All experiments were performed in a water tank which had a diameter and depth of 520 centimeters. The detector was a 2.54 cm diameter by 1.27 cm thick right cylinder of NaI(Tl) mounted on a RCA 6199 photomultiplier. Detector pulses were recorded on a twenty channel pulse-height analyzer. The detector was waterproofed so that it could be submerged at any depth in the tank. It should be noted that displacement of scattering medium by the detector reduces the flux below that found in an infinite medium.

Experiments, performed with point isotropic source geometry, consisted of observing pulse-height distributions at various distances from a small $Cs^{137}$ source immersed in the tank. Geometric conditions were such that neither source nor detector was ever closer than 200 cm to any boundary of the tank.

[1] L. V. Spencer and U. Fano, J. Research Natl. Bur. Standards **46**, 446 (1951).
[2] G. R. White, Phys. Rev. **80**, 154 (1950).
[3] E. Hayward, Phys. Rev. **86**, 493 (1952).
[4] M. M. Weiss and W. Bernstein, Phys. Rev. **92**, 1264 (1953).

In the plane-parallel source geometry a $Cs^{137}$ source was placed above the tank at a distance of 450 cm from the detector, which was 150 centimeters from the bottom of the tank. Data were taken at various penetration distances by increasing the water level in the tank. The source-to-water surface distance was always such that radiation on the surface was essentially parallel over an area large compared with the depths of penetration.

Pulse-height distributions in counts per second per Mev obtained for the plane parallel case are given in Fig. 1. This is plotted for a source strength of 0.636 photons/sec/cm$^2$. Figure 2 shows the pulse-height distribution produced by a point isotropic source. These data have been normalized to that corresponding to a source of strength equal to the reciprocal of the detector efficiency at the primary energy. Counting statistics were of the order of 1 percent at each point.

## ANALYSIS OF PULSE-HEIGHT DISTRIBUTION

The observed pulse-height distribution $N(E,\mu_0X)$ that results from the spectral distribution of gamma rays $f(E',\mu_0X)$ incident upon the crystal can be expressed as

$$N(E,\mu_0X)=\int_0^{E'_{\max}} K(E,E')f(E',\mu_0X)dE'. \quad (1)$$

Here, $\mu_0X$ represents the penetration depth in terms of the number of mean free paths of primary radiation. The kernel $K(E,E')$ is the response function of the detector and $K(E,E')dE$ represents the probability that a gamma ray of energy $E'$ will produce a pulse of height between $E$ and $E+dE$.

A response function neglecting secondary processes in the crystal is:

$$K(E,E')=\int_0^{\infty} g(E,\xi)\left[\frac{\mu_c(E')}{\mu_t(E')}X(\xi,E')+\frac{\mu_p(E')}{\mu_t(E')}\delta(\xi-E')\right]\epsilon(E')d\xi, \quad (2)$$

$g(E,\xi)$ is a Gaussian distribution about the energy $E$, and is normalized such that its integral is unity, i.e.,

$$g(E,\xi)=\frac{\exp[-(1.66/\Delta W)^2](E-\xi)^2}{\int_0^{\infty}\exp[-(1.66/\Delta W)^2](E-\xi)^2d\xi}. \quad (3)$$

Here $\Delta W$ is the experimentally determined full width at half maximum response of the detector at energy $\xi=E$. $\mu_c(E')$, $\mu_p(E')$, and $\mu_t(E')$ are the Compton, photoelectric, and total absorption coefficients for photons of energy $E'$ in a NaCl crystal. $\epsilon(E')$ is the efficiency of the detector for photons of energy $E'$ and

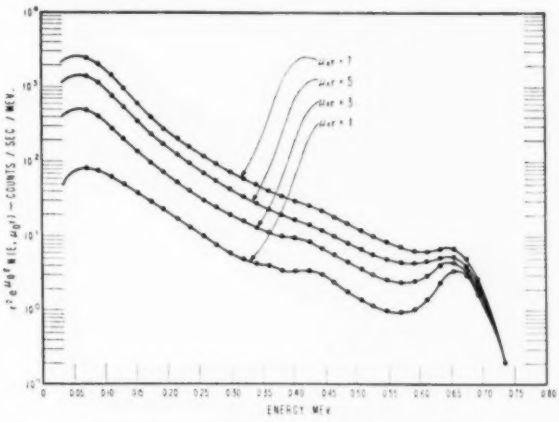


FIG. 2. Pulse-height distribution for a point isotropic source.

$\delta(E'-\xi)$ is the Dirac delta function. $X(\xi,E')d\xi$ is the probability of an electron having energy in the interval $\xi$ to $\xi+d\xi$ after interaction with a photon of initial energy $E'$, i.e.,

$$X(\xi,E')=\frac{\frac{1}{E'^2}\left[2+\xi\frac{\xi(E'+1)^2-E'(2E'+\xi^2)}{E'^2(E'-\xi)^2}\right]}{\int_0^{\xi_{\max}}\frac{1}{E'^2}\left[2+\xi\frac{\xi(E'+1)^2-E'(2E'+\xi^2)}{E'^2(E'-\xi)^2}\right]d\xi}, \quad (4)$$

where $E'$ and $\xi$ are in units of mc$^2$ and

$$\xi_{\max}=2E'^2/(1+2E').$$

To perform the inversion Eq. (1) may be expressed as the limit, $m\to\infty$ of the matrix equation:

$$N(E_i,\mu_0x)=\Delta E\sum_{j=1}^{j=m}K(E_i,E_j)f(E_j,\mu_0x) \qquad i=j=1,2\cdots m \quad (5)$$

where $E_{j+1}-E_j=\Delta E_j=\Delta E$.

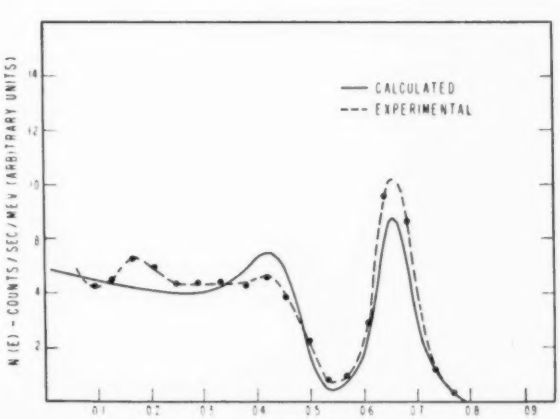


FIG. 3. Comparison of theoretical and experimental pulse-height distribution for gamma radiation from $Cs^{137}$.

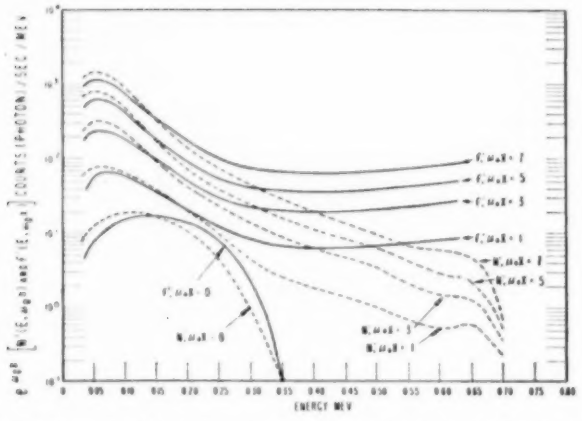

FIG. 4. Pulse-height and spectral distribution of scattered radiation at various penetration depths for a plane-parallel source.

The matrix $K(E_i,E_j)$ is obtained from Eq. (2) by substitution of appropriate values of $E_i$ and $E_j$ for $E$ and $E'$ respectively so that $K(E_i,E_j)$ becomes a square matrix.[5]

Solution of the matrix Eq. (5) for $f(E',\mu_0 x)$ may be obtained approximately by use of a finite value for $m$. This process involves the solution of $m$ linear equations for $m$ unknown quantities $f(E_j,\mu_0 x)$. The accuracy with which this solution represents the true spectral distribution $f(E',\mu_0 x)$ at the energies $E_j=E'$ is dependent upon the value of $m$ used. Of course, larger values of $m$ lead to a closer approximation. Inversion of the matrices involved here were carried out on a 12-channel analog computor.

The accuracy of these methods is best illustrated by comparison of theoretical and experimental pulse heights. If the spectral distribution $f(E',\mu_0 x)$ has the simple form $\delta(E'-E_0)$, which represents a line spectrum, then the corresponding pulse-height distribution is simply $K(E,E_0)$. Figure 3 compares theoretical values as computed from Eqs. (2)–(4) with experimental values of the pulse-height distribution for the 0.66-Mev gamma ray from $Cs^{137}$. The discrepancy between these curves indicates multiple processes do occur in the crystal. These processes increase the area under the photopeak as compared to that under the Compton distribution. A more accurate expression for Eq. (2) can be obtained by experimental determination of effective $\mu_c/\mu_t$ and $\mu_p/\mu_t$ for the particular crystal at several energies.

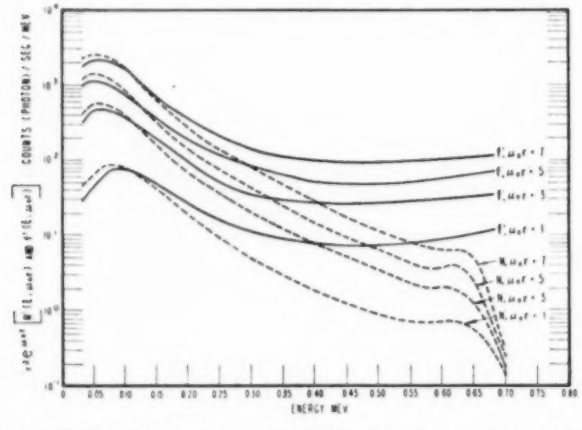

FIG. 5. Pulse-height and spectral distribution of scattered radiation at various penetration depths for a point isotropic source.

## ANALYSIS OF DATA

Pulse-height distributions were analyzed by first subtracting out the pulse height distributions resulting from unscattered gamma rays, e.g., $K(E,E_0)e^{-\mu_0 x}$. The scattered pulse-height distribution $N'(E,\mu_0 x)$ and the analyzed energy spectrum of scattered radiation $f'(E',\mu_0 x)$ are shown in Figs. 4 and 5 for the two geometries.

The energy build up factor, defined as the ratio of the energy of the scattered radiation to the energy of the unscattered radiation is shown in Fig. 6. Effect of the different source geometries is apparent from the build-up factors. The point isotropic geometry has generally a higher build-up factor than the plane-parallel source geometry.

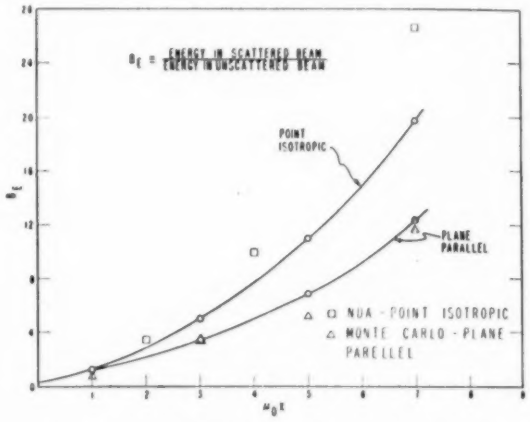


FIG. 6. Energy build-up factor for point isotropic and plane-parallel $Cs^{137}$ sources.

The point isotropic build-up factors of Fig. 6 are approximately 20 percent lower than computed values of NDA.[6] Displacement of scattering medium by the detector prevents an exact measurement of the quantity calculated for an infinite medium by the moment method. Results of a preliminary Monte Carlo calculation[7] for plane-parallel geometry agree with the experimental values within the accuracy of computation.

An interesting application of calculations of the spectral distribution, $f'(E',\mu_0 x)$ is to use the results to compute the counting rate, $C$, observed on a Geiger

[5] Whittaker and Watson, *Modern Analysis* (The Cambridge University Press, New York, 1952), fourth edition, pp. 211–217.

[6] Goldstein, Wilkins, and Preiser, NDA Memo 15C-20 (1953).

[7] J. D. Plawchan (private communication).

counter. The relative rate is given by

$$C(\mu_0 x)=\left[\int_0^{E'_{\max}} f'(E',\mu_0 x)\epsilon(E')dE'+\epsilon(E_0)e^{-\mu_0 x}\right]K,$$

where $\epsilon(E')$ is the efficiency[8] of the Geiger counter and $K$ is a normalization constant.

Geiger counter observations of the relative counting rate produced by a $Cs^{137}$ source in water are represented by the solid curve of Fig. 7. Statistics of the data were of the order of 1 percent and are not indicated on the curves. The circles represent the relative counting rate $C(\mu_0 x)$ as computed from Eq. (4).

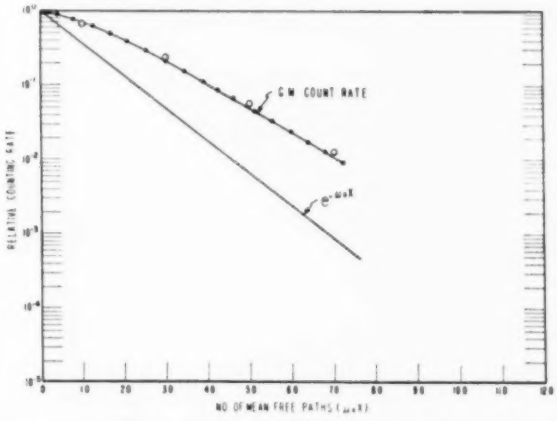


FIG. 7. Comparison of experimental Geiger-Mueller counting data and theoretical counting data at various penetration depths.

### ACKNOWLEDGMENTS

The authors wish to thank Dr. E. H. Krause for his interest and support and express their appreciation to Mr. T. H. DeRieux for aid in performing the experiments.

[8] Bradt *et al.*, Helv. Phys. Acta **19**, 77 (1946).

JOURNAL OF APPLIED PHYSICS VOLUME 26, NUMBER 3 MARCH, 1955

# Bistatic Radar Cross Sections of Surfaces of Revolution*

K. M. SIEGEL, H. A. ALPERIN, R. R. BONKOWSKI, J. W. CRISPIN, A. L. MAFFETT, C. E. SCHENSTED, AND I. V. SCHENSTED
*Willow Run Research Center, University of Michigan, Ann Arbor, Michigan*

(Received April 9, 1954)

The results obtained by applying the current-distribution method to the problem of approximating the scattering cross section, when the transmitter and receiver are separated, are presented for several simple geometric configurations. The method is applied for the case in which the transmitter is located on the axis of revolution and the ratio $l/\lambda$ is large, where $l$ is a "characteristic dimension" of the body and $\lambda$ is the wavelength. These results indicate that in most of the cases considered the cross section increases as the angle between the receiver and the transmitter increases.

## 1. INTRODUCTION

IN this paper, bistatic radar cross sections of simple configurations are obtained by applying an approximation method. In most of the cases considered the configuration is a surface of revolution, the transmitter is located on the axis of symmetry of the body, the polarization is specified, and the position of the receiver is allowed to vary in a plane containing the axis of the body.

The physical description of bistatic cross sections differs from that of monostatic cross sections in that the receiver and the transmitter are permitted to be located at separate positions. To specify the bistatic radar cross section of a body for a general location of transmitter and receiver more than one angle is required. However for most cases discussed in this paper, one angle, the angle $\beta$ shown in Fig. 1, suffices. The bistatic radar cross section, therefore, is denoted by $\sigma(\beta)$. It is evident that the monostatic backscattering cross section is a special case ($\beta=0$) of the bistatic cross section and can be denoted by $\sigma(0)$.

The approximation technique used is the current-distribution or physical-optics method. This method is applicable when the wavelength of the incident radiation is small with respect to the characteristic dimension

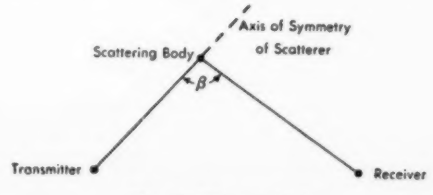


FIG. 1. The angle $\beta$.

* This paper is a condensation of the report UMM-115, "Studies in radar cross-sections VIII—theoretical cross-sections as a function of separation angle between transmitter and receiver at small wavelengths" by Siegel, Alperin, Bonkowski, Crispin, Maffett, Schensted, and Schensted, Willow Run Research Center University of Michigan, October, 1953. In addition, portions of this paper were presented in a talk "Determination of scattering cross-sections for the case of separated transmitter and receiver" by Siegel, Bonkowski, Crispin, and I. V. Schensted, presented at the Symposium on Microwave Optics, McGill University, Montreal, Canada, 1953.

of the body. In using any approximation method it is desirable to know how the results obtained from it compare with the physically expected or experimental results. In determining the monostatic radar cross section, when the wavelength is much less than the characteristic dimension of the body, the current-distribution method has provided many results which are in close agreement with experiment and with exact theoretical solutions.

The current-distribution method has been subjected to much criticism on both theoretical and experimental grounds.[1,2] For example, reasoning based on the assumptions of the current-distribution method would lead to the conclusion that this method should not be used when the surface has a point discontinuity. However, the method predicts the nose-on backscattering cross section of a semi-infinite cone to within experimental accuracies, if not exactly.[3,4]

When solving far-zone problems for which the bodies are infinite in the direction of propagation, Abelian limit processes usually are convenient unless the configuration's tangent at infinity is parallel or perpendicular to the propagation vector. The limit process is commonly used, because it is not possible to get infinitely far from an infinite body. If the viscosity or conductivity of the medium is introduced into the problem (although these quantities may be negligible), then the problem becomes formally the same as the previous one with the objection to the limit process removed. In this paper, an Abelian limit process is used in the discussion of the semi-infinite cone.

Some doubt has been thrown on the applicability of the physical-optics approximations to electromagnetic scattering problems in the past by the assertion that these approximations would always be in error by more than the corresponding physical-optics approximations to the acoustic problem. At least one apparent contradiction to this assertion is presented in references 3 and 4, where it is shown that physical-optics predicts the exact electromagnetic cross section for cones of small angle, whereas the same approximate methods predict a value four times as great as that predicted by the acoustic wave equation.

Although the quantitative theoretical explanation of this factor of four cannot be elaborated at the present time, it is clear that such a disagreement should not be unexpected. The acoustic wave equation which has been used is merely an approximation to the exact equation of the motion. This approximation is valid only when the wavelength is large (in comparison to the dimensions of the scatterer), because the influence of viscosity in acoustics is greatest at small wavelengths.[5] However, the physical-optics approximation is valid only when the wavelength is small in comparison to the dimensions of the scatterer. Hence, the physical-optics approximation cannot be expected to reproduce accurately the real situation of acoustic scattering at any wavelength, whereas the same approximation can be expected to reproduce accurately the real situation in electromagnetic scattering whenever the wavelength is small.

Although in the above only an infinite body was under discussion, there is nothing in the argument which requires that the surface be infinite; the same type of conclusion would be reached for a finite body in a real fluid.

The cone result shows that it is possible to treat by the current-distribution method at least some bodies which have point discontinuities. There is no proof available at the present time that pointed bodies in general can be treated by physical-optics. Such a proof would require a stronger basis than the present existence and uniqueness proofs in electromagnetic theory, since the papers of Weyl and Müller[6,7] and the Fredholm theory are based on the assumption that the body is "sufficiently smooth."

In addition to the cone solution, a point (or rather four such singularities) has been treated by Kouyoumjian in his solution for the cross section of a square flat plate[8] by the Levine-Schwinger variational procedure.[9] The physical-optics result was in fairly good agreement with the variational result in the region where the wavelength is equal to, or less than, the length of the side of the plate. Kouyoumjian's experimental results agree more closely with the variational curve than with the physical-optics curve, but no great error would be made if the optics result was used.

In addition, the physical-optics determination of the nose-on backscattering cross section of an ogive (still another pointed body) is also in close agreement with experimental results (see reference 3).

## 2. THE METHOD FOR DETERMINING BISTATIC CROSS SECTIONS

If the surface of the scattering body is assumed to be perfectly conducting, the equation for the scattered

[1] B. B. Baker and E. I. Copson, *The Mathematical Theory of Huygen's Principle* (Oxford University Press, New York, 1950), second edition.

[2] *Symposium on Microwave Optics* (Eaton Electronics Research Laboratory, McGill University, Montreal, Canada, 1953), Vols. I and II.

[3] Siegel, Alpern, Crispin, Hunter, Kleinman, Orthwein, and Schensted, "Studies in radar cross-sections IV—comparison between theory and experiment of the cross-section of a cone," Willow Run Research Center, University of Michigan, Report No. UMM-92 (February, 1953).

[4] Siegel, Crispin, and Schensted, J. Appl. Phys. **26**, 309 (1955).

[5] J. W. S. Rayleigh, *The Theory of Sound* (Dover Publications, New York, 1945), second edition.

[6] H. Weyl, Math. Z. **55**, 187–198 (1952).

[7] C. Müller, Math. Z. **56**, 80–83 (1952).

[8] R. G. Kouyoumjian, "Calculation of the echo area of several scatterers of simple geometry by the variational method," *Symposium on Microwave Optics* (Eaton Electronics Research Laboratory, McGill University, Montreal, Canada, 1953), Vol. I.

[9] H. Levine and J. Schwinger, Commun. Pure Appl. Math. Vol. III, No. 4, p. 355 (December, 1950).

magnetic field[10] can be written as

$$\mathbf{H}_{sc}=\frac{1}{4\pi}\int_S(\mathbf{n}\times\mathbf{H}_t)\times\nabla\left(\frac{e^{-ikR}}{R}\right)dS, \qquad (2\text{-}1)$$

where $\mathbf{H}_{sc}$ = the scattered magnetic field vector, $\mathbf{n}$ = the unit normal to the surface, $\mathbf{H}_t$ = the tangential component of the magnetic field on the scattering surface, $R$ = the distance separating the receiver and the integration point, $k=2\pi/\lambda$ ($\lambda$ = wavelength), and $S$ = the region of integration = the entire surface of the scatterer.

Under physical-optics assumptions, $\mathbf{H}_t$ can be approximated as twice the tangential component of the incident magnetic field on the "illuminated" side of the body and zero on the "shadow" side of the body.† Letting the incident magnetic field have a magnitude $H_0$ and a direction $\mathbf{a}$, then according to this approximation

$$\mathbf{H}_t=2\mathbf{i}_tH_0e^{-ik(\mathbf{k}\cdot\mathbf{r})}$$

on the illuminated side of the body,

$$\mathbf{H}_t=0$$

on the shadow side of the body,

where $\mathbf{k}$ = a unit vector directed from the transmitter, assumed to be infinitely far away, to the origin of the coordinate system; $\mathbf{r}$ = the radius vector from the origin to any point on the surface of the scatterer; and $\mathbf{i}_t=\mathbf{a}-(\mathbf{a}\cdot\mathbf{n})\mathbf{n}$.

If the receiver is at a very great distance from the body, if the body is finite, and if the incident magnetic field is of unit magnitude, then Eq. (2-1) can be expressed in the form

$$\mathbf{H}_{sc}=\frac{e^{-ikR'}}{R'}\mathbf{F}(\beta) \qquad (2\text{-}2)$$

where

$$\mathbf{F}(\beta)=\frac{ik}{2\pi}[(\mathbf{n}_0\cdot\mathbf{a})\mathbf{f}-(\mathbf{n}_0\cdot\mathbf{f})\mathbf{a}],$$

$$\mathbf{f}=\int_{\substack{\text{illuminated}\\ \text{region of body}}}\mathbf{n}\exp[-ik\mathbf{r}\cdot(\mathbf{n}_0+\mathbf{k})]ds$$

$$=\mathbf{i}_xI_x+\mathbf{i}_yI_y+\mathbf{i}_zI_z,$$

and $R'$ = the distance from the origin to the receiver.

The radar cross section is given by[11]

$$\sigma(\beta)=4\pi[|F_x|^2+|F_y|^2+|F_z|^2]. \qquad (2\text{-}3)$$

The amount of energy received is proportional to the square of the magnitude of the scalar product of the vectors $\mathbf{H}_{sc}$ and $\mathbf{d}$, where $\mathbf{d}$ is the direction of the receiver polarization; thus it is convenient to define

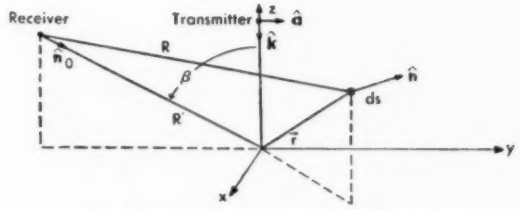


FIG. 2. Geometry for surfaces of revolution.

the effective cross section as

$$\sigma_e(\beta)=4\pi|\mathbf{F}\cdot\mathbf{d}|^2$$

$$\sigma_e(\beta)=\frac{4\pi}{\lambda^2}|(\mathbf{n}_0\cdot\mathbf{a})(\mathbf{f}\cdot\mathbf{d})-(\mathbf{n}_0\cdot\mathbf{f})(\mathbf{a}\cdot\mathbf{d})|^2. \qquad (2\text{-}4)$$

If $\mathbf{d}$ is given by a vector whose components are proportional to the complex conjugates of the corresponding components of $\mathbf{F}$, then $\sigma_e(\beta)$ reduces to $\sigma(\beta)$.

If the body is a surface of revolution (the axis of symmetry taken to be the $z$-axis), if the receiver is restricted to be in the $yz$-plane with $y\leqslant 0$, and if, in addition, the transmitter is located on the $z$-axis ($z>0$), then the geometry shown in Fig. 2 applies. With the situation as pictured in Fig. 2,

$$\mathbf{n}_0=\mathbf{i}_y\sin\beta-\mathbf{i}_z\cos\beta, \quad \text{and} \quad \mathbf{k}=-\mathbf{i}_z.$$

If the polarization of the incident wave is $\mathbf{a}=\mathbf{i}_y$ and if the surface is symmetric with respect to the $yz$-plane, then from Eq. (2-3)

$$\sigma_{\mathbf{a}=\mathbf{i}_y}(\beta)=\frac{4\pi}{\lambda^2}|I_z|^2 \qquad (2\text{-}5)$$

where

$$I_z=\int_{\substack{\text{illuminated}\\ \text{region of body}}}n_z\exp[-ik\mathbf{r}\cdot(\mathbf{n}_0+\mathbf{k})]ds.$$

In many cases, the integral $I_z$ can be evaluated easily with the aid of the following Double Stationary-Phase theorem (hereafter, this theorem will be referred to as the D.S.P. theorem):

*Theorem*:

Let

$$I=\int_c^d\int_a^b f(x,y)e^{ikg(x,y)}dxdy.$$

If

(1) $f(x,y)=X(x)Y(y)$ is analytic in the region $R=\{x,y\,|\,a\leqslant x\leqslant b,\quad c\leqslant y\leqslant d\}$,

(2) $g(x,y)$ is analytic in $R$,

(3) there exists one, and only one, point $(x_0, y_0)$ in the interior of $R$, such that

$$p_0=q_0=0 \quad \text{and} \quad r_0t_0-s_0^2\neq 0,$$

where

$$p=g_x, \quad q=g_y, \quad r=g_{xx}, \quad s=g_{xy}$$

[10] J. A. Stratton, *Electromangetic Theory* (McGraw-Hill Book Company, Inc., New York, 1941), p. 466.

† The shadow curve is the locus of points on the body for which $\mathbf{k}\cdot\mathbf{n}=0$. This curve separates the portion of the body "seen" by the transmitter (i.e., the illuminated side) from the shadow side.

[11] K. M. Siegel and H. A. Alperin, Report No. UMM-87, Willow Run Research Center, University of Michigan (January, 1952).

and

$$l=g_{vv},$$

and

(4) $X(\xi)/g_\xi(\xi,\eta)$ and $Y(\eta)/g_\eta(\xi,\eta)$ are of bounded variation for $(\xi,\eta)$ in $R$ but not in

$$R'=(x,y|x_0-\delta\leqslant x\leqslant x_0+\delta,y_0-\epsilon\leqslant y\leqslant y_0+\epsilon),$$

then

$$I=\frac{\pm 2i\pi e^{ikg(x_0,y_0)}f(x_0,y_0)}{k[r_0t_0-s_0^2]^{\frac{1}{2}}}+O\left(\frac{1}{k^{\frac{3}{2}}}\right)as\ k\to\infty.$$

For a surface whose first and second derivatives are continuous, the essential contribution to the cross section for short wavelengths can be obtained from the integral formulation of the current-distribution method if the integration is performed by the method of stationary phase. If the integration is performed exactly, a result dependent upon wavelength is usually obtained. Since the application of the method of stationary phase and the physical-optics integrals depend on the parameter $(kl)^{-1}$, where $k=2\pi/\lambda$, $l$ is the characteristic dimension of the body and $\lambda$ is the wavelength, it can be shown that the physical-optics result is a perturbation of the geometric-optics (or stationary-phase) result.

For a pointed body, the method of stationary phase cannot be applied directly for most values of $\beta$. The cross section predicted by geometric-optics is equal to $\pi R_1R_2$, where $R_1$ and $R_2$ are the two radii of curvature at the stationary-phase point. A stationary-phase point is one at which a plane of constant phase $(\mathbf{n}_0+\mathbf{k})\cdot\mathbf{r}=$const, is tangent to the surface of the body. Hence, if a finite body has a point singularity, its cross section by geometric-optics would be zero. In this case, the physical-optics answer cannot be obtained from the geometric-optics answer by perturbation because there is no nonzero solution to perturb. A solution can, however, be obtained by integrating the surface integrals obtained exactly in one variable and by stationary phase in the other.

It is sometimes possible, by known methods, to solve the bistatic problem if the transmitter is located on the axis of symmetry but not otherwise. Since it is often of more interest to have the receiver located in this position, the reciprocity theorem of electromagnetic theory[12] should be examined in the light of the approximation technic to be employed. This theorem allows the cross section to be determined for given positions of the transmitter and receiver if the problem has been solved with these positions interchanged.

With $\sigma_e(\beta)$ defined as in Eq. (2-4), it follows that when the wavelength becomes extremely short, all the contributions to $\mathbf{f}$ cancel out except those from the immediate vicinity of the stationary-phase point on the side of the body toward the transmitter. Clearly $\mathbf{n}=(\mathbf{n}_0+\mathbf{k})/|\mathbf{n}_0+\mathbf{k}|$ at a stationary-phase point, and, for extremely short wavelengths, $\mathbf{f}=A(\mathbf{n}_0+\mathbf{k})$ where $A$ is not changed by an interchange of transmitter and receiver. Therefore, in this limiting case, Eq. (2-4) becomes

$$\sigma_e(\beta)\approx\frac{4\pi}{\lambda^2}|A|^2|(1+\mathbf{n}_0\cdot\mathbf{k})(\mathbf{a}\cdot\mathbf{d})-(\mathbf{n}_0\cdot\mathbf{a})(\mathbf{k}\cdot\mathbf{d})|^2. \quad (2\text{-}6)$$

If $\mathbf{n}_0$ and $\mathbf{k}$ are interchanged, and simultaneously $\mathbf{a}$ and $\mathbf{d}$ are interchanged Eq. (2-6) is unaffected. Hence, reciprocity is obtained for the current distribution method in the limit of extremely short wavelengths.

*When a wavelength-dependent expression for the cross section is obtained by the current-distribution method, complete reciprocity is not obtained.* However, since the exact theory shows that there is reciprocity, whenever the current-distribution method yields an appropriate wavelength-dependent formula for one case, the result can be considered to be an adequate approximation for the reciprocal case.

## 3. CROSS-SECTION FORMULAS FOR VARIOUS SURFACES

In this section the method discussed in the preceding section is applied to several geometrical configurations. The method is applied directly in the cases of the prolate spheroid and the sphere in Section 3.1. A discussion of the application of the method to a finite cone appears in Section 3.2, and to an ogive in Section 3.3. Section 3.4 contains the results obtained for an infinite paraboloid which can be shown[13] to be the *exact* solution to the problem. Although the semi-infinite cone is a surface which does not satisfy the basic assumptions referred to in Section 2, the results obtained through the formal application of the method (with an Abelian limit procedure added) are given in Section 3.5. The results obtained through a formal application of the Luneberg-Kline method are also given. Section 3.6 contains an extension of the method of Section 2, as does Section 3.7. The elliptic cylinder is discussed in Section 3.6 and a special case (in which the integration can be done exactly) for the spheroid appears in Section 3.7.

### 3.1. The Prolate Spheroid and the Sphere

The direct application of the method described in Section 2 to the problem of determining $\sigma_a=i_y(\beta)$ for the prolate spheroid given by

$$\frac{x^2+y^2}{B^2}+\frac{z^2}{A^2}=1$$

and for the sphere

$$x^2+y^2+z^2=R_0^2$$

yields the following geometric-optics results:

[12] S. A. Schelkunoff, *Electromagnetic Waves* (D. Van Nostrand Company, Inc., New York, 1943).

[13] C. E. Schensted, J. Appl. Phys. **26**, 306 (1955).

For the prolate spheroid,

$$\sigma_{a=i_y}(\beta)=[4\pi B^4/A^2]\left[(1+\cos\beta)+\frac{B^2}{A^2}(1-\cos\beta)\right]^{-2},$$

$$\beta<\pi. \tag{3-1}$$

For the sphere,

$$\sigma_{a=i_y}(\beta)=\pi R_0^2, \quad \beta<\pi. \tag{3-2}$$

These geometric-optics results were obtained by using the D.S.P. theorem.

$\sigma_{a=i_y}(\beta)$ for both the prolate spheroid and the sphere were also determined by integrating once exactly and once by analog machine methods. The analog computing equipment consisted of standard Reeves analog computor units. The "analog evaluation" was performed for the special cases given by $A=10B$ and $kB=100$ for the prolate spheroid and $kR_0=100$ for the sphere. Good agreement between the analog results and the D.S.P. results was found to exist in the range $0°\leqslant\beta<160°$ for the prolate spheroid and in the range $0°\leqslant\beta<120°$ for the sphere. A graphical representation of these results appears in Fig. 3.

### 3.2. The Finite Cone

For a finite cone of slant length $r_0$ and one-half cone angle $\gamma$, the application of Eq. (2-5) yields the formula

$$\sigma_{a=i_y}(\beta)\approx\frac{4\pi r_0^2\sin4\gamma}{(b^2-c^2)^2}\{c^2J_0^2(kr_0b)+b^2J_1^2(kr_0b)\}, \tag{3-3}$$

where

$$b=\sin\beta\sin\gamma, \quad c=\cos\gamma(1+\cos\beta),$$

and $\beta$ is restricted by the inequality $0\leqslant\beta<\pi-2\gamma$. This formula was obtained by integrating the integral $I_z$ once by parts and once by stationary phase and then retaining only the dominant term (for large $k$).

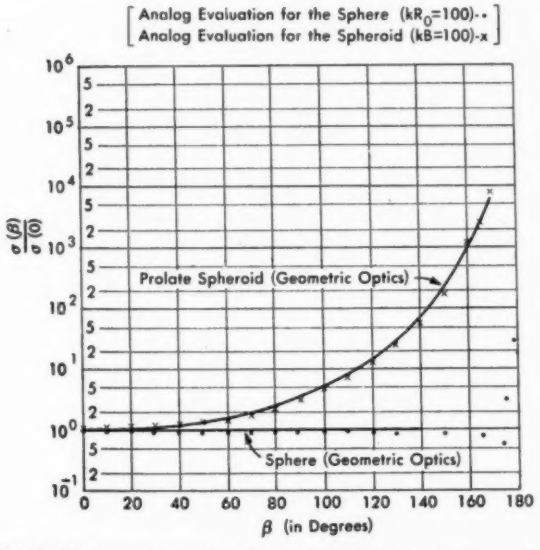
Analog Evaluation for the Sphere (kR0=100)-•
Analog Evaluation for the Spheroid (kB=100)-x
Prolate Spheroid (Geometric Optics)
Sphere (Geometric Optics)
β (in Degrees)

FIG. 3. Cross sections of a sphere of radius $R_0$ and of a prolate spheroid for which $A=10B$ as a function of the angle $\beta$.

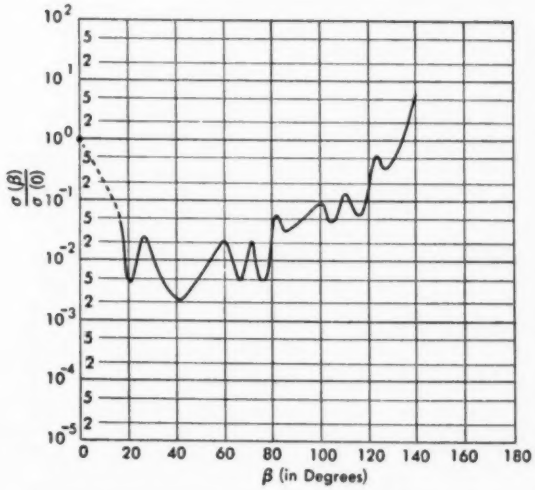


FIG. 4. Cross section of a finite cone of half-angle 15° and slant length equal to $100\lambda/\pi$.

A graphical representation of Eq. (3-3) appears in Fig. 4 for the special case of $\gamma=15°$ and $\pi r_0/\lambda=100$.

It should be pointed out that the sharp edge of the finite cone contradicts the assumptions of the current-distribution method. Thus, the result obtained here for the finite cone may not be as good an approximation to the exact cross section as the results obtained for other bodies.

### 3.3. The Ogive

The term "ogive" is not defined uniformly in the literature. For example, Hobson[14] refers to the figure obtained by revolving a minor arc of a circle about its chord as a spindle, whereas Hansen and Schiff[15] use the term spindle to describe the arc of a parabola revolved about its chord. Others use the term ogive as a general term of which both of the above configurations are examples. In the work presented here the term ogive refers to the minor arc of a circle revolved about its chord (Hobson's spindle) and the term spindle will be used for the parabolic arc revolved about its chord (Hansen and Schiff).

An ogive of length $L$, maximum diameter $d$, and half-angle $\alpha$ (using the cylindrical coordinates $w$, $\phi$, $z$) is given by the equation

$$(w+h)^2+z^2-P^2=0$$

with

$P=$ radius of the generating circular arc,

$|z|\leqslant(P^2-h^2)^{\frac{1}{2}}=L/2,$

$h\leqslant w+h\leqslant P,$

[14] E. W. Hobson, *The Theory of Spherical and Ellipsoidal Harmonics* (The Cambridge University Press, New York, 1931).

[15] W. W. Hansen and L. I. Schiff, "Theoretical study of electromagnetic waves scattered from shaped metal surfaces," Quarterly Report No. 3 (Microwave Laboratory, Department of Physics, Stanford University, May, 1948).

and

$$\alpha = \arccos(h/P).$$

Direct use of Eq. (2-5) (integrating once exactly and once by parts) implies that the contributions from the tip of the ogive and from the shadow rim are of the same order of magnitude. However, Hansen and Schiff, who obtained a similar result in their work on the spindle (see reference 15), showed by a more careful consideration of the contribution of the shadow rim that, in fact, the contribution of the shadow rim (or rather, the penumbra) is of a smaller order of magnitude than that of the point and that the "correct" answer can be obtained by merely evaluating the integral at the "tip." By applying an analysis similar to Hansen and Schiff's penumbra analysis to the ogive problem, i.e., ignoring the contribution from the shadow rim, it is found that $\sigma(0)$ for the ogive is given by

$$\sigma(0) = \frac{\lambda^2 \tan^4\alpha}{16\pi}, \quad b_0^{-\frac{1}{2}} < \alpha < \frac{\pi}{2} - b_0^{-\frac{1}{2}}, \qquad (3\text{-}4)$$

where $b = b(\beta) = kp(1+\cos\beta)$, and $b_0 = b(0)$. It should be pointed out that this result agrees with the electromagnetic theory answer for a semi-infinite cone having either a large cone-angle or a small cone-angle (see references 3 and 4).

Assuming that the tip will also dominate for most of the values of $\beta$ of interest (i.e., for $0 \leqslant \beta < \pi - 2\alpha - |\beta_0(\lambda)|$ where $\beta_0(\lambda) \to 0$ as $\lambda \to 0$) as it did for $\beta = 0$ and using an approach similar to that employed in obtaining (3-4) the tip formula for the ogive becomes

$$\sigma_{\mathbf{a}=\mathbf{i}_y}(\beta) = \frac{\lambda^2 \tan^4\alpha [1 - \tan^2\alpha \tan^2(\beta/2)]^{-3}}{16\pi \cos^3(\beta/2)}, \qquad (3\text{-}5)$$

with $0 \leqslant \beta < \pi - 2\alpha$. The application of the D.S.P. theorem yields

$$\sigma_{\mathbf{a}=\mathbf{i}_y}(\beta) = \frac{\pi L^2 [\sin(\beta/2) - \cos\alpha]}{4 \sin^2\alpha \sin(\beta/2)}, \quad \pi - 2\alpha < \beta < \pi. \qquad (3\text{-}6)$$

$\sigma(\beta)$ was evaluated on analog equipment for the case defined by $\alpha = 15°$ and $\pi d/\lambda = 100$. The nature of the integrand made it difficult to obtain reliable results over the entire range in $\beta$; however, fairly reliable results were obtained in the interval $\pi/2 < \beta \leqslant \pi$.

In summary, $\sigma_{\mathbf{a}=\mathbf{i}_y}(\beta)$ for the ogive has been determined by

(1) the "tip" method of determination

$$(0 \leqslant \beta < \pi - 2\alpha - |\beta_0(\lambda)|),$$

(2) the analog evaluation (reliable for $\beta > \pi/2$), and
(3) the D.S.P. method (valid for $\pi - 2\alpha < \beta < \pi$).

Examination of these results indicates that if a single curve were to be fitted through these data, it would follow the tip formula almost up to the $\pi - 2\alpha$ value of $\beta$ and then follow the trend indicated by the analog evaluations and the D.S.P. result. The analog evaluations and the D.S.P. result are in close agreement in the range $155° \leqslant \beta \leqslant 175°$ for the case considered on analog. A graphical representation of these results appears in Fig. 5.

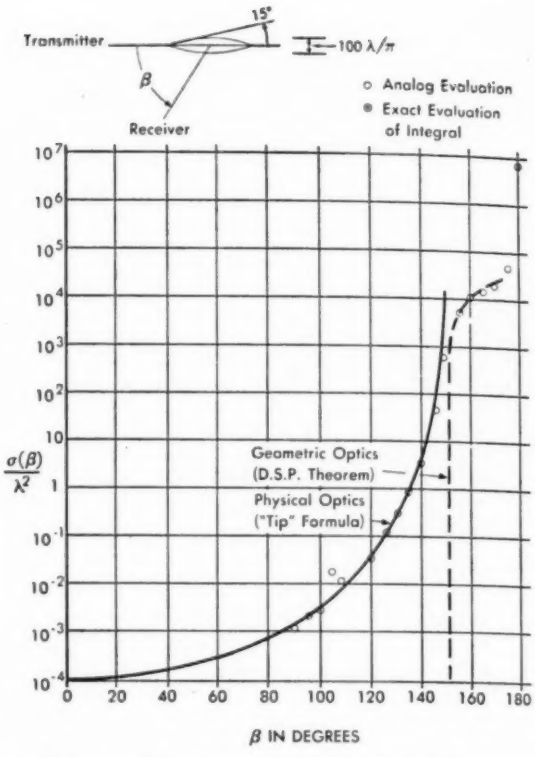


FIG. 5. Cross section of an ogive of half-angle 15° and maximum diameter equal to $100\lambda/\pi$.

### 3.4. The Paraboloid

Although the method given in Section 2 is based in part upon the assumption that the surface involved is finite, the application of Eq. (2-5) to the paraboloid defined by

$$x^2 + y^2 = -4Pz$$

yields an infinite integral which can be evaluated exactly. The method yields the formula,

$$\sigma_{\mathbf{a}=\mathbf{i}_y}(\beta) = 16\pi P^2/(1+\cos\beta)^2 = 4\pi P^2 \sec^4(\beta/2). \qquad (3\text{-}7)$$

Because of the relative simplicity of this formula, no graphical representation is given. It is shown (see reference 13) that (3-7) gives the *exact* cross section for axially symmetric scattering from a paraboloid of revolution.

### 3.5. The Semi-Infinite Cone

If the method of Section 2 is applied formally (the assumptions upon which Eq. (2-3) are based involve assuming that the body is finite in size and does not contain a point), and the integral involved is evaluated

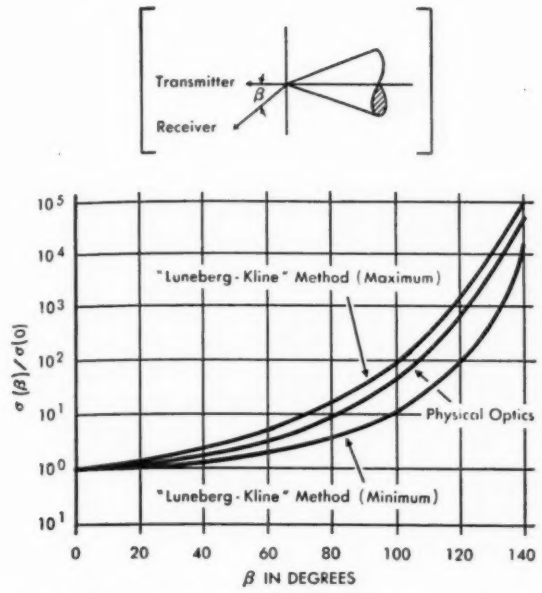


FIG. 6. Cross section of a semi-infinite cone of half-angle 15°.

with the aid of an Abelian limit process, the following formula for a semi-infinite cone is obtained:

$$\sigma(\beta)=\frac{\lambda^2\tan^4\gamma}{16\pi}\cdot\frac{2(1+\cos2\gamma)^3}{(1+\cos\beta)(\cos\beta+\cos2\gamma)^3} \tag{3-8}$$

where $\gamma=\frac{1}{2}$ cone-angle and $0\leqslant\beta<\pi-2\gamma$.

The Luneberg-Kline method cannot legitimately be applied to the cone problem, since the radius of curvature at the nose of the cone is zero. However, if the method is applied formally, the expression obtained has Eq. (3-8) as its first term. The "Luneberg-Kline answer" agrees with the intuitive expectation that the cross section should be a maximum in the plane of electric polarization. Also, the cross section obtained by the formal application of the Luneberg-Kline method increases as a function of the separation between transmitter and receiver (transmitter on the cone axis) in the expected fashion.

The formula obtained by this method is

$$\sigma(\beta)=\frac{\lambda^2\tan^4\gamma}{16\pi}\frac{2(1+\cos2\gamma)}{(1+\cos\beta)(\cos2\gamma+\cos\beta)}\times\left[\left(\frac{1+\cos2\gamma}{\cos2\gamma+\cos\beta}\right)^2+2\left(\frac{1+\cos2\gamma}{\cos2\gamma+\cos\beta}\right)\times\left(\frac{1-\cos\beta}{1+\cos\beta}\right)\cos2\phi+\left(\frac{1-\cos\beta}{1+\cos\beta}\right)^2\right] \tag{3-9}$$

where $\phi$ is the angle between the plane of polarization of the incident field, and the plane containing the axis of the cone and the receiver.

For backscattering, $\beta=0$, this reduces to

$$\sigma(0)=\lambda^2\tan^4\gamma/16\pi, \tag{3-10}$$

which is just the well-known physical-optics result for backscattering. It has previously been shown in reference 3, that the physical-optics answer agrees with the exact backscattering answer both for large cone angles and for small cone angles.

From Eq. (3-9) it can be seen that the maximum cross section is obtained when $\phi=0$ and $\phi=\pi$, while the minimum cross section is obtained for $\phi=\pi/2$ and $\phi=3\pi/2$. The physical-optics bistatic cross section of a semi-infinite cone, given above in Eq. (3-8), is independent of $\phi$. Since (3-9) is not independent of $\phi$ it is clear that the two solutions do not agree exactly. Examination of (3-8) and (3-9)†† however, shows that the physical-optics answer agrees very well with the answer obtained by the use of the Luneberg-Kline method and that it lies approximately halfway between the maximum and minimum "Luneberg-Kline" curves. This is shown in Fig. 6.

### 3.6. The Elliptic Cylinder

Consider an elliptic cylinder with semimajor axis $a$ and semiminor axis $b$ oriented with respect to the transmitter and the receiver as shown in Fig. 7. The angular positions of the transmitter and receiver are designated by $\theta_t$, $\phi_t$ and $\theta_r$, $\phi_r$ respectively.

By definition, the radar cross section is given by

$$\sigma=4\pi[|F_x|^2+|F_y|^2+|F_z|^2]$$

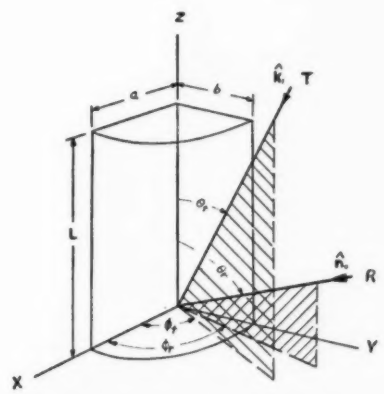


FIG. 7. Geometry for the elliptic cylinder.

†† *Note added in proof.*—Felsen (Report No. R-362-54, PIB-296, Microwave Research Institute of Brooklyn) has obtained the exact answer for small angle cones. His result agrees with Eq. (3-8) but not with Eq. (3-9) when the transmitter is on the cone axis. This is in agreement with a conjecture made by Siegel (see reference 2) that physical optics give the correct vector cross section for infinite bodies with an axis of symmetry in the direction of Poynting's vector.

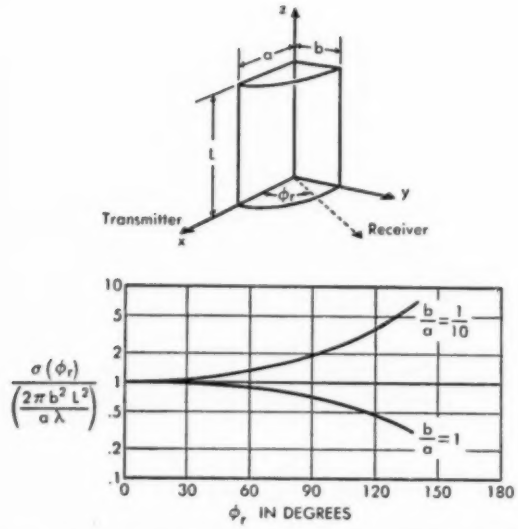


FIG. 8. Bistatic cross section of an elliptic cylinder for the case of transmitter and receiver in a plane perpendicular to the axis of the cylinder.

where

$$\mathbf{F}(\theta_t,\theta_r,\phi_t,\phi_r) = \frac{-ik}{2\pi}(\mathbf{n}_0\cdot\mathbf{a}) \int_{\substack{\text{illuminated}\\ \text{portion of}\\ \text{the surface}}} \exp[ik\mathbf{r}\cdot(\mathbf{k}+\mathbf{n}_0)]\mathbf{n}\,ds + \frac{ika}{2\pi} \int_{\substack{\text{illuminated}\\ \text{portion of}\\ \text{the surface}}} \exp[ik\mathbf{r}\cdot(\mathbf{k}+\mathbf{n}_0)](\mathbf{n}_0\cdot\mathbf{n})\,ds,$$

and all the other parameters are as defined in Section 2. The problem of finding the cross section is the problem of evaluating the integrals. This evaluation can be accomplished most simply in elliptic cylindrical coordinates $(\xi,\eta,z)$.

Integrating with respect to $z$ first and then by the method of stationary phase, we obtain

$$\sigma(\theta_r,\theta_t,\phi_r,\phi_t)=\frac{a^2b^2\lambda\,|e^{ikDL}-1|^2}{\pi D^2[(Aa)^2+(Bb)^2]^{\frac{1}{2}}}\{G_1^2+G_2^2+G_3^2\}, \tag{3-11}$$

where

$$G_1=A(a_y\sin\theta_r\sin\phi_r+a_z\cos\theta_r)-B(a_x\sin\theta_r\sin\phi_r),$$

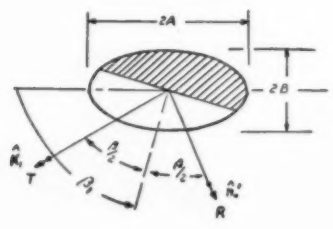


FIG. 9. Geometry for the prolate spheroid.

$$G_2=a_z\sin\theta_r(A\cos\phi_r+B\sin\phi_r),$$

$$G_3=B(a_x\sin\theta_r\cos\phi_r+a_z\cos\theta_r)-A(a_y\sin\theta_r\cos\phi_r),$$

$$A=\sin\theta_t\cos\phi_t+\sin\theta_r\cos\phi_r,$$

$$B=\sin\theta_t\sin\phi_t+\sin\theta_r\sin\phi_r,$$

and

$$D=\cos\theta_t+\cos\theta_r.$$

Figure 8 is a plot of the above relationship for the special case defined by $\theta_r=\theta_t=\pi/2$ and $\phi_t=0$. For the special case of backscattering in which $\phi_t=\phi_r=\phi$ and $\theta_t=\theta_r=\theta$ (3-11) becomes

$$\sigma(\theta,\phi)=\frac{a^2b^2\lambda\,|e^{ikDL}-1|^2\sin^4\theta}{\cos^2\theta[(Aa)^2+(Bb)^2]^{\frac{1}{2}}}. \tag{3-12}$$

### 3.7. The Prolate and Oblate Spheroids for Particular Choices of Transmitter and Receiver Directions

In Section 3.1 the bistatic cross section of a prolate spheroid was determined for the case in which the transmitter is located on the axis of symmetry. In this

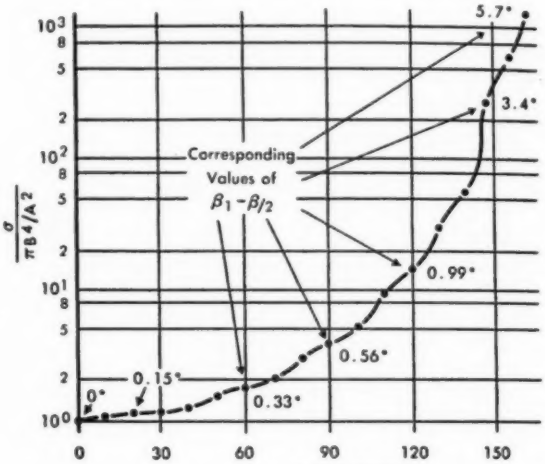


FIG. 10. Bistatic cross section of a prolate spheroid ($kA=25$ and $kB=2.5$).

section it will be shown that for each transmitter position (not necessarily on the symmetry axis) there is one particular receiver direction (or two when use is made of reciprocity) for which the current-distribution integral can be evaluated exactly, both for a prolate and an oblate spheroid.

The geometry used in this evaluation is shown in Fig. 9. The axis of the spheroid, $\mathbf{n}_0'$ and $\mathbf{k}_1$ all lie in the same plane and the angle between the axis and the normal to the phase planes is $\beta_1$. The angular separation between the transmitter, $T$, and the receiver, $R$, is $\beta$.

If $S$ is the surface, $S^*$ is a second surface bounded by the shadow curve, and $V$ is the volume contained

between $S$ and $S^*$, then the integral over the surface $S$, which one obtains in applying the current-distribution method, may be expressed as a sum of an integral over $V$ and an integral over $S^*$. For a spheroid, $S^*$ can always be chosen as the interior of an ellipse so that the second integral is easy to evaluate. If $S^*$ lies in a phase plane, the first integral is also easy to evaluate. This case is the particular case for which the cross-section integrals can be evaluated exactly.

Carrying out this method of approach yields

$$\sigma=\frac{\pi A^2B^4}{\rho_0^4}\left[1-2\frac{\sin(2M)}{2M}+\frac{\sin^2(M)}{M^2}\right] \tag{3-13}$$

where

$$M=k\rho_0\cos(\beta/2), \quad \text{and} \quad \rho_0^2=A^2\cos^2\beta_1+B^2\sin^2\beta_1.$$

Equation (3-13) applies only when the shadow curve lies in a phase plane. This condition is satisfied when

$$\tan(\beta/2)=\frac{A^2-B^2}{\rho_0^2}\sin\beta_1\cos\beta_1.$$

TABLE I. Other approximate monostatic cross-section formulas.

| Surface | Orientation of surface and radar | Cross section | Code to symbols |
|---|---|---|---|
| Torus | Direction of propagation is parallel to the axis of the torus | $\sigma=8\pi^3R_1^2R_2\lambda^{-1}$ | $R_1$ = distance to center of ring. $R_2$ = radius of ring. |
| Flat plate | Direction of propagation is normal to surface | $\sigma=4\pi W^2H^2\lambda^{-2}$ | $W$ = width of plate. $H$ = height of plate. |
| Large disk | Angle between direction of propagation and normal to disk given by $\theta$ | $\sigma=\frac{4\pi}{\lambda^2}\left[\frac{2\pi a^2\cos\theta J_1(x)}{x}\right]^2$ | $a$ = radius of disk. $x=\frac{4\pi a}{\lambda}\sin\theta$ |

The maximum separation between transmitter and receiver which is obtainable is given by

$$\tan(\beta/2)=\frac{A^2-B^2}{2AB} \quad \text{and} \quad \tan(\beta_1)=A/B.$$

These results are illustrated in Fig. 10 for the special case given by $kB=2.5$ and $kA=25$.

The method used in this section could also be applied to other quadric surfaces. For example, special cases could be integrated exactly for an ellipsoid having three nonequal axes.

### 3.8. $\sigma(\beta)$ for Other Surfaces

The methods discussed on the preceding pages may be applied to a variety of other surfaces. Tables I and II contain formulas which are readily obtainable upon the application of these techniques.

TABLE II. Other approximate bistatic cross-section formulas. (Geometry is as shown in Fig. 2.)

| Surface | Equation of surface | $\sigma_{\mathbf{a}}=i_v(\beta)$ |
|---|---|---|
| Ellipsoid | $\frac{x^2}{A^2}+\frac{y^2}{B^2}+\frac{z^2}{C^2}=1$ | $\frac{4\pi A^2B^2}{C^2}\left[(1+\cos\beta)+\frac{B^2}{C^2}(1-\cos\beta)\right]^{-2}$ $\beta<\pi$ |
| One branch of hyperboloid of two sheets | $z=-C\left[1+\frac{x^2}{A^2}+\frac{y^2}{B^2}\right]^{\frac{1}{2}}$ | $\frac{4\pi A^2B^2}{C^2}\left[(1+\cos\beta)-\frac{B^2}{C^2}(1-\cos\beta)\right]^{-2}$ $\beta<2\arctan(B/C)$ |
| Elliptic paraboloid (axis of symmetry is $z$-axis) | $\frac{x^2}{A^2}+\frac{y^2}{B^2}=-\frac{z}{C}$ | $\frac{\pi A^2B^2}{C^2(1+\cos\beta)^2}$ |
| Elliptic paraboloid (axis of symmetry is $y$-axis) | $\frac{x^2}{A^2}+\frac{z^2}{C^2}=+\frac{y}{B}$ | $\frac{\pi A^2C^2}{B^2(1-\cos\beta)^2}$ $\beta>0$ |

## 4. CONCLUSION

Bistatic radar cross sections have been obtained for simple shapes by optics approximations. It would be desirable to be able to compare these results with experiment. Unfortunately, very little experimental data exist. With these data absent one must examine the results in the light of previous experience. Considering the diffraction of electromagnetic waves through an aperture, it is well known that optics results for many applications yield poor approximations. On the other hand the nose-on radar cross section of a cone obtained by the optics approximation is in close agreement with, and possibly identical to, the exact solution for large and small cone angles (see references 3 and 4) and the cross section of the paraboloid for axially symmetric incident radiation is found exactly by an optics approximation. In the next paper evidence is given for the use of physical-optics approximations for general infinite bodies of revolution.

The results found in this paper should only be considered useful when the wavelength is small with respect to the major dimensions of the body. Questions as to the order of magnitude of the error must be deferred until more experimental results or further exact solutions have been obtained.

# Electromagnetic and Acoustic Scattering by a Semi-Infinite Body of Revolution

CRAIGE E. SCHENSTED
*Willow Run Research Center, University of Michigan, Ann Arbor, Michigan*
(Received April 9, 1954)

The first two terms of Kline's asymptotic expansion are obtained for the scattering of a plane wave incident along the axis of a perfectly reflecting semi-infinite body of revolution. When this method is applied to the paraboloid the *exact* electromagnetic solution is obtained in closed form. The accuracy of the method of physical optics is studied by using the asymptotic expansion.

MORRIS Kline has given an asymptotic solution to hyperbolic partial differential equations valid for short wavelengths.[1] This method can be readily applied to the scattering by perfectly reflecting bodies when there are no "shadow" regions present. In this paper the first two terms of this expansion are obtained for the scattering of a plane wave incident along the axis of a perfectly reflecting semi-infinite body of revolution. The first term of this expansion corresponds to geometric-optics, while the second term gives the deviation from geometric-optics when the wavelength is sufficiently small compared to the minimum radius of curvature of the body.

When the body is taken to be a paraboloid, the exact electromagnetic solution is given (in closed form) by the first term of the expansion.

At the end of the paper the asymptotic solution is compared with the result given by the current-distribution method[2] and its acoustic counterpart.

A brief resume of Kline's method, as it applies to the problem being considered, will be given here. The solution is given in terms of the function $S(x,y,z)$ which is defined so that $S(x,y,z)=\text{const}$ is a surface of constant phase in the geometric-optics approximation and so that $(\nabla S)^2=1$. The form of the asymptotic solution (in the electromagnetic and acoustic cases respectively) is

$$\mathbf{E}=\sum_{n=0}^{\infty}\lambda^n\mathbf{E}_n e^{i(kS-\omega t)}, \quad U=\sum_{n=0}^{\infty}\lambda^n U_n e^{i(kS-\omega t)}. \tag{1}$$

Here $\mathbf{E}$ is the electric field, $U$ is the velocity potential, $\lambda$ is the wavelength, $k=2\pi/\lambda$, and $\omega=kc$ where $c$ is the velocity of light. The wave equation then gives the following equations for $\mathbf{E}_n$ and $U_n$

$$\begin{aligned}\frac{\partial\mathbf{E}_n}{\partial S}+\tfrac{1}{2}\mathbf{E}_n\nabla\cdot\mathbf{s}&=\frac{i}{4\pi}\nabla^2\mathbf{E}_{n-1},\\ \frac{\partial U_n}{\partial S}+\tfrac{1}{2}U_n\nabla\cdot\mathbf{s}&=\frac{i}{4\pi}\nabla^2U_{n-1},\end{aligned} \tag{2}$$

where $\mathbf{s}=\nabla S$ and $\partial/\partial S\equiv\mathbf{s}\cdot\nabla$ (lower-case, boldface is used to denote a unit vector). For the electromagnetic problem the requirement that the divergence of the electric field vanish gives the additional equation

$$\mathbf{s}\cdot\mathbf{E}_n=\frac{i}{2\pi}\nabla\cdot\mathbf{E}_{n-1}. \tag{3}$$

In addition to the above equations, the following boundary conditions must be satisfied on the surface of the scatterer:

$$\mathbf{n}\times\mathbf{E}_n=0,$$

$$U_n=\frac{i}{2\pi}\frac{\mathbf{n}\cdot\nabla U_{n-1}}{\mathbf{n}\cdot\mathbf{s}}, \tag{4}$$

where $\mathbf{n}$ is the unit normal to the surface.

Along the rays incident on the scatterer, $\mathbf{E}_0$ and $U_0$ are taken to represent the incident fields; while all the other $\mathbf{E}_n$ and $U_n$ are taken to be zero. The initial values of $\mathbf{E}_n$ and $U_n$ on the reflected rays are obtained from (3) and (4). $\mathbf{E}_n$ and $U_n$ can then be obtained by integrating the ordinary differential equations given by (2). One component of $\mathbf{E}_n$ can be obtained more readily by (3).

The actual determination of $\mathbf{E}_n$ and $U_n$ from the

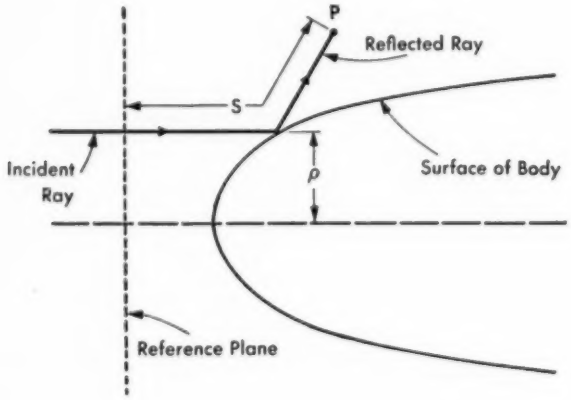


S is the distance along a ray to any point P from some reference plane.

ρ is the distance from the axis of the body at which the ray hits the body.

ϕ is a rotational angle about the axis of the body.

FIG. 1. Coordinate system used in calculations.

[1] Morris Kline, Commun. Pure Appl. Math. 4, 225–262 (1951).
[2] Samuel Silver, *Microwave Antenna Theory and Design* (McGraw-Hill Book Company, Inc., New York, 1949) p. 144.

above relations can be very cumbersome. A useful labor-saving device is the introduction of the coordinate system as shown in Fig. 1.

It may be seen that there are two sets of coordinates for each point because both an incident ray and a reflected ray go through each point. These two coordinate systems are used in the calculation of the incident and reflected fields, respectively.

The equation of the body can be taken to be $S=f(\rho)$ in either coordinate system. If an $x,y,z$ coordinate system is introduced with the $z$-axis along the body axis and the $x,y$-plane as the reference plane then (for the coordinate system after reflection)

$$\begin{aligned} x&=\rho\cos\phi+\frac{2f^{(1)}}{(f^{(1)})^2+1}(S-f)\cos\phi,\\ y&=\rho\sin\phi+\frac{2f^{(1)}}{(f^{(1)})^2+1}(S-f)\sin\phi,\\ z&=f+\frac{(f^{(1)})^2-1}{(f^{(1)})^2+1}(S-f), \end{aligned} \tag{5}$$

where $(f^{(n)})^m$ is the $m$th power of the $n$th derivative. The relationship between the two sets of unit vectors is

$$\begin{aligned} \mathbf{s}&=\frac{2f^{(1)}}{(f^{(1)})^2+1}\cos\phi\mathbf{i}+\frac{2f^{(1)}}{(f^{(1)})^2+1}\sin\phi\mathbf{j}+\frac{(f^{(1)})^2-1}{(f^{(1)})^2+1}\mathbf{k},\\ \boldsymbol{\varrho}&=-\frac{(f^{(1)})^2-1}{(f^{(1)})^2+1}\cos\phi\mathbf{i}-\frac{(f^{(1)})^2-1}{(f^{(1)})^2+1}\sin\phi\mathbf{j}+\frac{2f^{(1)}}{(f^{(1)})^2+1}\mathbf{k},\\ \boldsymbol{\phi}&=-\sin\phi\mathbf{i}+\cos\phi\mathbf{j}. \end{aligned} \tag{6}$$

The differential operators required in the calculation of $\mathbf{E}_n$ and $U_n$ can be expressed in terms of the $S$, $\rho$, $\phi$, coordinate system in the usual way by making use of (5). It turns out that the coordinate system is orthogonal. The final results are most easily expressed in terms of the metric coefficients

$$\begin{aligned} h_S&=1,\\ h_\rho&=1+\frac{2f^{(2)}}{(f^{(1)})^2+1}(S-f),\\ h_\phi&=\rho+\frac{2f^{(1)}}{(f^{(1)})^2+1}(S-f). \end{aligned} \tag{7}$$

For simplicity, only the case in which there is no multiple reflection will be obtained here. There would be no essentially new features introduced by the removal of this restriction, but the results would be much more complicated.

The calculations outlined above have been carried through for the incident fields $\mathbf{E}_i=\mathbf{i}e^{i(kS-\omega t)}$ and $U_i=e^{i(kS-\omega t)}$. The results are

$$\mathbf{E}_0=\left(\frac{\rho}{h_\rho h_\phi}\right)^{\frac{1}{2}}(-\cos\phi\boldsymbol{\varrho}+\sin\phi\boldsymbol{\phi}),$$

$$U_0=\left(\frac{\rho}{h_\rho h_\phi}\right)^{\frac{1}{2}},$$

$$\begin{aligned} \mathbf{E}_1=\frac{i}{2\pi}\left(\frac{\rho}{h_\rho h_\phi}\right)^{\frac{1}{2}}\Bigg\{&\Bigg[\left(\frac{1}{8\rho^2}-\frac{f^{(1)}f^{(3)}}{h_\rho((f^{(1)})^2+1)}\right)\\ &\times\frac{1}{2f^{(2)}}(1-h_\rho^{-1})+\frac{2f^{(3)}+\rho f^{(4)}}{16\rho(f^{(2)})^2}(1-h_\rho^{-1})^2\\ &-\frac{1}{16\rho f^{(1)}}-\frac{5(f^{(3)})^2}{48(f^{(2)})^3}(1-h_\rho^{-1})^3\Bigg]((f^{(1)})^2+1)\\ &\times(\cos\phi\boldsymbol{\varrho}-\sin\phi\boldsymbol{\phi})+\Bigg[\frac{f^{(2)}}{2}\left(1+\frac{(f^{(1)})^2-1}{(f^{(1)})^2+1}\frac{1}{h_\rho}\right)\\ &-\frac{f^{(1)}}{2\rho}(1-h_\rho^{-1})-\frac{(5(f^{(1)2})+1)(3(f^{(1)})^2-1)}{16f^{(1)}((f^{(1)})^2+1)h_\phi}\Bigg]\\ &\times\cos\phi\boldsymbol{\varrho}+\Bigg[\frac{f^{(2)}}{2}(1-h_\rho^{-1})-\frac{f^{(1)}}{2\rho}(1+h_\rho^{-1})\\ &+\frac{15(f^{(1)})^2-1}{16f^{(1)}h_\phi}\Bigg]\sin\phi\boldsymbol{\phi}+\Bigg[\frac{f^{(3)}}{2f^{(2)}h_\rho}(1-h_\rho^{-1})\\ &-\left(\frac{1}{2\rho}+\frac{f^{(1)}f^{(2)}}{(f^{(1)})^2+1}\right)\frac{1}{h_\rho}+\frac{3(f^{(1)})^2+1}{2((f^{(1)})^2+1)h_\phi}\Bigg]\cos\phi\mathbf{s}\Bigg\}, \end{aligned}$$

$$\begin{aligned} U_1=-\frac{i}{2\pi}\left(\frac{\rho}{h_\rho h_\phi}\right)^{\frac{1}{2}}\Bigg\{&\left(\frac{(f^{(1)})^2+1}{16\rho^2f^{(2)}}-\frac{f^{(1)}f^{(3)}}{2f^{(2)}h_\rho}\right)(1-h_\rho^{-1})\\ &+\frac{f^{(1)}+\rho f^{(2)}}{2\rho}(1+h_\rho^{-1})+\Bigg[\frac{1}{f^{(1)}h_\phi}-\frac{1}{\rho f^{(1)}}\\ &+\frac{2f^{(3)}+\rho f^{(4)}}{\rho(f^{(2)})^2}(1-h_\rho^{-1})^2\\ &-\frac{5(f^{(3)})^2}{3(f^{(2)})^3}(1-h_\rho^{-1})^3\Bigg]\frac{(f^{(1)})^2+1}{16}\Bigg\}. \end{aligned} \tag{8}$$

A particularly simple result is obtained on applying these formulas to the paraboloid $f=\rho^2/2R$ ($R$ is the radius of curvature at the nose of the paraboloid). In this case

$$\begin{aligned} \mathbf{E}_0&=\frac{\rho^2+R^2}{2R(S+R/2)}(-\cos\phi\boldsymbol{\varrho}+\sin\phi\boldsymbol{\phi}),\\ U_0&=\frac{\rho^2+R^2}{2R(S+R/2)},\\ \mathbf{E}_1&=0,\\ U_1&=-\frac{i}{2\pi R}\frac{\rho^2+R^2}{2R(S+R/2)}\left[1+\frac{\rho^2+R^2}{2R(S+R/2)}\right]. \end{aligned} \tag{9}$$

Since $\mathbf{E}_1 \equiv 0$, it follows from (2), (3), and (4) that $\mathbf{E}_n \equiv 0$ $(n \neq 0)$. Thus, in this case, the asymptotic expansion contains only a single term. Since the field given by this one term satisfies the wave equation, the divergence condition, the boundary condition, and the radiation condition,* the exact solution to the scattering problem has been obtained in closed form.†

For the acoustic problem the exact solution has been obtained in closed form by Horton and Karal.[3] The scattered field is

$$U_S = e^{i(kS-\omega t)} \frac{e^{-ikQ}[-si(kQ)+iCi(kQ)]}{2/kR - e^{-ikR}[-si(kR)+iCi(kR)]}, \quad (10)$$

where $Q \equiv R^2(R+2S)/(\rho^2+R^2)$ and $si$ and $Ci$ are the sine and cosine integrals

$$si(x) = -\int_x^\infty \frac{\sin t}{t}\,dt; \quad Ci(x) = -\int_x^\infty \frac{\cos t}{t}\,dt.$$

It is easily verified that the two terms of Eq. (8) are just the first two terms of the asymptotic expansion of (10).

If $\beta = 2\cos^{-1} R/(\rho^2+R^2)^{\frac{1}{2}}$ (the angle between the axis and the direction to the field point) then the differential scattering cross section is

$$\sigma_V = \frac{R^2}{4\cos^4(\beta/2)} \quad (11)$$

in the vector (electromagnetic) case and

$$\sigma_S = \frac{R^2}{4\cos^4(\beta/2)} \frac{1}{g(kR)}, \quad (12)$$

where

$$g(x) = (2 + x\cos x\, si(x) - x\sin x\, Ci(x))^2 + (x\sin x\, si(x) + x\cos x\, Ci(x))^2$$

in the scalar (acoustic) case. The factor $g(x)$ varies monotonically from $\frac{1}{4}$ for $x=0$ to 1 for $x=\infty$.

It is interesting to compare the asymptotic expansion given in (8) with the physical-optics (current-distribution) approximation. The physical-optics method is based on the following exact expression for the scattered fields[4]

$$\mathbf{E}_S = \frac{1}{4\pi}\int [ik(\mathbf{n}\times\mathbf{H}) - (\mathbf{n}\cdot\mathbf{E})\nabla]\frac{e^{ikr}}{r}\,dS,$$
$$U_S = \frac{1}{4\pi}\int U\mathbf{n}\cdot\nabla\frac{e^{ikr}}{r}\,dS, \quad (13)$$

where the integration is carried out over the scattering surface and $r$ is the distance between the integration and field points. The physical optics method consists of replacing the fields inside the integrals by their geometric-optics approximation. In the electromagnetic case this corresponds to using the geometric-optics approximations for the current and charge distributions on the scattering surface. If the incident fields are those assumed above, then the physical-optics approximations for the back-scattered fields at large distances from the body are

$$\mathbf{E}_S \approx \mathbf{i}\frac{i}{\lambda}\frac{e^{i(kS-\omega t)}}{S}\int_0^\infty e^{2ikz}A^{(1)}(z)\,dz,$$
$$U_S \approx -\frac{i}{\lambda}\frac{e^{i(kS-\omega t)}}{S}\int_0^\infty e^{2ikz}A^{(1)}(z)\,dz, \quad (14)$$

where $A(z)$ is the cross-sectional area of the body. If $A(z)$ is given by $A(z) = \pi\rho^2 = \pi a_1 z + \pi a_2 z^2 + \cdots$ then (14) takes the form

$$\mathbf{E}_S \approx -\mathbf{i}\frac{e^{i(kS-\omega t)}}{S}\left(\frac{a_1}{4} + i\lambda\frac{a_2}{8\pi} + \cdots\right),$$
$$U_S \approx \frac{e^{i(kS-\omega t)}}{S}\left(\frac{a_1}{4} + i\lambda\frac{a_2}{8\pi} + \cdots\right). \quad (15)$$

The corresponding expressions obtained from (8) are

$$\mathbf{E}_S \approx -\mathbf{i}\frac{e^{i(kS-\omega t)}}{S}\left(\frac{a_1}{4} + i\lambda\frac{a_2}{8\pi} + \cdots\right),$$
$$U_S \approx \frac{e^{i(kS-\omega t)}}{S}\left(\frac{a_1}{4} + i\lambda\frac{a_2-2}{8\pi} + \cdots\right). \quad (16)$$

From (15) and (16) it can be seen that, asymptotically, physical optics represents an improvement on geometric-optics in the electromagnetic case unless $a_2 = 0$. In the acoustic case physical optics gives an improvement on geometric-optics unless $|a_2 - 2| \leq 2$, but the improvement is not as great as it is in the electromagnetic case.

The above analysis lends support to the conjecture put forth by Siegel[5] that physical optics would give the exact electromagnetic back-scattering cross section for the type of problem under consideration in this paper.

* Since the paraboloid is of infinite dimensions the usual radiation condition must be modified. Peters and Stoker [Commun. Pure Appl. Math. **7**, 565 (1954)] have suggested that the field be required to have a decomposition $\mathbf{E} = \mathbf{A} + \mathbf{B}$ where $\mathbf{A}$ is specified in some definite way (they suggest letting $\mathbf{A}$ be the geometric-optics solution) and $\mathbf{B}$ is to satisfy the radiation condition. For the scattering of a plane wave incident along the axis of a perfectly conducting paraboloid we get $\mathbf{B} \equiv 0$. M. Lelchter (private communication) has shown that the uniqueness proof of Peters and Stoker can be extended so as to include this problem.

† By requiring that $\mathbf{E}_1$ or $U_1$ is zero on the scattering surface, it is found that geometric-optics can only give the exact solution in case (for a plane wave incident along the axis of a body of revolution) $f^{(1)}/\rho[f^{(1)} - \rho f^{(2)}/(f^{(1)})^2 + 1] = 0$ in the electromagnetic case or $f^{(1)} + \rho f^{(2)}/\rho = 0$ in the acoustic case. The general solutions of these two equations are $f = A + B\rho^2$ and $f = A + B\ln\rho$ where $A$ and $B$ are arbitrary constants. $B = 0$ gives an infinite plane in both cases. The general surface in the electromagnetic case is a paraboloid. The general surface in the acoustic case allows multiple reflections and the validity of geometric optics has not been tested for it.

[3] C. W. Horton and F. C. Karal, J. Acoust. Soc. Am. **22**, 855 (1950).

[4] J. A. Stratton, *Electromagnetic Theory* (McGraw-Hill Book Company, Inc., New York, 1941), pp. 460–466.

[5] K. M. Siegel, *Far Zone Assumptions Put to Use, Symposium on Microwave Optics* (Eaton Electronics Laboratory, McGill University, Montreal, Canada, June, 1953).

# Electromagnetic and Acoustical Scattering from a Semi-Infinite Cone*

K. M. SIEGEL, J. W. CRISPIN, AND C. E. SCHENSTED
*Willow Run Research Center, University of Michigan, Ypsilanti, Michigan*
(Received February 12, 1954)

The value of the nose-on back scattering cross section of a semi-infinite cone is determined by the exact methods of electromagnetic and acoustical theory, and by physical optics. It is shown that, to the degree of approximation used, the electromagnetic value and the physical-optics value are equal. The acoustical value is found to be less than the electromagnetic value by a factor which depends only on the cone angle; both are proportional to the square of the wavelength. It is shown that the electromagnetic and physical-optics answers agree with experimental data to within a factor of two. The electromagnetic theory results obtained hold for the cases in which the half-cone angle is close either to 0 or to $\pi/2$.

## 1. INTRODUCTION

IN order to determine the radar cross section, $\sigma$, of an object of specified shape and size, it is necessary to solve the vector equations $(\nabla^2+k^2)\mathbf{E}=0$ and $\nabla\cdot\mathbf{E}=0$, subject to vector boundary conditions. The radar cross section of a sphere was obtained forty-six years ago by Mie; since that time, radar cross sections have been obtained for a small number of other bodies. The results obtained in the consideration of one additional body, the semi-infinite cone, are discussed in this paper.

A number of approximations to this solution are possible in specific cases. When the wavelength is large with respect to the characteristic dimension of the scatterer, the Rayleigh approximation is valid. If the wavelength is small with respect to the characteristic dimension of the scatterer, the methods of physical optics are applicable. In the limit of vanishing wavelength, the simple methods of geometric optics are applicable. For the case of the semi-infinite cone, the characteristic dimension which can be associated with the object is infinite and this leads one to believe, since a finite wavelength is always small with respect to the characteristic dimension, that the physical-optics approximation is quite accurate for all finite wavelengths. This indeed turns out to be the case. In this paper it is shown that the physical-optics approximation, computed by the current distribution method, is virtually identical with the exact value of the nose-on cross section obtained from the vector equation for the cases in which the half-cone angle is close to zero or $\pi/2$. In fact, the agreement between these two determinations of $\sigma$ is better than the agreement between the exact solution and the best experimental measurements, although the agreement between theory and experiment is quite good.

In addition, it might appear that geometric optics would be applicable. However, since the principle cross section contribution is due to scattering from the tip, geometric optics yields no information because it predicts a cross section of zero.

The acoustical theory solution, in which a scalar equation is substituted for the vector equation, is often useful. In this paper the electromagnetic nose-on cross section is shown to be greater than the acoustic nose-on cross section by a factor which is independent of wavelength. The factor varies from *four* for a half-cone angle of approximately 0° to *unity* for a half-cone angle of approximately 90°.

This paper makes extensive use of the works of Spencer,[1] Hansen,[2] Hansen and Schiff,[3–5] and Sletten.[6] Without their individual work, whole sections of this paper would not appear. If their collective work had not appeared, the basis of this paper would not exist.

## 2. ANALYTIC EXPRESSIONS FOR THE CROSS SECTION

Before turning to the problem of obtaining numerical evaluations for the scattering cross section for a cone, a few general comments on the nature of the analytic solution, and the method by which this solution is made to yield numerical results, are in order. The basic geometry involved is shown in Fig. 1.

Hansen and Schiff, using a method due to Hansen, have obtained a solution for the semi-infinite cone problem for electromagnetic scattering, and have obtained an expression for axially symmetric backscattering from the cone.[5]

In the acoustical case, Carslaw[7] considered a boundary value problem differing from the one involved here in that the point source was located at a finite distance

* This paper is a portion of the report UMM-92: Siegel, Alperin, Crispin, Hunter, Kleinman, Orthwein, and Schensted, "Studies in radar cross-sections IV: Comparison between theory and experiment of the cross-section of a cone," Willow Run Research Center, University of Michigan, February, 1953.

[1] R. C. Spencer, Air Force Cambridge Research Laboratories, Report CRL-E5070, April 1951.
[2] W. W. Hansen, Microwave Laboratory, Stanford University, Quarterly Report No. 1, Contract W28-099-333, November 1947.
[3] W. W. Hansen and L. I. Schiff, Microwave Laboratory, Stanford University, Quarterly Report No. 2, Contract W28-099-333, February 1948.
[4] W. W. Hansen and L. I. Schiff, Microwave Laboratory, Stanford University, Quarterly Report No. 3, Contract W28-099-333, May 1948.
[5] W. W. Hansen and L. I. Schiff, Microwave Laboratory, Stanford University, Quarterly Report No. 4 (Final Report), Contract W28-099-333, September 1948.
[6] C. J. Sletten, Cambridge Research Center, Report CRC-E5090, July 1952.
[7] H. S. Carslaw, Math. Ann. **LXXV**, 1914.

from the cone. It can be shown[8] that by moving Carslaw's point source out to a point a very great distance from the scatterer, Carslaw's solution is transformed into the solution to the acoustical boundary value problem of interest in this paper.

In attempting to obtain numerical results from these analytic solutions to the boundary value problems, the electromagnetic and the acoustic, a difficulty arises, due to the fact, when the observation point is at a large distance from the tip of the cone, the series converge very slowly. In fact, if only the early terms of these series are investigated (by using the asymptotic form of the Bessel functions involved, the form which is valid when the argument is much greater than the order), the series appear to diverge. However, it can be demonstrated that these series are absolutely convergent, and so this difficulty can be circumvented by means of an appropriate summation technique, one which will improve the rapidity of the convergence and which will guarantee that only the early terms in the transformed series contribute to the numerical result.

Thus, in the expressions appearing below for $\sigma'(0)$, which is used to denote the nose-on radar cross section for the electromagnetic case, and for $\sigma(0)$, which is used to denote the nose-on radar cross section in the acoustic case, no upper limit is shown on the sums involved. This is done to indicate that only a finite number of terms have the form shown, and that the value of the sum is to be obtained by use of a summation technique. The summation method chosen for use in this paper is due to Euler.[9]

Examination of the results of Hansen and Schiff in the light of the above comments yields

$$\sigma'(0)=\frac{\lambda^2}{4\pi}\left|\sum_{i=0}\frac{n_i(n_i+1)e^{j\pi n_i}}{B_{n_i}}-\frac{m_i(m_i+1)e^{j\pi m_i}}{B_{m_i}}\right|^2, \quad (1)$$

where

$\lambda$ = the wavelength,

$n_i$ = the non-negative roots of the equation

$$P_{n_i}^1(x_0)=0.$$

$m_i$ = the non-negative roots of the equation

$$dP_{m_i}^1(x_0)/dx=0,$$

$$B_{n_i}=\int_{x_0}^1[P_{n_i}^1(x)]^2dx,$$

$$B_{m_i}=\int_{x_0}^1[P_{m_i}^1(x)]^2dx,$$

$x_0=-\cos\theta_1$, and

$\theta_1$ = half-cone angle $=\pi-\theta_0$.

[8] K. M. Siegel, H. A. Alperin, Willow Run Research Center, University of Michigan, Report UMM-87, January 1952.

[9] T. J. Bromwich, *An Introduction to the Theory of Infinite Series* (Macmillan and Company, Ltd., London, England, 1947).

A similar consideration of the acoustic case yields the following formula for the nose-on radar cross section (sound case):

$$\sigma(0)=\frac{\lambda^2}{\pi}\left|\sum_{i=0}\frac{n_i(n_i+1)e^{j\pi n_i}}{B_{n_i}}\right|^2. \quad (2)$$

Again no upper limit is shown on the sum appearing in Eq. (2) to indicate that only a finite number of terms in the sum has the indicated form, and that a summation process is to be used.

It is of interest to note that the sum in $\sigma'(0)$ can be expressed in the form of an integral, since by so doing we find that the sum is real. First rewrite Eq. (1) in the form

$$\sigma'(0)=\lim_{\alpha\to 0}\frac{\lambda^2}{4\pi}\left|\sum_{i=0}\left\{\frac{n_i(n_i+1)}{B_{n_i}}e^{j\pi n_i-\alpha(n_i+\frac{1}{2})}-\frac{m_i(m_i+1)}{B_{m_i}}e^{j\pi m_i-\alpha(m_i+\frac{1}{2})}\right\}\right|^2. \quad (3)$$

(It is known that this method always yields the same answer as the summation method employed whenever the latter method gives a finite answer.)

Expressing the $B_{n_i}$ and the $B_{m_i}$ in their expanded forms,[10] it can be observed that the resulting sum in Eq. (3) is the sum of the residues of the function

$$f_\alpha(z)=\frac{z(z+1)(2z+1)\exp[j\pi z-\alpha(z+\frac{1}{2})]}{(x_0^2-1)\dfrac{dP_z^1(x_0)}{dx}P_z^1(x_0)} \quad (4)$$

at the poles of the function where $\mathrm{Re}(z)>0$. Thus, if the contour shown in Fig. 2 is used, the sum in Eq. (3) can be shown to be equal to

$$-\left.\frac{e^{-\alpha/2}(x_0^2-1)^{-1}}{\dfrac{d^2P_z^1(x_0)}{dxdz}\dfrac{dP_z^1(x_0)}{dz}}\right|_{z=0}+\lim_{R\to\infty}\frac{1}{2\pi j}\int_{CR}f_\alpha(z)sd. \quad (5)$$

In the limit as $\alpha\to 0$, the expression in Eq. (5) then

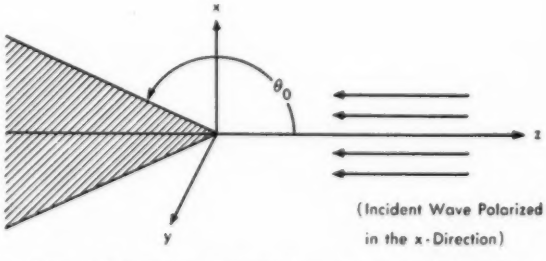


FIG. 1. Geometry of scattering from an infinite cone.

[10] Siegel, Crispin, Kleinman, and Hunter, J. Math. Phys. XXXI, No. 3 (October 1952).

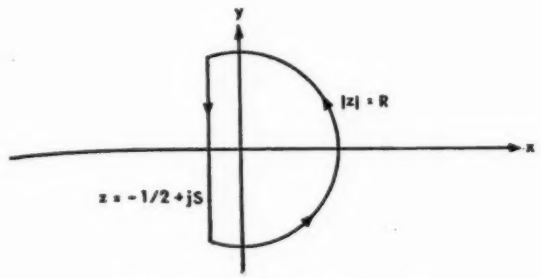


FIG. 2. The contour of integration.

reduces to

$$-\frac{1+x_0}{1-x_0}+\frac{1}{2\pi}\int_0^\infty \frac{S(4S^2+1)\sinh(\pi S)dS}{\dfrac{dK_S(x_0)}{dx}\left[x_0\dfrac{dK_S(x_0)}{dx}+(S^2+\tfrac{1}{4})K_S(x_0)\right]}, \tag{6}$$

where $K_S^m(x)=P^m_{-\frac{1}{2}+jS}(x)$. *Since the $K_S$ appearing in Eq. (6) is real, it follows that the sum appearing in Eq. (1) is real.*

### 3. THE NUMERICAL DETERMINATION OF $\sigma'(0)$ AND $\sigma(0)$

In order to effect the evaluation of the expressions given in Eqs. (1) and (2) for the nose-on vector cross section $\sigma'(0)$ and the nose-on scalar cross section $\sigma(0)$, the series are subjected to the Euler transformation

$$\sum_{n=1}^{\infty} v_n=\frac{1}{1-y}\left[v_1+\sum_{n=1}^{\infty}(v_{n+1}-yv_n)\right], \quad (y\neq 1). \tag{7}$$

The procedure is roughly the same for cones of small angle ($\theta_1\sim 0$) as it is for cones of large angle ($\theta_1\sim\pi/2$). First a formula is selected for the Legendre function which is appropriate to the range of $\theta_1$ which is of interest. For the small angle case, an appropriate formula is the following[11]:

$$P_\nu(-\cos\theta_1)=\frac{\sin\nu\pi}{\pi}\sum_{S=0}^{\infty}\frac{(-)^S\Gamma(\nu+1+S)}{(S!)^2\Gamma(\nu+1-S)}\times[\ln\delta+\psi(\nu+S)+\psi(\nu-S)-2\psi(S)]\delta^S+\cos\nu\pi\sum_{S=0}^{\infty}\frac{(-)^S\Gamma(\nu+1+S)}{(S!)^2\Gamma(\nu+1-S)}\delta^S, \tag{8}$$

where

$$\delta=\frac{1-\cos\theta_1}{2} \quad \text{and} \quad \psi(x)=\frac{d}{dx}[\ln\{\Gamma(x+1)\}].$$

For the large angle case the following expression is suitable[12]:

$$P_\nu^1(-\cos\theta_1)=\frac{2\cos\left(\frac{\nu+1}{2}\pi\right)\Gamma\left(\frac{\nu+2}{2}\right)}{(\pi)^{\frac{1}{2}}\Gamma\left(\frac{\nu+1}{2}\right)}(1-\epsilon^2)^{\frac{1}{2}}\times{}_2F_1\left(\frac{\nu+2}{2},\frac{1-\nu}{2};\frac{1}{2};\epsilon^2\right)-\frac{4\sin\left(\frac{\nu+1}{2}\pi\right)\Gamma\left(\frac{\nu+3}{2}\right)}{(\pi)^{\frac{1}{2}}\Gamma\left(\frac{\nu}{2}\right)}\epsilon(1-\epsilon)^{\frac{1}{2}}\times{}_2F_1\left(\frac{\nu+3}{2},\frac{2-\nu}{2};\frac{3}{2};\epsilon^2\right), \tag{9}$$

where $\epsilon=\cos\theta_1$.

The next step is to obtain $n_i$ and $m_i$ as expansions in $\delta$ (when $\theta_1\sim 0$) or $\epsilon$ (when $\theta_1\sim\pi/2$). To do this, one first observes that when $\theta_1\sim 0$, $n_i$ and $m_i$ are both approximately equal to $i$; and when $\theta_1\sim\pi/2$, $m_i$ is approximately equal to $2i$, while $m_i$ is approximately equal to $(2i-1)$. The small difference between the true values of $n_i$ or $m_i$ and the corresponding approximate values can then be easily expanded in terms of $\delta$ or $\epsilon$.

Once the expressions for $n_i$ and $m_i$ have been obtained, the terms of the cross-section series can be evaluated (as expansions in $\delta$ or $\epsilon$). It now remains only to sum the series. If the transformation given in Eq. (7) is applied $N$ times, the result is

$$\sum_{n=1}^{\infty} v_n=\sum_{m=0}^{N-1}\left(\frac{y}{1-y}\right)^{m+1}\Delta^m\left(\frac{v_n}{y^n}\right)_{n=1}+\left(\frac{y}{y-1}\right)^N\sum_{n=1}^{\infty}y^n\Delta^N\left(\frac{v_n}{y^n}\right). \tag{10}$$

The choice of $y$ determines the rapidity of convergence of the transformed series. In order to choose $y$ properly, it is necessary to make a brief investigation of the properties of the terms of the series. For a very large $i$, the difference between successive zeros becomes

$$n_{i+1}-n_i\approx m_{i+1}-m_i\approx\pi/(\pi-\theta_1).$$

Furthermore, the magnitudes of the terms of the series become approximately proportional to $i$. Thus, if $y$ is chosen to be $\exp[\pi^2 j/(\pi-\theta_1)]$, the magnitude of

$$\Delta^N\left(\frac{n_i(n_i+1)e^{j\pi n_i}}{B_{n_i}\exp\{j\pi^2 i/(\pi-\theta_i)\}}\right),$$

[11] S. A. Schelkunoff, *Electromagnetic Waves* (D. Van Nostrand Company, Inc., New York, 1943).

[12] W. Magnus and F. Oberhettinger, *Formulas and Theorems for the Special Functions of Mathematical Physics* (Chelsea Publishing Company, New York, 1949).

which appears in the transformed series, will decrease rapidly with an increase in either $N$ or $i$ (as long as $N \geqslant 2$). Clearly the same applies to the $m_i$ series.

Due to the large amount of algebra involved, the expansions of the cross section as a function of $\delta$ or $\epsilon$ were cut off after the second nonvanishing term. It was then found possible to perform all of the necessary summations exactly. The final expressions for the cross section are

$$\sigma'(0)=\frac{\lambda^2\delta^2}{\pi}[1+6\delta+\cdots] \tag{11}$$

in the small angle case and

$$\sigma'(0)=\frac{\lambda^2}{16\pi\epsilon^4}[1-2\epsilon^2+\cdots] \tag{12}$$

in the large angle case. For the scalar case

$$\sigma(0)=\frac{\lambda^2\delta^2}{4\pi}\left[1+\left(4\ln\frac{1}{\delta}-2\right)\delta+\cdots\right] \tag{13}$$

in the small angle case and

$$\sigma(0)=\frac{\lambda^2}{16\pi\epsilon^4}[1-4\epsilon^2+\cdots] \tag{14}$$

in the large angle case.

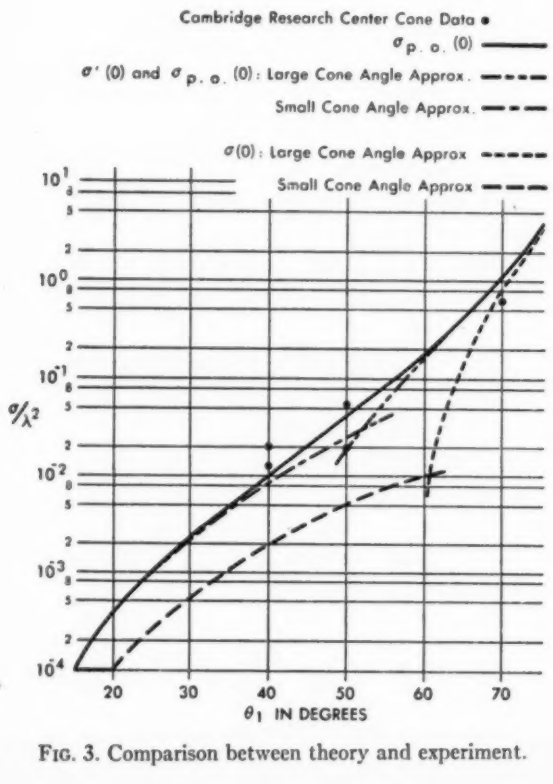


FIG. 3. Comparison between theory and experiment.

It is interesting to compare the above expressions with the tip-scattering formula of physical optics† since we have a closed expression for the latter, namely

$$\sigma_{p.o.}(0)=\frac{\lambda^2}{16\pi}\tan^4\theta_1 =\frac{\lambda^2\delta^2}{\pi}[1+6\delta+25\delta^2+\cdots] \tag{15}$$

in the small angle case, and

$$\sigma_{p.o.}(0)=\frac{\lambda^2}{16\pi}\tan^4\theta_1 =\frac{\lambda^2}{16\pi\epsilon^4}[1-2\epsilon^2+\epsilon^4] \tag{16}$$

in the large angle case. *To the order to which the cross sections have been expanded, there is complete agreement between electromagnetic theory and physical optics for both large and small cone angles.* The sound scattering cross section agrees closely with this common value for large cone angles, but is smaller by a factor of 4 for small cone angles.

If the values of the parameters $n_i$, $m_i$, $B_{ni}$, and $B_{mi}$ are known, the transformation given in Eq. (10) could be applied directly to Eqs. (1) and (2). An approximation method for the determination of these parameters was developed at the Willow Run Research Center, and the process was applied to the special case of $\theta_1=15°$.[10,13] The Institute of Numerical Analysis (I.N.A.) of the University of California at Los Angeles, has also considered the problem of determining the first and third parameters, and has found them to a much greater degree of precision than can be obtained from the approximate techniques discussed in references 10 and 13.

If the I.N.A. values of the parameters are used when $\theta_1=15°$, one obtains

$$\sigma(0)/\lambda^2=2.69\times10^{-5}. \tag{17}$$

Since the summation process is extremely sensitive to the first few values of these parameters, we recommend usage of numerical values of the "zeros" with the type accuracy attained by the I.N.A.

The "small cone angle" evaluation, Eq. (13) yields

$$\sigma(0)/\lambda^2=2.87\times10^{-5} \tag{18}$$

for $\theta_1=15°$, and this value and the "I.N.A. value" are certainly consistent with one another.

† This "tip-scattering" formula is quite well known, and a derivation of it appears in reference 8.

[13] Siegel, Crispin, Kleinman, and Hunter, J. Math. Phys. XXXII, Nos. 2-3 (July–October, 1953).

### 4. CONCLUSION

The exact nose-on radar cross section of a semi-infinite cone has been evaluated. The excellent agreement between physical optics, exact electromagnetic theory, and experiment is displayed in Fig. 3.

Examination of Fig. 3 shows that the theoretical values of $\sigma'(0)$ and $\sigma_{p.o.}(0)$ agree with the experimental values for a cone to within a factor of two. The comparison between scalar theory and electromagnetic theory is also seen to be good.

If $\sigma_{p.o.}(0)$ is computed up to the degree of approximation used in finding $\sigma'(0)$, there is complete agreement between $\sigma_{p.o.}(0)$ and $\sigma'(0)$. This complete agreement between the approximate determinations of $\sigma_{p.o.}(0)$ and $\sigma'(0)$ and their close agreement with the *exact* value of $\sigma_{p.o.}(0)$ *may* imply that the *exact* value of $\sigma'(0)$ is identically equal to the physical-optics value of

$$\sigma_{p.o.}(0)=\lambda^2 \tan^4\theta_1/16\pi.$$

It should be emphasized that many more experiments should be made in this field. The amount of experimental information on the cone and other bodies, such as the ogive, the prolate spheroid, and the paraboloid, is very small indeed. It is hoped that more experimenters will enter this field and help fill the gaps in classical electromagnetic theory.

---

JOURNAL OF APPLIED PHYSICS VOLUME 26, NUMBER 3 MARCH, 1955

# Techniques for Nuclear Magnetic Resonance Measurements on Granular Hygroscopic Materials

T. M. SHAW AND R. H. ELSKEN
*Western Utilization Research Branch, Agricultural Research Service, United States Department of Agriculture, Albany 10, California*

(Received April 26, 1954)

An investigation was made of the effects of nonuniformity in the magnetic fields and in the test specimens employed in the measurement of nuclear magnetic resonance absorption. Particular attention was given to the determination of relative integrated line intensity from derivative maxima independently of the uniformity of concentration of the subject nuclei through the available sample volume. The principal objective was to devise techniques applicable to granular hygroscopic materials. A technique applicable for the low-moisture range was tested for materials containing 7 to 16 percent water and found to be satisfactory.

### INTRODUCTION

IN previous reports,[1,2] experiments were presented to show that magnetic resonance absorption due to hydrogen nuclei can be used for the rapid, nondestructive measurement of the moisture content of solids. As noted earlier,[3,4] a serious limitation to the precision of the method is associated with lack of uniformity in the test specimens, which in most cases are composed of small particles. The basic cause for difficulty with materials of this type is the fact that the magnetic fields utilized in the absorption measurements are not uniform. The experiments reported herein were undertaken to explore the extent of these limitations and to develop satisfactory procedures for use in the determination of moisture in typical hygroscopic solids.

### THEORY

The magnetic resonance method is essentially a spectroscopic method, and the nature of the test specimen is an important factor which must be considered in setting up an analytical procedure and in the interpretation of results.

As will be shown in the following, uniform materials such as gases and liquids present no particular difficulties, and relatively simple standardized procedures can be employed to obtain precise quantitative results. The situation with solids, however, is complex. Typical specimens of solids may be in any one of a wide variety of forms ranging from a single piece to a group of particles of various sizes and shapes.

The essential problem in quantitative analysis by means of the methods of nuclear magnetism is, of course, to relate the magnitude of the measured quantity or "signal" to the number of magnetic nuclei of the type of interest in the sample.

Conventionally, the specimen forms the core of a short solenoid. Two possible arrangements of coil and specimen are shown in Fig. 1. A radio-frequency spectrometer[5] or an equivalent device furnishes a signal $D$ proportional to $\partial\chi''/\partial\nu$, the slope of the nuclear magnetic absorption curve. Curve *a*, Fig. 2, is a plot of $\chi''$, the imaginary component of the complex

[1] T. M. Shaw and R. H. Elsken, J. Chem. Phys. **18**, 1113 (1950).
[2] Shaw, Elsken, and Kunsman, Phys. Rev. **85**, 708A (1952).
[3] T. M. Shaw and R. H. Elsken, American Chemical Society Abs. 123rd Meeting, March 15, 1953, p. 1A.
[4] Shaw, Elsken, and Kunsman, J. Assoc. Offic. Agr. Chemists **36**, 1070 (1953).
[5] R. V. Pound and W. D. Knight, Rev. Sci. Instr. **21**, 219 (1950).

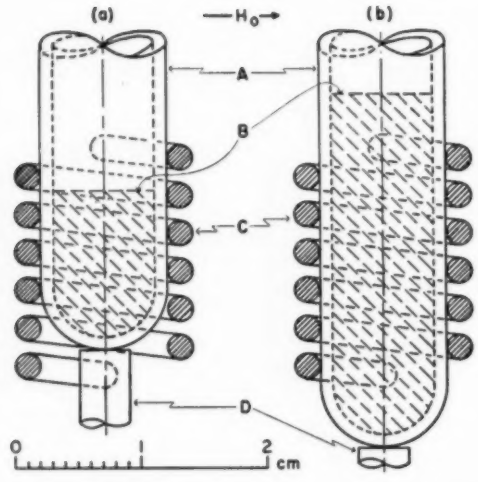


FIG. 1. Two possible arrangements of rf coil and sample; *a*, sample is contained entirely within coil; *b*, sample extends beyond coil boundary. The direction of the static magnetic field of magnitude $H_0$ is indicated. *A* is test tube, *B* is specimen, *C* is rf coil, and *D* is a stop.

nuclear susceptibility as a function of frequency $\nu$ and represents the variation of the magnetic absorption with frequency. Curve *b* is a plot of *D* as a function of frequeucy and represents the derivative signal, which is the type ordinarily obtained from high-sensitivity apparatus. It is with this type of signal that the following discussion is primarily concerned.

For the present purposes it will be assumed that the nuclei are exposed to a sufficiently weak radiofrequency field, that saturation effects are negligible, and that $\chi''$ can be expressed by the relation.[6]

$$\chi''=(\pi/2)\chi_0\nu_0 g(\nu). \tag{1}$$

In this equation $\nu_0$ is the frequency at the center of the resonance, $g(\nu)$ is a function which represents the experimentally observed shape of the absorption line as represented in (a) Fig. 2, and $\chi_0$ is given by the expression,

$$\chi_0=N_0\gamma^2\hbar^2I(I+1)/3kT. \tag{2}$$

Here $N_0$ is the number of magnetic nuclei of the species under observation per cubic centimeter of the substance, $\gamma$ is the magnetogyric ratio, $I$ is the nuclear spin, $k$ is the Boltzmann constant, and $T$ is the absolute temperature. We are concerned primarily with the absorption line derivative, (b), Fig. 2, and in particular with the quantity $D_{\max}$, which may be expressed,

$$D_{\max}\propto\zeta\left(\frac{\partial\chi''}{\partial\nu}\right)_{\max}=\zeta\frac{\pi}{2}\chi_0\nu_0\left[\frac{\partial g(\nu)}{\partial\nu}\right]_{\max}. \tag{3}$$

In this expression the quantity $\zeta$ is the filling factor for the coil which contains the specimen. $\zeta$ is defined as the fraction of the total rf energy of the circuit which is contained within the specimen. For a simple solenoid, the total rf energy $E_T$ is confined almost entirely within the volume $V_c$ of the coil. If the magnetic energy is uniformly distributed within the coil the amount of rf energy contained within the sample is proportional to $V$, the volume of the sample, equal to $m/\rho_0$, where $m$ and $\rho_0$ are the mass and density of the sample, respectively. In general, neither the magnetic energy nor the sample in the case of granular materials is uniformly distributed throughout the coil. For the coil and sample configuration shown in (a) Fig. 1, however, approximate calculations show the energy density throughout the space available to the sample varies by no more than $\pm10$ percent from the mean energy density $\epsilon$. Therefore, the errors in $\zeta$ because of rf field nonuniformity should be always somewhat less than 10 percent, provided the minimum amount of sample employed in the experiments is not less than about one-tenth of the total volume accessible to the sample. The experiments to be described later appear to support this conclusion.

Thus, for the coil and sample configuration shown in (a) Fig. 1, the filling factor $\zeta$ is equal to $(m/\rho_0)\epsilon/E_T$. When this relation is substituted in Eq. (3), one obtains the relation

$$D_{\max}\propto\frac{m}{\rho_0}\frac{\epsilon}{E_T}\frac{\pi}{2}\chi_0\nu_0\left[\frac{\partial g(\nu)}{\partial\nu}\right]_{\max}. \tag{4}$$

For the arrangement shown in (b) Fig. 1, the sample extends well beyond the ends of the coil. If the volume contained within the coil is to be used to calculate $\zeta$, then the sample must be distributed uniformly throughout the specimen container. To attain sufficiently uniform distribution for all types of granular materials, however, is difficult or impossible. Thus, the use of the arrangement shown in (b) Fig. 1 is limited for the most part to gases or liquids.

It is of interest now to consider how Eq. (4) is affected by the static magnetic field uniformity. Consider the hypothetical situation where the static magnetic field (of strength $H_0$) in which the nuclei are immersed is *perfectly uniform*. In this situation the experimentally observed shape function $g(\nu)$ is an intrinsic property of the material of which the specimen is composed. Thus, for the arrangement depicted in (a) Fig. 1 where the entire test specimen is contained within the part of the coil where the rf field is approximately uniform, it is clear from Eq. (4) that $D_{\max}$ will vary linearly with the mass of the sample and will be independent of the state of subdivision of the specimen. In this instance, $D_{\max}$ has satisfactory characteristics for use as a measure of magnetic absorption in quantitative analytical work.

Since a *perfectly uniform* magnetic field is not available, it is of interest to consider the application of Eq. (4) for fields of the type ordinarily used in magnetic resonance spectroscopy. When a specimen containing magnetic nuclei is placed in an inhomogeneous field,

[6] Bloembergen, Purcell, and Pound, Phys. Rev. **73**, 679 (1948).

the shape function $g(\nu)$ no longer represents an intrinsic property of the material being investigated. Rather, $g(\nu)$ includes, in addition, effects on the frequency distribution of the absorption owing to the fact that all nuclei in the specimen are not subjected to the same applied magnetic field. For a quantitative discussion, use may be made of the intrinsic line width of the resonance, $\Delta\nu$, and a line width, $\delta\nu=(\gamma/2\pi)\delta H$, equivalent to the inhomogeneity, $\delta H$, of the magnetic field over the sample space where $\gamma$ is the magnetogyric ratio of the nuclei under observation.

Now if the magnet inhomogeneity is small compared to the line width of the resonance ($\delta\nu \ll \Delta\nu$), the situation with respect to $D_{max}$ will be for all practical purposes the same as discussed above for a perfectly uniform field. To avoid complications owing to distortion of line shape, $\Delta\nu$ must always be greater than the modulation frequency.

If, however, $\delta\nu$ is not small compared to $\Delta\nu$, then $g(\nu)$ will be influenced by the magnet inhomogeneity and, in general, can be expected to vary with the volume occupied by the sample and with the position of the sample in the magnetic field. Because of the difficulty of making a correction to $g(\nu)$ for these effects, Eq. (4) is not satisfactory in this situation for correlating the magnetic absorption with the number of magnetic nuclei in the test specimen.

A solution to the difficulty is, of course, to determine the integrated or total magnetic absorption. This requires, however, a tedious graphical calculation of the total absorption from the derivative signal observed for the test specimen.[7] Because it has seemed desirable to avoid the additional complications introduced through use of the total absorption, experiments have been performed to determine if sufficiently homogeneous magnetic fields can be provided to justify the use of the quantity $D_{max}$ as a precise quantitative measure of the absorption.

## EXPERIMENTAL

The proton resonance was recorded by means of a radio-frequency (rf) spectrometer.[5] A magnetic field of 6380 gauss was provided by a permanent magnet with 6 inch diameter poles and a $1\frac{3}{4}$ inch gap. Sine-wave 50-cycle modulation was applied to coils mounted on the permanent magnet pole pieces. The rf coil was 10 mm inside diameter and 20 mm in length and was designed to accept standard Pyrex 10 × 75 mm test tubes which serve as containers for the test specimens.

The rf coil was placed in the magnet in a position close to the center of the pole pieces, where the most narrow proton-resonance line was observed for a 0.02$N$ aqueous solution of ferric nitrate. The coil was held fixed in this position throughout a series of tests. Stops were arranged so that the test tubes could be reproducibly positioned within the coil in the manner shown in Fig. 1.

In order to obtain a more uniform static-magnetic field over the region occupied by the specimen, small magnetic shims were placed in the air-gap in the vicinity of the rf coil. The shims were made of 0.001 in. nickel sheet. The size and position of the shims were determined empirically as guided by the appearance of the proton-resonance absorption line on an oscilloscope. The test specimen for the shimming operation was 0.3 ml of 0.02$N$ ferric nitrate solution. In the shimmed field the test specimen could be placed at various positions in the space available to the sample as indicated in (a) Fig. 1 with little or no change in the appearance of the proton-resonance absorption line on the oscilloscope.

## RESULTS AND DISCUSSION

Figure 3 shows derivative-type signals obtained for a dehydrated potato powder. This material is in the form of a fine powder and is typical of many of the solids encountered in moisture measurements. The line width and shape of the observed resonance line depend on the moisture content.

Figure 4 shows the results obtained for a potato powder containing about 11 percent water when the amount of the test specimen is varied. According to Eq. (4), $(D_{max}/m)$ should be independent of $m$, the mass of the specimen, provided the magnetic field is uniform over the space occupied by the specimen. Curve $b$ of Fig. 4 shows the results obtained with a field that does not satisfy this requirement. These results are to be explained as discussed earlier by effects of the magnet inhomogeneity on the shape function $g(\nu)$. The behavior shown is qualitatively in accord with an increase in the inhomogeneity of the magnetic field with increasing amount of specimen. By contrast, the results presented in curve $a$ of Fig. 4 for the shimmed magnetic field show that $(D_{max}/m)$ is independent of $m$, as is to be expected for constant $g(\nu)$. As a measure of the inhomogeneity of the shimmed field, the proton-resonance line width for a 1 ml sample

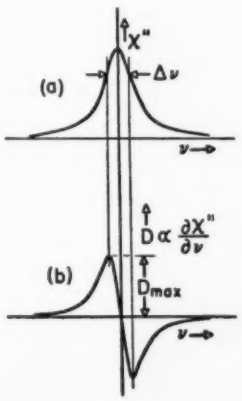


FIG. 2. Two types of signals utilized in nuclear magnetic resonance absorption spectroscopy are illustrated; $a$ shows the shape of the absorption signal; $b$ shows the shape of the derivative signal.

[7] The use of square-wave rather than sine-wave modulation offers the possibility of recording the total absorption directly. The authors, however, have not investigated this technique. An application of square-wave modulation is described by F. Reif and E. M. Purcell, Phys. Rev. **91**, 631 (1953).

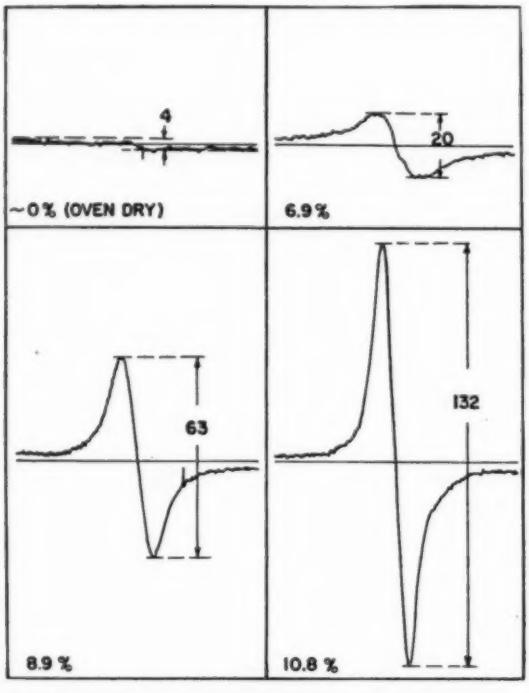


FIG. 3. Derivative-type signals observed for protons in water absorbed by dehydrated potato powders. The moisture content and the peak-to-peak amplitude of the curves are indicated. For a symmetrical absorption the peak-to-peak amplitude is numerically equal to 2 $D_{max}$.

of 0.02$N$ ferric nitrate was determined and found to be approximately 100 cycles. This value is about one-tenth of the intrinsic line width of the absorption line for the potato powder containing 11 percent water. The results shown in Fig. 4 for the shimmed magnet show that for a 5-fold variation in $m$ (0.1 to 0.5 gram), the ratio $(D_{max}/m)$ was constant to ±3 percent. This

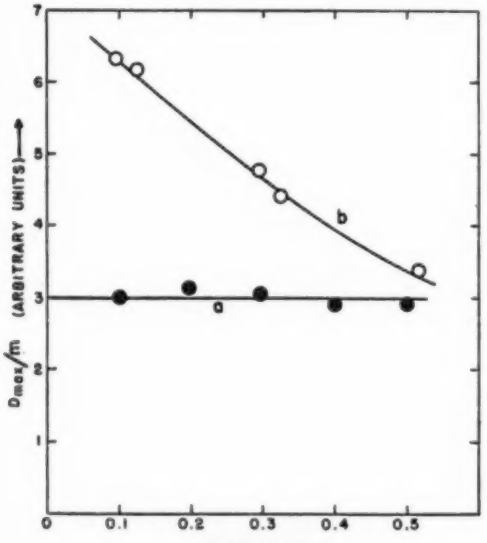


FIG. 4. Graphs to show dependence of $(D_{max}/m)$ on the amount of sample in the rf coil. Curve $a$ is for magnet with shims, and curve $b$ is for magnet without shims.

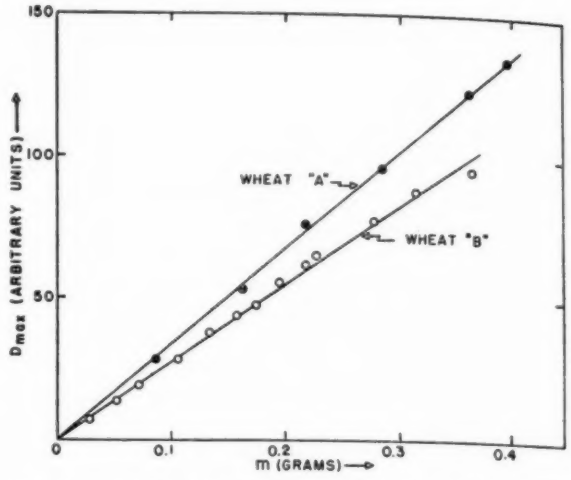


FIG. 5. Variation of $D_{max}$ with amount of sample in rf coil for two types of wheat containing approximately 11 percent water. Observations made in magnet equipped with shims.

variation is equivalent to an error in the moisture content of approximately ±0.3 percent. This may be assumed to be a maximum error because it is unlikely that in routine measurements the quantity of material in the test specimen would ordinarily vary by more than a factor of two.

As a further test of the performance of the shimmed magnetic field experiments were conducted with solids in which the test specimen consisted of only a small number of relatively large particles and where the effects of field inhomogeneities may be large. For these experiments wheat kernels were selected as a convenient source of coarse, irregular particles. Two types of

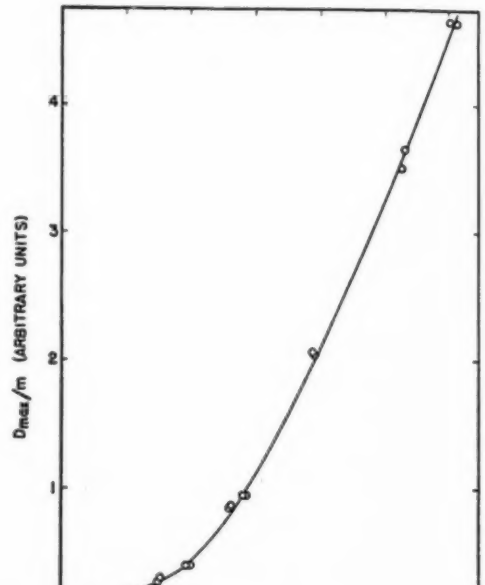


FIG. 6. Typical moisture calibration curve for dehydrated potatoes.

wheat were selected for the test. Wheat *A* consisted of rather large uniform kernels. Wheat *B* was composed of somewhat smaller and less uniform kernels. The moisture content in each case was roughly 11 percent. The results are shown in Fig. 5. The individual plotted points represent the contribution to the proton-resonance signal of the water contained in a single grain of wheat; under the conditions used to record the resonance the contribution of hydrogen nuclei in the solid constituents is negligible.[3,4] The experiment was performed by making a determination of $D_{max}$ and the weight of the filled cell, then repeating the process as the individual grains of wheat were removed. For both types of particle, $D_{max}$ is observed to vary linearly with the mass of wheat in the specimen container. The results show that the shimmed magnetic field over the region occupied by the sample is sufficiently uniform that $g(\nu)$ is effectively independent of the amount and arrangement of the wheat kernels in the test specimen. The line width of the proton resonance for wheat containing 11 percent water is about 1000 cycles.

Since the line width of the proton resonance decreases as the amount of water absorbed by hygroscopic solids increases, it is to be expected that the shimmed field will not be adequate at high moisture levels where the proton-resonance width becomes comparable with the magnet inhomogeneities. Tests on potato powders show however that satisfactory results were obtained at least up to 16 percent moisture. Typical results are shown in Fig. 6. The range of moisture for which data are shown is limited but is typical of the range over which analyses are required for many hygroscopic materials. The curve is a plot of the quantity $(D_{max}/m)$ as a function of the water content. The mass of sample in the rf coil $m$ varied from 0.4 to 0.5 gram for these measurements. The individual plotted points refer to separate samples and are generally consistent to within 0.1 percent moisture. The nonlinearity which is apparent at lower moisture contents has been discussed previously[4] and is attributed to an increase in the line width of the proton resonance of the absorbed water.[5]

A number of experiments similar to those discussed above for the 10 mm diameter rf coil have been undertaken for a larger (22 mm) rf coil. These experiments were initiated to provide for the use of larger and presumably more representative samples in analytical work. The experiments with the larger coil have been only partially successful, however, principally because of the difficulty of obtaining a sufficiently uniform static-magnetic field over the larger volume.

**ACKNOWLEDGMENT**

The authors wish to thank K. J. Palmer for helpful criticisms and suggestions.

[5] T. M. Shaw and R. H. Elsken, J. Chem. Phys. **21**, 565 (1953).

JOURNAL OF APPLIED PHYSICS VOLUME 26, NUMBER 3 MARCH, 1955

# Gap Problem in Antenna Theory

RONOLD KING
*Cruft Laboratory, Harvard University, Cambridge 38, Massachusetts*
(Received April 12, 1954)

The so-called gap problem in antenna theory is considered critically. It is shown that whereas there exist problems related to transmission-line end-effect and coupling between antenna and line, there is no gap, and hence no gap problem, when a physically realizable complete transmitting system is considered rather than an antenna with a fictitious mathematically convenient driving mechanism.

THE essential parts of a complete and practical transmitting circuit include an antenna, a transmission line, and a coil in which an emf is induced by an alternating impressed magnetic field maintained by a generator. Typical practical circuits involving conventional open-wire and coaxial lines are in Figs. 1 and 2. Note that both circuits from one end of the antenna along one conductor of the transmission line around the coupling coil, back along the other conductor of the line, and out to the other extremity of the antenna (which may be the distant edge of a ground screen or the opposite pole of a great sphere) provide *unbroken conducting paths*. If, in the interest of pedagogical simplicity, the transmission line is reduced to zero and the coupling coil is contracted to a short section of the antenna itself in which an emf is induced by a varying magnetic field, an idealized system is obtained which, in the physically unavailable limit in which the distance along the antenna where the inducing field is active is reduced to zero while the field is increased to maintain a given emf, is equivalent to a so-called delta function or slice generator. In this simple case, the radiating circuit, consisting of a single straight conductor, is *unbroken. Nowhere*, either in the practical systems with long transmission lines and extended coupling coils or in its idealized contraction is there a gap. Yet, in spite of the fact that in actual radiating systems *there are no gaps*, the so-called "problem of the gap" has been the subject

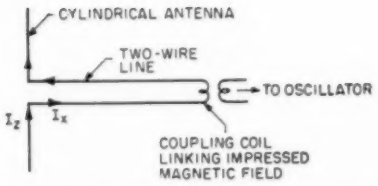


FIG. 1. Transmitting system with two-wire line.

of theoretical discussion.[1] Indeed, it has been asserted that the gap is "the essential part of the radiating system;" that it is "the only source of radiant energy."[2] Note that if this were true it would be necessary to conclude that none of the transmitters in practical operation could radiate ! It is interesting and instructive to study and attempt to clarify the confusions and misunderstandings that must underlie statements that are as positive as they are untenable.

The origin of the "gap problem" in the study of antennas—whether cylindrical, spheroidal, or biconical —is to be found in the attempt to analyze an antenna consisting, for example, of the two collinear conducting cylinders shown in Fig. 3 with adjacent flat ends separated a small distance $2\delta$, as if it constituted a complete transmitting system when a mathematically convenient electric field $E_z$ is postulated "across the gap." Actually, two essential components are missing. They are (1) the unbroken conducting path between the halves of the antenna, and (2), a localized induced emf along at least a part of the circuit. As soon as a transmitting system is completed in this manner, *the gap and, with it, the gap problem disappear.*

In the practical circuits of Figs. 1 and 2, where the conducting paths are conventional transmission lines and the driving emf is induced in a distant coil, the gap does not exist, there is no rotationally symmetrical exciting field $E_z$, and no currents arise from or vanish in the thin air of a gap. This is seen more clearly in Figs. 4 and 5 from which it is evident that the gap problem in Fig. 3 is replaced by precisely the *transmission-line problem* (including coupling and end effects) which has been analyzed.[3–5] Another type of circuit in which a gap is *apparently* retained is in Fig. 6. In this figure, the antenna consists of the same halves shown in Fig. 3, but the transmitting system is completed (note that Fig. 3 does not portray a complete transmitting system) in a theoretically possible, although physically unavailable, manner. The gap in Fig. 3 is bridged at its center by a thin, perfectly conducting wire in which an emf is induced. The presence of the wire and the generator *transforms the gap into a radial transmission line.*

Since the antenna is assumed to be perfectly conducting (or sufficiently highly conducting so that the skin depth is very small compared with the radius of the antenna), all currents are confined to a thin skin at the surface. Hence, radial sheets of surface current diverge from the center of the upper, converge to the center of the lower surface of the radial transmission line where it joins the vertical wire. Evidently, the determination of the electric field $E_z$ at the end $r=a$ of the transmission line where it has the cylindrical

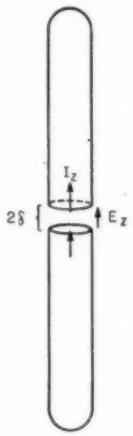


FIG. 3. Cylindrical antenna with gap, assumed field, and current.

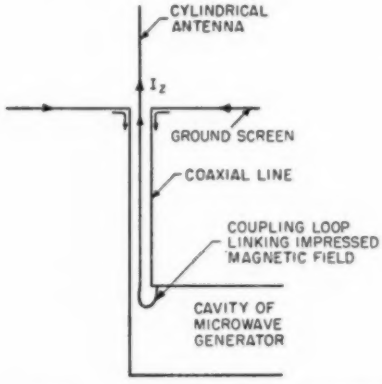


FIG. 2. Transmitting system with coaxial line.

antenna as its load, the definition of the voltage $V_\delta(r=a)$, and the evaluation of the current $I_\delta(r=a)$ in terms of the emf $V^e$ at $r=0$ are parts of a transmission-line problem that includes radial end-effects near $r=a$. Note that Fig. 6 differs from a simple antenna with external generator of delta-function type only in having the continuous conducting path at the center of the antenna reduced from a radius equal to that of the antenna to a vanishingly small value. This complicates the problem, on the one hand, by inserting a radial transmission line between the antenna and the localized emf; it simplifies it, on the other hand, by permitting the use of a cross-sectionally dimensionless delta-function generator instead of one distributed as a belt around the antenna.

[1] See, for example, L. Infeld, Quart. Appl. Math. **5**, 113–132, (1947).
[2] E. Albert and J. L. Synge, Quart. Appl. Math. **6**, 117–131 (1948).
[3] R. King, J. Appl. Phys. **20**, 832 (1949).
[4] R. King and K. Tomiyasu, Proc. Inst. Radio Engrs. **37**, 1134 (1949).
[5] R. King, Trans. Inst. Radio Engrs. AP-3, (April, 1955).

Instead of analyzing the circuit of Fig. 6, it is analytically more convenient and essentially equivalent to investigate the circuit shown in Fig. 7 where the radial transmission line is replaced by a biconical transmission line with a point-generator at its apex. This generator is mathematically attractive since it is equivalent to a singularity in the electric field. It may be approximated in practice by the arrangement in Fig. 8 where half of the cylindrical antenna is placed over a conducting ground screen and is driven from a conical transmission line. This, in turn, is connected at its apex to a coaxial transmission line of sufficiently small cross section so that the field at the outer end of the conical transmission line is the same as when driven by a point generator. For the present study of the "gap problem" the simpler circuit of Fig. 7 is more convenient. In this case, the driving voltage or emf of the delta-function generator is defined by

$$V^g = V(0) = \lim_{R\to 0} \int_{\pi-\theta_0}^{\theta_0} E_\theta(R) R d\theta. \tag{1}$$

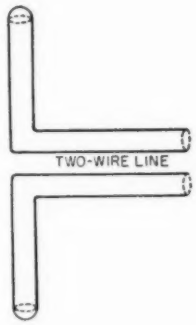


FIG. 4. Two-wire drive.

The current in the generator at the apex is $I(0)$, and the impedance of the biconical line with its end load is

$$Z_0 = V(0)/I(0). \tag{2}$$

As shown by Schelkunoff,[6] the total radial current $I_R(R)$ in the upper cone of the transmission line is given by

$$I_R(R) = I_d(R) + I_c(R), \tag{3}$$

where $I_d(R)$ is the dominant-mode current and $I_c(R)$ is the sum of the currents associated with the higher modes. These vanish identically at $R=0$ for all angles $\theta_0$ of the cone. The dominant-mode current is

$$I_d(R) = I(0)\cos\beta_0 R - jY_c V(0)\sin\beta_0 R, \tag{4}$$

where $Y_c = 1/Z_c$ is the characteristic admittance, and

$$Z_c \equiv \frac{\zeta_0}{\pi} \ln \cot \frac{\theta_0}{2} \tag{5}$$

is the characteristic impedance of the biconical transmission line. It can be shown that insofar as the current $I_d(0) = I_R(0)$ in the generator is concerned, the effect

[6] S. A. Schelkunoff, Proc. Inst. Radio Engrs. **29**, 493 (1941).

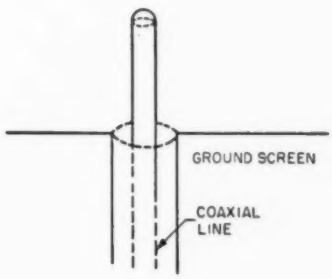


FIG. 5. Coaxial drive.

of the complementary currents in canceling all or part of the dominant-mode current may be simulated by ignoring the complementary currents and providing an apparent terminal admittance across the biconical line at $R=l$ of such value that the part of the current $I_R(l)$ which enters this terminal admittance is equal to the part canceled by the complementary currents. In the case of the thin biconical antenna with $\theta_0$ very small, the total current $I_R(l)$ is essentially zero so that virtually the entire dominant-mode current $I_d(l)$ is canceled by equal and opposite higher-mode currents since $I_d(l) \doteq -I_c(l)$. Hence, the complementary currents could be ignored only by providing an apparent dominant-mode terminal admittance $Y_{la}$ that carried the entire current $I_d(l)$. In the case at hand with $\theta_0$ near $\pi/2$ the situation is different since practically all of the dominant-mode current at $R=l$ becomes the axially directed surface current $I_z(z=\delta)$. When $\theta_0$ is sufficiently near $\pi/2$ the higher mode current $I_c(l)$ is very small and cancels an insignificant part of the dominant-mode current $I_d(l)$. Actually, the higher-mode current is responsible for transmission-line end-effects. Just as in the case of the two-wire line[3] these may be ignored in their effect on the current far from the load if an appropriate terminal-zone admittance is provided. Thus, the total *apparent* terminal admittance is given by

$$Y_{la} = Y_\delta + Y_T, \tag{6}$$

where $Y_\delta$ is the dominant-mode load impedance and $Y_T$ is the terminal-zone admittance that takes account of end-effect. With $\theta_0$ near $\pi/2$ it is essentially suscep-

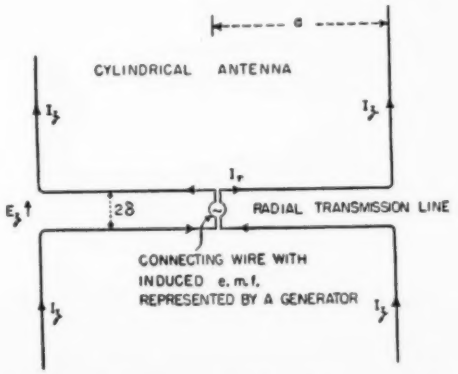


FIG. 6. Transmitting system with radial transmission line.

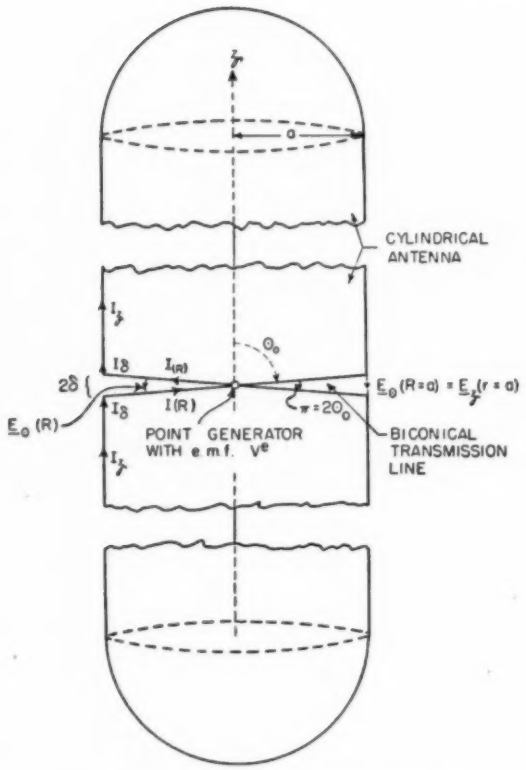


FIG. 7. Transmitting system with biconical line and point-generator.

tive, so that

$$Y_T \doteq j\omega C_T. \tag{7}$$

The load impedance $Z_\delta = 1/Y_\delta$ is defined by

$$Z_\delta \equiv \frac{V(l)}{I_\delta} = \frac{\int_{\theta_0}^{\pi-\theta_0} E_{d\theta}(l) l d\theta}{I_\delta}, \tag{8}$$

where $I_\delta$ is the radial current leaving the end of the upper conductor of the biconical line at $R=l \doteq a$ to become the axial surface current on the antenna. Since $E_{d\theta}(l)$ in (8) is the dominant-mode field in the biconical line where all currents are radial and, hence, perpendicular to the direction of $E_\theta$, it follows from the definition of the scalar potential by $-\text{grad}\,\phi = E + j\omega A$ that

$$E_{d\theta} = -\frac{1}{R}\frac{\partial \phi}{\partial \theta} - j\omega A_\theta \doteq -\frac{1}{R}\frac{\partial \phi}{\partial \theta}, \tag{9}$$

where $\phi$ is the scalar potential and $A_\theta$ a component of the vector potential. Substitution of (9) in (8) with $R=l$, gives

$$Z_\delta = \frac{V(l)}{I_\delta} = \frac{\int_{-\delta}^{\delta} d\phi}{I_\delta} = \frac{\phi(\delta)-\phi(-\delta)}{I_\delta}. \tag{10}$$

If the exterior field is expressed in terms of the current on the cylindrical antenna and matched to the internal field at $R=l \doteq a$, $\pi-\theta_0 \leq \theta \leq \theta_0$ or $-\delta \leq z \leq \delta$, the impedance (10) may be determined. A part of the exterior field is required to match the interior complementary field. This represents the terminal-zone coupling between antenna and biconical transmission line. The actual evaluation and matching of the interior and exterior fields is of no interest here.

The relation between the apparent load admittance $Y_{la}$ of the biconical transmission line and the driving-point admittance $Y_0$ is obtained from the well-known transmission-line formulas for the dominant-mode voltage and current. They are

$$V_d(l) = V(0)\cos\beta_0 l - jZ_c I(0)\sin\beta_0 l, \tag{11a}$$

and

$$I_d(l) = I(0)\cos\beta_0 l - Y_c V(0)\sin\beta_0 l. \tag{11b}$$

It follows that

$$Y_{la} = \frac{I_d(l)}{V_d(l)} = \frac{Y_0\cos\beta_0 l - jY_c\sin\beta_0 l}{\cos\beta_0 l - jZ_c Y_0\sin\beta_0 l}, \tag{12}$$

where

$$Y_0 \equiv I(0)/V(0) \tag{13}$$

is the driving-point admittance at the apex of the biconical line, and $Z_c = 1/Y_c$ is the characteristic impedance.

Up to the present, no restrictions have been placed on the length $l$ of the biconical transmission line. Since, with $\theta_0$ near $\pi/2$, $l \doteq a$, where $a$ is the radius of the cylindrical antenna which is assumed to satisfy

$$\beta_0 a \ll 1, \tag{14}$$

it follows that (12) reduces to

$$Y_{la} \doteq \frac{Y_0 - jY_c\beta_0 a}{1 - jZ_c Y_0\beta_0 a}. \tag{15}$$

This formula may be simplified further by noting that with $\theta_0$ near $\pi/2$, $Z_c = (\zeta_0/\pi) ln\,\cot(\theta_0/2)$ is very small. Hence,

$$Y_{la} \doteq Y_0 - jY_c\beta_0 a = Y_0 - j\omega C_g \tag{16}$$

where, with $\beta_0 = \omega/v_0$, $\zeta_0 = (\mu_0/\epsilon_0)^{\frac{1}{2}}$,

$$C_g \equiv ac_0 = \frac{a}{v_0 Z_c} = \frac{a\pi\epsilon_0}{\ln\cot(\theta_0/2)}. \tag{17}$$

In (17), $c_0$ is the capacitance per unit radial length of the biconical line. It follows with (6) and (7) that the driving-point admittance at the apex of the biconical line is

$$Y_0 \doteq Y_{la} + j\omega C_g = Y_\delta + j\omega(C_T + C_g). \tag{18}$$

Note that (18) is a special form of (12) solved for $Y_0$, *viz.*,

$$Y_0=\frac{Y_{la}\cos\beta_0 l+jY_c\sin\beta_0 l}{\cos\beta_0 l+jZ_cY_{la}\sin\beta_0 l} \tag{19}$$

when both $\beta_0 l$ and $Z_c$ are sufficiently small.

*The confusion regarding the significance of the gap in antenna theory arises from a failure to recognize that (18) is not a general form but is a special case of (19).*

The following "conclusions" may be drawn from (18). (1) The driving-point impedance $Y_0$ of a cylindrical antenna is equal to the impedance $Z_\delta=V_\delta/I_\delta$ (where $V_\delta$ is the voltage across the gap of length $2\delta$ and $I_\delta$ is the current entering the antenna at the edge of the gap) in parallel with the effective "gap capacitance" $C_g+C_T$ between the two adjacent end-surfaces of the antenna. (2) As the width $2\delta$ of the gap is decreased by making $\theta_0$ differ less and less from $\pi/2$, the essential part $C_g$ of the gap capacitance increases without limit. This is seen from (17). (3) It follows that in the limit $\delta\to 0$, the driving-point susceptance $B_0$ becomes infinite. Since the generator is short-circuited and completely enclosed by metal, no power can be radiated from the antenna. If it is now *assumed* that the interpretation of (18) is typical for all center-driven cylindrical antennas, the following "conclusion" is reached: (4) Only antennas with finite gaps can radiate. Finally, a *naive* application of the Poynting vector theorem suggests that: (5) All radiation comes out of the gap.

In what way are these "conclusions" erroneous? This may be discovered readily by rephrasing them in a manner consistent with the general formula (19) instead of the special formula (18).

(1) The driving-point admittance $Y_0$ of a section of transmission line of length $l$ with an apparent load admittance $Y_{la}$ is given by (19). If $l$ is sufficiently short and the characteristic impedance $Z_c$ sufficiently small, this reduces to (18). The apparent load admittance $Y_{la}$ is equal to the actual load admittance $Y_\delta=V_\delta/I_\delta$ in parallel with a lumped capacitance that takes account of terminal-zone effects.

(2) As the distance between the two conductors of the transmission line is reduced, the characteristic impedance $Z_c$ decreases without limit. For the biconical line this is seen from (5). For coaxial or parallel wire lines $Z_c$ has the factor $\ln(b/a)$ or $\cosh^{-1}(b/2a)$ which reduces to zero when $b$ approaches $a$ or $2a$, respectively.

(3) It follows from (19) that in the limit $\delta\to 0$ when $Z_c\to 0$ and $Y_c\to\infty$ the input susceptance of the section

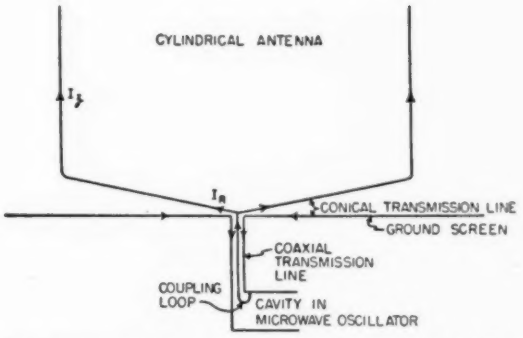


FIG. 8. Transmitting system with conical and coaxial lines.

of line is infinite since the two perfect conductors are everywhere in contact and *do not constitute a transmission line.* Since this leaves the antenna completely isolated from the generator, *no currents are maintained* in it and, therefore, no electromagnetic field is set up by them. That is, the antenna does not radiate.

(4) A transmission line like that in Fig. 7 that happens to be short, biconical, and inside the antenna so that it *looks like a simple gap* instead of a section of line is characteristic only of certain special cases that actually are highly artificial and impractical. Every short section of transmission line, whether two-wire, coaxial, biconical, or radial, is *not* merely a lumped capacitance in parallel with the load. *In all cases*, the entire current from the generator to the load traverses the two conductors—whether flat plates, cones, or wires—*in opposite directions.* They form necessary *series* connections between generator and load. It is obvious that only transmission lines consisting of two conductors with finite spacing can transmit power to a load. This is as true of two-wire lines as of biconical or radial lines; it has nothing to do with gaps. Every antenna in which currents are induced radiates in the sense that these currents maintain a far-zone field. Practical antennas never have gaps.

(5) It is readily verified that the Poynting-vector theorem is useful in *locating the generator* in a complete transmitting system, not the element that carries the currents that generate the radiation field. In order to radiate, i.e., produce far-zone fields, antennas must have currents maintained in them. This may be accomplished by direct connection to a transmission line from a distant generator or by coupling to a varying magnetic field maintained by a generator. A gap is not required. Thus, it may be concluded that there are transmission-line problems and coupling problems in antenna theory but *no gap problems.*

# Acceleration of Slender Bodies of Revolution through Sonic Velocity*

J. D. COLE†
*California Institute of Technology, Pasadena, California*
(Received January 11, 1954)

The linearized theory of slender bodies in arbitrary motion at zero angle of attack has been worked out. The results have been applied to a smooth body accelerating uniformly through sonic velocity. The results theory can be used to estimate the nonlinear or transonic effects.

For an accelerating body, the parameter $(bl/c^2)^{\frac{1}{3}}$ is important where $2b$=acceleration, $2l$=length of body, $c$=sound speed at infinity. For sufficiently high $(bl/c^2)^{\frac{1}{3}}$, transonic effects can be neglected. Using linearized theory to estimate the ratio of nonlinear terms in the differential equation gives

$$\lambda=\frac{\text{nonlinear terms}}{\text{significant linear terms}}=\frac{3}{4}(\gamma+1)\frac{\delta^2}{(bl/c^2)^{\frac{1}{3}}}\left\{\log\frac{2}{\delta^2}\left(\frac{c^2}{bl}\right)^{\frac{1}{3}}-\frac{9}{4}\right\},$$

where $\delta$=thickness ratio of body. The result above is evaluated at the maximum thickness of a symmetric parabolic arc body at the instant it passes through sonic velocity. For $\lambda<1$ transonic effects can be neglected while for $\lambda>1$ they begin to dominate. For practical applications the result shows that there is a possibility of a sufficiently long and slender missile accelerating fast enough to avoid transonic effects (e.g., 50 feet long, 5 percent thick, $3g$ acceleration). For conventional aircraft, transonic effects will dominate. An interesting side result is that when the acceleration is sufficiently large so that transonic effects do not matter the drag coefficient near sonic speed is independent of the acceleration ($C_D\doteq 3\delta^2$ for parabolic arc body).

## 1. INTRODUCTION

THE problem discussed here is a special case of the general problem of estimating the validity of linearized theory in the transonic range. The special case studied in detail is that of a slender body of revolution which accelerates uniformly through sonic speed. The method of attacking the problem is applicable to other similar problems of steady and unsteady flow. As a side result the general unsteady slender body expansion is presented.

The work presented here is concerned with the "breakdown" of linearized theory and the necessity for using a more complete theory. Linearized theory is identical in physical and mathematical content with the classical theory of acoustics.[1] The theory is derived from physical principles plus the assumption that all disturbances are so small that the squares can be neglected. The reason for the breakdown of linearized theory for bodies with thickness can be illustrated as follows. According to linearized theory, all disturbances in the gas travel with a constant speed $c$, the speed of sound. A body flying at an arbitrary speed is continually sending out such disturbances, which, in general, are left behind or escape to the front of the body. For the special case of a body flying steadily at the sonic speed $c$, these disturbances remain with the body, and build up indefinitely. For example, according to linearized theory the pressure on a slender body which starts impulsively with sonic speed at the time $t=0$, increases as $\log t$. These results show how linearized theory predicts infinite pressure everywhere on a body flying steadily at sonic speed.

The more accurate theory includes some of the quadratic terms and allows for the fact that the speed of disturbances varies according to local conditions. This refinement prevents the accumulation of disturbances at the body and predicts finite pressures in steady flight at sonic speed. At the same time shock waves must be allowed for in the more exact theory as there is a possibility of small disturbances overtaking one another. The above features are included in the usual transonic theory. Of course, linearized theory does not break down in steady flight only at sonic speed, but there is some neighborhood of Mach numbers about 1 for which it is a poor approximation.

Now, if a body accelerates through sonic speed there is no infinite pressure according to linearized theory, because disturbances do not remain with the body. Nevertheless, there is still some region of acceleration about zero acceleration for which the nonlinear effects are important. Linearized theory becomes valid only for sufficiently high accelerations.

In order to estimate the regions where nonlinear effects become important, the following procedure will be adopted. The equation of motion will be derived under the assumption of small disturbances, but the squared terms will be retained. The relationship of this to the usual acoustic and transonic equations will be shown. The linearized equation will be used to calculate the flow and the results of linearized theory used to estimate the significance of the nonlinear terms. In this way a test of the self-consistency of linearized theory can be obtained.

* This paper was presented at a meeting of the American Physical Society in Albuquerque, New Mexico, September 3, 1953. The research was carried out under ARDC Contract AF-18(600)-383.
† Assistant Professor of Aeronautics, California Institute of Technology, Pasadena, California.
[1] Lord Rayleigh, *Theory of Sound* (Dover Publications, New York, 1945).

## 2. SECOND-ORDER EQUATIONS OF MOTION

Consider a system of coordinates $(x,y,z,t)$ in which air is at rest at infinity. It will be assumed that any local, normal Mach numbers measured relative to any shock waves that occur, are not very different from 1. Thus entropy changes $\sim(M_x^2-1)^3$ are neglected. It follows from Crocco's vortex theorem[2] that the flow can be regarded as irrotational. These assumptions mean that the dependent variables can be reduced to $\mathbf{q}$=velocity, $P$=pressure, and $\rho$=density, where $P$, $\rho$ are always related by the isentropic law

$$P/P_0=(\rho/\rho_0)^\gamma, \tag{1}$$

where subscript 0 denotes conditions at infinity, and $\gamma$=ratio of specific heats. Furthermore, a potential $\phi$ exists so that

$$\mathbf{q}=\text{grad}\phi. \tag{2}$$

Now, assuming small disturbances, let

$$P=P_0(1+p), \quad \rho=\rho_0(1+s), \quad p,s\ll 1. \tag{3}$$

Then (1) becomes, to the second order (that is, neglecting cubed terms),

$$p=\gamma s+\frac{\gamma(\gamma-1)}{2}s^2. \tag{4}$$

The equation for conservation of momentum, in view of (2)

$$\mathbf{q}_t+\nabla\left(\frac{q^2}{2}\right)=-\frac{1}{\rho}\nabla p, \tag{5}$$

can be integrated by virtue of (2) and (4) to give a second-order Bernoulli law,

$$s=-\frac{1}{c^2}\phi_t-\frac{1}{2c^2}\left\{(\nabla\phi)^2+(\gamma-2)\frac{\phi_t^2}{c^2}\right\}, \tag{6}$$

where $c^2=\gamma(P_0/\rho_0)$=speed of sound at infinity. Thus, by using Eqs. (3), and (6), the kinematic requirements of continuity give the equation of motion for the velocity potential

$$\rho_t+\text{div}\,\rho\mathbf{q}=0, \tag{7}$$

and can be written:

$$\frac{1}{c^2}\left\{1+(\gamma-1)\frac{\phi_t}{c^2}\right\}\phi_{tt}+\frac{1}{c^2}\frac{\partial}{\partial t}(\nabla\phi)^2-\Delta\phi=0. \tag{8}$$

Equation (8) is the fundamental equation of motion, including all squared terms in $\phi$ but neglects all cubed or higher terms. The form of (8) is chosen for convenience; multiplying through by 1+(small quantity) gives equivalent forms. As will be shown in the next section, terms like $\phi_t\phi_{tt}$ and $\phi_x\phi_{xt}$, which account for the steepening of wave fronts in this system of coordinates, account for the change of type of the equations or the fact that stream tubes have throats at sonic speed, when viewed in a steadily moving coordinate system.

[2] R. Sauer, *Theoretical Gas-Dynamics* (Edwards Brothers, Inc., Ann Arbor, Michigan, 1947).

## 3. RELATIONSHIP TO ACOUSTICS AND TRANSONIC THEORIES

If all squared terms are omitted in (8), (6), and (4), the classical equations of acoustics are obtained,

$$(1/c^2)\phi_{tt}-\Delta\phi=0, \tag{9}$$

$$p/\gamma=s=-(1/c^2)\phi_t. \tag{10}$$

The speed of all disturbances is constant and equal to $c$.

Next, consider Eq. (8) in a system of coordinates moving at a constant speed $U$ in the negative $x$ direction. For steady flow in the new coordinate system, $\partial/\partial t$ in Eq. (8) is replaced by $U(\partial/\partial X)$, so that

$$(M^2-1)\phi_{XX}-(\phi_{yy}+\phi_{zz})+\frac{(\gamma-1)M^2+2}{c^2}U\phi_X\phi_{XX}+\frac{U}{c^2}\frac{\partial}{\partial X}(\phi_y^2+\phi_z^2)=0, \tag{11}$$

where

$$X=x+Ut, \quad T=t,$$

$M=U/c$=free stream Mach number in $(X,t)$ system.

When squared terms are neglected, (11) is the usual linearized equation of steady subsonic or supersonic flow. But when the nonlinear terms containing $\phi_X\phi_{XX}$ are retained in (11), on the grounds that the results of linearized theory hint that they are much larger than the others, the usual equation of transonic flow is obtained (for $M\doteq 1$, the factor $(1/c^2)\{(\gamma-1)M^2+2\}$ can be replaced by $(\gamma+1/a^*)M^2$, as in reference 3).

## 4. ESTIMATION OF NONLINEAR EFFECTS

In order to show how to estimate the relative importance of nonlinear effects, consider the case of steady flow as covered by Eq. (11). The reason for the breakdown of linearized theory at sonic speed is the vanishing of the term $(M^2-1)\phi_{XX}$ in the equation. The size of nonlinear effects can be measured by the ratio of the main nonlinear term in Eq. (11) to this term which vanishes at $M=1$, namely,

$$\lambda=\frac{\text{nonlinear terms}}{\text{linear terms}}=\frac{[(\gamma-1)M^2+2/c^2]U\phi_X\phi_{XX}}{(1-M^2)\phi_{XX}}\doteq\frac{(\gamma+1)M^2}{1-M^2}\frac{\phi_X}{U}. \tag{12}$$

Note that $\lambda=1$ corresponds to an estimate of the critical Mach number, that is, $\lambda=1$ means the local Mach number is one.

[3] A. Busemann, "Application of Transonic Similarity," National Advisory Committee for Aeronautics TN 2687 (1952).

Now, linearized theory itself can be used to evaluate $\lambda$ in (12). For example, in the case of two-dimensional flow past nonlifting air-foil of thickness ratio $\delta$, the pressure coefficient

$$c_p \doteq -2\frac{\phi_x}{U} \sim \frac{\delta}{(1-M^2)^{\frac{1}{2}}} M<1, \tag{13}$$

the usual Prandtl-Glauert rule.[4] Using the result of (13) in (12) shows that the transonic similarity parameter $\xi^3$ should be small compared to 1 for linearized theory to be valid, or

$$\lambda \sim \frac{(\gamma+1)M^2\delta}{(1-M^2)^{\frac{1}{2}}} = \xi^{\frac{1}{2}} < 1. \tag{14}$$

When $\lambda$ gets close to 1 the nonlinear terms are becoming important, and when $\lambda>1$ they definitely dominate. It is slightly more complicated to carry out the estimate for the case of a body of revolution as the simple proportionality of (13) no longer holds. However, the result can be illustrated by applications of slender-body theory[4] to the special case of a symmetric parabolic arc body of revolution of thickness ratio $\delta$. The result is that

$$\lambda = (\gamma+1)M^2\frac{\delta^2}{1-M^2}\left\{2\log\frac{2}{\delta(1-M^2)^{\frac{1}{2}}} - 3\right\} \tag{15}$$

when evaluated at the maximum thickness point. The result is typical for smooth bodies of revolution, but the constants vary a little with shape. Equation (15) shows how, as would be expected, a body of revolution can fly much closer to sonic speed than its two-dimensional counterpart without experiencing transonic effects. Figure 1 gives a plot of the results of Eq. (15) for several thickness ratios.

Now the same reasoning can be carried over to the general unsteady case in the transonic range. The transonic effects can be measured by the ratio of nonlinear to significant linear terms. The significant linear terms are $(1/c^2)\phi_{tt}-\phi_{xx}$, since under translation of axes these terms become $(M^2-1)\phi_{XX}$. Thus, from Eq. (8),

$$\lambda = \frac{(\gamma-1/c^4)\phi_t\phi_{tt}+(2/c^2)\phi_x\phi_{xt}}{(1/c^2)\phi_{tt}-\phi_{xx}}. \tag{16}$$

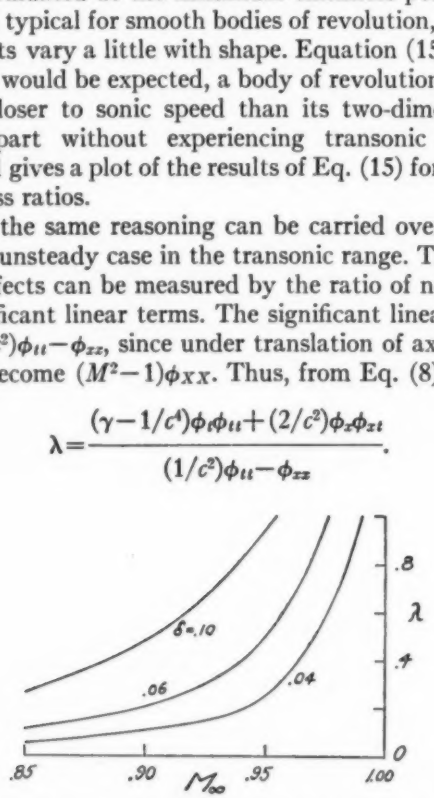


FIG. 1. Transonic parameter $\lambda$ *vs* Mach number $M_\infty$ at maximum thickness symmetric parabolic body.

[4] W. Sears and M. Adams, J. Aeronaut. Sci. **20**, 85 (1953).

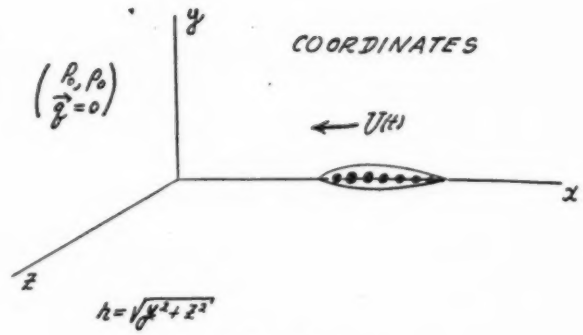


FIG. 2. Coordinate system.

## 5. UNSTEADY SLENDER-BODY THEORY

As before, the values of $\lambda$ given by (16) are to be computed on the basis of linearized theory. For a body of revolution at zero angle of attack, the potential is given by the solutions of

$$\frac{1}{c^2}\phi_{tt}-\phi_{xx}=\phi_{rr}+\frac{1}{r}\phi_r, \tag{17}$$

where $r=(y^2+z^2)^{\frac{1}{2}}$. A body of revolution moving along its axis (Fig. 2) can be represented by a distribution of sources, which vary in time, along the axis of flight. The potential is represented by an integral (expressing the superposition of spherical waves emanating from each point on the axis) of the retarded values of the source strength $S(x,t)$:

$$-4\pi\phi(x,r,t)=\int_{-\infty}^{\infty}\frac{s\left\{\xi,t-\dfrac{[(x-\xi)^2+r^2]^{\frac{1}{2}}}{c}\right\}}{[(x-\xi)^2+r^2]^{\frac{1}{2}}}d\xi, \tag{18}$$

The source strength is zero outside the body so that the integral in (18) covers only those values of $\xi$ which are common to the flight path and the surface of the retrograde Mach cone, $\tau=t-(1/c)[(x-\xi)^2+r^2]^{\frac{1}{2}}$, as shown in Fig. 3. There are integrals for the recent past $x_1$ to $x_2$, and the distant past $x_3$ to $x_4$, etc.

The source integrals can be approximated near the axis by using the fact that when $r$ is small, the main contribution comes from the neighborhood of $x=\xi$. The integral for the recent past can be analyzed for small $r$ by splitting it into

$$\int_{x_1}^{x-\epsilon(r)}, \quad \int_{x-\epsilon(r)}^{x+\epsilon(r)}, \quad \int_{x+\epsilon(r)}^{x_2}.$$

The expansion for the middle integral can be obtained by introducing the variable $\sigma$ as $x=\xi+r\sinh\sigma$, and then expanding in powers of $r$. A further expansion in powers of $r/\epsilon$ is possible since we assume $\epsilon>r$. For the outside integrals, expansions of $S$, and the square root in powers of $r$ can be made. Integration by parts in the outside integrals produces a result, the dominant terms

of which are independent of $\epsilon$, as $r$ and $\epsilon$ approach zero. The final result is the asymptotic expansion of the source distribution near the axis:

$$\phi(x,r,t)=\frac{1}{2\pi}S(x,t)\log\frac{r}{2}-\frac{1}{4\pi}\left\{S\left(x_1,\,t-\frac{x-x_1}{c}\right)\right.$$

$$\left.\times\log(x-x_1)+S\left(x_2,\,t-\frac{x_2-x}{c}\right)\log(x_2-x)\right\}$$

$$-\frac{1}{4\pi}\int_{x_1}^{x_2}\left\{\frac{1}{c}S_t\left(\xi,\,t-\frac{|x-\xi|}{c}\right)\right.$$

$$\left.+\operatorname{sgn}(x-\xi)S_x\left(\xi,\,t-\frac{|x-\xi|}{c}\right)\right\}\log|x-\xi|\,d\xi$$

$$-\frac{1}{4\pi}\int_{x_3}^{x_4}\frac{S\left(\xi,\,t-\dfrac{|x-\xi|}{c}\right)}{|x-\xi|}d\xi,\ \text{etc.}+\cdots+O(r^2\log r), \tag{19}$$

where $x_1(x,t)$, $x_2(x,t)$ are the values of $\xi$ in the recent past at which $\tau=t\mp(x-\xi)/c$, respectively, intersect the boundaries of the flight path (Fig. 3), and $x_3$, $x_4$ are similar values in the distant past.

Equation (19) is the general slender-body expansion. In most cases only the integrals in the recent past $(x_1,x_2)$ need be considered. The physical interpretation of Eq. (19) is as follows: the dominant $\log r$ term is the potential of a source in two-dimensional incompressible flow. This means that locally the conservation of mass can be computed in a cross-section plane. The next terms in the expansion are independent of $r$ and represent the effect of the sources at a distance from the local neighborhood. All the higher terms in the expansion can be obtained by the substitution of the first terms of (19) in the left-hand side of Eq. (17). This procedure results in terms like $r^2\log r$, $r^2$ etc. It can be expected that the first terms of the asymptotic expansion, that is Eq. (19), are a good approximation near a smooth slender body except in the neighborhood of the ends.

Using the slender-body approximation of (19) the source strength $S(x,t)$ is easily determined by the requirement that the flow be tangent at the surface. Within linearized theory this boundary condition is

$$\phi_r(x,R,t)=U(t)(\partial R/\partial x)(x,t), \tag{20}$$

where

$r=R(x,t)$ is the equation of the body shape,
$U(t)$ = velocity of the body in the negative $x$ direction.

For a body of fixed shape we obtain, from (20) and (19),

$$S(x,t)=U(t)A'(X), \tag{21}$$

where

$X=x+\int_0^t U\,d\tau$ is a coordinate fixed in the body.

$A(x)$ = cross-section area distribution.

The fundamental result (21), due to Frankl,[5] states that the source strength for arbitrary motion is the same as that for incompressible flow and is equal to the instantaneous velocity times the rate of change of cross-section area along the body. Once the source strength is known the velocities and pressure can be computed of course.

### 6. APPLICATION TO A BODY UNIFORMLY ACCELERATING THROUGH SONIC SPEED

Consider a body which passes through sonic speed at $t=0$ and lies between $-l$ and $+l$. Let the acceleration be $2b$ so that the velocity is

$$U(t)=c+2bt. \tag{22}$$

The limits of integration $x_1$, $x_2$ are then given by

$$\left\{\begin{aligned} x-x_1&=ct+\frac{c^2}{b}\left\{1-\left[1-\frac{b}{c^2}(x+l-ct)\right]^{\frac{1}{2}}\right\}\\ &=\frac{x+l+ct}{2}+O(b),\\ x_2-x&=ct+c\left(\frac{l-x-ct}{b}\right)^{\frac{1}{2}}. \end{aligned}\right\} \tag{23}$$

Furthermore, assume the body is pointed (or has zero slope) at the ends, so that

$$S\left(x_1,\,t-\frac{x-x_1}{c}\right)=S\left(x_2,\,t-\frac{x_2-x}{c}\right)=0.$$

Then, using (23) and (21), the velocity potential can be written out from (19). If now we consider cases in which the acceleration parameter $bl/c^2\ll 1$, which is

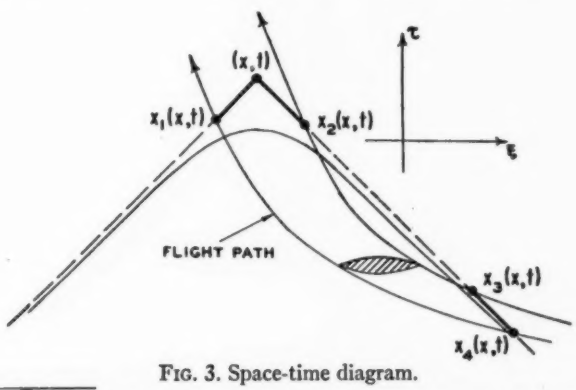


FIG. 3. Space-time diagram.

[5] F. I. Frankl, Effect of the Acceleration of Elongated Bodies of Revolution upon the Resistance in Compressible Flow, National Advisory Committee for Aeronautics TM 1230 (1949); translation of the Russian paper in Prikl. Mat. i. Mekh **10** (1946).

true in all practical examples, a further expansion of Eq. (19) can be made. The final result is

$$-4\pi\phi(x,r,t)=cA'(x+ct)\log\frac{2c}{r^2}\left(\frac{l-x-ct}{b}\right)^{\frac{1}{2}}(l+x+ct)$$

$$+\sum_{n=1}^{\infty}\frac{1}{n\Gamma(n+1)}\{\tfrac{1}{2}(l-x-ct)^n+(-)^n(l+x+ct)^n\}$$

$$\times\left(\frac{\partial}{\partial x}\right)^n A'(x+ct)-ct[b(l-x-ct)^{\frac{1}{2}}$$

$$\times\sum_{n=0}^{\infty}\frac{(l-x-ct)^n}{(n+\frac{1}{2})\Gamma(n+1)}\left(\frac{\partial}{\partial x}\right)^n A''(x+ct)$$

$$+fn(x+ct;\sqrt{b})+O(b\log b). \quad (24)$$

From (10), the main term in the pressure distribution contains $\phi_t$. On the surface of the body, at the instant of passing through sonic $t=0$, (24) gives

$$-\frac{4\pi}{c^2}\phi_t(x,R(x),0)=A''(x)\log\frac{2\pi c}{A(x)}\left(\frac{l-x}{b}\right)^{\frac{1}{2}}(l+x)$$

$$+\sum_{n=1}^{\infty}\frac{1}{n\Gamma(n+1)}\{\tfrac{1}{2}(l-x)^n+(-)^n(l+x)^n\}$$

$$\times\left(\frac{\partial}{\partial x}\right)^n A''(x)+O(\sqrt{b}). \quad (25)$$

From (25) it can be seen that, for any body, as the acceleration $b\to 0$ the pressure becomes logarithmically infinite, indicative of the manner in which the linearized theory breaks down. It can also be seen that the drag coefficient at sonic, calculated from the linearized pressure formula

$$c_p=-\frac{2}{U^2}\phi_t-\frac{1}{U^2}\phi_r{}^2+\cdots \quad (26)$$

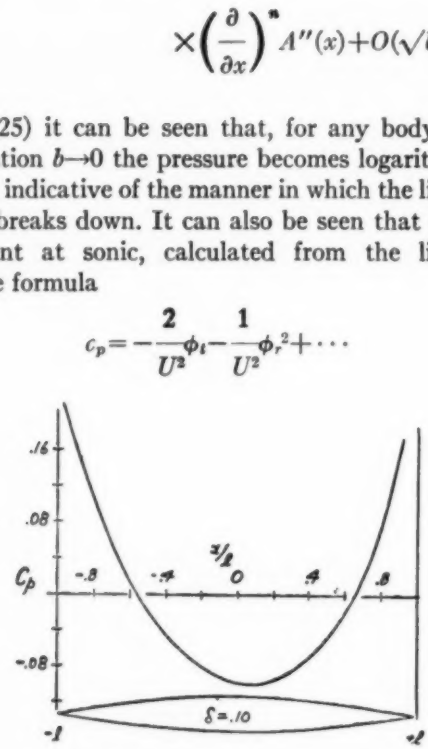


FIG. 4. Pressure distribution at sonic speed; uniform acceleration, $bl/c^2=0.026$.

is independent of the acceleration $b$. (Its value is not the same as that of steady supersonic slender-body theory as $M\to 1+$.) This result can be interpreted as follows. For slow accelerations, nonlinear effects are important, and there is a definite drag depending on the acceleration. As the acceleration increases, the drag coefficient at sonic decreases. For sufficiently large accelerations, linearized theory is valid and the drag coefficient approaches its asymptotic value independent of the acceleration.

As an illustration consider a symmetric parabolic arc body of thickness ratio $\delta$, whose shape is

$$r=R(x)=\delta l\left(1-\frac{x^2}{l^2}\right). \quad (27)$$

Then the pressure coefficient at sonic can be calculated from (26) and (25) to give

$$\frac{c_p}{2}=\delta^2\left(\frac{3x^2}{l^2}-1\right)\log\left\{\frac{2}{\delta^2}\left(\frac{c^2}{bl}\right)^{\frac{1}{2}}\frac{1}{\left(1+\frac{x}{l}\right)\left(1-\frac{x}{l}\right)^{\frac{1}{2}}}\right\}$$

$$+\frac{\delta^2}{4}\left\{9-6\frac{x}{l}-35\frac{x^2}{l^2}\right\}. \quad (28)$$

A special case of this formula is plotted in Fig. 4. The slight unsymmetry of the pressure distribution results in a drag

$$C_D{}^*=2.9\delta^2\{1+O(\sqrt{b})\}. \quad (29)$$

Finally the range of validity of linearized theory can be estimated by using (24) to evaluate the ratio $\lambda$,

$$\lambda\doteq\frac{(\gamma+1)(\phi_t\phi_{tt}/c^4)}{(1/c^2)\phi_{tt}-\phi_{xx}}=\frac{3}{4}(\gamma+1)\frac{\delta^2}{(bl/c^2)^{\frac{1}{2}}}$$

$$\left\{\log\frac{2}{\delta^2}\left(\frac{c^2}{bl}\right)^{\frac{1}{2}}-\frac{9}{4}\right\}. \quad (30)$$

It can be seen from (30) that for a fixed $\delta$, the accelera-

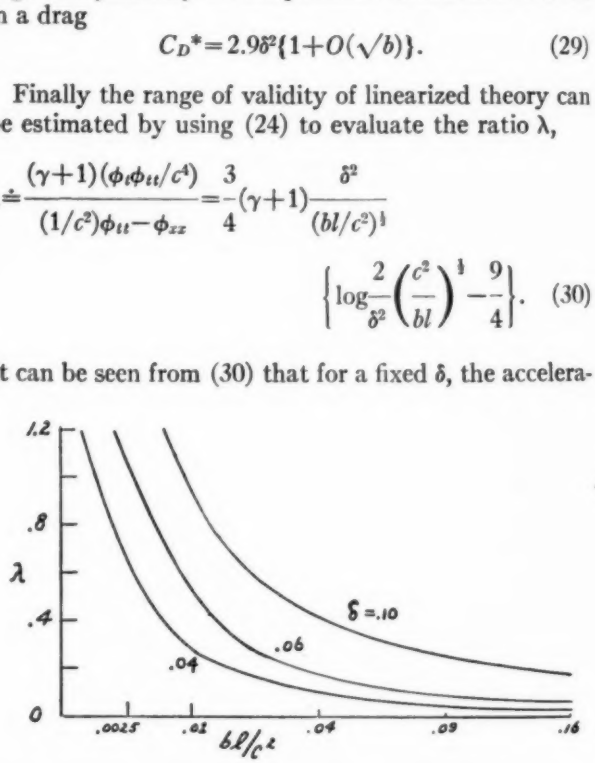


FIG. 5. Transonic effect parameter $\lambda$ *vs* acceleration parameter $bl/c^2$ at maximum thickness of symmetric parabolic arc body $M=1$.

tion parameter $bl/c^2$ can always be chosen large enough so that $\lambda<1$, and linearized theory is valid. A plot of Eq. (30) is given in Fig. 5. The numerical results show that for practical applications, it is possible for a sufficiently long and slender missile (for example, 50 ft long, $\delta=0.05$, $3g$ acceleration) to accelerate through sonic without experiencing transonic effects, while it is not possible for conventional aircraft to do so.

As a concluding remark, the author wishes to thank Dr. George Solomon for his able assistance.

---

JOURNAL OF APPLIED PHYSICS VOLUME 26, NUMBER 3 MARCH, 1955

# Use of Space Charge in Electron Optics

E. A. Ash
*Nuclear Particle Laboratory, Queen Mary College, London, England*
(Received December 28, 1953)

The electron optical properties of a cylindrical space charge cloud are derived. The possibility of achieving a system free from either spherical or chromatic aberration by combining a space charge lens with a space charge free converging lens is examined. It is concluded that the achromatization of a thin electric or magnetic lens is possible only if the resultant action of the combination is divergent. The correction of the spherical aberration of a high quality lens, such as an electron microscope objective, is shown to be impossible on account of electron interaction effects.

## INTRODUCTION

THE design of space charge free electron optical lenses with prescribed properties is restricted by the fact that the lens fields must be solutions of Laplace's equation. This limitation does not preclude the construction of a two-dimensional lens[1,2] (imaging coplanar line elements) free from spherical aberration, but in the case of a three-dimensional lens (imaging elements of area) it is not possible, as has been shown by O. Scherzer,[3] to eliminate either the spherical aberration (s.a.) or the chromatic aberration (c.a.) completely. The level to which the s.a. (which is always positive on the usual convention) can be reduced is limited by the maximum strength of the lens (magnetic or electric) which can be achieved in practice.

D. Gabor[4] has shown that if the fields are not required to obey Laplace's equation, it is possible to find a solution with the properties of an "ideal lens," which would form an undistorted image (though with unit magnification) of any finite volume element in the object space. The realization of such a lens would require an infinite spherically symmetric charge distribution, involving charges of both signs. Gabor[5] showed further the existence of a lens which has "semi-ideal" properties in the sense that it can image an element of area without s.a. and with a magnification greater than unity. Such a lens could be realized by an axially symmetric charge distribution of negative charges only.

Since an isolated electron cloud acts as a divergent lens, it would seem by analogy with optics that it might also be possible to achieve an achromatic system by combination with a converging lens. The elimination of s.a. and of c.a. by the use of space charge has been briefly considered by a number of authors, who have been well aware of the magnitude of the technical problems involved.

In the course of an experimental investigation on electron interaction effects,[6] it was found possible to produce a dense, stable electron cloud by very simple means. The essential features of the system, which are shown in Fig. 1, consisted of a hollow cylindrical cathode surrounding a concentric grid, held at a positive potential. It was shown, both theoretically and experimentally, that by the introduction of a weak axial magnetic field the radial distribution of space charge density could be adjusted so as to give a strong negative spherical aberration to the divergent lens formed by the space charge. It appeared that the technical difficulties which would be involved in perfecting this device to a degree where it could be of use in precision electron optics were not insuperable. In the light of these experiments the possibility of the use of space charge as correcting elements was re-examined.

When first proposing the correction of s.a. by means of space charge, Gabor observed that it was dependent on the electron interaction effect being sufficiently small to allow the representation of the electron cloud by a smooth space charge distribution. The possibility of the correction of c.a. depends on the variation, with the velocity of the electron beam, of the focal length of the space charge lens. The present investigation has led to the negation of both these possibilities. It is the purpose of this paper to show that the use of space charge as

[1] W. Glaser, Nature **162**, 455 (1948).
[2] N. Wax, J. Appl. Phys. **24**, 727 (1953).
[3] O. Scherzer, Z. Physik **101**, 593 (1936).
[4] D. Gabor, *The Electron Microscope* (Hulton Press, London, 1944).
[5] D. Gabor (unpublished).
[6] E. A. Ash and D. Gabor Proc. Roy. Soc. (London) A (to be published).

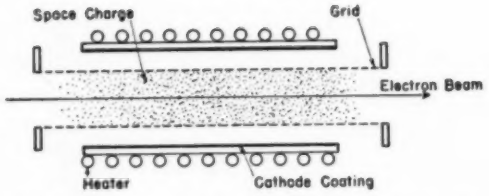


FIG. 1. Method of realizing a stable space charge cloud. The grid is positive with respect to the cathode, and electrons are shot radially into the central region, and eventually (possibly after several transits) absorbed by the grid. The radial distribution of space charge density can be controlled by appropriate design of the grid cathode geometry, and by the introduction of a weak axial magnetic field. The optical axis of the equivalent divergent electron lens coincides with the geometric axis.

correcting elements in precision electron optics is excluded by factors which are fundamental and which cannot be overcome by any technical advances. We will consider the special case in which the field of the converging lens and the field of the space charge lens are adjacent but do not overlap. The analysis is thereby simplified, and it is not believed that essentially different results would emerge from a more general treatment.

## FOCAL PROPERTIES OF A CYLINDRICAL ELECTRON CLOUD

We will begin by considering the focal properties of an isolated cylindrical electron cloud. Figure 2 explains some of the parameters used. The space charge cloud extends over $0<z<L$. We will assume a radial distribution of density of the form

$$\rho=\rho_0+\rho_1 r^2 \quad 0<z<L. \tag{1}$$

The field $E$ associated with this distribution is given by

$$\mathrm{div}(E)=-4\pi\rho. \tag{2}$$

By virtue of the assumed circular symmetry, and for $r\ll z$ and $r\ll(L-z)$

$$E_r=-4\pi/r\int_0^r r\rho dr$$
$$E_r=-\pi(2\rho_0 r+\rho_1 r^3) \quad E_\phi=E_z=0. \tag{3}$$

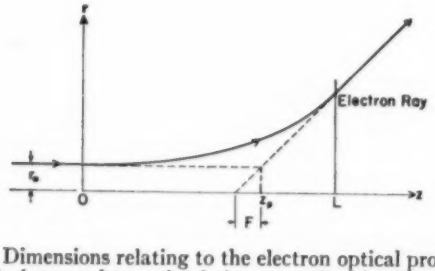


FIG. 2. Dimensions relating to the electron optical properties of a cylindrical space charge cloud. At any radius the density is constant for $0<z<L$ and zero outside this range. The position of only one of the principal planes is shown, the other being symmetrically placed with respect to $z=L/2$.

Thus the radial motion of an electron traversing the cloud is described by

$$m\ddot{r}=\pi e(2\rho_0 r+\rho_1 r^3). \tag{4}$$

This is a nonlinear second-order equation which can be solved[7] in terms of elliptic functions. For an initially parallel beam of radius $r_0$ and energy $V$ volts, we find

$$r_0/r=cn\left(P(1+\beta/2)^{\frac{1}{2}}z,\left(\frac{1+\beta/4}{1+\beta/2}\right)^{\frac{1}{2}}\right), \tag{5}$$

where $cn$ is an elliptic function with the argument $P(1+\beta/2)^{\frac{1}{2}}z$, and modulus $[(1+\beta/4)/(1+\beta/2)]^{\frac{1}{2}}$.

$$\beta=\rho_1 r_0^2/\rho_0$$
$$P^2=\pi\rho_0/V. \tag{6}$$

$\beta$ is in effect the fractional increase in space charge density at a radius $r_0$ with respect to the density on the axis. $P$ is a measure of the Gaussian strength of the divergent lens formed by the space charge. Typical trajectories described by Eq. (5) are shown in Fig. 3. In the following, the notation will be abbreviated by writing the elliptic functions without showing the argument or modulus, which will always be as indicated in Eq. (5). With reference to Fig. 2 it is seen that the focal length $F$ can be found from the angle of divergence of the emerging ray according to

$$|F|=r_0/(dr/dz)_{z=L}. \tag{7}$$

$dr/dz$ is obtained from Eq. (5), and we find

$$|F|=\frac{cn}{Psn}\left(1+\frac{\beta}{4}(1+1/cn^2)\right)^{-\frac{1}{2}}. \tag{8}$$

The Gaussian focal length $F_0$ can be obtained from $F$ by finding $\lim_{r_0\to 0} F=F_0$

$$|F_0|=(P\sinh PL)^{-1}. \tag{9}$$

The principal planes are at $z=z_{p1}$ and $z=z_{p2}$, where

$$z_{p1}=(\cosh PL-1)/P\sinh PL,$$

and

$$z_{p1}=L-z_{p2}. \tag{10}$$

The nondimensional spherical aberration coefficient $C$ can be defined in the form

$$C=\lim_{r_0\to 0}\left(\frac{F_0\Delta F}{r_0^2}\right), \tag{11}$$

where $\Delta F$ is the difference between the actual and the Gaussian focal length for an electron initially at the radius $r_0$. Thus

$$\Delta F=F_0-F. \tag{12}$$

[7] N. W. McLachlan, *Ordinary Non-Linear Differential Equations* (Oxford University Press, Oxford, 1950).

In this way we find

$$C=\frac{\rho_1}{16P^2\rho_0}\frac{2+3\cosh^2PL-PL\coth PL}{\sinh^2PL}. \quad (13)$$

Of particular interest for the correction of spherical aberration is the quantity $C/F_0^3$. From Eqs. (9) and (13) we find

$$\frac{C}{F_0^3}=\frac{P\rho_1}{16\rho_0}\{(2+3\cosh^2PL)\sinh PL-PL\cosh PL\}. \quad (14)$$

This expression remains finite as $\rho_0$ tends to zero with the limit

$$\lim_{\rho_0\to 0}(C/F_0^3)=\pi\rho_1L/4V. \quad (15)$$

This corresponds to a lens of zero Gaussian strength but finite spherical aberration.

## CORRECTION OF CHROMATIC ABERRATION

We will consider the system shown in Fig. 4. The image is at infinity, an idealization of the case of large magnification which is of greatest interest in practice. Under these conditions the action of the space charge is equivalent to that of a thin lens of focal length $F$, located at one of the principal planes. The converging lens which may be magnetic or electric, will for the present also be taken as "thin," in the sense that the separation between the principal planes is small compared with $a_2$. If the converging lens is electrostatic, it will also be considered "weak," in the sense that the fractional potential variation in the lens region is to be small. We will formulate the condition for zero chromatic aberration and see whether this is compatible with a total resultant converging action for the combination. Using the thin lens formula familiar from optics,[8] and with the sign convention indicated in the caption to Fig. 4,

$$a_1=\frac{f(a_3-F)}{F+f-a_3}. \quad (16)$$

The condition for zero chromatic aberration is

$$da_1/dV=0. \quad (17)$$

From Eqs. (9) and (10) this condition may be written in the form

$$\frac{1}{f^2}\frac{df}{dV}=\frac{P}{2V}\left\{\frac{PL+\sinh PL\cosh PL}{(Pa_2\sinh PL+\cosh PL)^2}\right\}. \quad (18)$$

The condition has been expressed in terms of $a_2$ rather than of $a_3$ as the latter is itself a function of the strength of the space charge lens. The dependence of $f$ on $V$ will

[8] A. C. Hardy and F. H. Perrin, *The Principles of Optics* (McGraw-Hill Book Company, Inc., New York, 1932).

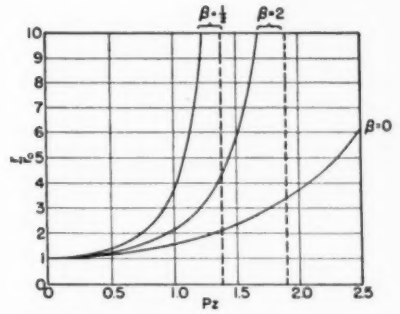


FIG. 3. Electron trajectories for an electron moving initially in a direction parallel to the axis and incident at the radius $r_0$. The radial distribution of density is $\rho=\rho_0(1+\beta r^2)$. The trajectories for values of $\beta>0$ are asymptotic to the ordinates shown dotted.

be described by the equation

$$f=cV^\alpha, \quad (19)$$

where $\alpha=1$ for the thin magnetic lens and $\alpha=2$ for the thin and weak electric lens. From Eqs. (18) and (19)

$$(PcV^\alpha)^{-1}=\frac{1}{2\alpha}\frac{PL+\sinh PL\cosh PL}{(Pa_2\sinh PL+\cosh PL)^2}. \quad (20)$$

To ensure a resultant convergent action, we require

$$a_1<0. \quad (21)$$

This condition can be expressed in terms of the lens constants and $a_2$ by means of Eqs. (9), (16), and (19).

$$\left.\begin{aligned} ncV^\alpha&=a_2+(P\tanh PL)^{-1}\\ n&>1.\end{aligned}\right\} \quad (22)$$

We can eliminate $c$ between Eqs. (20) and (22), and express the condition for simultaneous achromatization and resultant convergent action in the form

$$1<n=\frac{1}{2\alpha}\frac{PL+\sinh PL\cosh PL}{\sinh PL(Pa_2\sinh PL+\cosh PL)}. \quad (23)$$

Inspection of Eq. (23) shows that this condition cannot be satisfied unless $n>1/\alpha$. Reference to Eq. (19) reveals that neither the thin electric or magnetic lens satisfies this condition.

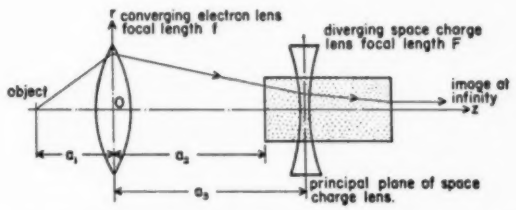


FIG. 4. Dimensions relating to the combination of a converging electron lens with a divergent space charge lens. The magnification of the combination is large so that the image may be considered to be at infinity. Distances measured in the direction of motion are taken as positive. On this convention $f$ is positive and $F$ negative.

We conclude that the achromatization of a thin lens by the system of Fig. 4 is not possible if the resultant action of the combination is to be convergent. The proof does not exclude the possibility of correcting a thick lens in this way, a possibility which could be examined only by a detailed consideration of the positions of the principal planes as a function of lens strength.

## CORRECTION OF SPHERICAL ABERRATION

We turn now to the problem of correcting the spherical aberration of a converging lens. The success of this scheme hinges on the question of whether the electron interaction effects are sufficiently small not to interfere with the imaging properties of the space charge cloud. If the random microscopic field due to the discrete nature of the space charge is of the same order as the macroscopic field required for correcting the lens, it is clear that the space charge can serve no useful purpose. The exact magnitude of the electron interaction effect* is not known with precision, but a reliable lower limit is expressed by the following equation:[9]

$$\theta \gtrsim 1.1\times 10^{-6}(NL)^{\frac{1}{2}}/V, \tag{24}$$

where $\theta$ is the rms scattering angle imposed on a beam accelerated by $V$ volts, in traversing a space charge cloud of length $L$, and density $N$ electrons/cm$^3$.

We will consider again the system of Fig. 4 and as before confine our attention to the case of importance in practice, $M\gg 1$. This allows us to treat the converging lens as if it were thin, and placed at the appropriate principal plane of the actual thick lens. Moreover, since the image will be far away, we may neglect the distance between the converging and the space charge lens. Thus we may apply the condition of zero s.a. for the case of "two thin lenses in contact" familiar from optics.

$$C_f/f^3=C_F/F^3, \tag{25}$$

where $C_f$ and $C_F$ are the nondimensional spherical aberration coefficients for the converging and the space charge lenses, respectively. In Eq. (14) we obtained an expression for the quantity $C_F/F_0^3$. In order to minimize the effect of electron interaction we see from Eq. (24) that $N$ must be kept as small as possible. We consider therefore the case of $\rho_0=0$, so that the Gaussian strength of the space charge lens will be zero. Thus, rewriting Eq. (15),

$$(C_F/F^3)_{\rho_0=0}=\pi\rho_1 L/4V. \tag{26}$$

We will proceed to calculate $\rho_1$ for a particular lens, corresponding to a typical high quality magnetic electron microscope objective. Taking $C_f=0.4$, $f=0.4$ cm, $V=50$ kv, $L=1$ cm, we find $\rho_1=3.3\times 10^{12}$.

It the objective has an aperture of 50$\mu$ (which is of the order required if an over-all improvement in resolution limit is to be achieved), the space charge density at the rim of the aperture will be $2\times 10^7$ electrons/cm$^3$. Using Eq. (24) it is possible to obtain a lower limit for the resolution limit imposed by electron interaction; in this example the limit is 10 A—of the same order as that of the uncorrected objective. This result can be readily understood when it is realised that the electron density required for correction corresponds to a mean distance between electrons of the same order as the aperture radius. Under these conditions it is not surprising that the random microscopic field of the space charge is as important as the macroscopic field. It must be concluded that the electron is too crude a tool to permit its use for the reduction of the spherical aberration of a high quality objective.

## CONCLUSIONS

Some of the electron optical properties of an isolated space charge cloud have been derived. The possibility of obtaining a combination of a space charge lens with a space charge free converging lens which is free from spherical or chromatic aberration has been investigated.

The discussion of achromatization leads to the conclusion that it is not possible to correct either the thin electric or the thin magnetic lens, if the resultant action of the combination is to be convergent.

The possibility of reducing the spherical aberration of an electron microscope objective is also rejected. The calculation shows that the random microscopic field due to the discrete nature of the space charge is greater than the small macroscopic field required for correcting the spherical aberration.

The system considered in both these cases was one in which the space charge fields do not overlap with the converging lens fields; the space charge was considered to be uniform over its length. It is not believed that the conclusions would be changed if these restrictions were removed.

## ACKNOWLEDGMENTS

The author would like to express his gratitude to Professor Willis Jackson, and to Dr. D. Gabor for encouragement and advice in the course of the work presented in this paper; Dr. Gabor suggested the problem. The work was carried out in the Electrical Engineering Department of Imperial College, London, during 1951-1952, as part of a doctorial dissertation. The author would like to acknowledge the support of the Institution of Electrical Engineers through the Oliver Lodge Scholarship which he held in this period.

* This effect is not to be confused with the random field which can be observed, for example in the rotating space charge cloud of a static magnetron (see L. Marton and D. Reverdin, J. Appl. Phys. **21**, 842 (1950)), an effect which is attributable to thermally excited macroscopic fluctuations.

[9] L. H. Thomas, Proc. Roy. Soc. (London) **A121**, 464 (1928).

JOURNAL OF APPLIED PHYSICS VOLUME 26, NUMBER 3 MARCH, 1955

# Radiation Characteristics of a Conical Helix of Low Pitch Angle

J. S. CHATTERJEE
*Institute of Radio Physics and Electronics, Calcutta University, Calcutta, India*
(Received August 10, 1953)

The present work is an extension of the author's prior work on the radiation characteristics of and current distribution in a conical helix, the helix used in the present case having a pitch angle much lower than of that studied previously. In this case the condition of the phase velocity adjusting itself automatically to maintain maximum directivity condition (which enables the radiation to be confined in the axial mode over a large band of frequencies) does not hold. Nevertheless the major fraction of energy could be radiated in the axial direction when the geometry of the helix and the distance of the apex from the ground were properly chosen, the conical helix together with the ground being regarded as tapered transmission lines (with the ground as one and the helix wire—with the distance of its elements from the ground line increasing continually,—as the other line).

Measurements of the field intensity and the current distribution were made in the frequency range of 100 Mc/sec to 500 Mc/sec with a conical helix antenna arrangement as follows. The helix was of six turns, the radius increasing uniformly from 5 cm at the apex to 65 cm at the base within an axial distance of 60 cm. The apex of the helix was placed at a distance of 17.5 cm from the "ground" provided by a 6-ft square copper netting of close mesh. It was found that within the range of frequency measured the major fraction of the energy was radiated in the axial direction. Theoretical expressions for $E_\phi$ and $E_\theta$ were derived by assuming a linear current distribution, and the calculated radiation patterns were found to agree with the experimentally determined ones.

## I. INTRODUCTION

A CYLINDRICAL helix is known to act as an efficient antenna when the length of one turn of the helix is comparable with the wavelength. Depending upon the ratio of the diameter to wavelength and pitch angle, the helix can radiate in three different modes. When the helix is conical, instead of cylindrical, its radiation characteristics change markedly. This has been studied[1] by the author for the case of a conical helix with pitch angle of 6°. It was found that when the base was near the ground and the feed was at the apex, the axial mode of radiation could be maintained over a band width much greater than one octave. Further, depending upon the limitations imposed by the practical difficulty of obtaining the smallest radius at the apex of the helix the band width can be increased to any desired extent.

In both the cylindrical and conical helices studied the maintenance of the axial mode of radiation over a large band width is due to the fact that the phase velocity along the helical conductor so adjusts itself automatically, that the condition of maximum directivity along the axis holds.[2] Further, in all these antennas, the "ground" plane is provided by a small conducting sheet placed very close to the helix, the "ground" serving as a launching device rather than as an image plane.

In this present paper we will describe the results of investigations on the radiation characteristics of a conical helix with pitch angle much lower than that studied above. The pitch angle, in fact, is so low that the condition of automatic adjustment of phase velocity does not hold. Further, the "ground" plane is made sufficiently large to allow the image to be well formed. Under such conditions the helix, mounted with its apex at a small appropriate distance above the "ground" plane, was found to radiate in the axial direction over a frequency range 5:1, which is much higher than the range for the conical helix previously considered.

In the next section will be described the results of experiments made on the determination of the polar diagram and the charge distribution along the length of such a conical helix of low pitch angle. Analysis for theoretical determination of the radiation pattern will then follow.

## 2. EXPERIMENTS WITH THE CONICAL HELIX

The conical helix used had the following dimensions. It was made of $\frac{5}{32}$-in. brass rod and had 6 turns. The radius at the apex was 5 cm and increased uniformly to 65 cm at the base within a height of 60 cm. A copper wire netting (40 per in., 6 ft square) provided the "ground." The apex of the helix was at a distance of 17.5 cm from the ground plane. It was excited by a

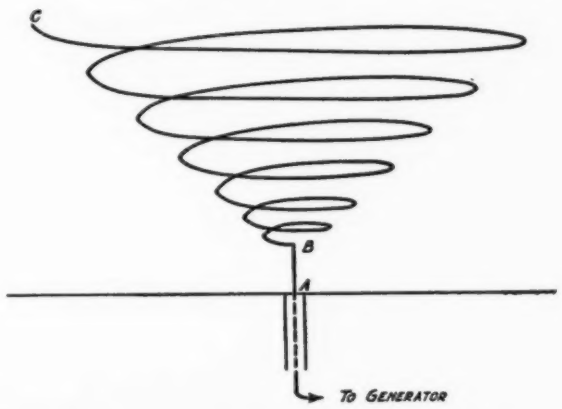


FIG. 1. Illustrating the method of feeding energy to the conical helix with respect to "ground."

[1] J. S. Chatterjee, J. Appl. Phys. **24**, 550 (1953).
[2] J. D. Kraus. Proc. Inst. Radio Engrs. **37**, 263 (1949).

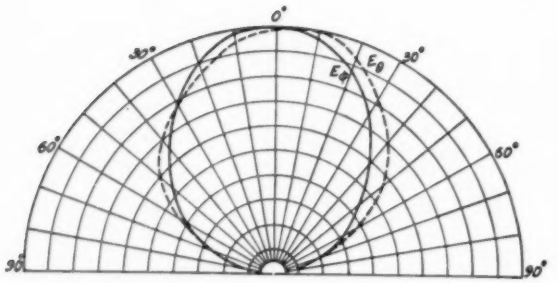


(a)

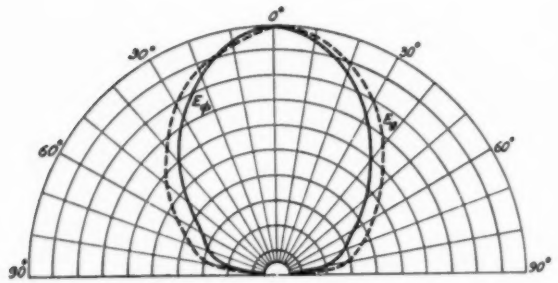


(b)

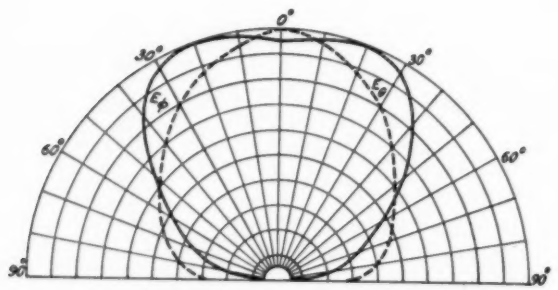


(c)

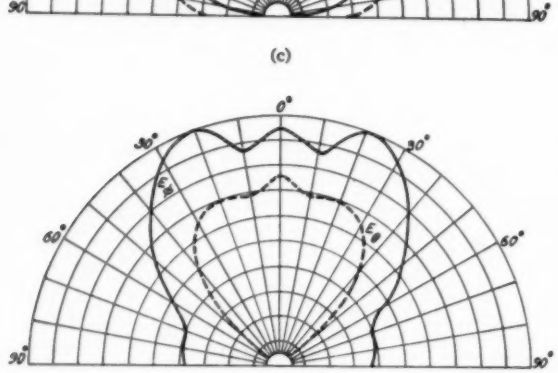


(d)

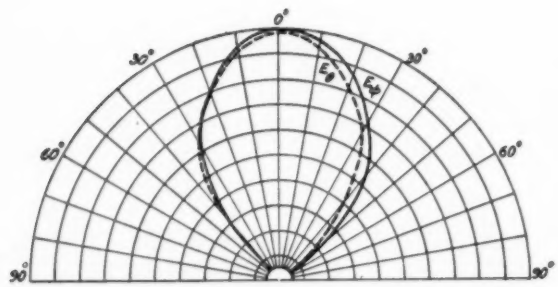


(e)

co-axial feeder, the outer conductor of which was connected to the ground plane and the inner to the apex as shown in Fig. 1. For the purpose of field measurements the helix system was mounted 12 ft above the floor level with the axis horizontal.

### Measurement of Electric Field

The vertical and horizontal components of the electric field were measured with a small dipole placed at a distant point and at the same height as the axis of the helical antenna. The polar diagrams obtained for a number of frequencies in the range 100 Mc to 500 Mc are shown in Fig. 2. The frequencies were fairly closely spaced and it was unlikely that the radiation patterns deteriorated in any of the intermediate frequencies. This is because the radiation patterns were not found to change markedly in form from one frequency to the next.

### Measurement of Charge Distribution

The charge distribution was measured by coupling capacitively a small probe to different parts of the helix conductor. The charge distribution for a number of frequencies in the range 100 Mc–500 Mc are shown in Figs. 3 and 4. The polar diagrams show that over a large range of frequencies the major fraction of the energy is radiated in the axial direction.

The following points may be noted from the charge distribution curves.

(a) The current is gradually attenuated along the helix and, for frequencies higher than 220 Mc, the current is completely attenuated at the end becoming entirely progressive. The charge and current distributions in this case are identical.

(b) For frequencies lower than 220 Mc, the current is not completely attenuated at the end and hence there is reflection. There are thus standing waves at the end of the helix due to which polar diagrams may be expected to be different from the case when only progressive current exists. If, however the reflected wave is not strong, its effect at the input end is negligible since it is further attenuated as it travels backwards.

(c) It follows from (a) that the helix presents a constant impedance at the input for all frequencies higher than 220 Mc.

## 3. THEORETICAL ANALYSIS

We shall derive expressions for the radiation field in the $\theta$ plane for the case when only progressive current is present. The radiation field for the general case can

FIG. 2. (a) $E_\phi$ and $E_\theta$ radiation patterns of the conical helix shown in Fig. 1. Frequency, 100 Mc/sec. (b) $E_\phi$ and $E_\theta$ radiation pattern of the conical helix shown in Fig. 1. Frequency, 220 Mc/sec. (c) $E_\phi$ and $E_\theta$ radiation pattern of the conical helix shown in Fig. 1. Frequency, 300 Mc/sec. (d) $E_\phi$ and $E_\theta$ radiation pattern of the conical helix in Fig. 1. Frequency, 400 Mc/sec. (e) $E_\phi$ and $E_\theta$ radiation patterns of the conical helix shown in Fig. 1. Frequency, 500 Mc/sec.

be obtained by adding the field produced by the reflected wave in correct phase.

The field at a distant point consists of the following components: (a) field of the helix $BC$ (Fig. 1), (b) field of the image of the helix, (c) field of the length $AB$ (Fig. 1), and (d) field of the image of (c).

We will calculate the fields separately for each of the above components and add them vectorially to get the total radiation field.

The electric field[3] at the distant point is given by

$$E=\frac{j\omega\mu_0}{4\pi R}\int[\mathbf{r}_0\times(\mathbf{r}_0\times\mathbf{s}_0)]Ie^{-j\beta R}ds, \qquad (1)$$

where $\omega$ = angular frequency, $\mu_0$ = the absolute permeability of space, $ds$ = an element of the helix conductor carrying a current $I$, $R$ = distance from the elements $ds$ of the point at which electric field is to be calculated, $\mathbf{r}_0$ = the unit radial vector in a spherical co-ordinate system $(r,\theta,\phi)$ with the helix at the origin,

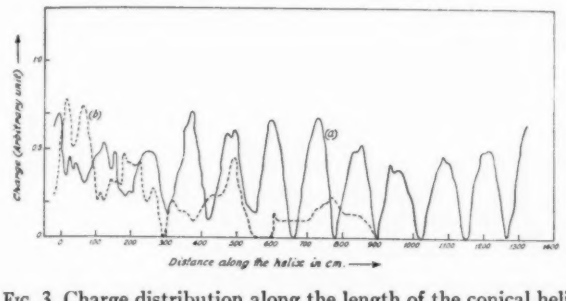


FIG. 3. Charge distribution along the length of the conical helix shown in Fig. 1. The zero point of the abscissa is at $B$. Excitation frequency, (a) 100 Mc/sec, (b) 220 Mc/sec.

and $\mathbf{s}_0$ = the unit vector along the axis of the helix conductor.

To calculate the field of the helix we first calculate the field for one of the turns and then combine the fields of all the turns. This is possible if the phase velocity along the helix is known.

The equation of the form of a simple conical helix in cylindrical coordinates is given by

$$a=a_0(1+k\phi), \qquad (2)$$

where $a$ = the distance of an element from the axis. Also

$$dz=a\tan\alpha d\phi, \qquad (3)$$

or

$$z=\int_0^{\phi}a_0(1+k\phi)\tan\alpha d\phi$$

$$=a_0\tan\alpha(1+\tfrac{1}{2}k\phi)\phi, \qquad (4)$$

where $\alpha$ = the inclination of an element of the antenna with the horizontal plane and is constant. From the

[3] R. W. P. King, *Electromagnetic Engineering* (McGraw-Hill Book Company, Inc., New York, 1945), Vol. I, p. 271.

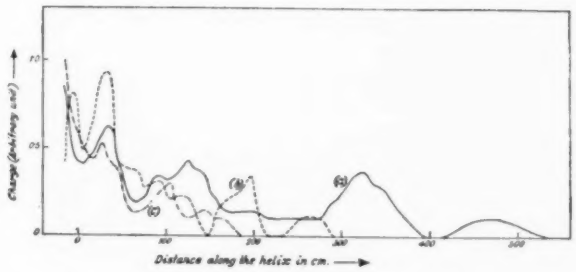


FIG. 4. Charge distribution along the length of the conical helix shown in Fig. 1. The zero point of the abscissa is at $B$. Excitation frequency, (a) 300 Mc/sec, (b) 400 Mc/sec, (c) 500 Mc/sec.

helix geometry it follows that for the $m$th turns,

$$ds=a_m(1+k_m\phi), \qquad (5)$$

$$s=a_m\sec\alpha(1+\tfrac{1}{2}k_m\phi)\phi, \qquad (6)$$

where $s$ = length of helix conductor from 0 to $\phi$. The distance of an element $ds$ in the $m$th turn from the distant point is given by (Fig. 5) where $z_m$ and $a_m$ are the values of $z$ and $a$ at $\phi=0$ in the $m$th turn, and $k_m$ is the value of $k$ when the equation of the helix is written such that $\phi=0$ at the center of $m$th turn.

$$R_m=R_0-(z_m+z)\cos\theta-a\sin\theta\cos\phi$$
$$=R_0-z_m\cos\theta-a_m\tan\alpha\phi(1+\tfrac{1}{2}k_m\phi)\cos\theta$$
$$-a_m(1+k_m\phi)\sin\theta\cos\phi, \qquad (7)$$

The current falls off exponentially along the helical conductor. For simplicity of calculation it is, however, assumed that the current is constant over a turn and then changes by appropriate amount in the next adjacent turn. Thus, the current in the $m$th turn is given by

$$I=I_m'e^{-j\nu_m}e^{-j\beta s}, \qquad (8)$$

where $I_m'$ is the value of current at $\phi=0$ in the $m$th turn and $\nu_m$ is the phase difference between the center of $m$th turn and current at the input.

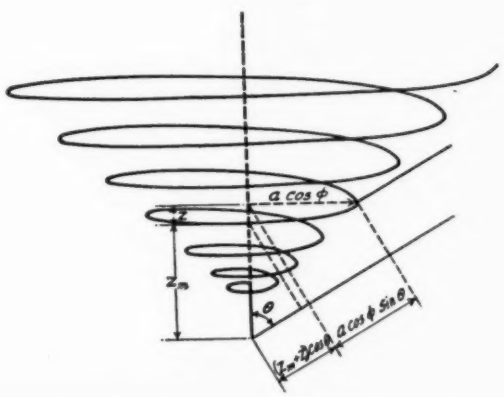


FIG. 5. Illustrating the calculation of the distance from a point in the far zone, of an element $ds$ of a loop of the helix with reference to the distance of the same point from the origin.

Substituting Eqs. (8) and (5) in Eq. (1),

$$E_m=\frac{j\omega\mu_0}{4\pi R_0}\int[-\boldsymbol{\phi}s_\phi-\boldsymbol{\theta}s_\theta]I_m'e^{-j\nu_m}e^{-j\beta R_m}\times a_m(1+k_m\phi)\sec\alpha]d\phi. \quad (9)$$

In this equation we have replaced $R_m$ by $R_0$, except in the phase term. The direction cosines between $\mathbf{s}_0$ and the $\phi$, $\theta$, spherical coordinate axes are given by

$$S_\phi=\cos\alpha\left[\cos\phi+\frac{k_m\sin\phi}{1+k_m\phi}\right], \quad (10)$$

$$S_\theta=-\cos\alpha\cos\theta\left[\sin\phi-\frac{k_m\cos\phi}{1+k_m\phi}\right]-\sin\alpha\sin\theta. \quad (11)$$

Substituting Eqs. (7) and (10) in Eq. (9) and rearranging terms, the component of the electric field at the distant point for the $m$th turn is given by

$$E_\phi{}^m=-\frac{j\omega\mu_0e^{-j\beta R_0}}{4\pi R_0}a_mI_me^{-j\nu_m}e^{j\beta z_m\cos\theta}\times\int_{-\pi}^{+\pi}\left[\{\cos\phi(1+k_m\phi)+k_m\sin\phi\}\times\exp-j(\beta a_m\sec\alpha-\beta a_m\tan\alpha\cos\theta)\phi\times\exp-j\left(\beta a_m\sec\alpha\frac{k_m}{2}-\beta\alpha_m\frac{k_m}{2}\tan\alpha\cos\theta\right)\phi^2\times\exp(\delta j\beta a_m\sin\theta\cos\phi)\times\exp(j\beta a_mk_m\sin\theta\phi\cos\phi)\right]d\phi. \quad (12)$$

We introduce the following abbreviations,

$$E_0=\frac{j\omega\mu_0I_0\exp(-j\beta R_0)}{4\pi R_0},$$

$$g_m=\beta a_m\sec\alpha,$$

$$b_{\theta m}=\beta a_m\tan\alpha\cos\theta,$$

$$D'=\beta a_m\sec\alpha\frac{k_m}{2}-\tfrac{1}{2}a_mk_m\beta\tan\alpha\cos\theta=D-\delta,$$

$$p_{\theta m}=\beta a_mk_m\sin\theta,$$

$$d_{\theta m}=\beta a_m\sin\theta,$$

$$\eta_{\theta m}=\beta z_m\cos\theta,$$

$$I_m'/I_0=I_m. \quad (13)$$

Since $D'$ is small and $\phi^2\leqq\pi^2$, we put

$$\exp(-jD'\phi^2)\doteqdot(1-jD'\phi^2). \quad (14)$$

Further, since $p_{\theta m}$ is very small except near $\theta=\pi/2$ and $\phi=\pi$, we put

$$\exp(jp_{\theta m}\phi\cos\phi)\doteqdot 1. \quad (15)$$

We also note that

$$\exp(jd_{\theta m}\cos\phi)\sum_{-\infty}^{+\infty}\gamma^nJ_n(d_{\theta m})\exp(jn\phi, \quad (16)$$

where $J_n(d_{\theta m})$ is the $n$th root of the Bessel function for the argument $d_{\theta m}$.

Using (14), (15), and (16), and neglecting $k_mD'\phi^2$ and $k_mD'\phi^3$, the field $E_{\phi h}$ due to helix alone is obtained by carrying out the integration in Eq. (12) and is given by

$$E_{\phi h}=-E_0\sum_{m=1}^{N}a_mI_me^{-j\nu_m}e^{j\eta_{\theta m}}\sum_{-\infty}^{+\infty}j^nJ_n(d_{\theta m})\times\left[\left\{(1-jk_m)\frac{\sin x\pi}{x}+k_m\left(-j\pi\frac{\cos x\pi}{x}+j\frac{\sin x\pi}{x^2}\right)-jD'\left(\pi^2\frac{\sin x\pi}{x}+\frac{2\pi\cos x\pi}{x^2}-\frac{2\sin x\pi}{x^3}\right)\right\}+\left\{(1+jk_m)\frac{\sin y\pi}{y}+k_m\left(-j\pi\frac{\cos y\pi}{y}+j\frac{\sin y\pi}{y^2}\right)-jD'\left(\pi^2\frac{\sin y\pi}{y}+2\pi\frac{\cos y\pi}{y^2}-\frac{2\sin y\pi}{y^3}\right)\right\}\right], \quad (17)$$

where

$$x=n-g_m+b_{\theta m}+1=\nu+1,$$
$$y=n-g_m+b_{\theta m}-1=\nu-1. \quad (18)$$

Putting

$$j\pi\frac{\cos x\pi}{x}+j\frac{\sin x\pi}{x}=f_x, \quad (19)$$

$$\pi^2\frac{\sin x\pi}{x}+2\pi\frac{\cos x\pi}{x^2}-\frac{2\sin x\pi}{x^3}=F_x, \quad (20)$$

the total field due to the real source and image is given by

$$E_\phi=E_0\sum_{m=1}^{N}a_mI_m\exp(-j\nu_m)\sum_{-\infty}^{+\infty}j^nJ_n(d_{\theta m})\times\left[\left\{(1-jk_m)\left(\frac{\sin x'\pi}{x'}e^{-j\eta_{\theta m}}-\frac{\sin x\pi}{x}e^{j\eta_{\theta m}}\right)+(1+jk_m)\left(\frac{\sin y'\pi}{y'}e^{-j\eta_{\theta m}}-\frac{\sin y\pi}{y}e^{j\eta_{\theta m}}\right)+k_m\{(f_{x'}+f_{y'})e^{-j\eta_{\theta m}}-(f_x+f_y)e^{j\eta_{\theta m}}\}-jD\{(F_{x'}+F_y')e^{-j\eta_{\theta m}}-(F_x+F_y)e^{j\eta_{\theta m}}\}\right], \quad (21)$$

where

$$x'=n-b_{\theta m}-g_m+1=\nu'+1,$$

$$y'=n-b_{\theta m}-g_m-1=\nu'-1.$$

In Eq. (21) we have neglected $\delta$.

To calculate the $\theta$ component of the electric field we note that $E_\theta$ is given by

$$E_\theta=E_{\theta h}+E_{\theta h}'+(E_{\theta A}+E_{\theta A}'), \tag{22}$$

where $E_{\theta h}$ = field produced by the helix, $E_{\theta h}'$ = field produced by the image of the helix, and $E_{\theta A}$ and $E_{\theta A}'$ are fields caused by the axial length of the antenna and its image, respectively.

We note that

$$E_{\theta A}+E_{\theta A}'=-2E_0 lj\sin\theta\frac{1-\cos\beta l(1-\cos\theta)}{\beta l(1-\cos\theta)}, \tag{23}$$

where $l$, the length $AB$ (Fig. 1) carries a uniform current $I_0$.

Proceeding as before we obtain from Eq. (22) the $\theta$ component of the electric field $E_\theta$, which is given by

$$E_\theta=E_0\sum_{m=1}^{N}a_mI_m\exp(-j\nu_m)\sum_{-\infty}^{+\infty}j^nJ_n(d_{\theta m})$$

$$\times\Big[\cos\theta\Big\{(-j-k_m)\Big(\frac{\sin x'\pi}{x'}e^{-j\eta_{\theta m}}-\frac{\sin x\pi}{x}e^{j\eta_{\theta m}}\Big)$$

$$\times(-j+k_m)\Big(\frac{\sin y'\pi}{y'}e^{-j\eta_{\theta m}}-\frac{\sin y\pi}{y}e^{j\eta_{\theta m}}\Big)\Big\}$$

$$-k_m\cos\theta\{(f_{x'}-f_{y'})e^{-j\eta_{\theta m}}-(f_x-f_y)e^{j\eta_{\theta m}}\}$$

$$+D\cos\theta\{(F_{x'}-F_{y'})e^{-j\eta_{\theta m}}-(F_x-F_y)e^{j\eta_{\theta m}}\}$$

$$+2\sin\theta\tan\alpha\Big\{\Big(\frac{\sin\nu'\pi}{\nu'}e^{-j\eta_{\theta m}}-\frac{\sin\nu\pi}{\nu}e^{j\eta_{\theta m}}\Big)$$

$$+jk_m(f_{\nu'}e^{-j\eta_{\theta m}}-f_\nu e^{j\eta_{\theta m}})-jD(F_{\nu'}e^{-j\eta_{\theta m}}+F_\nu e^{j\eta_{\theta m}})\Big\}$$

$$-2E_0 lj\sin\theta\frac{1-\cos\beta l(1-\cos\theta)}{\beta l(1-\cos\theta)}\Big]. \tag{24}$$

## 4. DISCUSSION

The $E_\phi$ and $E_\theta$ components of the electric field at the distant point may be computed from the right-hand expressions of Eqs. (21) and (24), respectively. The expressions are long and complicated but fortunately, for practical computation, a number of approximating assumptions may be made since some of the terms are quite small compared to others. For example, the terms involving $\tan\alpha$ may be neglected as $\tan\alpha=0.045$. Again, in most of the cases only the terms $J_0(d_{\theta m})$ and $J_{\pm1}(d_{\theta m})$ in the summation $\sum_{-\infty}^{+\infty}j^nJ_n(d_{\theta m})$ need be retained. The higher order term $J_2(d_{\theta m})$ needs consideration only for the fields due to bigger turns and for large angles. Also, $\sum_{m=1}^{N}a_mI_m$ need not be considered for all the turns, as its contribution is significant only for the turns in which the current has not died out completely. Thus, in the case of 300 Mc, only 4 turns are to be considered, because the current in the fifth turn is zero. The computed values of $E_\phi$ and $E_\theta$ from Eqs. (21) and (24) for 300 Mc are plotted in Fig. 6 for comparison with the experimentally obtained curves. Only first-order terms have been retained in the computation.

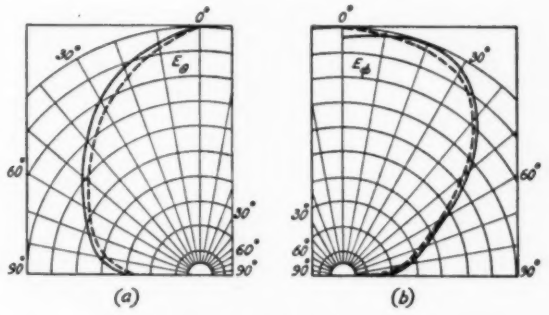


FIG. 6. Calculated (dotted lines) and experimentally observed (solid lines) radiation patterns of (a) $E_\theta$ and (b) $E_\phi$. Frequency, 300 Mc/sec.

An examination of the curves in Fig. 2 shows that over a large band of frequencies the radiation pattern from the conical helix with low pitch angle is a single lobe with the maximum in the axial direction. This effect is similar to that already considered for a conical helix with moderate pitch angle, though as already pointed out, the condition of phase velocity adjustment, necessary for maximum directivity condition does not hold in this case. That a major fraction of energy is still radiated in the axial direction is due to the fact that the geometry of the helix and the distance of the apex from the ground have been chosen appropriately. The conical helix together with the ground in this case may be regarded as tapered transmission lines. The ground is one of the "lines" and the helix wire, with the distance of its elements from the ground continually increasing, is the other "line."

Regarding the property of maintenance of axial mode of radiation over a large band of frequencies, there is little to choose between the two types of conical helices (moderate or low pitch angle). For radiation in the vertical direction, the latter, however, on account of its smaller axial height for the number of turns required, possesses a greater practical advantage over the former where the helix is to be designed for low frequencies. This is because for such frequencies helices of moderate pitch angle become unmanageably large.

## ACKNOWLEDGMENT

Grateful thanks are due Professor S. K. Mitra for constant encouragement and many helpful discussions during preparation of the paper.

# Studies of the Diffraction of Electromagnetic Waves by Circular Apertures and Complementary Obstacles: The Near-Zone Field

MORRIS J. EHRLICH,* SAMUEL SILVER,† AND GEDELIAHU HELD
*Electronics Research Laboratory, Division of Electrical Engineering, University of California, Berkeley, California*
(Received April 5, 1954)

The diffraction of electromagnetic waves by circular apertures in extended conducting screens and by complementary obstacles was investigated experimentally to determine the structure of the field in the near zone. Techniques for measuring both the electric and magnetic field distributions are presented and the general experimental problems are discussed. Data are given for the tangential components of the electric and magnetic vectors in the principal planes in the immediate neighborhood of the diffracting structures, and axial distributions for the corresponding components. The results extend the range of the data available previously. The predicted uniformity of the tangential magnetic field in the aperture plane, for the case of a wave incident normally, is verified. An experimental test was made also of the electromagnetic Babinet principle.

## INTRODUCTION

THE classical problems of diffraction by apertures constitute a major topic in the field of microwave optics. They have become increasingly important with the growth of the microwave techniques of using lenses and reflectors to produce beams of various shapes. Diffraction theory is also a fundamental aspect of the general subject of slot radiators. While the general outlines of a rigorous treatment of the diffraction of electromagnetic waves by aperture systems is quite clear there are many details to be filled in. Suitable approximation techniques for calculating the far-zone field are available and the well-known developments of variational principles for the far-zone field by Levine and Schwinger[1] have placed those techniques in their proper setting in relation to exact theory. The subject of the near-zone field, however, when the dimensions of the aperture exceed several wavelengths, is still enveloped by complexities of the computations and is in need of more extensive study. It is now recognized that a more complete knowledge of the near-zone field structure is required to make further progress possible on the practical side.

Much can be learned from the planar diffraction problems: diffraction by apertures in infinite perfectly conducting screens of zero thickness and by complementary thin obstacles having the same size and shape as the apertures. The work of Andrews[2] on the tangential electric field distribution in the plane of a circular aperture and its immediate neighborhood generated much interest in the subject after the war. Notable contributions of experimental data and approximate theory have been made by Woonton and his co-workers[3] at McGill University and by Severin[4] in Germany. Bouwkamp[5] has developed the correct asymptotic behavior of the exact solution for a circular aperture for diameters that are very small compared with the wavelength, and Meixner and Andrejewski[6] have obtained a rigorous solution in terms of spheroidal functions and have succeeded in converting it into numerical form for diameters comparable with the wavelength. The problem has engaged our attention for some time and under the auspices of the Office of Naval Research we have been conducting an experimental and theoretical study of the near-zone field of a circular diffracting structure. We have extended the range of the data to a diameter of $36\lambda$ and have made magnetic field measurements as well as the more usual electric field measurements. Brief surveys of the project[7] have been presented at several specialized symposia. The purpose of this paper is to make our results more available than they are in the form of our technical reports.[8]

We shall confine our attention in this paper to experimental techniques and results. At a later date we shall present a report of our various theoretical investigations. The measurements are quite tedious and many more are yet to be taken to make up a complete map of the field. Like other workers on this problem we have concentrated on the field distributions in the principal planes for the case of a wave incident normally on the

* Now with the Microwave Radiation Company, Venice, California.

† On leave 1953–1954; John Simon Guggenheim Foundation Fellow, currently at the Cavendish Laboratory, Cambridge University.

[1] H. Levine and J. Schwinger, Phys. Rev. **74**, 958 (1948); **75**, 1423 (1949). Comm. Pure and Appl. Math. **3**, No. 4, 355 (1950).

[2] C. L. Andrews, Phys. Rev. **71**, 777 (1947); also J. Appl. Phys. **21**, 761 (1950).

[3] G. A. Woonton, Eaton Electronics Research Laboratory Tech. Rept. No. 17 (1952); R. B. Borts and G. A. Woonton, Eaton Electronics Research Laboratory Tech. Rept. No. 21 (1952); G. Bekefi and G. A. Woonton, Eaton Electronics Research Laboratory Tech. Rept. No. 24 (1952).

[4] H. Severin, Z. Naturforsch. **1**, 487 (1946); Nuovo cimento, Suppl. to Vol. IX, 381 (1953); Z. angew. Phys. **2**, No. 12, 499 (1950).

[5] C. J. Bouwkamp, Philips Research Repts. **5**, 321, 401 (1950).

[6] J. Meixner and W. Andrejewski, Ann. Physik **7**, 157 (1950); W. Andrejewski, Naturwissenschaften **38**, 406 (1951).

[7] S. Silver, Proc. Ninth General Assembly of the Union Radio Scientifique Internationale, Vol. 2 (1950); Nuovo cimento, Suppl. to Vol. IX, 400 (1953).

[8] (a) M. J. Ehrlich, Ph.D. thesis (1951); (b) S. Silver and M. J. Ehrlich, Antenna Laboratory Rept. No. 181 (1951); (c) Silver, Ehrlich, and Held, Antenna Laboratory Rept. No. 185 (1952), University of California, Berkeley.

diffracting structure. Further work is yet to be done on oblique incidence and other types of controlled phase errors over the aperture, on the depolarization effect of an aperture, and, of course, on apertures of other than circular shape.‡

## EXPERIMENTAL TECHNIQUES

The two basic types of setups—a full-space and a half-space system—are shown in Fig. 1. The incident wave is ideally a linearly polarized plane wave. When the aperture (obstacle) has a set of planes of symmetry and the incident electric vector is parallel to one of those planes the diffraction field has likewise a set of orthogonal symmetry planes. The one containing the incident electric vector is known as the principal $E$ plane; the one transverse to it, which contains the incident magnetic vector, is known as the principal $H$ plane. The half-space technique is based on the fact that if the region is bisected by an infinite perfectly conducting sheet in the $H$ plane the field remains the same in the two half-spaces.

In the study of the aperture field the screen must be large enough to represent a practical realization of the infinite screen. One criterion of a practical realization is that the effect of diffraction by the edges of the screen is negligible in the region of the aperture field. The size of the apparatus scales with the wavelength, assuming that the primary feed system is being scaled in the same way. With regard to over-all size the shorter the wavelength the better. However, from the standpoint of the relationship which the size of the aperture bears to the reliability of measurements close to the aperture the longer the wavelength the better. In the case of the half-space technique the size of the ground plane is a significant factor, and advantage of size accrues with decreasing wavelength. We have found the 3-cm region to be a satisfactory compromise between the factors of size and ease and accuracy of measurement for diameters ranging from one to sixteen wavelengths. The same equipment could then be used at a wavelength of one centimeter to study larger values of $D/\lambda$. We found that at a nominal wavelength of 3.2 cm a screen sixty wavelengths on a side provides a sufficient approach to the infinite screen for all the aperture sizes involved, and a ground plane 150 wavelengths long is a reasonable approximation to the infinite $H$-plane sheet. Even at that it was necessary to set up an absorbing wall around the boundary of the ground plane to eliminate edge effects and also to provide protection from stray scattering by nearby objects.

In the theoretical treatment of the diffraction problem it is usually assumed that the incident field is an infinite homogeneous plane wave. It is, therefore, desirable to approach that type of illumination as closely as possible practically. The use of a collimated beam obtained by means of a paraboloidal reflector or a lens, as was done by Andrews, is a satisfactory method provided that the screen or obstacle is far enough away from the "optical" system. A reflector (or lens) has a near-zone field very like that of the aperture in a screen. The structure does not smooth out until the distance from the aperture is $D^2/\lambda$. To obtain a good amplitude and phase distribution over the aperture in the screen it is desirable to have it located at a distance from the optical system somewhat greater than $D_{opt}^2/\lambda$. The result is that a large physical space is required for the setup.

We have preferred to use a horn having a rather small aperture so that the screen could be located conveniently in the far zone of the horn. The beam from such a horn is quite broad and it is possible to obtain fairly uniform illumination over the aperture in the screen. In the case of the largest aperture with which we dealt the amplitude of the incident field at the edge of the aperture was not less than 0.9 of the value at the center. Uniformity of phase is a more important factor to be considered in determining the distance from the horn to the diffracting structure. The wave from the horn is distinctly spherical and there is, therefore, an attendant phase variation over the aperture. In the case of our largest aperture the maximum value of the phase deviation from a uniform field was of the order of 100°.

The full-space setup is used generally to make a study of the complete space pattern. The probe as-

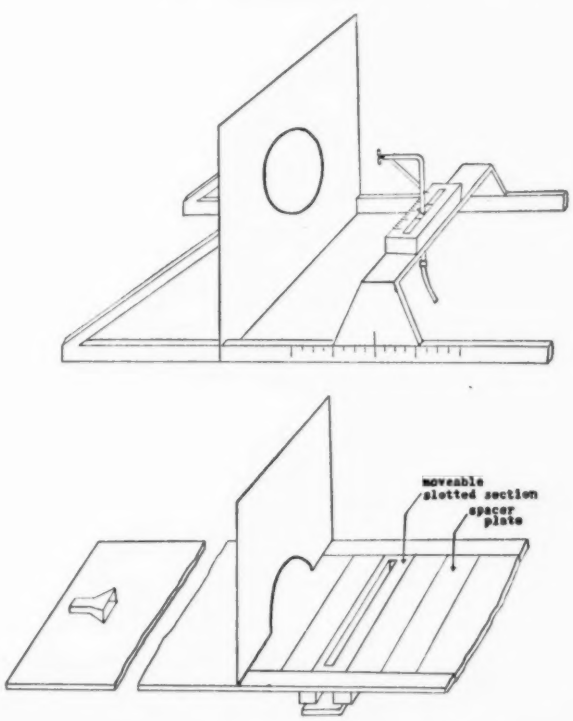


FIG. 1. Full-space and half-space techniques.

‡ The work by S. J. Buchsbaum of McGill University on apertures of other than circular shape has been recently released as Report No. b9, McGill University, on contract with Air Force Cambridge Research Center, Cambridge, Massachusetts.

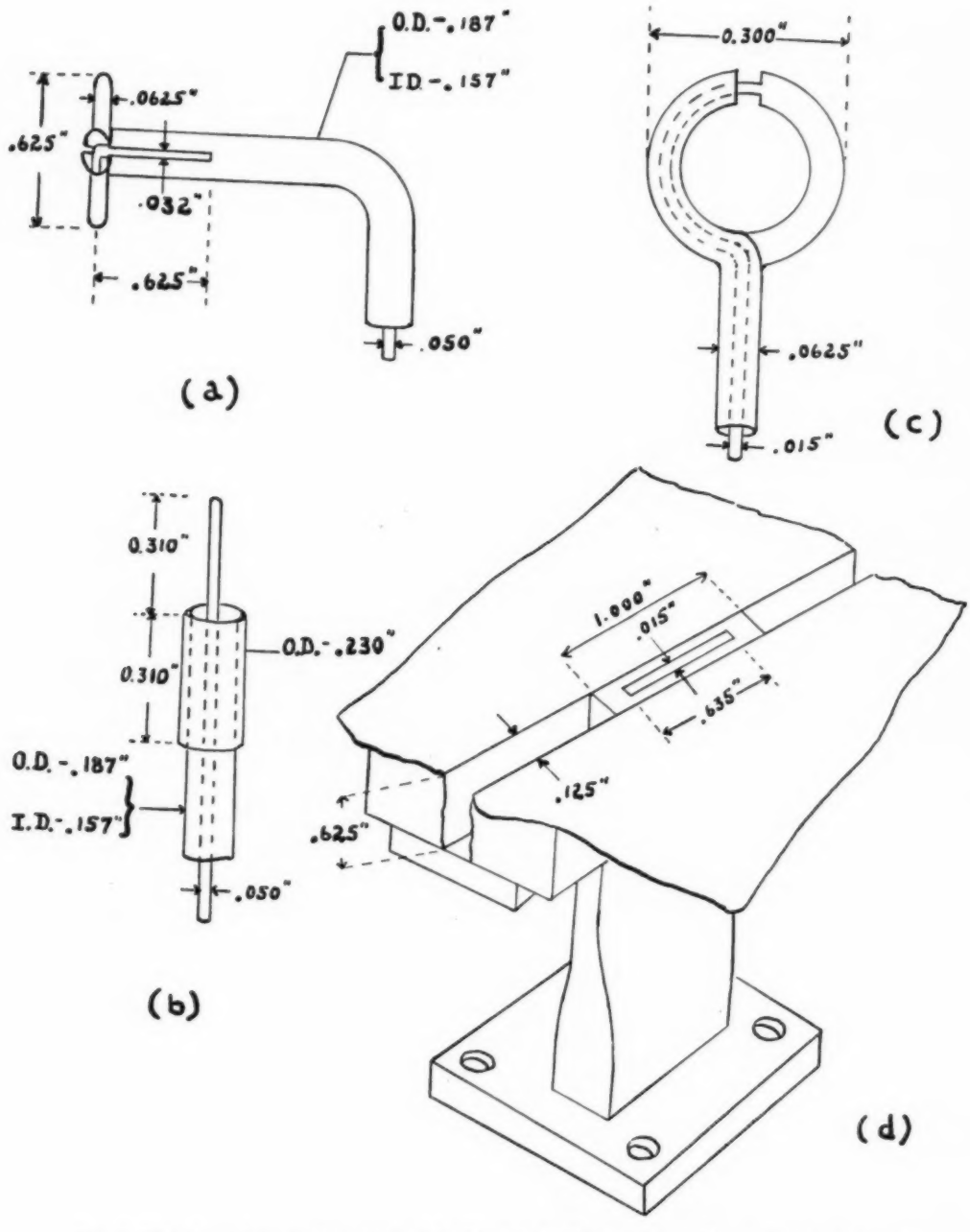


FIG. 2. Electric and magnetic probes: (a), (b) electric dipole probes; (c) magnetic loop probe; (d) ground plane slot magnetic probe.

sembly consists of a carriage which permits translation of the probe along a line parallel to the screen; the carriage is mounted on a track extending in the direction perpendicular to the screen. In the case of the circular aperture the entire space pattern can be explored by moving the probe in a horizontal plane that passes through the horizontal diameter of the aperture. The plane is covered for successive orientations of the plane of polarization of the incident wave obtained by rotating the feed system. The probe itself must be provided with the third degree of freedom so that the polarization axis of the probe can be aligned properly with respect to the incident field vector.

Although the technique is simple in principle there are many practical difficulties. The probe assembly intrudes seriously into the field and introduces spurious scattering. The trouble can be reduced somewhat by building the mount and carriage so that the main structure lies well outside the boundary of the geometrical shadow. This, however, necessitates the use of a long slender transmission line to the probe. The attendant mechanical problems are obvious, for the

probe must move accurately in a plane that is parallel to that of the screen. Rigidity can be obtained by means of dielectric supports, but these may not be massive, for they too introduce measurable perturbations.

Care must be taken to protect the system from scattered radiation from nearby objects. Ground reflections become serious as the distance from the aperture is increased, giving rise to noticeable asymmetry in the pattern when the polarization of the incident wave is other than vertical. Ground reflection is a disturbing factor on the incident side; it causes fluctuations in the amplitude and phase distribution in the incident field. Power supplies and receivers must be kept at a considerable distance from the setup; consequently long lines are involved giving rise to erratic results, particularly in measurements of phase.

The ideal probe for measuring the electric field at a point is an infinitesimal dipole. The extent to which the size of a probe can be reduced in practice is limited by the difficulties of matching the impedance of the device to the transmission line and by the sensitivity of the detector system. In the full-space arrangement, again, the transmission line leading to the probe is necessarily in the field and plays an important part in the measurement. The probe must be designed with a choke system to isolate it from the currents on the transmission line. Figure 2 (a) shows the type of probe which we used for measuring the electric field. The slotted dipole is an excellently balanced device when the slot is narrow. Slot length can be varied to some extent to facilitate impedance matching, but there is not too much leeway for adjustments of that type. Magnetic field probes are even more difficult to make. In principle, a small loop constitutes a magnetic dipole antenna and should be usable as a probe. Great care must be taken to make a balanced loop with the proper transformation to the coaxial line. It is almost impossible to construct a loop of the required small dimensions at 3 cm which is entirely free from an electric dipole component in its structure. The structure consequently measures a mixture of the magnetic and electric vectors. The latter can be separated out by use of the electric field data measured independently, but the procedure is extremely tedious and the errors are large. The problems of fabricating the probes can be appreciated from the dimensions shown in Fig. 2.

The half-space technique has the advantages that the bulk of the equipment is located under the ground plane and is out of the way. It is particularly convenient for studying the field around circular plates since there is no problem of supporting the plates. The half-space arrangement is especially suited to the measurement of the $H$-plane patterns since the probe can be brought up from below and line interference effects are eliminated. It is of course necessary to provide a means for free motion across the ground plane at successive distances from the diffracting structure. One method is to make the ground plane out of two pieces, one of which can slide out from under the other. The sliding section carries the probe, which is free to move in a long slot cut across the ground plane parallel to the screen. The fixed plate must be made of rather thin stock to avoid a marked step in the structure. We have found that such a step introduces significant errors in the measurement of the field in the immediate neighborhood of the screen.

A second method whereby a variable axial position can be obtained is to cut a long rectangular plate in which a slot is milled to one side of the long axis. Two closely spaced positions relative to the screen are obtained by turning the plate over. The slotted plate can be set at successive distances from the screen by means of spacer plates. The plates must be milled accurately so that they fit together without vertical steps, and they must be supported from below to prevent bowing.

The slot in the plate in which the probe rides causes some distortion of the field. Its disturbing effect is reduced by making the probe carriage in the form of a half-wavelength cavity relative to the slot. The short circuit at the bottom of the cavity is transformed to a short circuit in the plane of the slot. The general lines of the design of the movable probe system follow those of the probe system of a slotted section used for impedance measurements. The skirt dipole [Fig. 2 (b)] forms a satisfactory electric field probe for this setup. The skirt serves as a choke decoupling the probe from the coaxial line. Uniformity of motion is obtained by setting the probe in a dielectric plug in the slot. This also eliminates contact troubles. An excellent magnetic probe for measuring the component of magnetic field along the surface of the ground plane consists of a narrow slot cut into the ground plane. Such a slot is free from an electric dipole moment (in any case the component of the electric field along the surface is zero) and measures directly the component of the surface current which is transverse to the axis of the

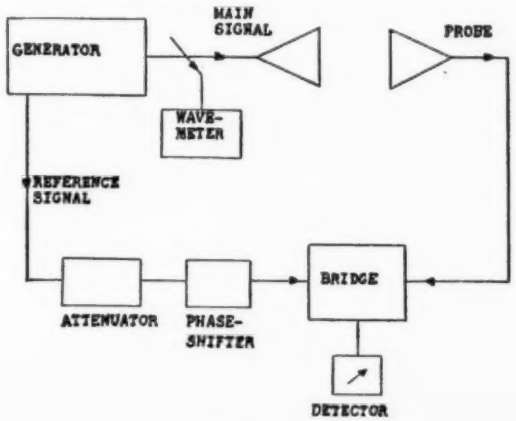


FIG. 3. Block diagram of circuitry.

slot, and hence the component of magnetic field intensity along the axis of the slot. We employed a device of this type, the feed line to the slot consisting of a wave guide compressed in the narrow dimension. The wave guide was brought to the ground plane through the cavity under the slotted slab referred to previously. A check of the magnitude of the perturbation of the surface current by the slot in the plate was made. Flanges were fitted to the side of the wave guide probe, and the magnetic field distribution was measured. The change in data was found to be negligible, and it was concluded that the slot did not significantly perturb the surface current flow.

The half-space arrangement can be used in measuring the field at points other than in the $H$ plane by bringing a probe up over the structure. The types of probes that can be used are the same as those described for the full-space arrangement. The same general problems arise as in the full-space setup. There is an added difficulty in that the image effect enters. This is particularly significant when measurements are made close to the ground plane surface. The half-space arrangement has, however, the over-all advantage that ground reflection problems on the incident side are eliminated, the main bulk of the equipment is out of the way, and generally shorter line lengths are involved.

Figure 3 is a block diagram of the circuitry used in the measurements. The reference signal is taken from the main wave guide output from the oscillator by means of a directional coupler so that the oscillator is unaffected by changes in the impedance accompanying the change in the phase shifter setting. An attenuator serves to provide further protection. Its main function, however, is to equalize the reference signal and probe signal levels to maximize the sharpness of the phase comparison. The phase shifter is adjusted to bring the reference signal 180° out of phase with the probe signal, changes in the phase shifter settings thus measuring the phase distribution in the diffraction field. Another directional coupler is used to tap the oscillator output for frequency measurements.

The measurement of the field close to the edge of an aperture or close to a plate is affected strongly by multiple scattering between the probe and the sheet. Multiple scattering makes itself felt elsewhere also. Its effect at points removed from the diffracting structure is recognized as a fine structure in the field pattern. An index of the importance of multiple scattering is obtained by measuring the variation in the impedance of the probe with position when the probe is used as a transmitter in the setup. The reciprocity theorem can be applied to make a first order correction to the data. The fine structure was removed completely from the patterns by such a procedure.

## DISCUSSION OF RESULTS

In the following the plane of the aperture is referred to as the $xy$-plane; the incident electric vector is taken to be in the direction of the $y$-axis. The $x$ and $y$ components of the field vectors are designated as tangential components regardless of the value of the $z$-coordinate.

### 1. Small Apertures, Diameter $D \leq \lambda$

Figures 4–6 show some of the measured distributions of the tangential electric field for apertures of diameter

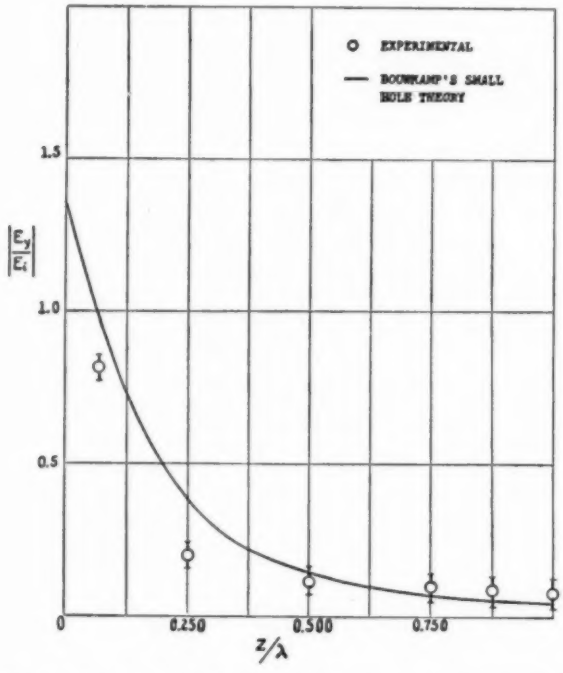


FIG. 4. Distribution of the principal tangential component of electric field along the axis; aperture diam=0.5λ.

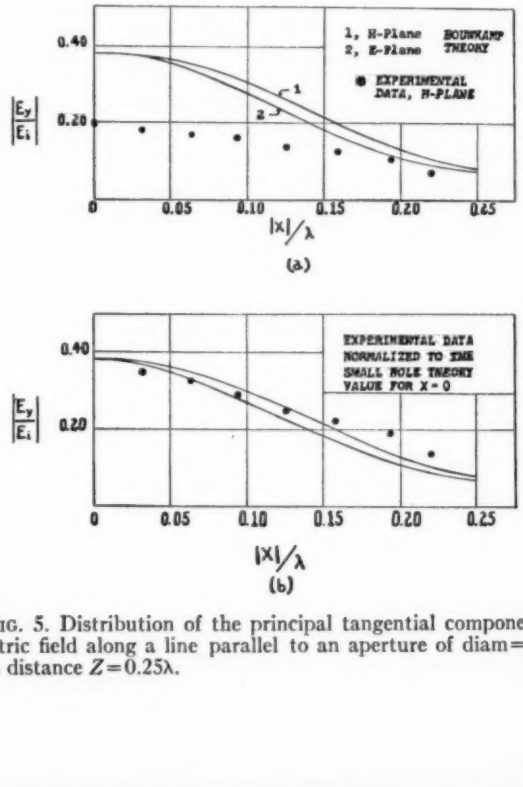


FIG. 5. Distribution of the principal tangential component of electric field along a line parallel to an aperture of diam=0.5λ, at a distance $Z=0.25\lambda$.

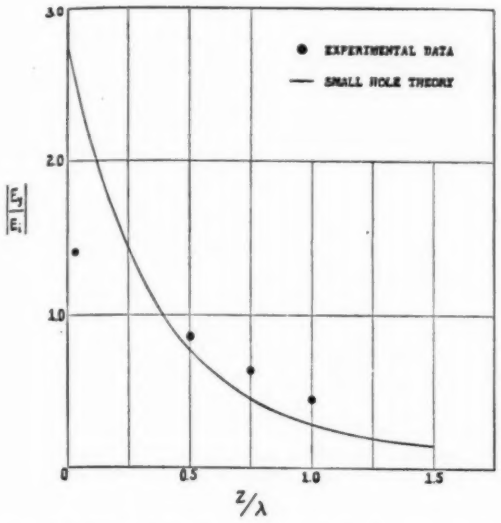


FIG. 6. Axial distribution of the principal component of the electric field; aperture diam = 1.0λ.

$D=0.5\lambda$ and $D=1.0\lambda$. In both cases the axial distribution decreases from the aperture, as might be expected from the fact that for any point on the axis the aperture subtends less than one Fresnel zone. Sharp interference effects are, therefore, not expected.

It is interesting to compare the measured distributions with those given by the small hole theory. Bouwkamp's work in this connection was noted already. His expressions are correct up to terms of relative order $(ka)^2$ and, therefore, may be expected to give good results for apertures of size such that

$$ka<1 \quad \text{or} \quad a<\lambda/6.$$

The two cases to which our figures apply, $a=\lambda/4$ and $a=\lambda/2$, are outside this range. However, it is observed that the small hole theory is still of semiquantitative value for these cases. The small hole theory predicts a larger value of intensity than that which is observed, but it does run close to the measured axial distribution outwards from a small distance beyond the aperture. We realize, of course, when the aperture is so small measurements in the aperture may be seriously affected by interaction between the screen and the probe. Figure 5 shows the distribution in a plane parallel to the aperture for the $a=\lambda/4$ case. Only $H$-plane data are shown. The $E$-plane data do not differ substantially. It will be noted that the small hole theory does not agree insofar as absolute level is concerned. But, as Fig. 5b shows, the theory serves well for the relative distribution. Similar results were found for the larger aperture ($a=0.5\lambda$). When the radius exceeded $0.5\lambda$ no particularly meaningful connection between the small hole theory and the experimental results could be observed. The small hole theory necessarily loses significance when the aperture contains more than one Fresnel zone.

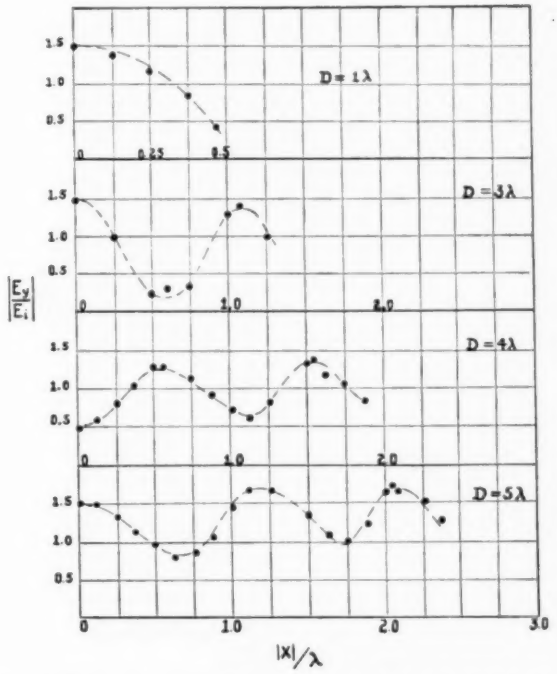


FIG. 7. Principal tangential component of electric field in the aperture; normalized to unperturbed plane wave; $Y=0$.

## 2. Tangential Field Components in the Aperture; $D>\lambda$

When the diameter of the aperture is greater than one wavelength the near-zone field pattern is marked by fluctuations in the magnitudes of the field vectors. The pattern of the tangential components in the aperture itself is of particular interest in connection with the development of an adequate theory. It was pointed out by Andrews that for the *tangential component of the electric field* the interference pattern is most marked in the aperture itself. Similar results have been obtained by the group at McGill University and by Severin. Our data shown in Figs. 7–11 inclusive are in good agreement with the other results and confirm the complexity of the field structure.

It is seen that the $H$-plane pattern shows more variation in structure than the $E$-plane pattern. Up to a diameter of $16\lambda$ there appears to be a systematic relationship between the number of maxima and minima and the size of the aperture. When the diameter $D=n\lambda$, $n$ being an integer, the number of maxima in the $H$-plane pattern is equal to $n$. When $n$ is even, the pattern has a minimum in the center of the aperture; when $n$ is odd, the pattern has a maximum in the center. This type of relationship can be visualized in terms of a standing wave in the aperture associated with the boundary condition that at the edge the component of **E** which is tangential to the edge vanishes. The behavior of the field at the center can also be correlated with the number of Fresnel zones subtended

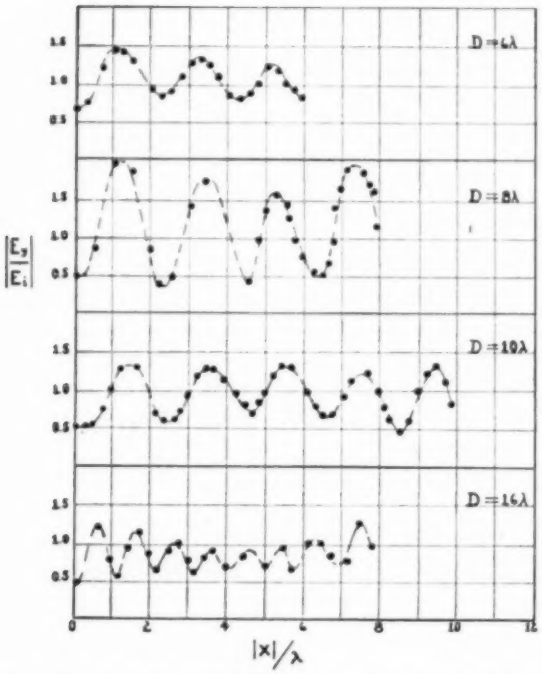


FIG. 8. Principal tangential component of electric field in the aperture; normalized to unperturbed plane wave; $Y=0$.

by the aperture, in the limiting sense, at the center. This was discussed by Andrews.

The preciseness of the relationship stated above may be questioned on the basis of Fig. 9 which shows the $H$-plane pattern for the case of $D=36\lambda$. The latter differs from the smaller apertures not only with respect to the number of maxima and minima but also in the detailed form of the pattern. In the smaller apertures the maxima and minima are relatively uniform in size, whereas in the large aperture there is considerable variation in size. The form of the variation is suggestive of a modulating function of longer space periodicity. A trend toward this latter structure is in evidence in the $16\lambda$ aperture. The work of Hogg[9] indicates that the phenomena are due to the variation of the phase of the incident field over the aperture, but further theoretical study should be made.

The distribution of $\mathbf{E}_{\tan}$ in the aperture is, of course, dependent on conditions all around the edge, not merely at any two special points. The behavior of the field at the edge has been the subject of much discussion over the past few years. Bouwkamp[10] called attention to the role of the singularities in diffraction theory and on the basis of the Sommerfeld solution[11] for the half-plane postulated certain edge conditions for the general aperture case. These were developed in greater detail by Meixner[12] and others. If we let $E_t$ and $E_{n'}$ be the components of $\mathbf{E}_{\tan}$ which are, respectively, tangential and normal to the edge of the aperture, the conditions are

$$E_t \simeq r^{\frac{1}{2}}, \qquad E_{n'} \simeq 1/r^{\frac{1}{2}},$$

where $r$ is the distance along $\mathbf{n}'$ from the edge. These conditions are based on the condition that the screen has zero thickness. We attempted to determine the field behavior at the edge of the aperture but could not obtain clear quantitative results. It is observed that in each case of Fig. 8 the intensity drops sharply at the edge of the aperture, but the law of fall cannot be established. Singularities, if present, should be most evident in the $E$-plane pattern. We could not detect a sharp rise near the edge. It should be mentioned that

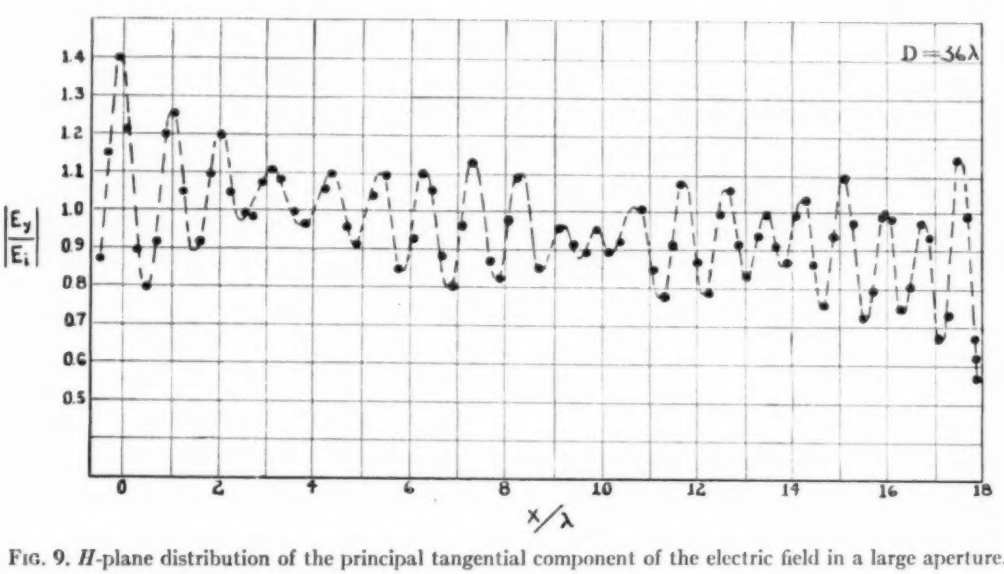


FIG. 9. $H$-plane distribution of the principal tangential component of the electric field in a large aperture.

[9] D. C. Hogg, J. Appl. Phys. **24**, 110 (1953).
[10] C. J. Bouwkamp, Physica, XII **7**, 467 (1946).
[11] A. Sommerfeld, Vol. II of P. Franck and R. von Mises, *Different-und Integralgleichungen der Physik* (reprint, Mary Rosenberg Press, New York).
[12] J. Meixner, Ann. Physik **6**, 1 (1949).

we filed the aperture boundary to a sharp edge to approach the ideal situation of zero thickness. There are two factors which limit the quantitative value of our data near the edge. The interaction between the probe and screen becomes particularly significant in that region, and the resolution is limited by the finite size of the probe.

The field structure shown in Fig. 9 is at variance with the ideas generally entertained about large apertures. The argument is frequently set forth that, on physical grounds, one should expect the field in the aperture to approach the unperturbed incident field with increasing aperture size, the diffraction effects becoming limited to small regions in the neighborhood of the edge. This view is suggested further by the argument that when the radius of the aperture is large, the diffraction problem for any small section of the edge is locally the same as that of diffraction of a plane wave by a straight edge. It is apparent, however, that the height of the central maximum in Fig. 9 is not appreciably different from that observed in the smaller apertures. The phenomenon is understandable if we think of the edge as forming a distribution of sources of diffraction wavelets; then, with the circular geometry these wavelets are all in phase at the center, and although the amplitude of each component wavelet may be small, decreasing in fact with increasing diameter, the sum total is large and is essentially independent of the radius of the aperture. The phase of the resultant with respect to the incident wave is, however, a function of the radius, and there results a maximum or a minimum according to the dimensions of the aperture. Further work on a different aperture shape will aid in understanding what does take place.

The behavior of $\mathbf{H}_{\tan}$ in the aperture is radically different from that of $\mathbf{E}_{\tan}$. The rigorous formulation of the diffraction problem and the application of the fundamental boundary conditions in the aperture directly establish that $\mathbf{H}_{\tan}$ in the aperture is the same as that of the unperturbed incident field. In the case of a plane wave at normal incidence $\mathbf{H}_{\tan}$ should, therefore, be constant over the aperture. This property shows up beautifully in the patterns shown in Fig. 12. The apparent deviation from the theoretical result in the case of $D=1\lambda$ is again due to the limited resolving power of a finite probe and interaction between the probe and screen. The behavior of the magnetic field outside the aperture is of interest to the formulation of a high frequency approximation for the diffraction problem. It is observed that $\mathbf{H}_{\tan}$ drops sharply to virtually zero at the edge of the aperture and becomes sensibly equal to zero within a very short distance in the shadow region.§ This means that the perturbation

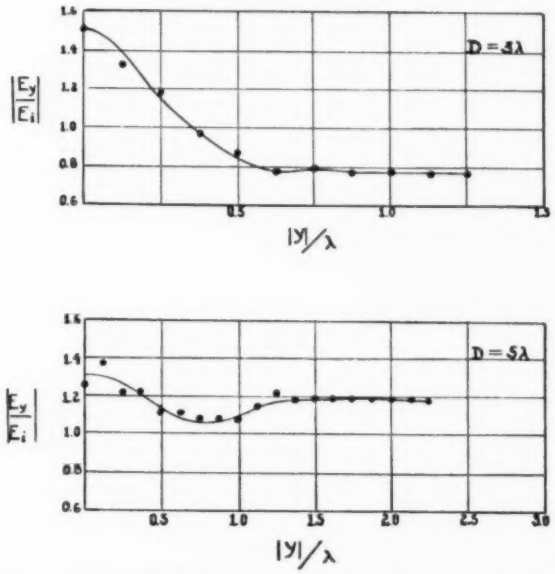


FIG. 10. $E$-plane ($X=0$) patterns of the principal tangential component of the electric field in the aperture.

currents over the shadow surface are confined to a narrow annular region around the edge. Our results are for the $H$ plane only. In a private communication, however, Professor Woonton has informed us that the group at McGill University were able to carry out similar measurements with a loop at much longer wavelengths

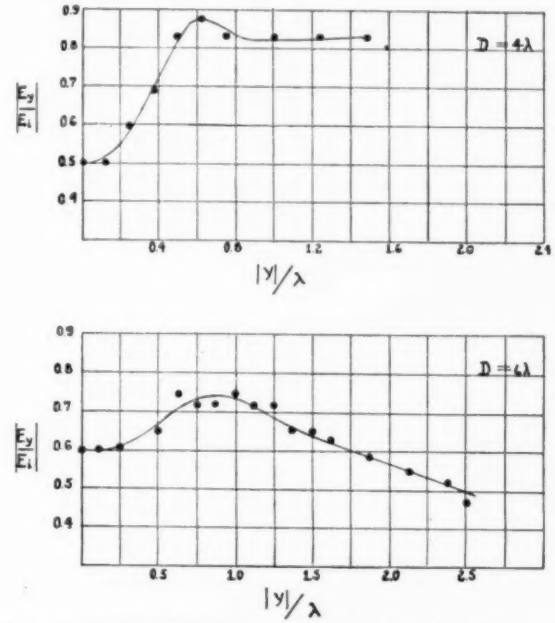


FIG. 11. $E$-plane ($X=0$) patterns of the principal tangential component of the electric field in the aperture.

§ In references 8(a) and 8(b) we have developed a high frequency approximation for the diffraction field based on the assumption that $\mathbf{H}_{\tan}$ is strictly equal to zero over the shadow surface of the screen. A similar formulation has been published by H. Severin, Z. Physik **129**, 426 (1951). In a more recent paper G. Bekefi, J. Appl. Phys. **24**, 1123 (1953) has carried through an alternative development starting from the Hertz vector rather than the field vector, and has discussed the agreement between theory and experiment for the smaller apertures. We have found unexpected discrepancies between the theoretical and experimental results in the case of the larger apertures which may be due to phase errors. We have not yet completed our computations on this point.

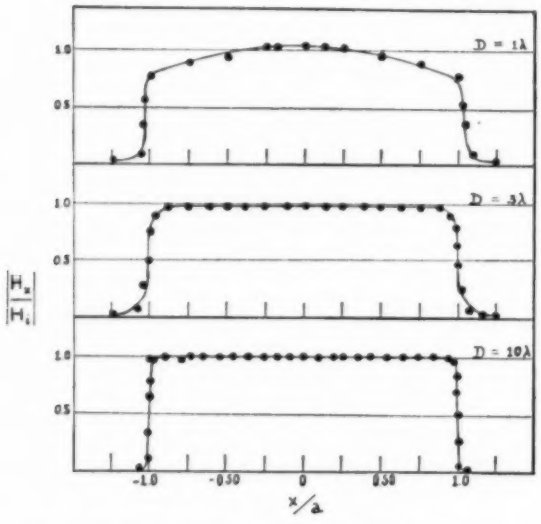


FIG. 12. *H*-plane pattern of the principal component of the magnetic field, $Z=1$ mm.

and found the same properties of the magnetic field over the entire aperture region.

### 3. Complementary Obstacles—Tangential Components

It is interesting to compare the diffraction field of an aperture with that of the complementary obstacle. Figure 13 shows typical field patterns of $\mathbf{E}_{tan}$ and $\mathbf{H}_{tan}$ in the *H* plane for the complementary obstacles of diameters 3λ and 5λ. The behavior of $\mathbf{E}_{tan}$ outside the boundary of the disk is very much like that of the diffraction field of a straight edge. The amplitude of oscillation diminishes with increasing distance and the field approaches the unperturbed incident field value.

$\mathbf{H}_{tan}$ exhibits the constant value over the open area predicted by rigorous theory. It is observed that the field amplitude drops sharply at the edge of the disk

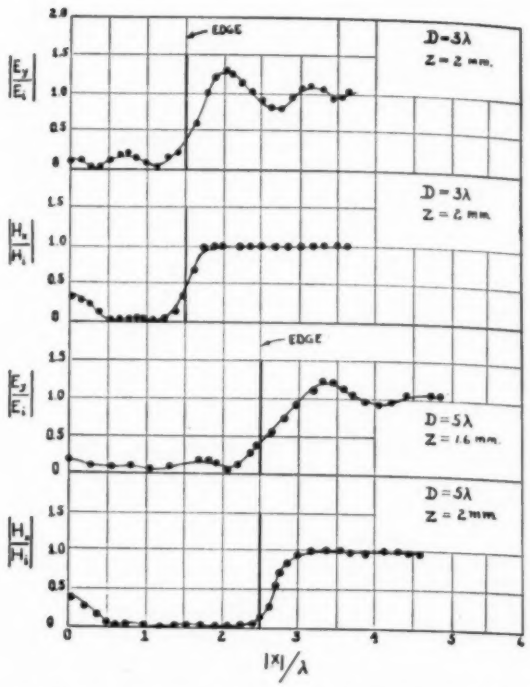


FIG. 13. *H*-plane patterns of the principal component of the electric and magnetic fields for the complementary obstacles.

and is virtually zero over the shadow region. The perturbation currents are again confined to the neighborhood of the edge. It will be noted that there is a peak in the $\mathbf{H}_{tan}$ distribution at the center of the disk on the shadow side. This will bring to mind the familiar bright spot observed on the axis in the diffraction pattern of a circular object in the optical region. The Fresnel zone interpretation of the effect is well known.

One of the important theoretical results concerning apertures and complementary obstacles is the electromagnetic Babinet principle which was formulated by

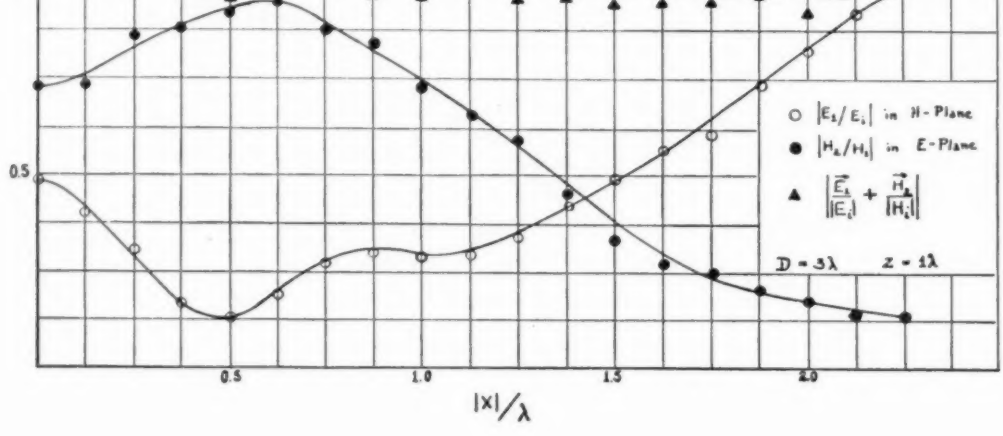


FIG. 14. Electromagnetic Babinet principle.

Booker.[13] The principle is as follows: Suppose that we have a field $\mathbf{E}_{ia}$, $\mathbf{H}_{ia}$ incident on an aperture, and $\mathbf{E}_1$, $\mathbf{H}_1$ is the diffraction field in the region $z>0$. Then, if in the case of the complementary obstacle we have an incident field

$$\mathbf{E}_{ib}=(\mu/\epsilon)^{\frac{1}{2}}\mathbf{H}_{ia},$$
$$\mathbf{H}_{ib}=(\epsilon/\mu)^{\frac{1}{2}}\mathbf{E}_{ia},$$

and $\mathbf{E}_2$, $\mathbf{H}_2$ is the corresponding diffraction field, the two diffraction fields satisfy the relation

$$\mathbf{E}_1+(\mu/\epsilon)^{\frac{1}{2}}\mathbf{H}_2=\mathbf{E}_{ia},$$
$$\mathbf{H}_1-(\epsilon/\mu)^{\frac{1}{2}}\mathbf{E}_2=\mathbf{H}_{ia}.$$

The principle affords a basis for checking the reliability of the experimental technique. Figure 14 shows the results of measurements of complementary fields along a line parallel to the aperture plane. Since the field components are normalized to the incident field values the result of the superposition should be unity. The deviations from unity shown by the data are within the estimated errors of the measurements. The best mean line through the sum data shows a downward trend across the line of measurement. This may represent the effect of the small degree of taper in the incident field illumination.

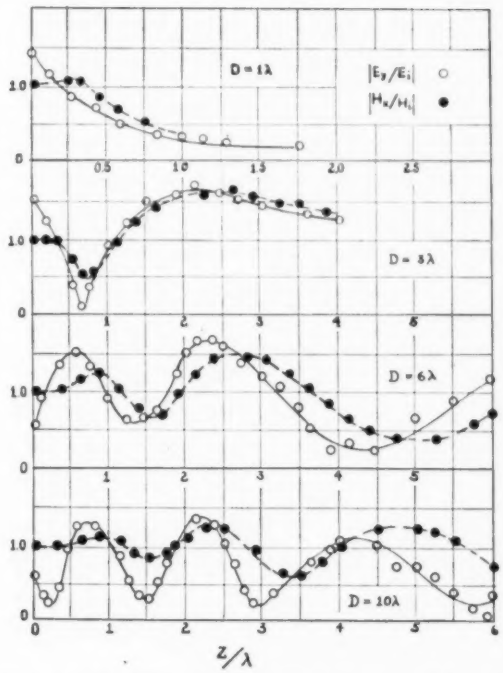


FIG. 15. Axial distributions of the principal tangential component of the electric and magnetic fields for circular apertures.

### 4. Axial Distributions, Apertures, $D>\lambda$

The axial distributions of $\mathbf{E}_{\tan}$ and $\mathbf{H}_{\tan}$ for a sequence of aperture sizes are shown in Fig. 15. It is observed that in each case $\mathbf{H}_{\tan}$ approaches unity as $z\rightarrow 0$, in agreement with the boundary condition on the magnetic field which we have discussed. Both $\mathbf{E}_{\tan}$ and $\mathbf{H}_{\tan}$ show the fluctuations in amplitude that are characteristic of the near-zone field. The two vectors are not related, however, simply as in the case of a plane wave, as is indicated by the different locations of the maxima and minima in their respective distributions. With increasing distance from the aperture the distributions become more nearly coincident and when the far-zone region is reached the dominant parts of the field vectors have the plane wave relationship. The locations of the maxima and minima in the axial distribution of $\mathbf{E}_{\tan}$ are accounted for quite accurately by simple Fresnel zone considerations up to a diameter of $6\lambda$. It was pointed out by Andrews that the Fresnel zone analysis can be applied at the aperture plane itself and that there should be a minimum (maximum) in the axial distribution at $z=0$ for diameters that are an even (odd) number of wavelengths. It is seen, however, that in the case of the $10\lambda$ aperture the minimum occurs somewhat beyond the aperture plane. We thought that we were in error in that the diameter was not precisely $10\lambda$. The data shown here were obtained at a wavelength of 3.2 cm. We repeated the measurements at the $K$ band and examined the change in position of the minimum over a range of frequencies around that corresponding to the precise $10\lambda$ value for the aperture. The $K$-band data are in excellent agreement with those shown here, and we feel quite certain that the displacement of the minimum is real. We are investigating the possibility that the effect is the result of a phase error in the incident field distribution over the aperture.

[13] H. Booker, J. Inst. Elec. Engrs. (London) **93**, Pt. IIIA, No. 4, 620 (1946).

#### ACKNOWLEDGMENTS

The support tendered by the Office of Naval Research was noted already. The work was initiated by means of a grant made to one of us (S. Silver) by the Faculty Research Committee and funds from the Bureau of Ships. The assistance of Mr. Priedigkeit with instrumentation is gratefully acknowledged.

# Replica Studies of Bulk Clays*

J. J. COMER AND J. W. TURLEY
*College of Mineral Industries, The Pennsylvania State University, State College, Pennsylvania*
(Received April 23, 1954)

The electron microscope examination of the surfaces of bulk clays by replica techniques is difficult because of the porosity of the clays and the necessity of using hydrofluoric acid to dissolve the clay from the replicas. The surfaces of some bulk endellite clays were examined by means of collodion, silica, and preshadowed replicas. Collodion and two-step silica replicas were unreliable and difficult to use because of penetration of the collodion or plastic into the pores of the clay. Collodion strippings were of some value in removing layers of clay particles from the surface for direct examination in the microscope. Best results were obtained with the preshadowing technique which employed a shadowing layer of platinum backed by a layer of evaporated carbon or by Parlodion. Micrographs of replicas prepared by the latter technique show the surface of a highly porous endellite clay to consist of tubes in various orientations.

## INTRODUCTION

MOST of the clay minerals have been subjected to examination in the electron microscope and excellent micrographs have been compiled by workers in the field to show the characteristic morphology of the individual species. These micrographs show only the clay particles resulting from grinding or dispersing the bulk material. The results of one attempt to study the surface of clays is found in the work of Hast,[1] whose technique consisted essentially of stripping a single layer of clay particles from the bulk material by use of a plastic film.

This paper concerns a study initiated by an interest in the size, shape, and orientation of endellite, $Al_2O_3 \cdot 2SiO_2 \cdot 4H_2O$, in the bulk form. From a practical point of view a better understanding of the bulk clay might help one to predict its potential value as a catalyst as used in the petroleum industry. It has been shown by Bates, Hildebrand, and Swineford[2] that particles of this mineral broken from the bulk clay may be identified as tubes of varying dimensions. However, what may have happened to the clay particles upon separation and subjection to dispersion techniques was uncertain.

The results of an intensive study of bulk halloysites of different degrees of porosity by means of collodion, silica, and preshadowed replicas have helped to form a more realistic picture of these clays. Two representative clays will be discussed with emphasis on the replica techniques and their interpretation rather than on the mineralogical aspects.

The micrographs were obtained with an RCA EMU-2D electron microscope. Micrographs of the shadowed specimens are reproduced as negative images so that the shadow areas appear dark.

FIG. 1. Clay *A*. Ground and dispersed in amyl acetate.

## SAMPLES

Clay *A* is the least porous of the three examined and fractures to yield a relatively hard smooth surface. Clay aggregates were broken up by wetting with amyl acetate and by thorough grinding. A large percentage of lath-like particles can be seen in the micrograph in Fig. 1. The tubes are not very clearly defined, presumably because of partial uncurling. From the examination of a large number of preparations it was found that the diameters of the tubes ranged from less than 300 A to over 900 A. It was shown by Bates *et al.*[2] that many of the tubes consist of concentric layers of the clay mineral so that the wall thickness of the tube could be 50 A or greater. This will be illustrated by some of the micrographs of replicas included in this paper.

Clay *B* is an extremely soft, highly porous clay. It was ground in water to break down the aggregates. Figs. 2(a) and 2(b) show the tubular particles characteristic of this sample. These particles vary from about 200 A to over 800 A in diameter, wall thickness of from 50 A to as high as 150 A being evident. The lath-like particle (A) in Fig. 2(a) is the probable result of the uncurling of a tube. The tapering at one end is due to the fact that some curl still remains. Other tubes in different stages of uncurling may be seen in both Figs. 2(a) and 2(b). Similar particles can be seen in preshadowed

* This paper was presented in part at the Eleventh Annual Meeting of the Electron Microscope Society of America, Pocono Manor, Pennsylvania, November 5, 1953. Contribution No. 53-62.

[1] N. Hast, Nature **159**, 354 (1947).

[2] Bates, Hildebrand, and Swineford, Am. Mineralogist **35**, 463 (1950).

replicas of this clay. Collodion replicas could not be made because of the rapid penetration of the solution into this clay.

Both clays were predried in a vacuum desiccator before replication. Replicas of clay *A* were made on fresh fractures while those of clay *B* were made on surfaces cut with a knife or on polished etched sections.

## REPLICA TECHNIQUES

### 1. Collodion Replicas

Collodion replicas of clay *A* were backed with a film of Formvar, from solution in ethylene dichloride, before being stripped from the surface with Scotch tape. They were then shadowed and separated from the tape by dissolving the Formvar. The resulting replicas were like those prepared by Hast[1] in that they contained particles of the clay which were transferred from the surface of the bulk material to the collodion film. Other collodion replicas were prepared by dissolving clay particles by floating the stripped film on the surface of 48 percent hydrofluoric acid for 3 minutes. Longer treatment in the acid frequently altered the surface of the collodion. After washing in distilled water the replica was dried and shadowed with platinum-palladium at an angle of incidence of 10°. Considerable searching in the microscope was necessary to find clean areas of the replica.

### 2. Silica Replicas

Negative plastic replicas could not be made by pressure molding because the fragility of the clays make it necessary to use lacquers on the clay or to apply a monomer and polymerize it on the surface. In practice it was not feasible to use polystyrene, lucite or n-butyl methacrylate because of possible changes in the surface structure caused by the 1-hour treatment in 48 percent hydrofluoric acid necessary to remove the clay. It was found that a negative replica formed from a lacquer of Duco cement[3] in acetone was not attacked by the acid. The presence of solid particles found in this cement could not be detected on the replicas.

The Duco-cement replicas were stripped from the clay and after the acid treatment were shadowed with platinum and backed with an evaporated film of silicon dioxide. The combined platinum-silica films were removed by dissolving the negative replicas in acetone.

### 3. Preshadowed Replicas

The preparation of these replicas was based on the technique described by Williams and Wyckoff.[4] Sections chosen for replication were shadowed with 8 to 10 A of platinum. Two methods of adding a supporting film were tried. In the first method the metal film was backed with a 1-percent solution of Parlodion in amyl acetate. Excess clay was cut from the replica until the section was only 1–2 mm in thickness. The replica was then floated with the clay side down on the surface of 48 percent hydrofluoric acid until the clay was removed. By lifting on a section of paraffin-coated screen the replica was removed from the acid and deposited on fresh acid for 15 minutes. In a similar manner the replica was washed in 3 changes of distilled water. It was then picked up on large sections (1 in. square) of 200-mesh stainless steel screen from which were punched $\frac{1}{8}$-in. disks. As the porosity of the clays increases, it becomes more difficult to remove all of the clay from the replica because of protection from the acid by Parlodion which coats some of the particles.

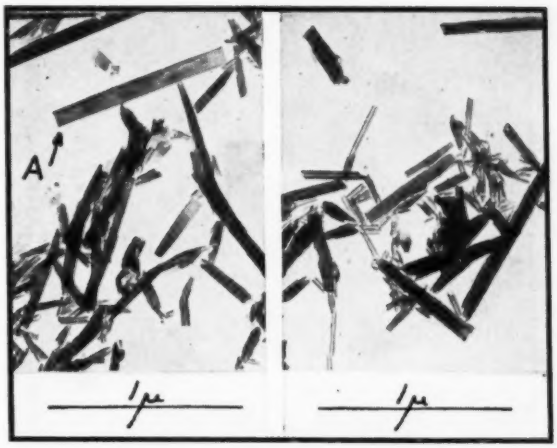


(a) (b)

FIG. 2. Clay *B*. Ground and dispersed in distilled water. Note the almost completely uncurled particle (*A*).

The second method of preparing preshadowed replicas depended on the deposition of an evaporated film of carbon[5] on the platinum film in place of the Parlodion. The replica was embedded tightly in heat-softened polystyrene before acid treatment to prevent breakage and to permit easy handling. Frequently most of the clay could be removed from the replica by placing the embedded specimen in water for several minutes. Remaining clay particles were removed by treatment in hydrofluoric acid. The replicas were removed from the polystyrene by dissolving the plastic in ethylene dichloride. Some replicas were mounted on collodion substrates to prevent breakage during evaporation of the solvent. Thicker ones could be mounted directly on the specimen screen. The method of backing the platinum with carbon was found to be superior to the first method in several ways. Removal of the clay from the replica was more complete, contrast was higher, and replicas were more stable under the electron beam.

[3] Made by DuPont Chemical Company, Wilmington, Delaware.
[4] R. C. Williams and R. W. G. Wyckoff, Science **101**, 594 (1945).
[5] D. E. Bradley, Brit. J. Appl. Phys. **5**, 65 (1954).

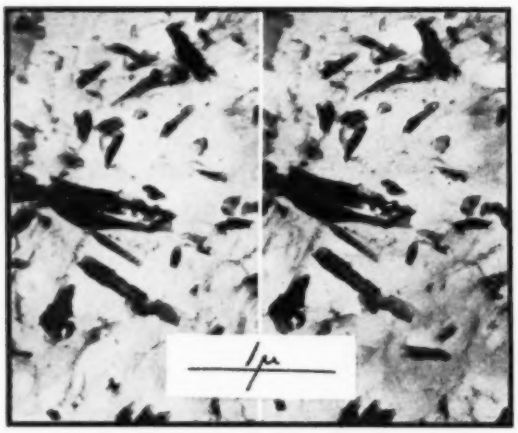


FIG. 3. Clay *A*. Stereopair of collodion stripping. Note the tubular endellite particles removed from the bulk material.

## DISCUSSION OF MICROGRAPHS

### 1. Collodion Replicas

Collodion replicas of the two endellites were found to be of no value except when used as a means of stripping clay particles from the surface of the bulk material. Figure 3 shows stereomicrographs of replicas of sample *A*. It will be noted that the transfer of clay particles from the surface is not at all complete. For comparison, a stereopair of a collodion stripping of a third clay, *C*, consisting largely of montmorillonite with some endellite is shown in Fig. 4. A more complete transfer of clay particles was effected here, probably because of better contact between the platy montmorillonite particles and the collodion film. It is noted that many of the endellite particles in Fig. 3 do not lie flat but are at various angles with respect to the plane of the substrate.

Figure 5 is a micrograph of an area of a collodion replica of clay *A* from which the clay was dissolved before shadowing. Based on a comparison with the Duco-silica and preshadowed replicas, Figs. 6 and 7, the structure bears little relation to the actual surface of the clay. The replica seen in Fig. 5 shows a pattern formed by penetration of the collodion beneath the surface of the clay. The extremely light patches represent areas of heavy concentration of collodion caused by deep penetration.

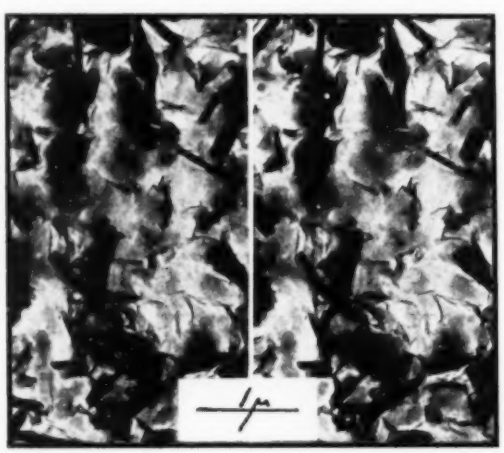


FIG. 4. Clay *C*. Stereopair of collodion stripping showing plates of montmorillonite and tubular endellite particles removed from the bulk material.

### 2. Silica Replicas

Silica replicas of clay *A* were valuable in showing gross changes in structure. For example, in Fig. 6(a) there is an irregular distribution of the particles except in one area of radially-aligned tubes. Figure 6(b) shows one of these areas at higher magnification. This particular structure was found to occur about once every other opening of the specimen screen. In examining dispersed specimens of this clay a few aggregates of oriented tubes were found equal in size to those shown in the replica, but in most of the aggregates the tubes were apparently unoriented as suggested by the replica. It is difficult to resolve individual particles except in areas showing orientation. Some improvement over the collodion replica in showing surface structure is believed due to the use of acetone as the solvent for the lacquer instead of the less volatile solvent, amyl acetate, used with the collodion. Evaporation of the solvent occurred before the lacquer could penetrate deeply into the body of the clay.

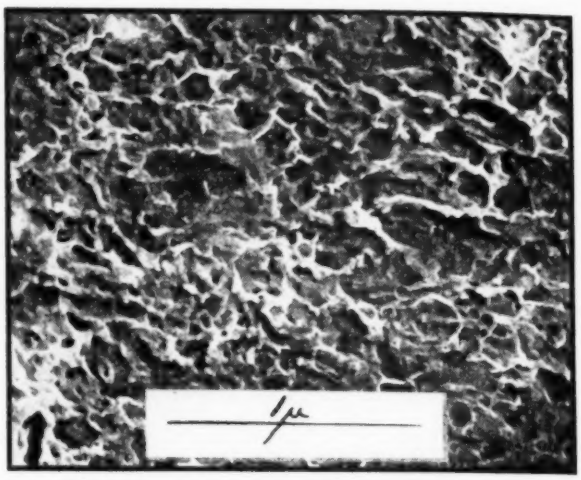


FIG. 5. Clay *A*. Collodion replica after treatment in 48 percent hydrofluoric acid. No tubular particles can be seen.

The structure found on Duco-silica replicas of clay *B* is not unlike that found on the collodion replicas of clay *A*. Instead of obtaining a true surface replica a pattern was formed which may be related to the penetration of the Duco lacquer into the body of this highly porous clay. The result is the fibrous structure seen in Fig. 7. Duco-silica replicas of dispersions of this same clay on glass slides showed how this transition from accurate replication of particles separated on the

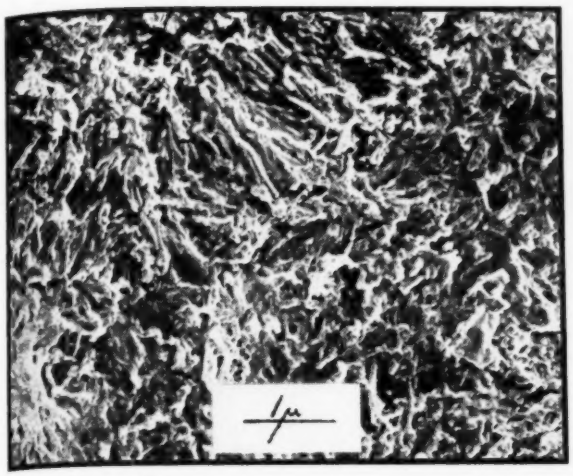


FIG. 6(a). Clay *A*. Duco cement-silica replica showing area of oriented tubes in upper left. Shadowing angle: 20 degrees.

FIG. 6(b). Clay *A*. Duco cement-silica replica showing oriented tubes. Shadowing angle: 20 degrees.

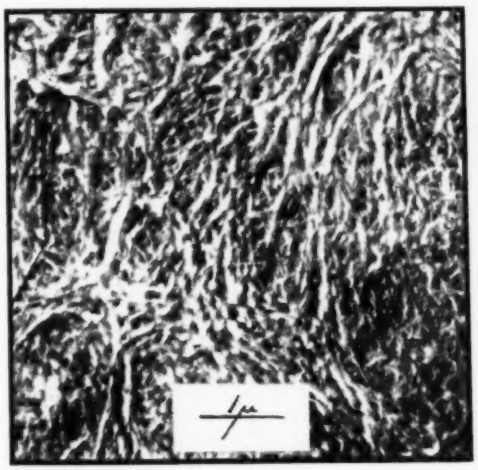


FIG. 7. Clay *B*. Duco cement-silica replica. The fibrous structure is caused by penetration of the laquer into the clay. Compare with the collodion replica of clay *A*, Fig. 5. Shadowing angle: 45 degrees.

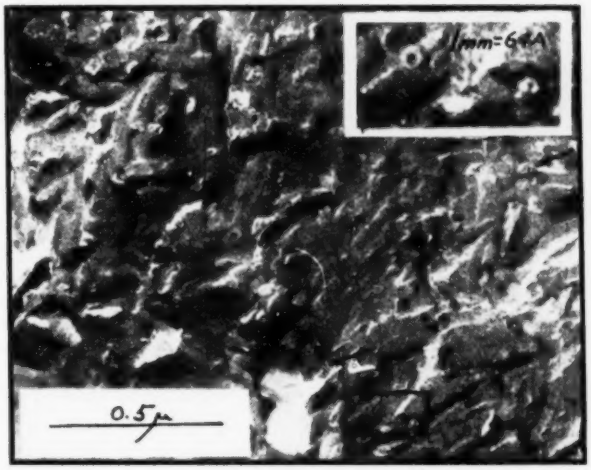


FIG. 8. Clay *A*. Preshadowed replica of fresh fracture. Inset shows tube ends at higher magnification. Shadowing angle: 10 degrees.

slide to the type of structure seen in Fig. 7 can occur as more tubes are piled up to form several layers of particles in random orientation. This type of replica may give some indication of the relative porosities of different clays but is obviously useless in studying surface structure.

### 3. Preshadowed Replicas

In Fig. 8 are seen the outlines of tubular particles in clay *A* as defined by the preshadowing technique. The arrows indicate tubes in a vertical or nearly vertical position. One area, outlined in ink, has been enlarged optically to show this structure in greater detail. The

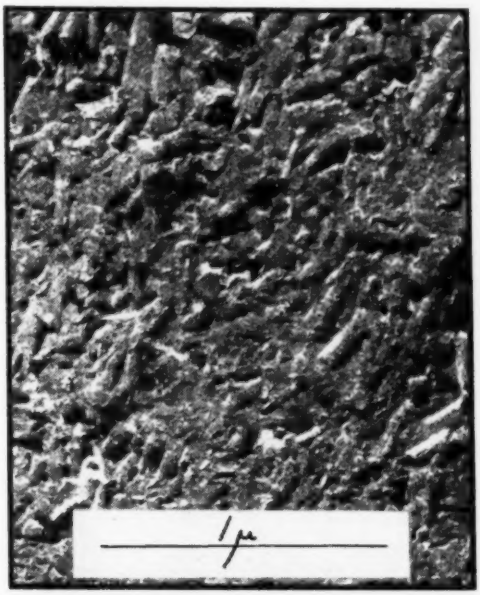


FIG. 9. Clay *B*. Preshadowed replica. Surface cut with knife to obtain flat surface. Shadowing angle: 20 degrees.

FIG. 10. Clay *B*. Preshadowed replica of surface polished and etched in 48 percent hydrofluoric acid. Inset shows laths similar to those found in the dispersed clay, Figs. 2(a) and 2(b). Arrow (*B*) shows a tube in a nearly vertical position. Shadowing angle: 20 degrees.

rings, from 250 to 300 A in diameter, agree in size with the diameter of many of the tubes found in the dispersed sample. The wall thickness, about 40 A, is also in agreement. Keeping in mind the appearance of the dispersed clay as shown in Fig. 1, it appears that this replica presents an accurate picture of the fracture surface.

Figure 9 illustrates the surface of clay *B* after cutting with a knife to obtain a flat surface. In some areas individual tubes are more clearly defined than in others. This is due to deformation and tearing of some particles at the surface. At lower magnifications the over-all structure due to the knife blade can be seen in the micrograph. It will be noted that the tubes appear unoriented. A few tube ends can be seen but in general the knife appears to have destroyed this fine structure.

Preliminary attempts at etching polished clays before replication have been rewarding. Figure 10 illustrates the results obtained with a 20-second etch in 48 percent hydrofluoric acid. The tubes are very clearly defined. The area in the rectangle shows some particles aligned so that the open ends of the tubes are visible. The insert shows this area at higher magnification. Arrow *B* shows a single tube in a nearly vertical position. The laths (*A*) were probably formed by uncurling of some tubes. Their size is in good agreement with similar laths found in the dispersed clay, Fig. 2. The width of the laths indicates that the size of the original tubes was about

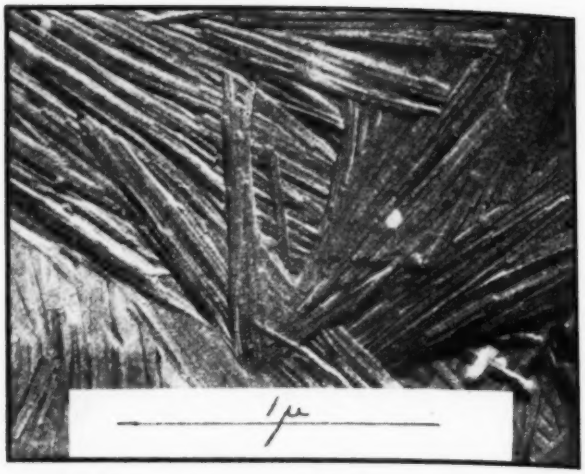


FIG. 11. Attapulgite. Preshadowed replica of fresh fracture illustrating the quality of replicas obtained by using evaporated carbon films to support the shadowing metal. Shadowing angles: 15 degrees and 45 degrees.

600 A in diameter, a value within the range of sizes found for tubes of this sample.

Figure 11 is included to show the excellent quality of replicas prepared by using the preshadowing technique with a supporting film of evaporated carbon.

## SUMMARY

The preshadowing technique is essential for the preparation of replicas of surfaces such as clays which cannot be subjected to heat or pressure and which are too porous to permit the use of laquers. The use of platinum to form the replica permits the use of hydrofluoric acid to remove the clay. The high resolution possible with this technique is necessary for detection of the fine structure of tubular endellite.

Replica studies of some typical bulk endellites, known to be tubular in the dispersed state, have shown them to consist of tubes for the most part unoriented.

Although porous bulk clays preclude the use of plastic lacquers for a study of surface structure, these lacquers can be used to strip surface layers of clay particles which are best suited for examination by means of stereo-electron micrographs. Because of penetration of the laquer into the body of the clay some measure of the degree of porosity may be obtained by the use of one-step plastic or Duco cement-silica replicas after removal of the clay from the plastic in hydrofluoric acid.

## ACKNOWLEDGMENT

The authors are indebted to T. F. Bates, whose interest in the electron-microscope study of clays was responsible for this study, and to Miss Ann Thomas and Mrs. Ann Comer who prepared many of the replicas.

# Letters to the Editor

## Velocity Spectrography of Electron Dynamics in a Traveling Field*

O. T. PURL AND H. M. VONFOERSTER
*University of Illinois, Urbana, Illinois*
(Received October 18, 1954)

IN experimental studies of uhf modulated electron beams, it is sometimes quite useful to have an accurate picture of the velocity distribution of the electrons at a given point of interest along the beam during one complete cycle.

An analyzing system accomplishing this purpose is schematically drawn in the section labeled "Analyzer" in Fig. 1. This system consists of two main parts—a phase deflector and a velocity spectrograph. At the point of observation, the beam is sinusoidally deflected in the vertical direction by a pair of shorted lecher wires[1] excited at the same frequency at which the circuit modulating the electron beam is driven. The velocity spectrum of each phase element is spread out horizontally by an electrostatic field existing between 63.5° sections of two coaxial cylinders. Hence, the resulting spectrograms, displayed on a cathode-ray tube screen, have an ordinate proportional to the sine of the phase, with the abscissa proportional to the ac velocity. If a field-free region separates the observation point and the point of interest, a simple linear transformation can be carried out to obtain a spectrogram at the point of interest.

Currently this analyzer is employed in an over-all investigation of the dynamic behavior of electrons in the beam of a traveling wave tube. In this short note, however, its usefulness may be demonstrated with examples of electron dynamics taking place near the input end of the tube.

In tubes where a strong attenuating region separates the input from the output under certain conditions, the signal at the input will not yet be strongly affected by the beam. This will be particularly true if the current density of the beam is very small. Where such a condition exists, the electronic motion will be governed by an almost unattenuated traveling field, for which a theoretical treatment can easily be developed.

Two situations are particularly simple, one where the unperturbed electrons are in perfect synchronism with the traveling field, and another where there is a strong asynchronism between these two velocities.

*Synchronism.*—At synchronism, the injection speed of the electrons equals the velocity of propagation of the signal along the helix, so that an observer moving with the velocity of the unperturbed electrons will see a stationary sinusoidal electric field. Such an observer can exactly compare the motion of each electron with the motion of a pendulum,[2] i.e., a mass point under the influence of gravitation, constrained in its motion to the periphery of a vertical circle and having an angular amplitude corresponding to the start phase of the electron in the cycle. Since initially all electrons are evenly distributed over all phases, the analogy is complete if we assume a large number of such pendulums initially evenly distributed around the periphery. The well-known solution of the equation of motion for each electron in the cycle is then the elliptic integral of the first kind. Electrons starting near the potential minimum approximate a sinusoidal oscillation about the zero point, with a period given by

$$T = 2\pi(m\lambda_g/e2\pi E_z)^{\frac{1}{2}}, \qquad (1)$$

where $\lambda_g$ is the guide wavelength and $E_z$ represents the amplitude of the longitudinal field strength on the axis of the helix. The electronic charge to mass ratio is $e/m$.

If the time $t_0$, during which the traveling field is acting upon the electrons, is shorter than $T/2$, an observer located at the potential minimum will see all the electrons belonging to one-half of the cycle streaming in one direction, the other half in the other direction. For $t_0 = T/2$, electrons in the vicinity of the potential minimum will come to a stop, and for $t_0 > T/2$, they will stream back toward their original start position—in strong contrast to the behavior of electrons in the drift space of a klystron where, without space charge, retardation of electrons does not occur.

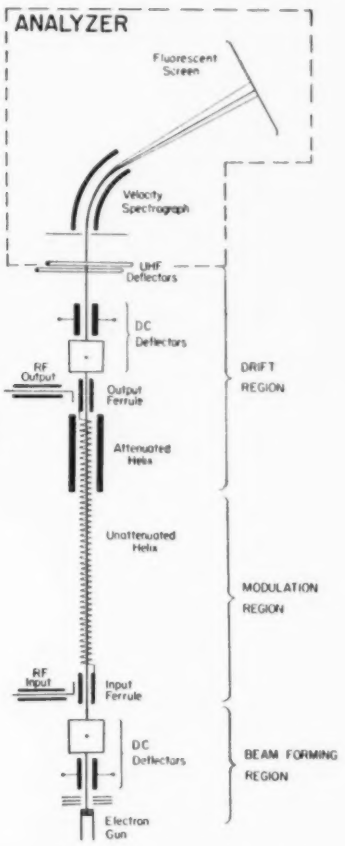


FIG. 1. Schematic diagram of a system for studying the modulation of an electron beam by a traveling field.

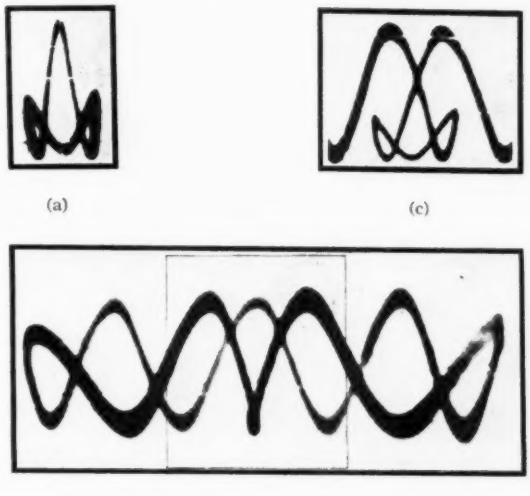


FIG. 2. Spectrograms depicting three moments of electron oscillations in a beam modulated by a synchronous traveling field. (a) Forward motion ($t_0 = 1.81$ mμs; $T = 17.8$ mμs). (b) Stop point ($t_0 = 6.54$ mμs; $T = 13.1$ mμs). (c) Backward motion ($t_0 = 6.54$ mμs; $T = 11.3$ mμs). (The traces of the electrons around the potential maximum have been removed to emphasize the effects near the potential minimum.) Abscissa is proportional to ac velocity with zero value at symmetry line. Ordinate represents the sine of the arrival phase at the observation point (uhf deflector). Synchronous beam voltage 2920 volts, signal frequency 3000 mcs.

In order to make observations of these and other related processes in the input section of a traveling wave tube, the helix of a X-190S† tube operating at about 3000 mcps is used as a modulator. This tube was modified by shifting the attenuator to the end of the helix and making the length of the input section variable by changing the length of the attenuator.

The three instances of electron motion as described above are captured in the three spectrograms presented in Figs. 2(a)–(c). A bilateral symmetry was chosen to suggest the bilateral symmetry of the pendulum analogy referred to earlier where the symmetry line represents zero velocity in the moving coordinate system. The bottom point on this line shows the electron in stable equilibrium at the potential minimum, and the top point the electron in unstable equilibrium at the potential maximum. In Fig. 2(a) electrons along the whole cycle are just developing momentum ($t_0/T=0.102$). Figure 2(b) shows about the instant when electrons around the potential minimum—all those within an amplitude of about 30°—have come to a stop ($t_0/T=0.500$), whereas later in 2(c) ($t_0/T=0.577$) electron having an amplitude between approximately ±90° have reversed their velocity and are streaming back to their original start position [note reversal of Fig. 2(a)], while those having an amplitude greater than ±90° are still streaming in the forward direction. In order to emphasize the process under investigation, the last spectrogram is only a detail of the whole spectrum and corresponds to a velocity range as indicated by the rectangle drawn in spectrogram 2(b). Since

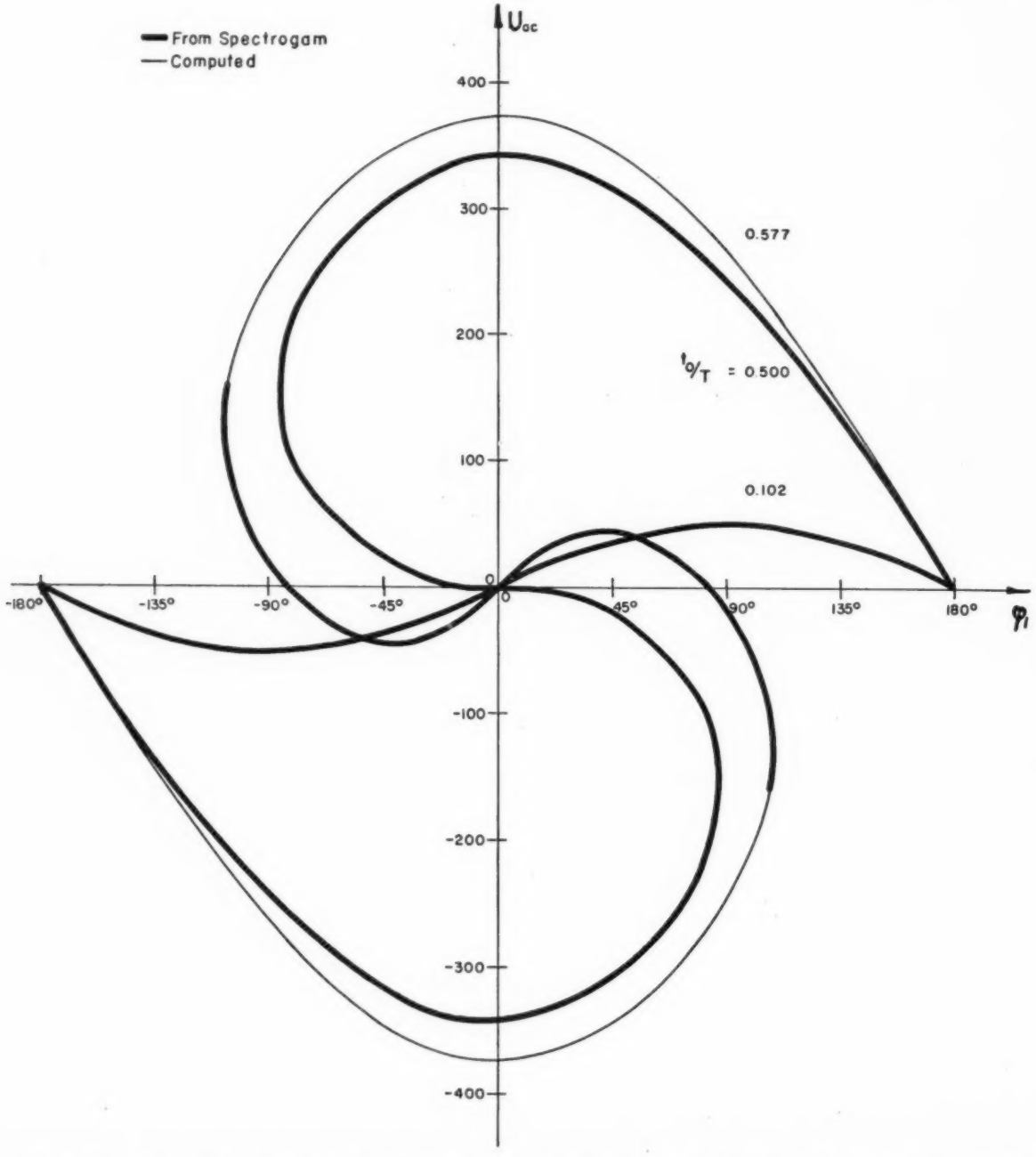


FIG. 3. Velocity distribution at the point of interest (end of unattenuated helix) obtained from spectrograms of Fig. 2. Abscissa represents arrival phase at point of interest, ordinate the ac energy in volts. Parameter is $t_0/T$. Theoretical curves computed for these cases do not give any appreciable deviations within the limits of this graphical representation.

the attenuator at the end of the helix acts as a drift space separating the point of interest from the observation point and thus accounting for some of the multivaluedness, the spectrograms have been translated back to the point where the electrons emerge into the field free region. In Fig. 3, which plots velocity against phase at this point, comparison can be made with the theoretical expectations for the three values of $t_0/T$ just discussed. While for the smallest of these values it is sufficient to calculate with a sinusoidal approximation, for the other two cases the exact solution had to be used, where in the last case, $T$ was determined by noting the phase of the electrons which have just come to a stop. On the other hand, by computing $t_0$ from the modulation length and beam velocity, and $T$ from Eq. (1) using Pierce's helical sheath relation[3] to find $E$ as a function of power input, the resulting values for $t_0/T$ agree to within 3 percent.

*Asynchronism.*—At strong asynchronism, the displacement of the electrons can be assumed to be negligible. Under this condition, the amplitude, $v_{ac}$, of the velocity modulation of an electron beam caused by the by-passing of a traveling wave field can easily be predicted.

$$\frac{v_{ac}}{v_{0ac}}=\frac{\sin\Phi/2}{\Phi/2}, \tag{2}$$

where $v_{0ac}$ is the ac-velocity amplitude at synchronism and $\Phi$ is the phase displacement of the beam relative to the wave resulting from their different velocities during the time the beam was under the influence of the wave. To demonstrate experimentally this analogy with the beam coupling coefficient[4] in the finite gap, $\Phi$, of a klystron cavity, it suffices to operate only the velocity spectrograph since no phase relationships are to be investigated.

Figure 4 shows a comparison of Eq. (2) with observed values of the ac-velocity amplitude for a wide variation of the dc beam velocity, keeping the input power constant. In this particular case the attenuator is negligibly short (≈2.5 cm long) and the maximum amplitude indicates synchronism for the unattenuated region (≈19 cm long). This may be doublechecked by calculating it from two of the minima.

If, however, some lumped attenuation is present, the maximum represents a compromise between the synchronous velocity in the unattenuated and in the attenuated sections, depending upon the amount of attenuation and the lengths of the sections. This experimental approach can be used to investigate the effects of attenuation upon phase velocity and velocity modulation in traveling wave tubes.

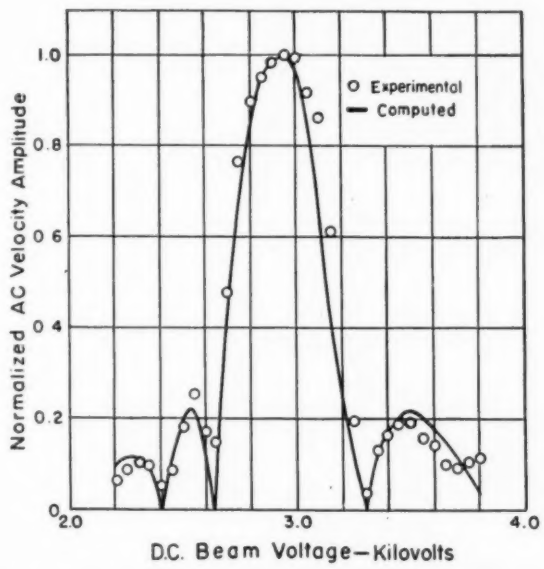


FIG. 4. Velocity modulation of an electron beam by a traveling field as a function of the beam velocity. Circles indicate values measured with the spectrograph. Solid line is computed according to Eq. (2). Length of the modulation region is approximately 19 cm. Phase velocity of the signal along the axis of the helix corresponds to 2920 volts.

* This study is sponsored by the U. S. Air Force Cambridge Research Center.

† Courtesy of Federal Telecommunication Laboratories.

[1] L. R. Bloom and H. M. VonFoerster, Rev. Sci. Instr. **25**, 649–653 (1954).

[2] J. C. Slater, *Microwave Electronics* (D. Van Nostrand Company, Inc., New York, 1950), p. 264 ff.

[3] J. R. Pierce, *Traveling Wave Tubes* (D. Van Nostrand Company, Inc., New York, 1950), p. 27.

[4] K. R. Spangenberg, *Vacuum Tubes* (McGraw-Hill Book Company, Inc., New York, 1948), p. 540 ff.

## A Novel Microwave Attenuator Using Germanium

J. B. GUNN AND C. A. HOGARTH
*Radar Research Establishment, Great Malvern, Worcestershire, England*
(Received November 26, 1954)

THE phenomenon of minority carrier injection into semiconductors by means of rectifying contacts or *p-n* junctions is now well understood and widely applied.[1] The converse effect of carrier extraction has recently been discussed[2,3] and it has been shown that under suitable conditions the concentration of minority and of compensating majority carriers can be greatly reduced by the application of an electric field. It is therefore of interest to note that by employing the principle of the "magnetic rectifier" described by Weisshaar and Welker[4] either phenomenon can, for the first time, be produced in marked degree throughout the volume of an extended semiconductor specimen.

In the magnetic rectifier one of the broad faces of a thin rectangular slab of long lifetime germanium is treated by abrasion and the other by etching, resulting in a large and small value respectively for the recombination velocity $s$ at the two surfaces. Ohmic connections are made to opposite narrow sides of the slab through which a current is passed, and a magnetic field is applied in the plane of the broad faces, normal to the direction of current flow. This magnetic field has the effect of deflecting *both holes and electrons* either towards the surface of large $s$ or away from it, depending on the direction of current flow. In the first case the carrier concentration is decreased (extraction) since the minority carriers and compensating majority carriers are destroyed at this surface, and are generated only slowly elsewhere in the specimen. In the latter case the density is increased (injection) since free carrier pairs excited at the surface are removed from it and can recombine only slowly. These effects can become quite large in high-resistivity material, or in lower-resistivity material at elevated temperatures, when the minority carriers contribute appreciably to the electrical conductivity. Conductivity changes as large as 30 times are readily observed in *n*-type 40 ohm cm 500-microsecond lifetime germanium.

Since the attenuation by germanium of electromagnetic radiation of wavelengths greater than the absorption edge (1.8 microns)

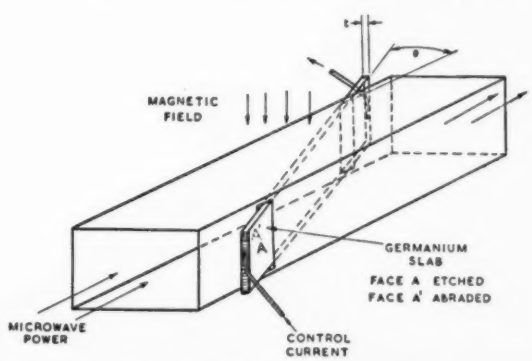


FIG. 1. Schematic arrangement of attenuator.

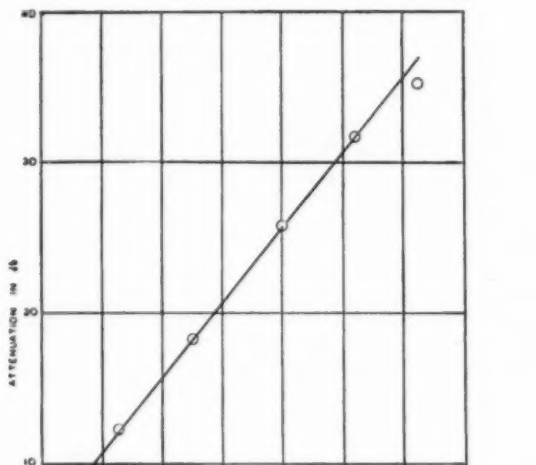


FIG. 2. Attenuation as a function of pulsed control current.

is governed largely by the concentration of free carriers, such large changes of carrier concentration should be useful in the construction of modulating devices such as that described by Gibson.[5] At wavelengths of a few microns the absolute change in carrier concentration is insufficient to produce efficient modulation since the carrier absorption cross section is small. At wavelengths of the order of 1 cm however, the cross section should be large and efficient modulation is possible in specimens of practicable size. In order to utilize this effect we have constructed an electrically controllable microwave attenuator[6] by passing microwave energy through a magnetic rectifier slab which is set across a wave guide.

Figure 1 shows the construction adopted. Slots are cut in the narrow faces of the guide to admit the germanium slab which is set at an acute angle $\theta$ across the guide in order to reduce reflection effects. A field of several thousand oersteds is applied in the direction shown by means of a permanent magnet. Connection to the slab is made by means of thin wires soldered to the end faces. In a typical example using a slab of 40 ohm cm $n$-type germanium with a thickness $t$ of about 0.006 inch and an angle $\theta$ of about 30°, the following results were obtained:

| | |
|---|---|
| minimum attenuation (extracted condition) | 3.7 db |
| maximum attenuation (dc control current of 10 mA) | 17.7 db |
| maximum attenuation (pulsed control current of 60 mA) | 33 db |
| response time (attenuation increasing) | 4/μsec |
| response time (attenuation decreasing) | 1/μsec |
| voltage standing wave ratio | 1.4 to 1. |

Figure 2 shows the variation of attenuation with pulsed control current. The upper limit of attenuation with dc was determined by undesirable heating effects, whereas under pulse conditions no limit was observed for the pulsed current sources available.

Acknowledgment is made to the Chief Scientist, British Ministry of Supply, for permission to publish this paper. British Crown Copyright reserved. Reproduced by permission of the Controller, H.B.M. Stationery Office.

[1] W. Shockley, *Electrons and Holes in Semi-conductors* (D. Van Nostrand Company, Inc., New York, 1950).
[2] Arthur, Bardsley, Brown, and Gibson, Proc. Phys. Soc. (London), (to be published.)
[3] R. C. Prim, Bell System Tech. J. **32**, 665 (1953).
[4] E. Weisshaar and H. Welker, Z. Naturforsch. **8a**, 681 (1953).
[5] A. F. Gibson, Proc. Phys. Soc. (London) **B66**, 588 (1953).
[6] J. B. Gunn and C. A. Hogarth, British Patent Application 16037/54.

## Circularly Polarized Cavities for Measurement of Tensor Permeabilities

E. G. SPENCER, R. C. LECRAW, AND F. REGGIA
*Diamond Ordnance Fuze Laboratories, Washington 25, D. C.*
(Received October 18, 1954)

THE use of a degenerate microwave cavity for measurement of the tensor permeability of a ferrite has been described by other investigators.[1] Experimentally, a small ferrite sample is placed in a cylindrical transmission-type cavity in a position of maximum magnetic rf field, and the cavity is excited by a linear polarized wave. As the steady magnetic field is increased, the degeneracy of the cavity is removed by the interaction of the ferrite with the microwaves, the resonance line being broadened, then separating into two lines near resonance which coalesce at a magnetic field higher than at resonance. The impedance matrix of the cavity system was derived[2] on the basis of Slater's normal mode treatment as was the interaction of the microwaves with the ferrite.[3] The tensor permeability is completely described by quantities which may be computed if the frequency shift and absolute absorption of both resonance lines are measured as a function of the steady magnetic field. With this method, however, the overlap of the two resonance lines makes complete and precise measurements very difficult.

Rather than the normal mode treatment of Lax and Berk, the Bethe-Schwinger[4] perturbation method may be used together with the cavity energy method,[5] which results in

$$\delta f/f = -\delta W/W, \tag{1}$$

where $f$ is the complex frequency and $W$ is the total complex energy in the cavity. If the rf magnetic field is circularly rather than linearly polarized, the above equation becomes, for a small spherical sample placed in a position of zero rf electric and maximum rf magnetic field in a TE mode cylindrical cavity,

$$\frac{\delta f^{\pm}}{f^{\pm}} = \frac{-(\mu \mp K - 1)V_s}{AV_c}, \tag{2}$$

where $V_s$ is the volume of the sample, $V_c$ is the volume of the cavity, $A$ is a constant depending on the geometry of the cavity, $f^{\pm}$ is the complex frequency of the positive and negative circularly polarized waves, and $\mu$ and $K$ are the diagonal and off-diagonal components of the tensor permeability.[6] The real part of $\delta f^{\pm}$ is the frequency shift. The imaginary part may be written as $\delta(1/Q^{\pm})$, where $Q^{\pm}$ is the quality factor of the line. By measuring

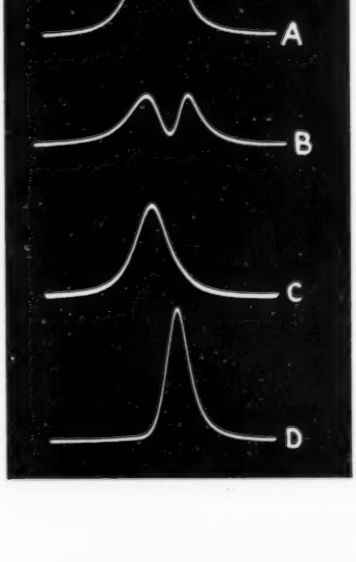


FIG. 1. Cavity resonance lines for $TE_{111}$ mode cylindrical cavity containing 1.34 mm ferrite sphere. The magnetic field is near but below resonance. Curve $A$: linear polarization. Curve $B$: arbitrary elliptical polarization. Curves $C$ and $D$: positive and negative circular polarizations, respectively.

the frequency shifts and the widths of the resonance lines for the two cases of circular polarization as functions of magnetic field, the tensor permeability components are obtained without the restricting difficulty of the overlap of the two resonance lines.

A $TE_{112}$ mode cylindrical-transmission cavity is excited by two linear polarized waves, in space and time quadrature, which set up either a positive or negative circularly polarized resonant mode. Simply by shifting the phase of one of the input waves by 180° the positive or negative circularly polarized mode may be selected. Figure 1 shows oscillograms of the resonance lines using such a circularly-polarized cylindrical cavity containing a 1.34 mm sphere of a magnesium-manganese ferrite,[7] placed in a steady magnetic field below but near ferromagnetic resonance. The oscilloscope gain and the magnetic field are the same for the four curves. Curve *A* shows the cavity excited with linear polarization, curve *B* with an arbitrary elliptical polarization, and curves *C* and *D* with positive and negative circular polarizations, respectively. The two lines overlapping in curve *A* are clearly separated in curves *C* and *D*, thus demonstrating that with this method each mode may be measured without the interference of the other mode.

[1] J. A. Artman and P. E. Tannenwald, Phys. Rev. **91**, 1014 (1953).
[2] A. D. Berk and B. Lax, Convention Record of the Institute of Radio Engineers March 23–26 (1953).
[3] B. Lax and A. D. Berk, Convention Record of the Institute of Radio Engineers March 23–26 (1953).
[4] H. A. Bethe and J. Schwinger, N.D.R.C. Report D1–117 (March, 1943).
[5] C. G. Montgomery, *Techniques of Microwave Measurements*, Radiation Laboratory.
[6] D. Polder, Phil. Mag. **40**, 99 (1949).
[7] General Ceramics Corporation, Keasby, New Jersey, R-1 (formerly called 1331) ferrite.

## Sparked Hydrogen Treatment of Germanium Surfaces*

NICK HOLONYAK, JR.,† AND HARRY LETAW, JR.
*Electrical Engineering Research Laboratory, University of Illinois, Urbana, Illinois*
(Received November 10, 1954)

SPARKED hydrogen treatment was initially suggested as a means of removing the oxide layer from a germanium surface. This experiment has been carried out by subjecting the germanium surface to a discharge induced in low-pressure hydrogen by a Tesla coil. An irreversible increase in surface recombination velocity occurred without material change in channel effects observed on untreated junctions.[1] Germanium specimens exposed to sparked hydrogen behaved as though sandblasted on an atomic scale. At present, it is not known whether or not chemical changes were produced in the germanium surface.

Rectangular rods of germanium and fused indium-germanium junctions (approximately 0.01 cm in radius) were used. The electrical behavior of both types was examined in the gaseous ambients used by Brattain and Bardeen.[2] Following the hydrogen treatment, electrical behavior was re-examined.

Prior to the hydrogen treatment, the rectangular rods had surface recombination velocities[3,4] of the order of 200 to 300 cm/sec. These values increased by at least two orders of magnitude even with short duration (15 sec) hydrogen treatment. The surface recombination velocities of the untreated rods were found to be sensitive to gaseous ambient changes while the treated rods displayed no such response. This can be attributed either to a true lack of sensitivity to ambient changes, or more likely, to changes small in comparison with the greatly increased surface recombination velocity.

The conductances of the untreated rods were found to be sensitive to changes both in gaseous ambient[5] and in illumination. The conductances of the treated rods responded to gaseous ambient changes but were insensitive to changes in illumination. The latter effect could be expected in view of the greatly increased surface recombination produced by hydrogen treatment. It is assumed that carrier concentrations at the two surfaces vary similarly with ambient.

The *p-n* junctions used in this work were examined under pulsed light. It was found that prior to hydrogen treatment, the pulsed light gave rise to a linearly decaying floating potential of approximately 0.8-v peak and duration of roughly 150 $\mu$sec. After hydrogen treatment, the floating potentials were reduced approximately a decade in both magnitude and duration. In some cases, it was impossible to observe the floating potential of the hydrogen treated junctions.

The reverse current-voltage characteristics of the junctions were examined. It was found that hydrogen treatment reduced hole-storage effects without greatly impairing the reverse characteristics. Hydrogen treatment doubled or, at worst, tripled the reverse saturation currents and produced an increase of a factor of two or three in the slopes of the reverse characteristics. The treated junctions still possessed good diode properties with reduced hole-storage effects. Treated junctions were observed to be sensitive to gaseous ambient changes and channel effects.[1]

The effects caused by hydrogen treatment were stable over a period of weeks during which the junctions were subjected to room air and to the gaseous ambients used by Brattain and Bardeen.[2]

The authors thank Professor John Bardeen for advice and encouragement and the Semiconductor Research Staff of this laboratory for their interest. Dr. John Saby and the General Electric Company and Texas Instruments, Incorporated are gratefully acknowledged for providing the germanium specimens used in this work.

* Supported in part by the Office of Naval Research.
† Now at Bell Telephone Laboratories, Murray Hill, New Jersey.
[1] N. Holonyak, Jr., thesis, University of Illinois (1954).
[2] W. H. Brattain and J. Bardeen, Bell System Tech. J. **32**, 1 (1953).
[3] A. Many, Proc. Phys. Soc. (London) **B67**, 9 (1954).
[4] W. Shockley, *Electrons and Holes in Semiconductors* (D. Van Nostrand Company, Inc., New York, 1950).
[5] S. R. Morrison, J. Phys. Chem. **57**, 860 (1953).

## Barkhausen Noise from a Cylindrical Core

D. HANEMAN*
*University of Sydney, Sydney, Australia*
(Received March 15, 1954)

AN expression for Barkhausen noise has been derived by Krumhansl and Beyer,[1] but rather complex methods of analysis were involved and agreement with experiment was poor. Some of the mathematical complexities of the problem may be circumvented by the consideration of a type of sawtooth instead of a sine-wave exciting field, when a direct application of Campbell's theorem, as derived for the usual shot noise case, may be made.

We consider a cylindrical ferromagnetic core of cross-sectional radius $a$ excited by an external field so that it is carried through a hysteresis loop. The core is closely surrounded by a coil across whose terminals the noise is observed. Instead of the usual "flip over" of domains[1-3] we consider in the body of the core a random distribution of sudden flux changes which give rise to a distribution of voltage pulses in the surrounding coil, and take into account the propagation of the flux changes through the core.

The form of the voltage pulse $e_r(t)$ resulting from a single Barkhausen discontinuity occurring in a core such as the above has been derived by Tebble, Corner, and Skidmore.[4]

$$e_r(t)=\frac{-d\varphi}{dt}=\frac{\varphi_0}{2\pi\mu\sigma a^2}\sum_{n=1}^{\infty}\frac{\lambda_n J_0(\lambda_n r/a)}{J_1(\lambda_n)}\exp(-\lambda_n^2\xi), \qquad (1)$$

where $\varphi_0$ is the flux of induction over the cross section of the cylinder due to the discontinuous change in magnetic moment assumed to take place over a small area $\Delta S$ about a point $P$ distant $r$ from the core axis. This corresponds to a discontinuous change in induction $\Delta B_0$ over an area $\Delta S$, and the change in flux

over the whole of the specimen is

$$\varphi_0 = \Delta B_0 \Delta S,$$

which is retarded by eddy currents set up about $P$. The permeability of the core is $\mu$ and $1/\sigma$ is the resistivity. $J_n$ is an $n$th order Bessel function of 1st kind, $\lambda_n$ is the $n$th root of $J_n(\lambda)=0$ and $\xi = t/4\pi\mu a^2\sigma$.

Certain reasonable assumptions[4] have been made in the derivation of Eq. (1). For the following analysis we assume (a) the total change in magnetization is caused by irreversible processes; this assumption is in close accord with reality for fields up to the order of that at which the knee in the hysteresis loop occurs. (b) The discontinuity $X$ yielding $\varphi_0$ is taken sufficiently small for every observed Barkhausen jump to be regarded as composed of an integral number of $X$'s occurring together.

We consider a random distribution of Barkhausen discontinuities occurring in a thin cylindrical shell of radius $r$, thickness $dr$, inside the body of the core ($r<a$), it being assumed that the region over which each magnetization change takes place is sufficiently small to be considered as localized within the thin shell. We expand $e_r(t)$ as a Fourier integral

$$e_r(t) = \frac{1}{\pi}\int_0^\infty S_r(\omega)\cos[\omega t + \psi(\omega)]d\omega. \tag{2}$$

If the range of appreciable values of $e_r(t)$ is limited to $0<t<\Delta t$, then $e_r(t)$ acts, in the low-frequency range to which our considerations are confined, like an impulse of strength

$$M = \int_0^\infty e_r(t)dt = \int_0^{\Delta t} e_r(t)dt; \tag{3}$$

thus

$$S_r(\omega) = M, \quad \psi(\omega) = 0. \tag{4}$$

In order to make a direct application of Campbell's theorem,[5] it is necessary that the ensemble average of $E_r$, the resultant function produced by the superposition of the $e_r(t)$'s, be independent of time. This is the case if the flux through the core is changing such that

$$B = \text{const } t, \tag{5}$$

where $B$ is the magnetic induction.

For fields up to the order of that at which the knee of the hysteresis loop occurs, $H_0$, the slope $\mu$ of the sides of the hysteresis loop is approximately constant, and the dominant change in magnetization is caused by Barkhausen discontinuities, so (5) may be written

$$H = \text{const } t. \tag{6}$$

We thus deal with the case of a type of sawtooth field of period $T$ given by

$$\begin{aligned} &H = \text{const } t; \quad t = 0 \text{ to } T/4, \frac{3T}{4} \text{ to } \frac{5T}{4}, \\ &H = -\text{const } t; \quad t = T/4 \text{ to } \frac{3T}{4}, \frac{5T}{4} \text{ to } \frac{7T}{4}, \end{aligned} \tag{7}$$

giving rise to corresponding voltages $\langle E\rangle$ for $H=\text{const } t$ and $-\bar{E}$ for $H=-\text{const } t$, where $\langle E\rangle$ is supposed measured by a rectifying ac voltmeter. If $F$ is the frequency about which the noise band being measured is centered, we require $F \gg 1/T$ in order to satisfy the above conditions.

We may now assume that on the average $2\pi r K(r)dr$ discontinuities occur per second in the shell of radius $r$. Using Campbell's theorem we have

$$(E_r - \bar{E}_r)^2 = 2\pi r K(r)dr \int_{-\infty}^{\infty} e_r^2(t)dt \tag{8}$$

for the mean square fluctuation about the ensemble average $\bar{E}_r$ which itself is given by

$$\bar{E}_r = 2\pi r K(r)dr \int_{-\infty}^{\infty} e_r(t)dt. \tag{9}$$

From the Fourier integral energy theorem,

$$\int_{-\infty}^{\infty}[e_r(t)]^2 dt = \frac{1}{\pi}\int_0^\infty [S_r(\omega)]^2 d\omega, \tag{10}$$

we obtain, using (8) and (10),

$$\langle (E_r - \bar{E}_r)^2\rangle_{Av} = 2\cdot 2\pi r K(r)dr \int_0^\infty [S_r(\omega)]^2 df \tag{11}$$

where $\omega = 2\pi f$. For a frequency range $F$, $F+\Delta F$, we have

$$\langle (E_r - \bar{E}_r)_{\Delta F}^2\rangle_{Av} = 2\cdot 2\pi r K(r)dr \int_F^{F+\Delta F} [S_r(\omega)]^2 df \tag{12}$$

giving the mean square fluctuation in $E_r$ in the frequency band $\Delta F$.

We next assume, for $\alpha$ a constant, that

$$K(r) = \alpha/2\pi, \tag{13}$$

which means that the number of Barkhausen discontinuities occurring per second in any section of shell of given surface area in the specimen is the same. This assumption does not contradict anything that is known of the Barkhausen effect and appears to be a reasonable one to make.

Integrating over $r$, the average coil voltage

$$\bar{E} = \alpha \int_{-\infty}^{\infty} dt \int_0^a r e_r(t)dr \tag{14}$$

and the Barkhausen noise in the frequency range $F$, $F+\Delta F$, produced by the ferromagnetic core excited by a field of form (7) is

$$\langle (E - \bar{E})_{\Delta F}^2\rangle_{Av} = 2\alpha \int_F^{F+\Delta F} df \int_0^a r S_r^2(\omega)dr. \tag{15}$$

Here $\alpha$ is given by (14) and $S_r(\omega)$ by (4) in terms of $e_r(t)$ which itself is given by (1). Hence,

$$\langle (E - \bar{E})_{\Delta F}^2\rangle_{Av} = \left[2\bar{E} \Big/ \int_0^\infty \int_0^a r e_r(t)dr dt\right]^2 \times \int_0^a r\left[\int_0^\infty e_r(t)dt\right]^2 dr \Delta F, \tag{16}$$

since the field is applied at time $t=0$ and $\int_0^\infty e_r(t)dt$ is frequency independent.

The evaluation of the integrals, when (1) is substituted into (16), is somewhat complicated, but inspection shows that the noise is directly proportional to the mean voltage and the width of the frequency band over which the noise is being measured.

For a sine wave exciting field $H = H_1 \sin\omega t$, the coil voltage is proportional to $\omega\cos\omega t$ which can be regarded as approximately constant in the region of the peak of the cosine wave. It appears not unreasonable to suppose that the formula applies to this region, whence it can be inferred that the noise in the vicinity of the peak of the voltage wave is directly proportional to the frequency. This is also the region where Barkhausen noise is known experimentally to be a maximum in its variation round the excitation cycle. Hence for a sine wave applied field it may be concluded that the maximum Barkhausen noise from a ferromagnetic core is of the order given by (16) being proportional to the frequency of the applied field.

Some arbitrariness exists in assigning a value to $\varphi_0$ in Eq. (1) for particular cores. One method would be to assign its value from experimental measurements of Barkhausen noise, and then use this value for subsequent noise predictions.

The author wishes to thank the research grants committee of the University of Sydney for the award of a studentship, and Dr. R. E. B. Makinson, Dr. K. Landecker, and Dr. G. Builder for their assistance.

* Now at the Division of Radiophysics, Commonwealth, Scientific and Industrial Research Organization, Sydney, Australia.

[1] J. A. Krumhansl and R. Beyer, J. Appl. Phys. **20**, 582 (1949).
[2] S. Goldman, *Frequency Analysis, Modulation and Noise* (McGraw-Hill Book Company, Inc., New York, 1948).
[3] R. M. Bozorth and Joy Dillinger, Phys. Rev. **39**, 353 (1932).
[4] Tebble, Corner, and Skidmore, Proc. Phys. Soc. (London) **A63**, 739 (1950).
[5] S. O. Rice, Bell System Tech. J. **23**, 287 (1944).

# Books Reviewed

**Irradiation Services.** Pp. 27. Argonne National Laboratory, Box 299, Lemont, Illinois. Free.

This booklet describes the facilities and procedures for research irradiations in the CP-5 and EBR reactors and the Argonne cyclotron.

**Thermodynamic Properties of Molybdenum Compounds.** Pp. 8. Climax Molybdenum Company, 500 Fifth Avenue, New York 36, New York. Free.

This booklet tabulates thermodynamic properties on molybdenum and on the dioxide, trioxide, disulfide, trisulfide, carbides, nitride, silicides, and halides of molybdenum.

**Gas Dynamics of Thin Bodies.** F. I. FRANKL AND E. A. KARPOVICH. Translated from the Russian by M. D. Friedman. Pp. 175+viii. Interscience Publishers, New York, 1953. Price $5.75.

This book is intended to aid engineers, graduate students in aerodynamics, and applied mathematicians in their study of the linearized problems of compressible flow theory. The principal topics are the motion of a body of revolution, the steady motion of a wind, unsteady motion and propeller theory, and conical flow. The literature cited is predominantly Russian.

**Mechanical Failures of Metals in Service.** JOHN A. BENNETT AND G. WILLARD QUICK. Pp. 36, Figs. 102, Table 1. National Bureau of Standards Circular 550. (Order from the Government Printing Office, Washington 25, D. C.) Price $.30.

For many years the National Bureau of Standards has been requested to examine metal parts that have failed in service for evidence bearing on the causes of these failures. The examinations have been undertaken at the request of other Government agencies such as the Civil Aeronautics Board, the Interstate Commerce Commission, and the Coast Guard.

This circular describes 35 such cases representing the most frequently observed types of failures. The factors of design, fabrication, or use contributing to these failures are presented. The characteristics by which the various types of fractures can be recognized are discussed, and recommended precautions that should be observed to reduce mechanical failures of metals in service are included.

The volume is well illustrated with photographs of the failures discussed along with photomicrographs showing sources of failure.

**Laplace Transforms for Electrical Engineers.** B. J. STARKEY. Pp. 279. Iliffe and Sons, London, 1954, price 30s, and Philosophical Library, Inc., New York.

It is the author's intention to present, in a physical rather than a purely mathematical vocabulary, an introduction to the theory of the Laplace transformation. The language used is well known to engineers, especially to electrical engineers, who should find the method of explaining the problems quite familiar. The text is designed for those whose mathematical training may not have proceeded beyond the differential and integral calculus and the theory of complex numbers and vector analysis.

Among the topics treated are Fourier transformations, Laplace transformations, functions of a complex variable, and integration in the complex plane. Applications to circuit theory are numerous. Included are discussions of network synthesis, bridge circuits, and electron tubes.

Two appendices are devoted to descriptions of analytic and higher mathematical functions. A thirteen-page table of inverse Laplace transforms completes the book.

**Practical Photography.** B. K. JOHNSON. Pp. 145. Hutchinson's University Library, London, 1954. Price $1.80.

The purpose of this book is to help the amateur photographer to get better results from his camera. This volume does not attempt to cover the entire field of photography but includes the basic scientific information which is essential to good picture making. It does not include lists of available materials and their characteristics but is intended to supplement this information by explaining the principles underlying these characteristics.

After a survey of the history of photography, this book contains sections on photographic chemistry, dark rooms, optics, cameras, exposure times, range finders and enlarging. It also includes sections on such specialized topics as lantern slides, microfilms, photomicrography, stereo-photography, and color photography.

**Physical Measurements in Gas Dynamics and Combustion.** EDITED BY R. W. LADENBURG, B. LEWIS, R. N. PEASE, AND H. S. TAYLOR. Pp. 578+xvi. Princeton University Press, Princeton, New Jersey, 1954. Price $12.50.

This book is volume nine of a series of twelve on the subject "High Speed Aerodynamics and Jet Propulsion," a series which treats the aerodynamic and propulsion problems of high-speed flight and surveys the underlying basic sciences.

The present volume is divided into two parts, the first concerning itself with physical measurements in gas dynamics and the second dealing with the corresponding measurements in combustion processes. In the first section are found detailed discussions of the experimental methods used to measure density, pressure, velocity, and temperature by means of optical, afterglow, spectral-absorption, x-ray, hot-wire, and other techniques. Extensive studies of turbulence measurements and analogue methods making use of the water tank and the hodographic tank are also presented.

The section on physical measurements in combustion processes treats methods of measuring flame temperature, pressure, velocity and burning velocity. In addition there are chapters on flame photography, mass spectroscopy, the spectroscopy of combustion, and the analysis of the combustion wave by pressure effects and spectroscopy.

This book represents the contributions of twenty-two authors and should provide fruitful reading to the experimental researcher.

**Thermoelectric Thermometry.** PAUL H. DIKE. Pp. 90+x, Figs. 30. Leeds and Northrup Company, Philadelphia, Pennsylvania, 1954. Price $1.00.

This is a paperbound review of temperature measurement by the use of thermocouples. It includes discussions of suitable alloys, fabrication, and installation. The processes of measurement, standardization and calibration are critically discussed. Temperature scales for four common thermocouples are provided in an appendix.

Persons desiring large quantities of this book for educational purposes are invited to write to the Leeds and Northrup Company, Advertising Division.

**Engineering Cybernetics.** H. S. TSIEN. Pp. 289+viii. First edition. McGraw-Hill Book Company, Inc., New York, 1954. Price $6.50.

This book gives a comprehensive treatment of the principles of control and guidance systems and may be used either as a reference or textbook by the research engineer.

A large portion of the book deals with subjects not usually included in any book on servomechanisms. Topics included

are elementary servomechanism theory, noninteracting controls, linear systems with time lag, nonlinear servomechanisms, control design by perturbation theory, optimalizing control, noise filtering, control design with specified criteria, ultrastability and multistability, and control of error.

## Errata

The prices of three books reviewed in J. Appl. Phys. **25**, 1444 (1954) were incorrect. The correct prices are: Jost, **Diffusion in Solids, Liquids, and Gases,** $12.00. Rochester and Wilson, **Cloud Chamber Photographs of the Cosmic Radiation,** $10.80. Sommerfeld, **Lectures on Theoretical Physics,** Vol. I, $6.50; Vol. III, $6.80.

## Books Received

**Hugh Roy Cullen.** Ed Kilman and Theon Wright. Pp. 376 +viii. Prentice-Hall, Inc., New York, 1954. Price $4.00.

**Exploring Mars.** Robert S. Richardson. Pp. 261, illustrated. McGraw-Hill Book Company, Inc., New York, 1955. Price $4.00.

**Engineering Cybernetics.** H. S. Tsien. Pp. 289+xii, Figs. McGraw-Hill Book Company, Inc., New York, 1954. Price $6.50.

**Laplace Transforms for Electrical Engineers.** B. J. Starkey. Pp. 279, Figs. Iliffe and Sons Ltd., London, S.E.1, 1954. Price 30s net. Philosophical Library, Inc., New York.

**High-Energy Accelerators.** M. Stanley Livingston. Pp. 157 +viii, Figs. Interscience Publishers, Inc., New York, 1954. Price $3.25.

**The Bomb Survival and You.** Fred N. Severud and Anthony F. Merrill. Pp. 264, illustrated. Reinhold Publishing Corporation, New York, 1954. Price $5.95.

**Relativity for the Layman.** James A. Coleman. Pp. 131, Figs. 24. William-Frederick Press, Inc., New York, 1954. Price $2.75.

**Jet (The Story of a Pioneer).** Sir Frank Whittle. Pp. 320, illustrated. Philosophical Library, Inc., New York, 1954. Price $6.00.

**Development of the Guided Missile.** Kenneth W. Gatland. Pp. 292, illustrated. Philosophical Library, Inc., New York, 1954. Price $4.75.

**Glass Reinforced Plastics.** Phillip Morgan. Pp. 248+vii, illustrated. Philosophical Library, Inc., New York, 1954. Price $10.00.

**Mathematics in Type.** Pp. 58+xii, Figs. 5. The William Byrd Press, Richmond, Virginia, 1954. Price $3.00.

**Television and Radar Encyclopedia.** Edited by W. MacLanachan. Pp. 216+viii, Figs. 225. Second edition. Pitman Publishing Corporation, London, 1954. Price $6.00.

# Announcement

## Conference on Magnetism and Magnetic Materials, June 14–16, 1955, at the Hotel William Penn, Pittsburgh, Pennsylvania

A symposium is to be held by the **Magnetics Subcommittee of the Basic Science Committee of the American Institute of Electrical Engineers** in cooperation with the American Physical Society and the American Institute of Mining and Metallurgical Engineers. The purpose is to bring together those interested in basic and applied work on magnetism.

Presentations of original and review papers will vary from 5 to 30 minutes. It is planned to have exhibits of apparatus of interest to those in attendance, and trips to companies and institutions in the Pittsburgh area.

Programs containing abstracts of all talks will be distributed before the meeting. Abstracts of 200 to 500 words are to be sent to R. M. Bozorth by April 20 to be included in the printed program.

Publication of the complete proceedings is planned. Full papers are to be handed in at the conference; these will be printed in the proceedings subject to the approval of the program committee. Abstracts and oral presentations may be made without publication of full paper if desired.

The meeting is open to all interested. Further information may be obtained from Dr. R. M. Bozorth, Bell Telephone Laboratories, Murray Hill, New Jersey.

## Cover Photograph

The photograph depicts amplification of light in a simple phosphor film (zinc sulfide, manganese-activated) as demonstrated recently by the General Electric Research Laboratory. A chemical vapor-deposition process is used to achieve a uniform, continuous surface. An electric field across the film is created by "sandwiching" it between two conducting layers: the front layer a transparent coating of $TiO_2$, and the back a silver paste. In the demonstration shown, a lantern slide of a television test-pattern is projected on the phosphor surface with a lantern-slide projector utilizing ultraviolet light. Gradual application of a direct-current field causes the original dim image to become many times brighter. (Emission is yellow.) At 100 volts, the number of photons emitted has been measured to be ten times the number of ultraviolet photons striking the surface. Because of the almost linear relation of incident ultraviolet to emitted yellow, the "gray-scale" of the test-pattern is maintained. Application of dc does not of itself cause the phosphor to emit light. Ultraviolet falling on the screen causes faint emission. Amplification occurs only with the combination of both the applied voltage and the incident ultraviolet.

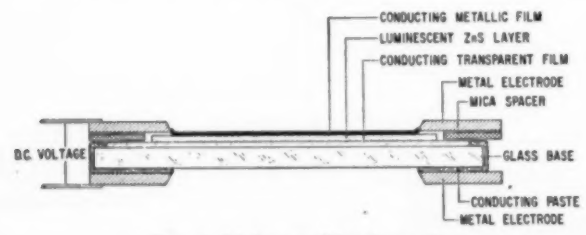


FIG. 1. Light amplification cell.

This photograph and explanation were furnished by Dr. F. E. Williams and D. A. Cusano of the General Electric Research Laboratory.